EPFL

Thèse n° 10 112

Visualization and modelling of dynamic flow in fibrous preforms for liquid composite molding

Présentée le 24 mars 2023

Faculté des sciences et techniques de l'ingénieur
Laboratoire de mise en oeuvre de composites à haute performance
Programme doctoral en science et génie des matériaux

pour l'obtention du grade de Docteur ès Sciences

par

Helena Luisa TEIXIDO PEDARROS

Acceptée sur proposition du jury

Dr A. Hessler-Wyser, présidente du jury
Prof. V. Michaud, directrice de thèse
Prof. C. Binetruy, rapporteur
Prof. C. González, rapporteur
Prof. E. Amstad, rapporteuse

École polytechnique fédérale de Lausanne

2023

Acknowledgements

This research project was carried out at the Laboratory for Processing of Advanced Composites (LPAC) at the Ecole Polytechnique Fédérale de Lausanne (EPFL, Switzerland) and was possible thanks to the Swiss National Foundation grant, SNF n° 200021_182669.

Over the past four years, I have gained invaluable professional and personal experience, which would not have been possible without the amazing people who accompanied me on this journey. I want to express my deepest gratitude to all the talented individuals who introduced me to the world of Composites, and to those who supported and helped me in achieving my goals. Thank you all for shaping me into the person I am today.

First and foremost, I extend my most sincere gratitude to my thesis director Prof. Véronique Michaud for granting me the opportunity to pursue a PhD at EPFL. Her unwavering support, availability and involvement throughout the project were exceptional. I greatly admire her passion and knowledge in the field as well as her dedication into teaching. I will always be impressed about her constant energy and good mood which results in a laboratory environment that feels like a second family. It has really been an absolute pleasure and honor to be part of the LPAC.

I also deeply acknowledge Dr. Baris Caglar, former post-doc of the project, for all his contributions to the Dynaflow discussions even after moving to Delft. I thank him for all the valuable insights, guidance and his great talent in finding interesting scientific stories to tell.

I want to gratefully thank the jury committee Prof. Esther Amstad, Prof. Christophe Binetruy and Prof. Carlos González for their willingness to read, review and evaluate this thesis, with a special mention to Prof. Esther Amstad who agreed to be expert and evaluate my work throughout the entire thesis.

Acknowledgements should also go to Dr. Vincent Revol, for his support on the EVITA X-ray phase contrast system and collaboration in the first stage of this work. I would like to express my heartfelt gratitude to Gary and Albert, the X-ray masters from the PIXE platform, for the valuable assistance and precious help with the X-ray measurements and 3D scan processing.

I am also thankful to the mechanical workshop ATMX team for helping with the design and manufacturing of tools and setups.

Many thanks to Cécile Chariatte for her kindness, availability and help with administrative related questions, to Raphaël Charvet for the IT support which was crucial to pursue this work and to Gavin Waddell for his assistance in the processing room. I gratefully acknowledge Dr. Pierre-Etienne Bourban for the TPs coordination and for engaging nice literature discussions and Dr. Yves Leterrier for ensuring the lab safety and bringing an artistic touch to the lab.

I could not have achieved the outcome of this thesis without the support of my present and former colleagues. For that, a huge thought to all the LPAC members for creating a unique working atmosphere, for the nice desserts in the kitchen table and for making every day enjoyable. A deep thank you to Jeroen, my Dynaflow colleague, for his support and help, in particular during the trips to Alpnach. I would like to give a special shoutout to my office mates: Céline, with whom I shared the love for plants, I am deeply grateful to her for gifting me a printed version of her exceptional thesis which served as a reference and guide; Guillaume, for generously sharing his modelling expertise and making a very valuable contribution to this work, his moral support during the final steps of the thesis was essential; Jialiang for his kindness and support, and for making me discover the Chinese culture. Many thanks also to my neighbor office mates: Alex, for the discussions sharing the difficulties, Massimo for his nice drawings and specially Nour for all the time spent together and the amazing Baklava from Beyrouth that I will always remember. A big thank to the LPAC activities organizers Aigoul, Vincent and Alex, for promoting the dynamism of the lab and for all the coffee breaks with delicious Swiss chocolate. Thank you to Valentin for the constructive discussions about wettability and to Feyza for the help in chemistry-related questions, to Alper for taking care of the plants and to Maryna for her gentle nature.

I am also grateful to all the friends I have made in Switzerland who were essential in my everyday life, and a warm thank you to "la Casita" members for the incredible collaborative, nature-friendly and festive homely atmosphere.

Finally, I would not been able to complete this work without the unconditional support of my family, specially my parents Jordi and Montse, my sister Adriana, my niece Emma and my beloved grandmothers Mia, Ia and Iaia.

And the most special and eternal thanks to my partner Hervé for his infinite patience and huge support, and of course, his much-appreciated great cooking skills!

Abstract

Nowadays, Liquid Composite Molding techniques are often used to manufacture high quality fiber reinforced composite parts at a relatively low cost. These involve an infiltration process, in which a liquid resin is forced to ingress into a dry fibrous porous medium confined into a shaped mold. An optimal control of the material and process parameters is hence sought since multiple factors can contribute to process uncertainties that may compromise the mechanical performance of the final composite part.

Fabrics commonly employed in composite industry are made of dense fiber tows weaved to form textiles that present a dual-scale architecture with micro-pores in between the fibers and meso-voids in between the tows. A dual-scale flow is known to stem from this particular pore distribution from which a void-trapping mechanism arises. Researchers agree with the existence of an optimal injection condition, corresponding to a given flow velocity at which fluid flows with the same speed in micro-spaces in the tows and in meso-spaces in between tows and the amount of voids is minimum. Unfortunately, this optimal condition is specific for a given fabric/resin system, and is mostly found by trial and error. Given the strong complexity of flow in porous media, due to the interplay of several factors such as heterogeneity of the porous network, fluid properties (viscosity, density, and surface tension), wettability, flow displacement speeds, void formation and transport mechanisms as well as the considered length scales, the quantification and analysis of the spatial distribution of fluid flow in porous media is to date a major scientific challenge in composites but also in many other natural and engineering occurrences.

The goal of this thesis is thus to gain a better understanding of flow in fibrous media as found in composite manufacturing, where the porous medium is a non-translucent textile formed of an assembly of fiber tows, and where the infiltrating fluid, due do its viscosity, may show dynamic wetting effects. To this end, the study focuses on (i) designing a novel X-ray based dynamic flow visualization method adapted to carbon based textiles, (ii) developing a two-phase flow model to describe the progressive preform saturation as a function of the flow rate conditions, and identify the velocity dependent capillary pressure and relative permeability, and (iii) investigating the effect of the fluid static wetting properties and the textile pore geometry on flow patterns and pore formation.

The potential of an in-situ X-ray phase contrast imaging technique was investigated, to observe the through-thickness flow progression through translucent and non-translucent preforms in a lab scale

setup, with an imaging time of 9 seconds per shot. This interferometric technique enhances the contrast between low density materials that present a highly heterogeneous microstructure (such as fibrous sheets). We were thus able to successfully track the displacement of a model fluid through different translucent and non-translucent fibrous preforms, thus extracting the fluid saturation as a function of time and position, and investigated the effect of several material parameters on the signal quality.

Alternatively, to increase the resolution of the flow patterns in capillary led flows, we explored conventional X-ray absorption imaging together with contrasting agents added to the fluid. We performed experiments with the same UD carbon fabric and model fluid, over a range of imposed flow rates, and extracted the corresponding saturation curves. We observed that, by increasing the flow rate, as expected, the flow front patterns changed from a capillary led flow in the tows, to a viscous led flow in the meso-spaces. In light of these results, we used a two-phase flow model to identify the hydraulic functions corresponding either to drainage and imbibition displacements and demonstrated its suitability to model unsaturated flows into fibrous porous media, over a range of flow rates. We also compared the multiphase approach to a simpler slug-flow model and demonstrated a good correlation between them through the use of an apparent dynamic contact angle.

Based on the visualization method proposed, we improved it by reducing the acquisition time, increasing the image resolution and conducting full 3D XCT scans before and after impregnation. We analyzed the fluid progression into three woven carbon architectures and related the impregnation quality to the meso-pore geometry using a pore-network model, and the fluid wetting properties. Results showed that the probability of meso-void entrapment in capillary led flows increases when the fabric displays a wide pore size distribution together with throats that form an angle with respect to the fluid direction. The increased wettability of the fluid also enhanced the occurrence of corner flows, thus leading to more void formation when crossing obstacles.

As a conclusion, the in-situ observation of infiltration dynamics, using X-ray scattering or absorption methods, is a suitable tool to elucidate the progressive saturation of carbon fiber preforms, which could be further extended beyond model fluids to the actual resin systems. The resulting saturation curves, coupled to higher resolution static 3D tomographs, can be exploited using a multiphase flow approach to identify the relevant hydraulic parameters, as a function of the flow conditions, paving the way for a systematic analysis of dynamic wetting and void formation in composite processing.

Keywords: liquid composite molding, resin flow, carbon fibers, fibrous preforms, dual-scale flow, capillary effects, dynamic saturation, two-phase flow modelling, wettability, void formation, X-ray imaging.

Resumé

De nos jours, les techniques de moulage de composites par voie liquide sont souvent utilisées pour fabriquer des pièces renforcées de fibres de haute qualité à un coût relativement faible. Elles impliquent un processus d'infiltration dans lequel une résine liquide est forcée à pénétrer dans un milieu poreux fibreux sec, confiné dans un moule de forme donnée. Un contrôle optimal des paramètres du matériau ainsi que du procédé est requis, car de multiples facteurs peuvent entraîner des incertitudes dans le procédé, qui peuvent compromettre la performance mécanique de la pièce composite finale.

Les tissus couramment utilisés dans l'industrie des composites sont constitués de mèches de fibres compactes, tissées pour former des textiles qui présentent une architecture à double échelle avec des micro-pores entre les fibres et des méso-pores entre les mèches. Il est connu que l'écoulement à double échelle qui résulte de cette distribution particulière des pores engendre un mécanisme de création de vides. Les chercheurs s'accordent sur l'existence d'une condition d'injection optimale, correspondant à une vitesse d'écoulement donnée à laquelle le fluide s'écoule avec la même vitesse dans les micro-pores des mèches et dans les méso-pores entre les mèches, pour laquelle la porosité est minimale. Malheureusement, cette condition optimale est spécifique pour chaque combinaison de tissu/résine et est le plus souvent trouvée par tâtonnement. Étant donné la grande complexité des écoulements dans les milieux poreux, due à l'interaction de facteurs tels que l'hétérogénéité du réseau poreux, les propriétés du fluide (viscosité, densité et tension superficielle), la mouillabilité, les vitesses de déplacement de l'écoulement, les mécanismes de formation et de transport des porosités ainsi que les échelles de longueur considérées, la quantification et l'analyse de la distribution spatiale de l'écoulement des fluides dans les milieux poreux constituent à ce jour un défi scientifique majeur dans le domaine des composites mais aussi dans de nombreux autres phénomènes naturels ou d'ingénierie.

L'objectif de cette thèse est donc de mieux comprendre l'écoulement dans les milieux fibreux tels qu'on les trouve dans la fabrication de composites par voie liquide, où le milieu poreux est un textile non translucide formé d'un assemblage de fibres, et où le fluide infiltré, en raison de sa viscosité, peut présenter des effets de mouillage dynamique. À cette fin, l'étude se concentre sur (i) la conception d'une nouvelle méthode de visualisation de l'écoulement dynamique basée sur les rayons X et adaptée aux textiles à base de fibres de carbone, (ii) le développement d'un modèle d'écoulement biphasique pour décrire la saturation progressive de la préforme en fonction des conditions de débit, et identifier la pression capillaire et la perméabilité relative dépendant de la vitesse, et (iii) l'étude de l'effet des

propriétés de mouillage statique du fluide et de la géométrie des pores du textile sur les schémas d'écoulement et la formation de pores.

Le potentiel d'une technique d'imagerie in-situ par contraste de phase aux rayons X a été étudié, afin d'observer la progression de l'écoulement à travers l'épaisseur de préformes translucides et non translucides dans une installation à l'échelle du laboratoire, avec un temps d'imagerie de 9 secondes par acquisition. Cette technique interférométrique améliore le contraste entre les matériaux de faible densité qui présentent une microstructure très hétérogène (comme les couches fibreuses). Nous avons ainsi pu suivre avec succès le déplacement d'un fluide modèle à travers différentes préformes fibreuses translucides et non-translucides, extrayant ainsi la saturation du fluide en fonction du temps et de la position, et avons étudié l'effet de plusieurs propriétés des matériaux sur la qualité du signal.

Alternativement, pour augmenter la résolution des schémas d'écoulement dans les débits capillaires, nous avons exploré l'imagerie conventionnelle par absorption de rayons X en ajoutant des agents de contraste au fluide. Nous avons réalisé des expériences avec le même tissu UD en carbone et le même fluide modèle, sur une gamme de débits imposés, et extrait les courbes de saturation correspondantes. Nous avons observé que, en augmentant le débit, la morphologie du front d'écoulement change, passant d'un écoulement capillaire progressant d'abord dans les mèches à un écoulement visqueux progressant d'abord dans les méso-espaces comme prévu. A la lumière de ces résultats, nous avons utilisé un modèle d'écoulement biphasique pour identifier les fonctions hydrauliques correspondant aux déplacements de drainage et d'imbibition et nous avons démontré son aptitude à modéliser les écoulements non saturés dans les milieux poreux fibreux sur une gamme de débits. Nous avons également comparé l'approche multiphasique à un modèle d'écoulement saturé plus simple ("slug-flow") et démontré une bonne corrélation entre les deux grâce à l'utilisation d'un angle de contact dynamique apparent.

Sur la base de la méthode de visualisation proposée, nous avons proposé des améliorations en réduisant le temps d'acquisition, en augmentant la résolution de l'image et en réalisant des scans XCT 3D complets avant et après l'imprégnation. Nous avons analysé la progression du fluide dans trois architectures de tissus de carbone et avons relié la qualité de l'imprégnation à la géométrie des mésopores en utilisant un modèle de réseau de pores, et aux propriétés de mouillage du fluide. Les résultats ont montré que la probabilité de piégeage des mésopores dans les flux capillaires augmente lorsque le tissu présente une large distribution de la taille des pores ainsi que des constrictions qui forment un angle par rapport à la direction du fluide. L'augmentation de la mouillabilité du fluide a également favorisé l'apparition d'écoulements en coin, entraînant ainsi une plus grande formation de vides lors du franchissement d'obstacles.

En conclusion, l'observation in-situ de la dynamique d'infiltration, en utilisant les méthodes de diffusion ou d'absorption des rayons X, est un outil approprié pour élucider la saturation progressive des préformes en fibre de carbone, qui pourrait être étendu au-delà des fluides modèles aux systèmes de résine réels. Les courbes de saturation résultantes, couplées à des tomographies 3D statiques à plus

haute résolution, peuvent être exploitées en utilisant une approche d'écoulement multiphasique pour identifier les paramètres hydrauliques pertinents, en fonction des conditions d'écoulement, ouvrant la voie à une analyse systématique du mouillage dynamique et de la formation de vides dans la fabrication de composites.

Mots-clés: moulage de composites par voie liquide, flux de résine, fibres de carbone, écoulement à double échelle, effets capillaires, saturation dynamique, modélisation d'écoulement diphasique, mouillabilité, formation de porosités, imagerie rayons X.

Contents

Acknowledgment . . . iii
Abstract . . . v
Resumé . . . vii

List of Figures **xv**

List of Tables **xix**

Abbreviations **xxi**

Symbols **xxiii**

Glossary **xxvii**

1 Introduction **1**
1.1 Motivation . . . 1
1.2 Objectives . . . 3
1.3 Structure and approach . . . 4

2 State of the art **7**
2.1 Polymer matrix composites . . . 8
2.1.1 Fiber reinforced polymer composites . . . 8
2.1.2 Complex composite systems . . . 10
2.2 Liquid composite molding techniques . . . 11
2.2.1 Liquid composite processing . . . 11
2.2.2 Defects in LCM . . . 12
2.3 Flow through porous media . . . 13
2.3.1 Fluid flow modelling . . . 13
2.3.2 Capillary effects . . . 15
2.3.3 Dual-scale flow . . . 17
2.4 Modelling of unsaturated flows . . . 20
2.4.1 Slug-flow assumption . . . 20
2.4.2 Unsaturated flow . . . 24
2.4.3 Additional challenges in flow kinetics . . . 28

2.5 Physics of voids . . . 29
2.6 Impregnation assessment . . . 30
2.6.1 Post-mortem measurements . . . 30
2.6.2 In-situ flow visualization practices . . . 31
2.6.3 Flow visualization by means of X-ray techniques . . . 33
2.7 X-ray phase contrast imaging . . . 35
2.7.1 X-ray Talbot-Lau interferometry . . . 35
2.7.2 Applications . . . 38
2.8 Conclusions . . . 39

3 Materials and methods **41**
3.1 Materials . . . 41
3.1.1 Porous materials . . . 41
3.1.2 Fluids . . . 43
3.2 Impregnation experiments . . . 44
3.2.1 Wettability characterization . . . 44
3.2.2 Impregnation setup . . . 44
3.3 Flow assessment . . . 45
3.3.1 Visualization by means of X-ray phase contrast . . . 45
3.3.2 Acquisition methodology . . . 46
3.3.3 Saturation curve construction . . . 47
3.3.4 Three-dimensional measurements . . . 49
3.3.5 Segmentation of 3D reconstructions . . . 50
3.4 Flow modelling . . . 51
3.4.1 Two-phase flow approach . . . 51
3.4.2 Numerical modelling . . . 54
3.4.3 Parameters identification . . . 54

4 Visualization of dynamic flows with X-ray phase contrast imaging **57**
4.1 Introduction . . . 58
4.2 Materials and methods . . . 58
4.2.1 Materials . . . 58
4.2.2 Methods . . . 59
4.3 Results . . . 60
4.3.1 Validation with a glass fabric . . . 60
4.3.2 Carbon fabric . . . 63
4.3.3 Flax fabrics . . . 66
4.3.4 Polymeric structure . . . 67
4.4 Discussion . . . 68
4.4.1 Effect of the number of layers and fiber diameter . . . 68

4.4.2 Effect of the material composition . . . 69
4.4.3 Effect of the structure . . . 69
4.5 Conclusions . . . 70

5 Assessment of dual-scale flows for impregnation studies 73
5.1 Introduction . . . 74
5.2 Materials and methods . . . 74
5.2.1 Materials . . . 74
5.2.2 Methods . . . 74
5.3 Results and discussion . . . 75
5.3.1 Observation of flow regimes by X-ray phase contrast . . . 75
5.3.2 Observation of flow regimes by X-ray radiography . . . 77
5.3.3 Visualization methods comparison . . . 80
5.3.4 Examples with other systems . . . 81
5.4 Conclusion . . . 83

6 Modelling of dynamic fluid saturation in carbon reinforcements 85
6.1 Introduction . . . 86
6.2 Materials and methods . . . 87
6.2.1 Materials . . . 87
6.2.2 Flow experiments . . . 87
6.2.3 Dynamic saturation assessment . . . 88
6.2.4 Numerical modelling . . . 88
6.2.5 Permeability measurement . . . 90
6.2.6 Parameters identification . . . 91
6.3 Results . . . 91
6.3.1 Flow experiments . . . 91
6.3.2 Numerical simulation and optimization . . . 93
6.3.3 Hydraulic functions as function of capillary regime . . . 96
6.3.4 Comparison with the slug-flow approach . . . 99
6.4 Conclusions . . . 103

7 Effect of wettability and textile architecture on fluid displacement and pore formation 105
7.1 Introduction . . . 106
7.2 Materials and methods . . . 107
7.2.1 Materials . . . 107
7.2.2 Flow experiments . . . 107
7.2.3 Unsaturated length measurement . . . 108
7.3 Results . . . 109
7.3.1 Static contact angle measurement . . . 109

7.3.2 Front displacement behavior in the UD carbon fabric 109
7.3.3 Comparison of front displacements in the UD modified and the twill fabrics . . 114
7.3.4 Void motion phenomena 116
7.3.5 Void morphology and location 118
7.3.6 Relation between void content and unsaturated length 120
7.3.7 Pore network modelling 123
7.4 Conclusions 126

8 Conclusions and perspectives **129**
8.1 Conclusions 129
8.2 Perspectives 132
8.2.1 Flow kinetics in porous media 132
8.2.2 Imaging method 133

9 Annexes **135**
9.1 Annexes - Materials and Methods 135
9.1.1 Infiltrating liquids 135
9.2 Annexes - Modelling of dynamic fluid saturation in carbon reinforcements 136
9.2.1 Optimization procedure to find β, L and N 136

Bibliography **139**

List of Figures

1.1 Schematic of phenomena and parameters influencing the flow kinetics during the infiltration step. 2
1.2 Thesis charter. 5

2.1 Summary of common 2D fiber architectures found in composite processing. 9
2.2 Schematic representation of the steps of a typical RTM process. 12
2.3 Force balance and liquid drop shapes in wetting and non-wetting conditions. 16
2.4 Schematic of wetting and non-wetting fluids in a capillary tube surrounded by air. 17
2.5 Phase diagram of fluid patterns as a function of the viscosity ratio and the capillary number. . . 18
2.6 Influence of the capillary number on the void formation and final part properties based on fluids paths under capillary- and viscous-dominated flow regimes. 19
2.7 Saturation and pressure profiles for slug-flow and unsaturated flow descriptions. 20
2.8 Determination of the capillary pressure drop ΔP_γ in constant pressure and constant flow rate experiments. 22
2.9 Dynamic contact angle as a function of the capillary number for a carbon-epoxy system. 23
2.10 Schematic of the dual-phase approach with delayed impregnation of the tows. 24
2.11 Schematic of drainage and imbibition in fibrous preforms. 26
2.12 Stages of void life during resin infiltration in LCM. 29
2.13 Flow progression recorded by synchrotron radiation computed laminography. 34
2.14 Representation of a Talbot-Lau interferometry setup, using three optical gratings. 35
2.15 Representation of the X-ray wave front perturbations introduced by an object, which are translated into intensity variations and thereafter measured by a detector. 36
2.16 Schematic of the X-ray front and the amplitude transmission function (I_f) perturbations induced by a pure absorber, refractive and scatterer objects. 36
2.17 Representation of a measured intensity I_{pix} in function of the relative grating position over the pattern period (x_g) by a detector. 37

3.1 Reference twill glass translucent fabric. 41
3.2 Reference non-translucent unidirectional and twill carbon fabrics. 42
3.3 Twill and unidirectional flax fabrics. 42
3.4 Pictures of the 3D printed structure. 43
3.5 Impregnation setup. 45
3.6 Images obtained with X-ray phase contrast imaging of a drop of liquid into a carbon fiber. 46
3.7 Representation of the acquisition procedure. 47

3.8 Methodology for the construction of $S(z)$ curve form the grayscale of X-ray acquisition images from an example of a scattering image of an impregnation in a carbon fabric. 48
3.9 Impregnation setup adapted for X-ray tomographic scans. 49
3.10 Segmentation of two-dimensional cross-sections for dry and wet states of the UD carbon fabric. . 51

4.1 Example of flow patterns observed in optical, absorption, refraction and scattering images obtained for the different reinforcements: Twill Glass, UD Carbon, Twill Flax, UD Flax fabrics and the 3D printed structure. 61
4.2 Flow patterns in the twill glass fabric imaged by a digital microscope. 62
4.3 Comparison of $S(z,t)$ curves built from optical and X-ray acquisitions. 63
4.4 $S(z)$ curves taken every 4 acquisitions (corresponding to approximately 37 s) and three reconstructions of the impregnation along the fabric length at three instants. 64
4.5 Comparison of scattering images obtained for the different impregnation configurations for the carbon preform with the corresponding histograms, where volume fraction and number of layers were varied for the carbon. 65
4.6 Comparison of scattering images obtained for the carbon preform impregnation with an increased number of layers with the corresponding histograms. 66
4.7 Comparison of contrast in scattering images through the twill (using 3 and 9 layers) and UD (using 6 and 12 layers) flax fabrics with an increase of fabric layers. 67
4.8 Intensity range of scattering images versus the fabric number of layers. 68
4.9 Scattering images resulting of a rotating the setup 45° and reference at 0°. 70

5.1 Absorption, refraction and scattering images obtained for the UD carbon impregnated with the PEG 16.67% solution. 76
5.2 Superimposed absorption, refraction and scattering images for visualization of flow patterns. . . . 77
5.3 Absorption, refraction and scattering images obtained for the UD carbon impregnated with the PEG 16.67% + CA1 solution. 78
5.4 Meso-void formation observed in absorption images. 79
5.5 Schematic of the influence of the fabric architecture on capillary and viscous flow patterns. . . . 79
5.6 Comparison of histograms for absorption, refraction and scattering images. 80
5.7 Representative absorption images of the twill flax fabric impregnation. 82
5.8 Representative absorption images of the unidirectional flax fabric impregnation. 82
5.9 Visualization of the twill carbon fabric impregnation. 83

6.1 Schematic of the terminology employed in the current chapter. 87
6.2 Saturated permeability results. 90
6.3 X-ray absorption images showing the flow progression at three different times for the four injection conditions. 92
6.4 ΔP pressure measurements. 93
6.5 Experimental and numerical $S(z,t_i)$ curves. 95
6.6 Hydraulic relative permeability function $k_r(S)$. 96
6.7 Hydraulic retention function $S(P_c)$. 97
6.8 Schematic representation of ΔP_γ determination from the saturation and pressure of the fluid phase versus the position z. 100

6.9 Representation of ΔP_γ determination from drainage-imbibition curves. . . . 101
6.10 Drop analysis on a carbon fiber. . . . 101
6.11 Influence of the fluid velocity on the capillary pressure drop and the resulting $\theta(Ca)$ curve. . . . 102

7.1 Original unidirectional, modified unidirectional and twill carbon fabrics. . . . 107
7.2 Droplets of the two model fluids on carbon and glass fibers. . . . 109
7.3 Sequence of images showing the fluid distribution in the unidirectional carbon reinforcement for viscous to capillary dominated flows for the PEG-based solution. . . . 110
7.4 Sequence of images showing the fluid distribution in the unidirectional carbon reinforcement for viscous to capillary dominated flows for the glycerol-based solution. . . . 111
7.5 Flow paths elucidated with a variance filter. . . . 113
7.6 ΔP measurements of UD fabric impregnation experiments. . . . 114
7.7 Sequence of images showing the fluid distribution in the modified unidirectional carbon reinforcement for capillary dominated flows. . . . 115
7.8 Sequence of images showing the fluid distribution in the twill carbon reinforcement for capillary dominated flows. . . . 115
7.9 Example of snap-off and break up from three pictures taken at successive times. . . . 116
7.10 Void motion in the TW fabric under capillary dominated flows. . . . 117
7.11 3D view of an entrapped void in a channel constriction. . . . 117
7.12 3D volume rendering of meso-void distribution for capillary driven tests. . . . 118
7.13 Meso-void location in two UD fabric layers stacking configurations. . . . 119
7.14 Void fraction and unsaturated length resulting from the UD fabric impregnation with PEG and glycerol-based fluids as a function of capillary number. . . . 120
7.15 Void fraction and unsaturated length resulting from the UD, UDM and TW fabrics for capillary dominated flows impregnations with PEG and glycerol-based fluids as a function of capillary number. . . . 121
7.17 Unsaturated length versus void fraction and the W/D ratio for the low speed impregnation of the UD, UDM and TW fabrics. . . . 122
7.18 3D views of the pore-network of the scanned fabrics (UD, UDM, TW) and corresponding histograms for the pore-body and pore-throat radii as well as pore-throat lengths. . . . 124
7.19 3D histograms of the angle of throats with respect to the z-direction and the throat volume for UD, UDM and TW fabrics. . . . 126

8.1 Comparison between X-ray and neutron attenuation. . . . 134

9.1 Viscosity-temperature curve of the designed fluids and their X-ray attenuation. . . . 135
9.2 Scatter plot matrix of the minimal error difference as a function of β, L and N fitting parameters. 137
9.3 Example of saturation curves for test #3, showing self-similar curves and test #4 with curves with more different shapes over time. . . . 138

List of Tables

2.1 Hydraulic functions descriptions. 27

3.1 Properties of test fluids. 44

4.1 Fibrous reinforcement properties. 58
4.2 Impregnation experiments visualized by X-ray phase contrast. 59
4.3 Comparison of flow progression during in-situ flow imaging. 63
4.4 Absorption and refraction properties of carbon, silica and cellulose at 60 keV. 69

5.1 Considered fluids properties. 74
5.2 Impregnation experiments. 75
5.3 Advantages and disadvantages between the studied visualization methods. 81

6.1 Impregnation experiments. 88
6.2 Selected instances for optimization. 94
6.3 Parameters identification results. 94

7.1 Impregnation experiments. 108
7.2 Inter-bundle over bundle width results. 122
7.3 Pore network model results. 124

Abbreviations

CA	Contrasting Agent
DP	Differential phase
FEM	Finite Element Method
FRPC	Fiber Reinforced Polymer Composites
LCM	Liquid Composite Molding
nw	Non-wetting phase
PEG	Poly(Ethylene Glycol)
PMMA	Poly(Methyl Methacrylate)
PNM	Pore Network Model
REV	Representative Elementary Volume
RTM	Resin Transfer Molding
SAS	Small Angle Scattering
UD	Unidirectional
UDM	Unidirectional Modified
T	Transmission
TW	Twill
V	Visibility
WMSE	Weighted Mean Square Error
w	Wetting phase
XCT	X-ray Computed Tomography

Symbols

α	Refers to wetting or non-wetting phase	-
β	Van Genuchten law parameter	m^{-1}
γ	Surface tension	$N \cdot m^{-1}$
δ	Refraction coefficient	-
ΔP_γ	Capillary pressure drop	Pa
ΔP_{app} / ΔP	Applied pressure difference	Pa
η	Viscosity	$Pa \cdot s$
θ	Dynamic contact angle	rad
θ_e	Static contact angle	rad
θ_α	Volume content	-
λ	Brooks and Corey parameter	-
μ	Linear absorption coefficient	m^{-1}
τ	Capillarity coefficient	-
ϕ	Pore space	-
ψ	Slope of L^2 versus t curve	$m^2 \cdot s^{-1}$
ρ	Density	$g \cdot cm^{-3}$
ρ_f	Fiber density	$g \cdot cm^{-3}$
A	Preform cross sectional area	m^2
A_w	Fabric areal weight	$g \cdot m^{-2}$
B	Arrhenius law fitting parameter	$Pa \cdot s$
C	Capacity	Pa^{-1}

Ca	Capillary number	-
Ca_{mob}	Critical capillary number for void mobilization	-
Ca_{opt}	Optimal capillary number	-
c_T	Tanner's coefficient	-
D	Inter-bundle distance	mm
E_a	Activation energy	$\mathrm{J} \cdot \mathrm{mol}^{-1}$
g	Gravitational constant	$\mathrm{m}^2 \cdot \mathrm{s}^{-1}$
h	Preform height	m
h_c	Capillary rise in a tube	m
H_b	Bubbling pressure head	m
H_p	Capillary pressure head	m
I_{pix}	Recorded pixel intensity	-
K	Permeability tensor	m^{-2}
K_{sat}	Saturated permeability	m^{-2}
K_{uns}	Unsaturated permeability	m^{-2}
k_r	Relative permeability	-
M_η	Viscosity ratio	-
M_w	Molecular weight	$\mathrm{g} \cdot \mathrm{mol}^{-1}$
L_f	Fabric length	m
n	Number of fabric layers	-
N	Van Genuchten law parameter	-
p_c	Microscopic capillary pressure	Pa
P_c	Macroscopic capillary pressure	Pa
P_α	Pressure in the phase α	Pa
Q_{out}	Outcoming flow rate	$\mathrm{m}^3 \cdot \mathrm{s}^{-1}$
R	Gas constant	$\mathrm{J} \cdot \mathrm{K}^{-1} \cdot \mathrm{mol}^{-1}$

R_l	Fluid penetrativity	$\mathrm{N} \cdot \mathrm{m}^{-1}$
R_s	Permeability ratio	-
r_f	Fiber radius	μ m
S	Saturation	-
$\dot{S}$	Desaturation rate	-
S_f	Specific surface area	m^{-1}
t	Time	s
T	Temperature	K
u	In-plane speed	$\mathrm{m} \cdot \mathrm{s}^{-1}$
U	Superficial speed	$\mathrm{m} \cdot \mathrm{s}^{-1}$
V_a	Air volume fraction	-
V_l	Liquid volume fraction	-
V_f	Fiber volume fraction	-
W	Bundle width	mm
x	Spatial coordinate	m
y	Vertical spatial coordinate	m
z	Vertical spatial coordinate	m

Glossary

Absorption	X-rays can be absorbed (or attenuated) by materials. Absorption images represent the intensity of X-rays that passed through the materials and reached the detector plate.
Drainage	Refers to the displacement of a wetting fluid by a non-wetting fluid inside a porous medium.
Capillarity	Phenomenon in which a liquid flows in a narrow space without any external force assistance.
Composite	Material made out of two or more different materials presenting synergetic properties.
Contrast	Ability to distinguish differences by means of pixel intensity values in an image.
Density	Substance's mass per unit of volume.
Dual-scale	Textiles present two main pore lengths: a micro-scale porosity inside the compacted tows and a meso-scale porosity in between tows and fabric layers.
Fiber reinforced composite	Polymeric material reinforced with textiles resulting in a final material with outstanding mechanical properties at a relative low weight.
Flow	Continuous movement of a fluid.
Imbibition	Refers to the displacement of a non-wetting fluid by a wetting fluid inside a porous medium. Imbibition is the contrary of Drainage.
Interferometry	Technique using the interference of waves to extract information.
Permeability	Intrinsic property of a porous medium which describes its ability to let a fluid flow through it.
Porous medium	A solid structure with sufficient open space to enable a fluid to pass through it.
Grating	Device with a periodic structure used to diffract an electromagnetic spectrum.
Pore	Empty region of a fibrous reinforcement before impregnation by a resin.

Porosity	Fraction of total free are in the porous media, also equal of total of those non-impregnated pores before impregnation.
Refraction	Redirection of an incident wave when passing from one medium to another. X-rays refraction is very small when compared to attenuation.
Resolution	Resolution quantifies the detail in an image.
Saturation	Fraction of the available pore volume of a porous medium occupied by a fluid.
Segmentation	Processing of images to locate and identify objects and boundaries.
Scattering	Deviation of X-rays from its straight trajectory by localized non-uniformities when passing through a solid medium.
Snap-off	Breakup of a continuous non-wetting fluid due to surface tension, phenomenon influencing residual trapping.
Specific surface area	Total surface area of a solid per its volume.
Surface tension	Property of a liquid surrounded by another fluid to shrink into the minimum surface area possible due to cohesive forces.
Tow	Untwisted bundle of continuous fibers.
Viscosity	Defines the resistance of a fluid to deformation or flow and determines its consistency either thick, stick or semi-fluid.
Void	Remaining empty regions in a fibrous reinforcement after impregnation.
X-ray	High-energy electromagnetic radiation.
Wettability	Measurement of a liquid's ability to wet a solid in the presence of a second fluid and is quantified through the contact angle.

Chapter 1

Introduction

1.1 Motivation

There is a stringent need for the development of lighter and stronger structures, with the aim of reducing the carbon footprint of transportation and thus mitigating the major concern that global warming represents. Fiber Reinforced Polymer Composite materials (FRPC) turn out to be a very attractive alternative given their versatility in terms of mechanical properties and design space. Fibers and polymers can be selected according to the final part requirements, and in terms of manufacturing. Since parts with complex shapes can be produced, the waste and the use of joints or fasteners is significantly decreased. In addition to their excellent mechanical properties, composites offer good resistance to fatigue, moderately high temperature and corrosion, and can even include additional phases to obtain newer "cutting-edge" multifunctional materials with enhanced properties, i.e. self-healing properties [1, 2]. As a result, the ascending demand for customized materials has boosted the composite market in diverse industries such as automotive, aerospace or wind energy among others [3].

Nevertheless, the mechanical properties of composites strongly depend on the adhesion between fibers and the polymer matrix, which is somehow linked to the chosen manufacturing process. Two main routes are mainly employed to embed the stacked fiber sheets in a polymer, namely (i) consolidation of pre-impregnated stacks or (ii) infiltration processing of stacked dry fabric. Liquid Composite Molding techniques, which belong to the second category are widely employed as structural parts with complex geometries can be achieved in a cost-efficient manner [4]. The principle of those processes is to inject a liquid polymeric resin into a dry fibrous preform placed inside a closed mold by applying a pressure gradient. Once the preform is filled, the resin is cured and the composite demolded. During the infiltration step, the liquid has to travel through the whole pore space and it is sought that all the pores end up filled. Hence, this step is crucial and needs to be well controlled to ensure that no defects such as unfilled areas or voids remain before the resin final solidification by curing [5].

For the sake of producing final parts with outstanding properties at minimal cost and time, a large body of research has been carried out to better understand physical phenomena taking place during

the infiltration and therefore better predict and control the flow kinetics [6, 7]. However, even if flow through porous media is a largely studied phenomenon as it occurs in many engineering branches, a thorough understanding has never been reached so far, owing to the interplay of several physical phenomena taking place at different scales thus triggering a very complex process. As presented in Fig. 1.1, textiles employed in composites industry are formed by an assembly of tows containing several thousands of fibers, forming a dual-scale architecture with micro-pores in between fibers and meso-pores in between the tows. Furthermore, when multiple fabric layers are stacked, a complex porous space results. Then, the resin properties (density, viscosity and surface tension) together with the processing parameters such as the injection conditions (constant pressure or flow rate) will have a direct impact on the interaction with the fibrous solid and thus the physics of impregnation.

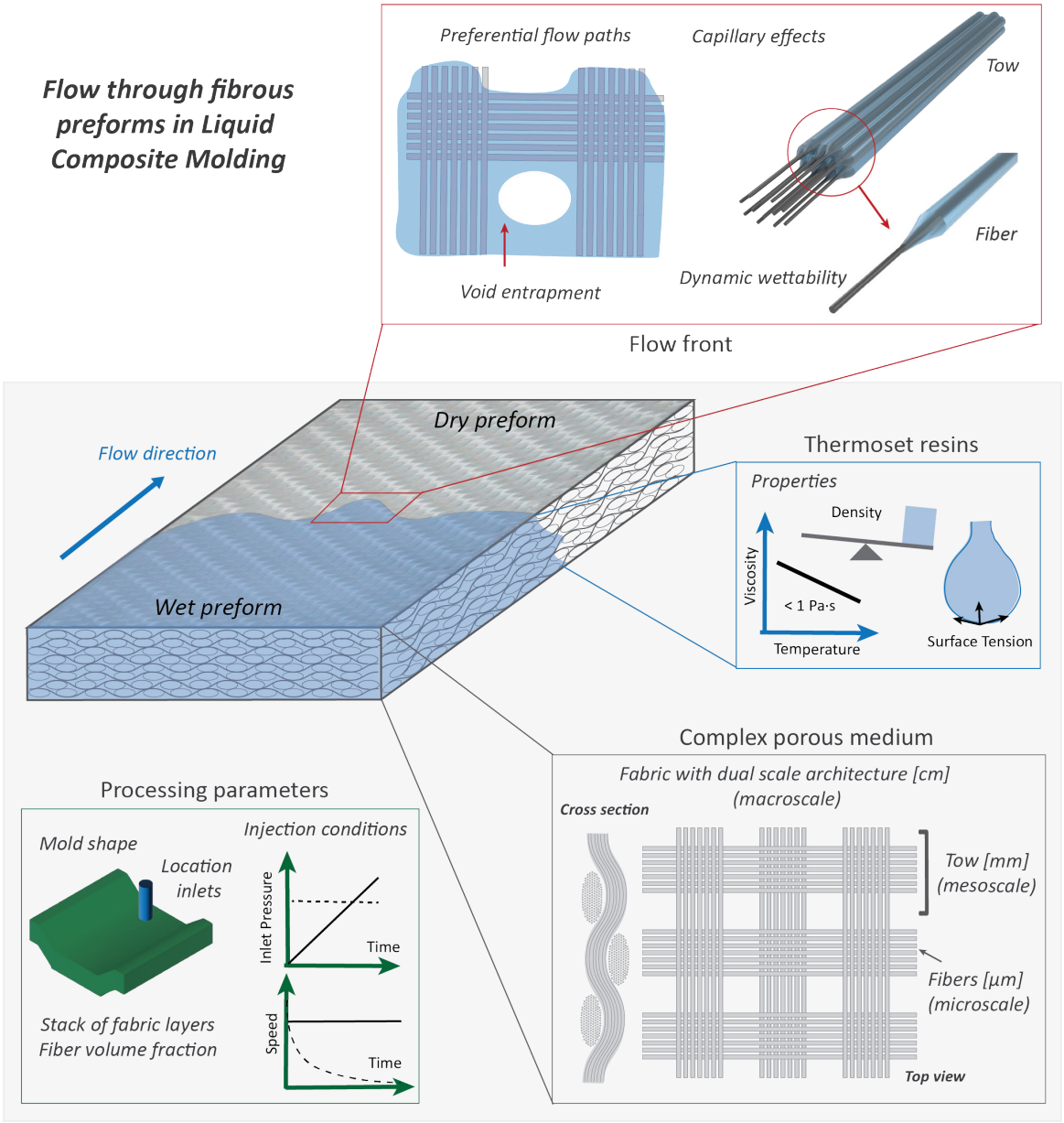

Figure 1.1: Schematic of phenomena and parameters influencing the flow kinetics during the infiltration step.

Researchers sought to assess the role of processing parameters and the geometrical and physical properties of both fibers and polymers. For that, experimental methods based on optical observations of the flow are usually coupled to mathematical models [7]. A special attention is made on visualizing the flow front since researchers found that many phenomena take place there, such as strong capillary forces resulting from the narrow interstices created within compacted tows, a dynamic wettability influenced by the fluid speed and a void entrapment mechanism arising from an inhomogeneous filling which has proved to be the most common flow induced-defect in this type of processing. However, a lack of precise time-resolved experimental tools, e.g. that can observe the flow through non-translucent preforms and of accurate numerical models, e.g. that considers the phenomena from micro to macro-scales, has limited the quantification of fluid kinetics and pore formation.

1.2 Objectives

The goal of this thesis is to deeply probe the dynamics of flow in porous media as applied to advanced liquid composite molding manufacturing. Based on the infiltration characteristics presented in Fig. 1.1, the study focuses on the exploration of physical phenomena occurring during impregnation of fibrous preforms by model resins. The approach is based on an experimental observation of flow patterns, to analyse the correlation between the optimal flow conditions and the materials physical and microstructural properties. The main research questions we aim to address are:

> *Which methodology can be applied to observe fluid flow patterns in LCM processing for a given set of materials, in particular for non-translucent carbon textiles?*
>
> *How to reliably extract the degree of saturation as a function of position and time from the visualization experiments?*
>
> *Which numerical model can be suitable to describe the progressive fluid filling in infiltration experiments, taking into account the flow patterns?*
>
> *How do physical properties such as the fluid wetting characteristics and the porous medium architecture affect the fluid displacement in a fibrous medium?*

To answer those questions, the main research activities are defined as followed:

1. Develop novel, fast and precise experimental methods to visualize the progressive filling of fibrous reinforcements at the macroscale, in particular for non-translucent preforms such as carbon fiber preforms.
2. Evaluate the contrast resolution to assess dual-scale flow patterns typically encountered in textiles.
3. From optical observations, build the saturation curves describing the preform progressive filling.
4. Model the displacement of resin inside the fibrous medium with a two-phase flow approach by using the saturation curves as inputs.

5. By employing the developed techniques, investigate the interplay of specific physical phenomena on flow kinetics as well as pore formation.

1.3 Structure and approach

The diagram on Fig. 1.2 presents the structure of the current research study. The thesis is structured in eight chapters as follows:

Chapter 2. State of the art reviews the research carried out on the analysis of resin flow behavior trough fibrous preforms to describe infiltration in the frame of LCM.

The porous reinforcements, infiltrating model fluids and setups employed as well as the methodology to visualize and model the progressive saturation are presented in *Chapter 3. Materials and methods*.

The *Chapter 4. Visualization of dynamic flows with X-ray phase contrast imaging* explores the potential of X-ray based Talbot-Lau interferometry to visualize through-thickness the impregnation of different fibrous preforms (which nature, architecture and thickness were varied) and a 3D printed structure by conventional model fluids. Scattering images, specific to this technique provided an increased fluid/fabric contrast when compared to conventional absorption, notably for carbon fabrics.

The next *Chapter 5. Assessment of dual-scale flows for impregnation studies* highlights the strengths and weaknesses of X-ray phase contrast on observing dual-scale flows. X-ray phase contrast allows to track the flow progression even with conventional resins, however, it lacks the adequate resolution to depict capillary flows. This is why an alternative solution combining conventional X-ray radiography and contrasting agents added to the model fluid was then adopted.

The following *Chapter 6. Modelling of dynamic fluid saturation in carbon reinforcements* focuses on the modelling of unsaturated curves extracted from the grayscale analysis of the images acquired with the visualization approach presented in the previous chapter. A two-phase flow approach is employed and revealed to be in accordance with the widespread slug-flow assumption.

The *Chapter 7. Effect of wettability and textile architecture on fluid displacement and pore formation* introduces the use of X-ray computed tomography to assess the pore geometry and final void content for different fluid/fabric impregnated systems. Additionally, how wettability and pore space geometry influence flow kinetics and void entrapment mechanisms is discussed with particular emphasis on capillary dominated flows.

Finally, the chapter *Chapter 8. Conclusions and perspectives* summarizes the findings and exposes the project outlook.

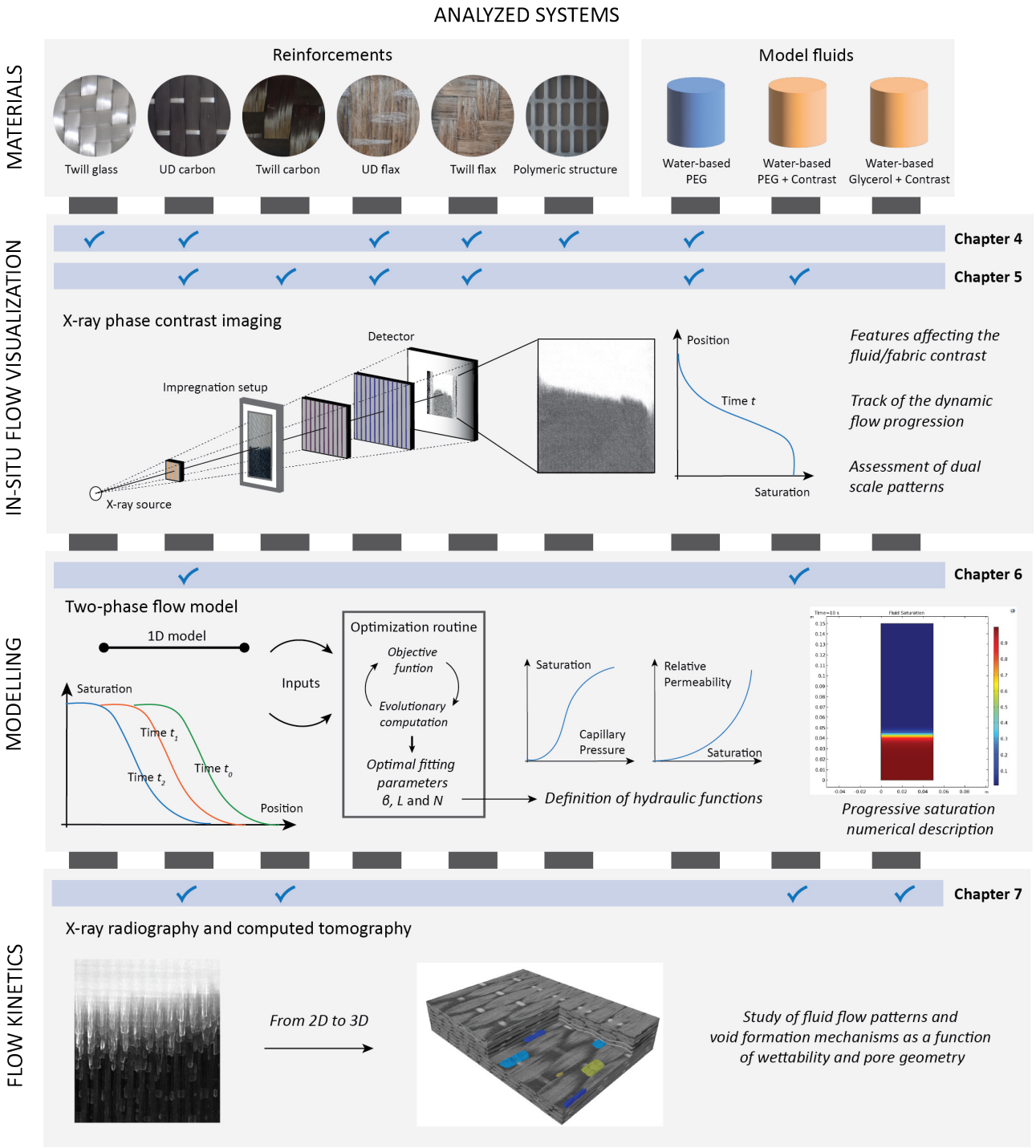

Figure 1.2: Thesis charter.

Chapter 2

State of the art

Composites are a combination of two materials resulting in a new material with specific properties, defined to fulfill a given application. They are either produced by nature such as wood or muscles, or by human beings such as chocolate with hazelnuts or reinforced concrete among an infinity of examples. In particular, fiber reinforced polymers combine thin fibers and polymers to produce lightweight materials that can be easily shaped, and with outstanding mechanical properties. Liquid composite molding (LCM) is one of the most employed techniques to manufacture these composite parts and encompasses a family of processes whereby a liquid resin is infiltrated inside a dry fibrous preform placed inside a closed shaped mold. In order to obtain final parts with desired final properties, a controlled and optimized impregnation is essential. The resin progression can be described by the simultaneous displacement of two fluids (liquid and air) inside a porous medium which is governed by several physical phenomena taking place at different scales and thus triggering a very complex process which has been the aim of intense research. This chapter reviews the state of the art on flow studies approaches by:

- Introducing the different materials constituting fiber reinforced polymer composites (section 2.1),
- Explaining how those materials are manufactured (section 2.2),
- Describing the main physical phenomena taking place in infiltration processes (section 2.3),
- Presenting the common equations and models used to describe fluid flow inside a porous medium (section 2.4),
- Highlighting succinctly the physics of voids arising from the impregnation step (section 2.5),
- Reviewing the different techniques employed by researchers to observe and characterize resin flows (section 2.6).
- In section 2.7, the visualization technique employed in the frame of this thesis is presented.

Part of this chapter has been published as:

Helena Teixidó*, Jeroen Staal*, Baris Caglar, Véronique Michaud. "Capillary Effects in Fiber Reinforced Polymer Composite Proceesing: A review". Frontiers in Materials, Volume 9, 2022 [8].
(*Same contribution)

2.1 Polymer matrix composites

Polymer matrix composites are versatile engineering materials made out of a combination of two or more materials with unique synergetic properties such as light weight, high stiffness, freedom of design and excellent environmental resistance among others. This is why composites are spread in an increasingly number of industrial sectors and composite manufacturing has thus received much attention to achieve cost effective and reliable processing methods to produce high quality final parts.

2.1.1 Fiber reinforced polymer composites

In fiber reinforced polymer composite materials (FRPC), fibers are the structural material responsible for the primary load-bearing and the polymer matrix is used to hold the fibers together and transfer the load through the interfaces. Fibers' contribution to the final composite properties depends on their nature and thus their intrinsic mechanical properties, their surface interaction with the resin, their volume fraction in the final part and their arrangement and orientation. Commonly, glass and carbon fibers are used as reinforcements. Carbon fibers offer the best properties in terms of mechanical performance (modulus range from 200 to 500 GPa or more), including high stiffness in both tension and compression and high resistance to creep and fatigue, but owing to their high cost, their usage is limited to high-end products. Despite the lower mechanical properties of glass fibers compared to carbon (e.g. higher density, lower fatigue resistance and stiffness around 70-80 GPa), they still present good properties at a relatively low cost and are as a result the most employed fibrous material in composite manufacturing for high-volume applications. Other fiber types can also be good candidates depending on the product requirements. For instance, polymeric fibers such as aramid fibers, are widely used in aerospace and ballistic applications due to their excellent physical and chemical properties, and natural fibers such as flax or hemp gain interest due to their lower environmental impact as well as good damping properties [9].

The configuration and orientation of fibers are also key in composite design. Fibers are usually distributed in tows or yarns (composed of several thousands of fibers) which are later combined by textile techniques to form porous sheets (fabrics). Depending on their architecture, fabrics can be two- or three-dimensional. Two-dimensional fabrics are the most common and are usually classified in three categories: aligned fibers (unidirectional or multidirectional), randomly arranged (mat) and textiles made by weaving, braiding or knitting techniques as shown in Fig. 2.1. Unidirectional fabrics (UD) are highly anisotropic; in the fiber direction, composites present high mechanical properties, close to those of the individual fiber contribution depending on the level of crimp. Fabrics with multidirectional

fibers such as non-crimp fabrics are made by stitching unidirectional fabric stacks (plies) in different orientations, obtaining a more isotropic response. This enables to tailor the fabric architecture reinforcing selected directions and build a material that suits a particular loading case. Woven fabrics are made by weaving two set of yarns (weft and warp) and many different woven architectures can be designed (plain, twill and satin are the most common). Knitted fabrics are made by creating multiple loops which are intermeshed leading to a complex topology with a spring-like behavior, giving an excellent elasticity compared to woven fabrics, but a lower tensile modulus. Braided fabrics are made by interlacing fibers, creating tubular or flat fabrics. Three-dimensional fabrics, as interlock fabrics, are used in composites to increase properties in the through the thickness direction and improve the delamination resistance [10].

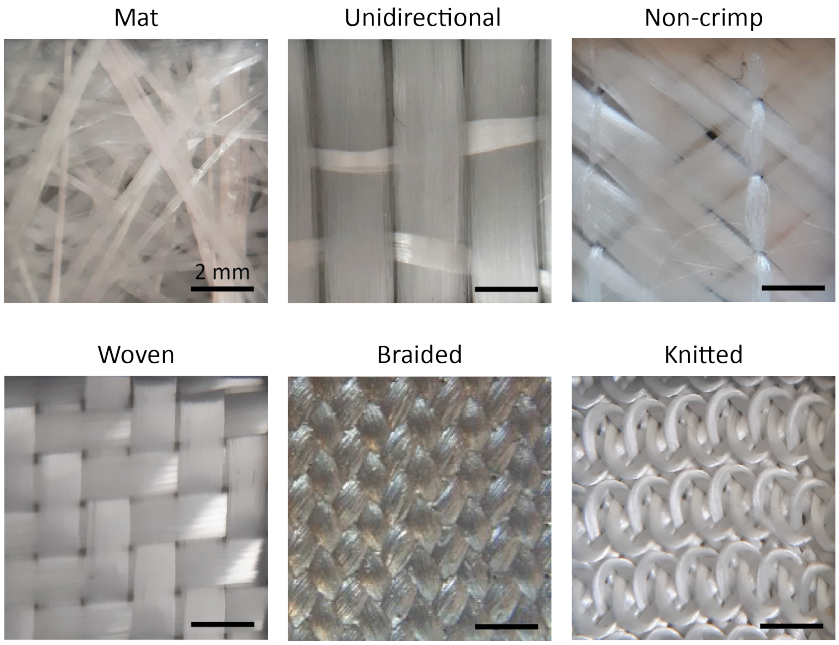

Figure 2.1: Summary of common 2D fiber architectures found in composite processing.

The matrix nature also plays an important role since it provides to the composite, additional properties such as thermal and chemical resistance, electric insulation, ductility and toughness. Thermoset and thermoplastic polymers can be used, but since their chemo-rheology properties are very different, the matrix choice determines the manufacturing process. Thermosets (e.g. epoxy, polyester and phenolic resins) are the most widely employed due to their high stiffness and strength, good chemical resistance and low cost. However, they are not easily recyclable and present low toughness and ductility. They are formed in-situ by an irreversible curing reaction between a monomer and a curing agent (resin and hardener) or between a monomer and a catalyst. Once polymerized, a thermoset polymer cannot be re-melted or returned to its original state. Besides, if thermosets are heated above their characteristic glass transition temperature, their properties will decrease significantly (to a rubbery state, and finally to thermal decomposition). Before curing, thermosets in their initial monomer state are low viscosity fluids (< 1 Pa $\cdot$ s) and can easily impregnate a preform. Contrariwise, thermoplastics (e.g. polyolefins, polyamides and polystyrene) are macromolecules, and can be remelted and thermoformed by increasing

the temperature above their glass transition and, if semi-crystalline polymers, melting temperatures. Although thermoplastics have many advantages such as recyclability and impact resistance, they generally present a high viscosity and need to be processed at high temperatures with a significant amount of applied pressure.

2.1.2 Complex composite systems

Composites are attracting considerable interest due to their versatility and freedom in design that allows tailoring the material according to the final product specific requirements. Nevertheless, the infinite freedom of materials assembly adds complexity to the composite system and makes manufacturing more challenging.

For example, natural fibers (mainly cellulose-based) are nowadays gaining interest in the composite field due to their renewable sourcing, easy biodegradability and low cost. In particular, flax fibers are promising given their abundance and outstanding mechanical properties (e.g. stiffness similar to glass fiber with better damping properties than carbon and glass fibers). Nevertheless, one of the main drawbacks of natural fibers is their high hygroscopy that produces dimensional changes in the fiber and in consequence, results in a weak fiber-matrix interaction [11, 12]. Some researchers tried to overcome this problem and proposed many surface treatments to enhance the bonding interface [13–16]. In addition, compared to synthetic fibers, natural fibers present irregular and complex morphological and surface properties. Fibers are built-up from elementary cells with a given length and an irregular cross-section, and are composed of a hierarchical sequence of wall layers of different composition and thicknesses around an internal closed cavity called the lumen [17]. Depending on the extraction conditions, fibers can be present in the fabric as elementary fibers with variable diameters (from 20 to 80 μm) or technical fibers (several elementary fibers bonded together with the middle lamella which acts as matrix) with larger variable sizes in the order of some hundred micrometers [18]. The fiber surface roughness together with the composition of lignin, cellulose and hemi-cellulose of the outer layer define the wetting properties of the natural fiber.

Sometimes, two or more different type of fibers are employed in a single part for properties shaping and cost lowering, those are mentioned as “hybrid composites”. Five types of hybridisation are distinguished depending on how fibers of different nature are arranged: intercalated layers (interply hybrid), fibers mixed into the same fabric layer (intraply hybrid), fibers are randomly distributed (intermingled hybrid), strategic placement of fiber type depending on the properties required in a specific location (selected hybrids) and composites containing metal foils or composites (super hybrid) [19]. The use of different types of fibers will influence the porous medium architecture and wetting properties.

Additional material phases can also be incorporated into composites with the aim of adding specific properties beyond their primary structural properties, such as self-healing capability, magnetic properties or heat protection, those are called Multifunctional Composites (MFC) [20]. The nature of these

additional phases mainly depends on the desired function but also on the composite manufacturing process [21]. In LCM, functional phases are generally a polymer or a flexible material which is added to the dry textile preform and thus should survive the impregnation step, without affecting the structure and properties of the final part. For example, some researchers sought to design self-repairing composite materials, for the sake of increasing their lifespan by healing interlaminar damage since delamination and crack growth easily occur in composites after being subjected to mechanical loading by adding capsule-based systems, vascular systems with hollow fibers and intrinsic resins with reversible covalent bonds [2].

2.2 Liquid composite molding techniques

The process route and conditions that matrix and reinforcement will go through to manufacture the composite will directly impact its final properties and performance. In all composite processing techniques, the resin is forced to flow within a potentially compressible porous media. However, depending on the flow path length, techniques are classified as either *consolidation* or *infiltration* processes. Liquid composite molding technologies belong to the second family. Compared to prepreg technologies that will fit in the first category, in LCM the fluid needs to travel large distances (distance is assumed to be greater than the length-scale of the reinforcement) to fully impregnate the preform.

2.2.1 Liquid composite processing

In LCM, a low viscous liquid resin is injected under a constant applied pressure or flow rate into the reinforcement which is placed in a total or partly rigid mold. LCM represents a wide range of techniques that can even include variants. Resin transfer molding (RTM) and vacuum infusion (VI) (or vacuum assisted resin transfer molding (VARTM)) are the most frequent methods. RTM manufacturing steps are illustrated in Fig. 2.2. First, the fabric preform is placed carefully in the bottom part of the mold with the desired orientation. For complex shapes, it is possible to first prepare a preform and stack the different layers with a binder or a previous stitching operation. Once the fabric is fitted, the mold is closed and clamped. Then, the resin is pushed into the mold cavity through one or more inlets by an injection unit. When the resin starts exiting the mold through the vent ports, injection is stopped and ports are closed. At this point, the resin cures (mold can be heated to accelerate this process), the final composite part can be demolded and some final operations can be performed.

In RTM, impregnation takes place into a closed and rigid mold which enables a good control of the final part thickness whereas in VARTM, the top is flexible (vacuum-proof bag often including a high permeability layer to ensure a faster, through thickness impregnation of the preform) and the vacuum is responsible to drive the resin flow along the preform and also to compact the preform. Thermoset resins are commonly used in those processes due to their low viscosity, resulting in reasonably fast impregnation under relatively low pressure differentials (around 1 bar). Although these processing methods are not commonly used for thermoplastics, some techniques have been developed, albeit still under research [22], one example is reactive TP-RTM [23, 24]. LCM processes are thus very versatile

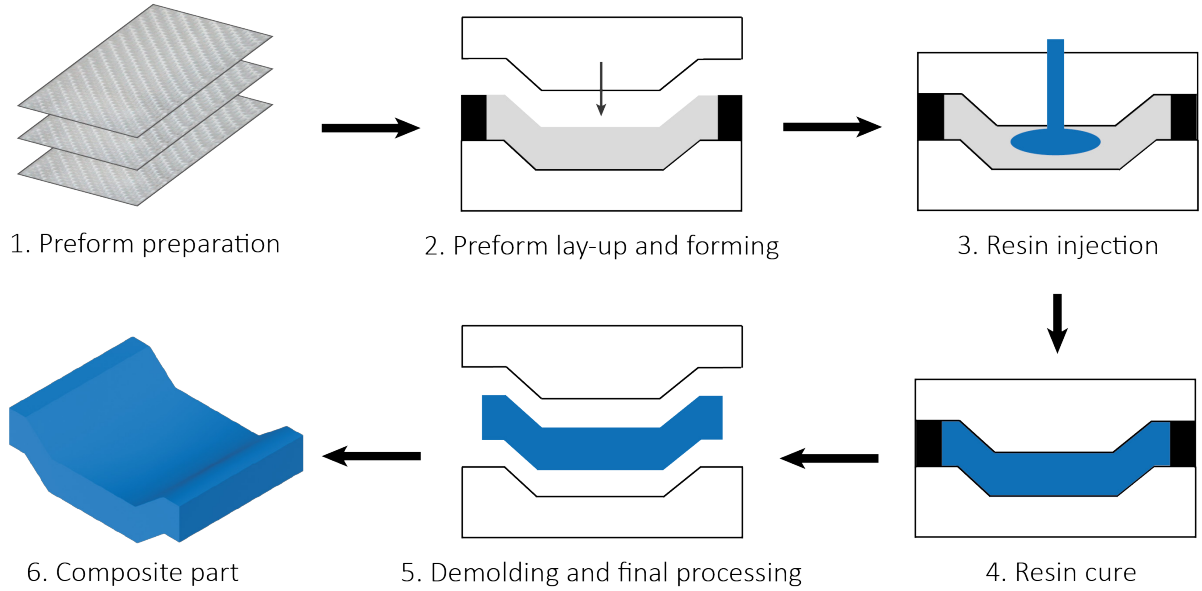

Figure 2.2: Schematic representation of the steps of a typical RTM process.

and by adjusting some processing parameters such as the injection pressure, the temperature and the fabric compaction, it is possible to manufacture final parts with higher efficiency and flexibility at a relatively low cost, resulting in an attractive process for complex structures in serial production [25].

2.2.2 Defects in LCM

The wider usage of LCM in structural applications can be limited by process induced defects. Several defects types arise in LCM and they can be classified either by their location: fiber (e.g. waviness, misalignment, broken fibers), interface (e.g. fiber/matrix weak adhesion, delamination) and matrix defects (e.g. inadequate curing and voids) [26] or by the processing step in which they appear: preform defects, flow induced defects and cure induced defects [27]. In particular, void type defects, i.e. entrapped voids or unfilled areas, have proved to be of great importance since they detrimentally affect the final part mechanical properties such as interlaminar shear, flexural and compressive strength [28]. For instance, a void fraction lower than 1-2 % is generally required for high performance composites.

In the frame of LCM processes, air entrapment stemming from the preform filling step turns out to be the main mechanism of void creation. Owing to the highly anisotropic pore network of textiles, the medium permeability is heterogeneous causing local variations in the resin speed. Voids are generally formed at three different scales: macro (dry spots usually coming from a distorted flow of an improper injection, observable with the naked eye), meso and micro (arising from the dual-scale architecture of fabrics, their formation and evolution is controlled by more complex physical phenomena). In order to characterize voids and figure out where they come from, their content, shape, size, location and distribution should be analyzed. In particular, the material properties (e.g. wettability of fibers

by resins or rheological properties) and impregnation conditions (temperature, pressure) are closely linked to void content and distribution whereas the geometry of the porous media will rather define the void shape, size and location. Hence, a thorough understanding of the correspondence between flow kinetics and void generation physics is crucial to produce composite parts without flaws [26].

2.3 Flow through porous media

Modelling of flow kinetics has driven a large body of applied research with the aim of predicting manufacturing strategies to produce optimal quality parts at minimal cost and cycle time. However, infiltration of fibrous preforms is complex because it is governed by a combination of several physical phenomena taking place at various scales, which are in addition influenced by the processing parameters (e.g. fluid speed, temperature, mold design), the geometrical properties of the fabric (e.g. pore size distribution), the physical properties of the resin (e.g. viscosity, surface tension) and the fiber-resin wettability. Although it is well known that flow phenomena are scale-dependent, to date no rigorous connections between flow descriptions at different scales have been achieved. In composites, the fibrous porous medium is usually defined at two scales: microscopic, where fluid flow is described by Navier-Stokes equation on a small volume element between individual fibers, and macroscopic where fluid flow is considered in an averaged volume with volume elements containing tows and inter-tow spaces, and where usually Darcy's law is used. The considered scale is thus crucial for flow studies and in the frame of this work, flow will be regarded as a macroscopic phenomenon, close to the real processing scale.

2.3.1 Fluid flow modelling

To model flow kinetics, a representative elementary volume (REV) with the different phases present: air, fibers and liquid with respective volume fractions V_a, V_f, V_l, such that $V_a + V_f + V_l = 1$, is generally defined. In composites, the fiber volume fraction V_f can be easily calculated as:

$$V_f = \frac{nA_w}{\rho_f h} \tag{2.1}$$

where n is the number of layers, A_w the areal mass of the fabric, ρ_f the fiber material density and h the height of fabric. The pore space of the porous media ϕ is equal to $1 - V_f$ [7]. Then, resin infiltration is generally modelled with a continuum mechanics approach [6] and it is commonly assumed that the resin is an incompressible Newtonian fluid and that infiltration takes place without heat exchange (this assumption can be relaxed by adding an equation for thermal transport). Then, mass conservation equations for the fluid phase and the solid (fibers) are written as follows:

$$\frac{\partial V_f}{\partial t} + \nabla \cdot (V_f \vec{u_f}) = 0 \tag{2.2}$$

$$\frac{\partial V_l}{\partial t} + \nabla \cdot (V_l \vec{u_l}) = 0 \tag{2.3}$$

where $\vec{u_f}$ and $\vec{u_l}$ are the average local velocities of the solid and liquid respectively and t the time. The saturation S of the fluid phase in the porous media is the ratio between the injected liquid volume and the total pore of the porous medium:

$$S = \frac{V_l}{1 - V_f} \tag{2.4}$$

S varies between 0 and 1, 0 corresponding to a preform not yet impregnated and 1 to a preform fully saturated with liquid. Finally, Darcy's law is applied to write the momentum equation [29]:

$$(1 - V_f)S(\vec{u_l} - \vec{u_f}) = -\frac{K}{\eta}\nabla P \tag{2.5}$$

where K is the permeability tensor of the porous medium in the REV (the symbol K can cover several descriptions of the permeability), η the liquid viscosity and ∇P the pressure gradient that drives the flow. The fabric preform is often assumed to be an incompressible porous medium with interconnected porosity and $\vec{u_s} = 0$ (even though some researchers have worked on the effect of compressibility of preforms on flow dynamics [30]). The superficial (also called infiltration or Darcy) velocity U is defined as the product of the flow front velocity times the total pore volume and was also initially defined by Darcy as the ratio of the volumetric flow rate Q_{out} coming out of a porous medium, over the porous medium cross section A:

$$U = \phi u_l = \frac{Q_{out}}{A} \tag{2.6}$$

Darcy's law as written above relates the instantaneous flow rate through a homogeneous porous medium, the dynamic viscosity and the pressure drop over a given distance, this is why equation (2.5) is commonly applied for flow progress and mold filling time measurements.

Permeability of a porous medium is an intrinsic property of the medium, assimilated to a hydraulic conductivity, and defines how easily a fluid can be conducted into it under an applied pressure gradient. Fibrous structures present an anisotropic permeability which is described by a second order tensor. By definition, the saturated permeability (when the preform is fully saturated) K_{sat}, depends only on the geometrical characteristics of the preform and does not vary with the nature of the infiltrating fluid. The most common technique to determine permeability is experimentally and it is possible to measure flow kinetics through radial-, rectilinear- or through-thickness impregnation but since impregnation occurs predominantly along the fabric plane, in-plane (radial and rectilinear) flow experiments are often carried out. For unidirectional measurements, its value can be easily obtained from integration

of Darcy's law:

$$K_{sat} = -\frac{Q_{out}\eta L_f}{A\Delta P_{app}} \tag{2.7}$$

where L_f the fabric's length (in the flow direction) and ΔP_{app} the fluid pressure difference between the outlet and the inlet [31]. In literature, permeability measurements are a source of debate due to existing discrepancies arising from a large list of factors: inhomogeneity of the material, different experimental setups or measurement techniques, an inadequate fabric cutting or placement, among others. There is an urgent need to develop a reliable and reproducible method and this is why, for almost thirty years, efforts are being made in order to standardize permeability measurement methods [32–39]. Alternatively, computation-based simulations are increasingly proposed for permeability prediction to bypass long and arduous experimental tasks [40, 41].

Besides its void fraction and permeability, a dry porous medium is defined by its specific surface S_f and the size and the shape of the different pores existing which will also influence the fluid dynamics [31]. Considering fibers being perfect cylinders arranged in a square array configuration, S_f can easily be calculated as:

$$S_f = \frac{2}{r_f}\left(\frac{V_f}{1-V_f}\right) \tag{2.8}$$

with r_f the fiber radius. However, fibers can present some roughness leading to an increased surface area differing from the geometrical one. It is quite difficult to measure the specific surface of a reinforcement, it can be done by using either the BET technique [42] or by modelling the geometric architecture, even though pore size and distribution are also two parameters hard to measure. Nowadays, X-ray tomography is gaining interest to define and characterize 3D fibrous pore structures [43–45].

2.3.2 Capillary effects

Owing to the micron-sized pore space in fiber preforms, capillary effects manifest themselves significantly in composite processing. Those are generated in the compacted tows and are exacerbated by the degree of fiber compaction [46]. In particular, many researchers observed that the permeability within the fiber tows is lower by several orders of magnitude as compared to the bulk preform permeability. Consequently, a high pressure gradient is generated inside the tows (when compared to the inter-tow region) to counteract this lower permeability [47–49].

Capillary action is defined as the phenomenon whereby a fluid phase is displaced by another immiscible fluid phase on a solid surface (for example a fiber) under no external forces. This effect arises from the competition between intermolecular forces between phases, and the difference in surface energies between the various phases in presence. Considering a system surrounded by air, the force balance

between the interfacial energies in static conditions is described by Young's equation as:

$$\gamma_{sa} = \gamma_{fl} + \gamma_{la} \cos\theta_e \tag{2.9}$$

where $\cos\theta_e$ is the static contact angle and γ_{sa}, γ_{fl}, γ_{la} are the surface tension for fiber-air, fiber-liquid and liquid-air interfaces, respectively. The wettability, defined as the affinity of a fluid to a solid surface in the presence of another fluid and quantitatively described by $\cos\theta_e$, is governed by the competition between adhesion and cohesion forces in the liquid phase as shown in Fig. 2.3. If $\theta_e < 90°$, adhesive forces are dominant and the fluid is wetting (w). Inversely, if $\theta_e > 90°$, cohesive forces are stronger and the fluid is non-wetting (nw).

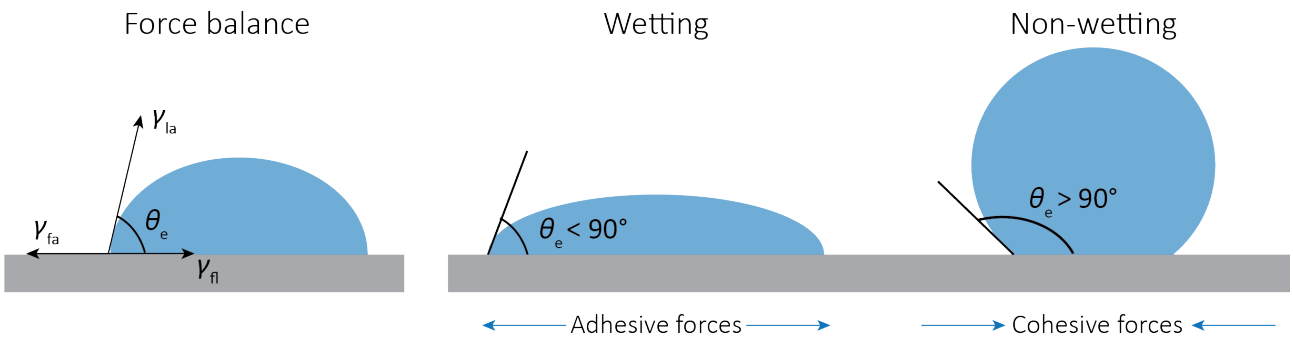

Figure 2.3: Force balance and liquid drop shapes in wetting and non-wetting conditions.

The capillary pressure p_c at the microscopic level is then defined as the difference between the air and fluid interfaces arising from the surface and interfacial tensions. An example of wetting and non-wetting fluids in a capillary tube of radius r with the pressure balance and the capillary rise h_c is shown in Fig. 2.4. The capillary pressure drop p_c can be written as the difference between the non-wetting and wetting phases pressures, p_{nw} and p_w:

$$p_c = p_{nw} - p_w \tag{2.10}$$

In the particular case of the cylindrical tube with a radius r, p_c is equal to:

$$p_c = -\frac{2\gamma_{la}\cos\theta_e}{r} \tag{2.11}$$

p_c is negative in the wetting case (capillary suction), and positive in the non-wetting case (capillary depression). When the fluid is wetting (concave meniscus), it pulls itself towards the solid surface and thus the displacement is governed by capillary forces (in the absence of viscous forces). In the non-wetting case (convex meniscus), an extra force should be applied in order to initiate the fluid movement [50].

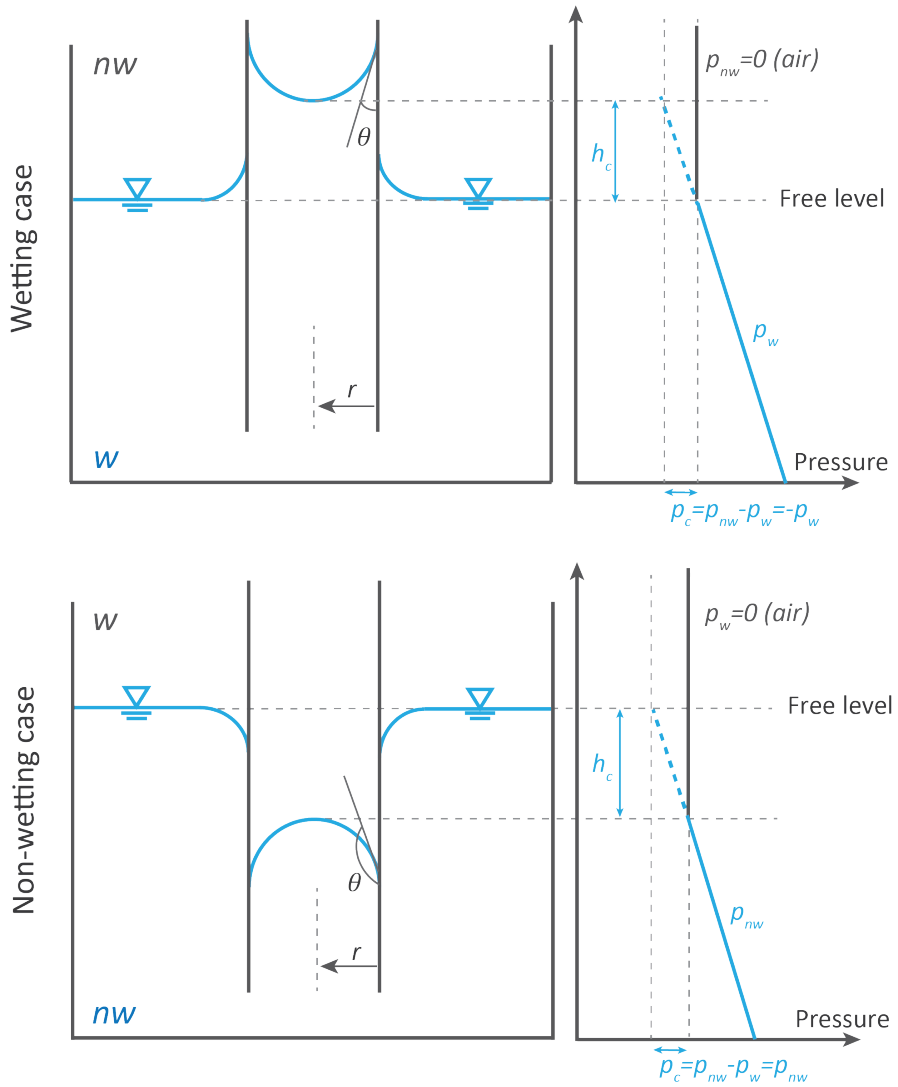

Figure 2.4: Schematic of wetting and non-wetting fluids in a capillary tube surrounded by air (air pressure is assumed to be 0).

In LCM, since the flow is mainly driven by an externally applied pressure due to the high viscosity of resin when compared to water, the magnitude of capillary effects is rather low when compared to hydrodynamic effects [51]. Therefore, capillary effects have henceforth largely remained overlooked but are now rapidly gaining interest as researchers observed that they play a significant role at the fluid flow front. Neglecting them may lead to errors in measurements and misunderstanding of infiltration processing. However, capillary effects and wettability are pore scale phenomena and the upscaling of microscopic to macroscopic flow behavior is still the topic of intense debate.

2.3.3 Dual-scale flow

The flowing patterns resulting from the displacement of air by a fluid within a porous medium are shown in the diagram in Fig. 2.5 and are described by the invading to displaced fluid viscosity ratio M_η and the dimensionless capillary number Ca which is the ratio between the viscous and capillary

forces:

$$M_\eta = \frac{\eta}{\eta_{air}} \tag{2.12}$$

$$Ca = \frac{U\eta}{\gamma_{la}} \tag{2.13}$$

Some authors proposed a modified capillary number Ca^* including the apparent static contact angle and they defined R_l as the fluid penetrativity [52]:

$$Ca^* = \frac{U\eta}{\gamma_{la}\cos\theta_e} = \frac{U\eta}{R_l} \tag{2.14}$$

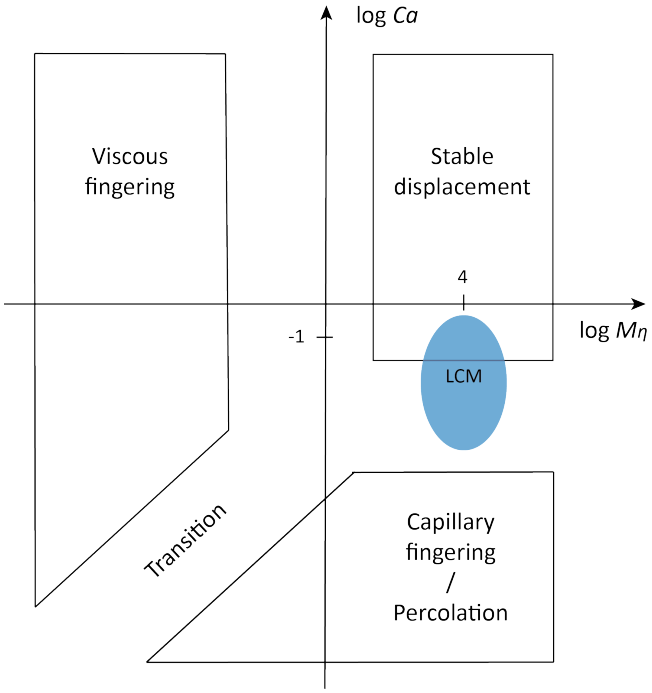

Figure 2.5: Phase diagram of fluid patterns as a function of the viscosity ratio and the capillary number. The blue ellipse indicates the location of typical LCM processes. Figure adapted from [7].

Textiles used in composite processing present a complex pore architecture, usually assumed to be bimodal with meso-pores in between the bundles (inter-tow spaces) and micro-pores in between the fibers inside the bundles (intra-tow spaces), thus triggering a fluid/fabric interaction at different scales, found to be linked to an air entrapment mechanism [28, 53]. The different flow patterns arising from the non-uniform fluid progression and the quantity of voids are determined by the extent of viscous and capillary flows.

In particular, at high impregnation speeds (high Ca), fluid is driven by viscous forces and preferentially fills meso-spaces in between the tows, hence micro-voids remain trapped inside the tows (Fig. 2.6).

In this case, the pressure gradient between the inlet and the outlet is the promoter of the injection at a macroscopic level and is the only force considered by Darcy's law to describe fluid movement. Conversely, at low impregnation speeds (low Ca), fluid is driven by capillary wicking and preferentially fills micro-spaces inside the tows, meso-voids in this case remain trapped in between the tows.

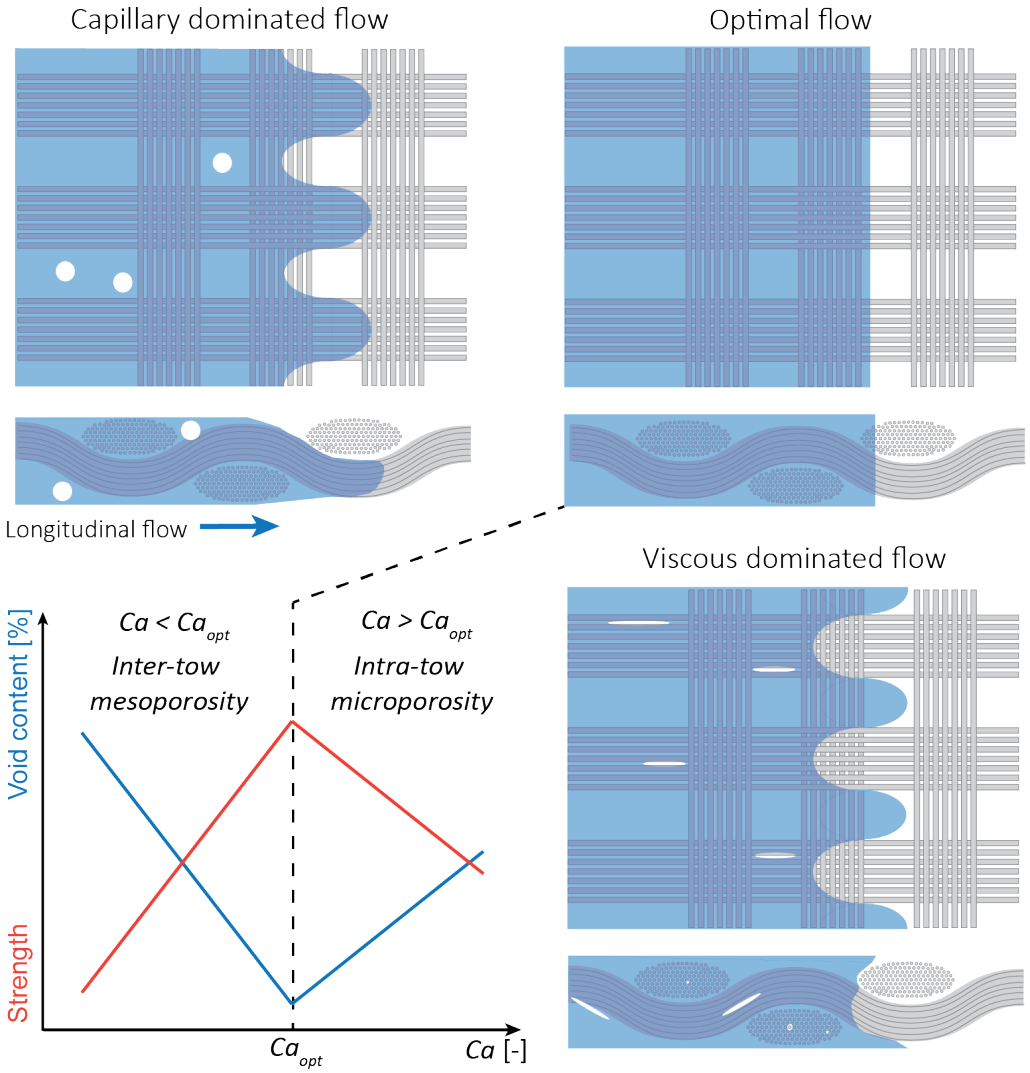

Figure 2.6: Influence of the capillary number on the void formation and final part properties based on fluids paths under capillary- and viscous-dominated flow regimes.

A constant competition between viscous and capillary forces take place at the flow front and researchers agree with the existence of an optimal capillary number Ca_{opt}, for which capillary and viscous effects compensate each other and the amount of the voids is minimal (flow velocities are comparable in inter- and intra-bundles regions) [54–56]. It was found experimentally [55] and numerically [57] that the void content in function of the capillary number or impregnation velocity creates a "V-shaped" curve which varies nearly logarithmically. Since Ca_{opt} is influenced by the textile architecture and the fluid properties, it is specific for a given resin/reinforcement system. To date, its value is measured experimentally and no one has been able to predict it quantitatively or clearly explain the fundamental physics behind this parameter.

2.4 Modelling of unsaturated flows

A thorough study of flow front is sought since many phenomena are taking place there directly affecting the filling quality. For the sake of facilitating numerical models, it is often preferred to describe the flow at the processing scale and microscopic effects are regrouped and regarded as a macroscopic phenomenon. Several approaches have been proposed towards the development of reliable numerical models to describe fluid displacements at a realistic scale.

2.4.1 Slug-flow assumption

For simplicity, it is often considered that the liquid progresses with a fully saturated front and homogeneously fills the preform, resulting in a step function of the saturation as shown in Fig. 2.7. This is known as the slug-flow assumption and solution of the equations turn out to be quite straightforward since capillary effects are lumped in the saturated fluid flow equations as a pressure difference created at the flow front, called the capillary pressure drop ΔP_γ and written as [6, 42, 44]:

$$\Delta P_\gamma = -S_f \gamma_{la} \cos(\theta) \tag{2.15}$$

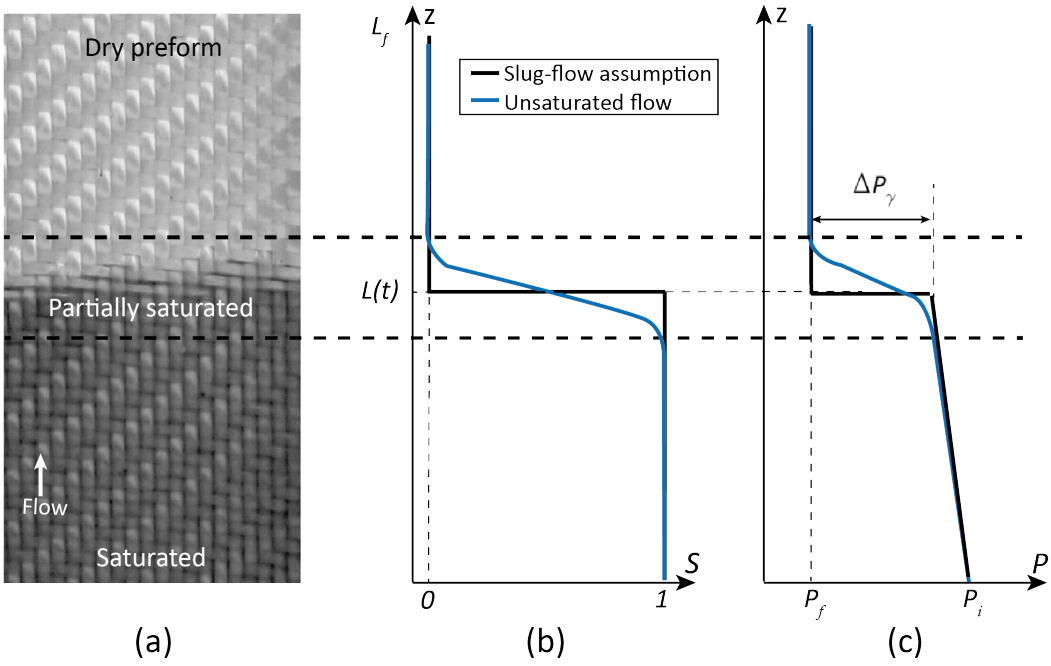

Figure 2.7: Saturation and pressure profiles for slug-flow and unsaturated flow descriptions: (a) optical image a flow front progression in a glass preform, (b) saturation and (c) pressure versus position curves.

By influencing the pressure profile, ΔP_γ has an impact on the infiltration kinetics. Indeed, if ΔP_γ is negative, the fluid has a wetting behavior and a spontaneous infiltration occurs enhanced by capillary suction. Inversely, if ΔP_γ is positive, the resin has a non-wetting behavior and a pressure must be applied for infiltration to take place. Nonetheless, when the fluid moves with a certain velocity u_l, the thermodynamic equilibrium is not respected anymore. The wettability becomes a dynamic property of the resin-fabric system which can be either wetting or non-wetting depending on the fluid speed

[42, 58–61]. The deviation between the dynamic contact angle θ from the static contact angle θ_e can be defined by Tanner's law [62]:

$$\theta^3 - \theta_e^3 \approx c_T Ca \tag{2.16}$$

where c_T is the Tanner coefficient, that has to be experimentally measured. Consequently, ΔP_γ strongly depends on the capillary number and equation 2.15 can be rewritten as [42]:

$$\Delta P_\gamma = -S_f \gamma_{la} \cos\left(\sqrt[3]{c_T Ca + \theta_e^3}\right) \tag{2.17}$$

At the fiber scale, the dynamic contact angle and resulting capillary pressure can be measured by a tensiometric method coupled to Wilhelmy's equation [63–67]. The setup consists of extracting the force needed to pull or push (advancing and receding) a fiber or a tow partially submerged in a liquid. As a similar approach, wicking experiments have been also performed on single tows [68–71], and single fabric layers [63, 72–74], the capillary pressure and advancing dynamic contact angles can be determined by means of Lucas-Washburn's equation [75]. Since this method assumes a constant porous geometry and does not consider attraction forces between fibers, arising from elasto-capillary effects leading to a densification phenomenon, some modifications have been proposed [63, 71, 74, 76]. Based on the Lucas-Washburn's equation, Lebel et al. [54] proposed a simplified method to obtain the optimal flow speed for a given resin/fabric system, used thereafter in Refs. [52, 77–79].

At the fibrous stack scale, the capillary pressure drop can be quantified within an experiment in which the fluid is injected into the preform either at constant pressure or constant flow rate. In unidirectional cases it is possible to track the fluid movement using Darcy's law and the Dupuit-Forchheimer approximation according to:

$$\frac{dL}{dt} = -\frac{K}{\eta(1 - V_f)} \frac{dP}{dz} \tag{2.18}$$

where $L(t)$ is the position of the flow after a time t and ΔP is the fluid pressure difference at a certain position z. The total fluid pressure difference ΔP is defined as the pressure difference ΔP_{app} between the inlet (i) and the outlet (f) (ΔP_{app} has thus a negative value) considering the capillary forces:

$$\Delta P = P_f - P_i = \Delta P_{app} + \Delta P_\gamma \tag{2.19}$$

P_f is assumed to be the pressure of the air typically the atmospheric pressure. Thereupon, if the fluid is injected under constant pressure, (dP/dz) from equation 2.18 is constant and is equal to $\Delta P/L(t)$. Thus, $L^2(t)$ versus t is linear and the slope is equal to $L^2(t)/t = \psi^2$ which can be written as:

$$\psi^2 = -\frac{2K_{uns}(\Delta P_{app} + \Delta P_\gamma)}{\eta(1 - V_f)} \tag{2.20}$$

where K_{uns} is the unsaturated permeability. Based on equation 2.20, ψ^2 is a kinetic parameter that

can be plotted against the applied pressure difference ΔP_{app}. After several measurements at different inlet pressures, the obtained curve should be linear and the capillary pressure drop ΔP_γ value corresponds to the x-intercept of the plot ψ^2 as a function of ΔP_{app} (Fig. 2.8a).

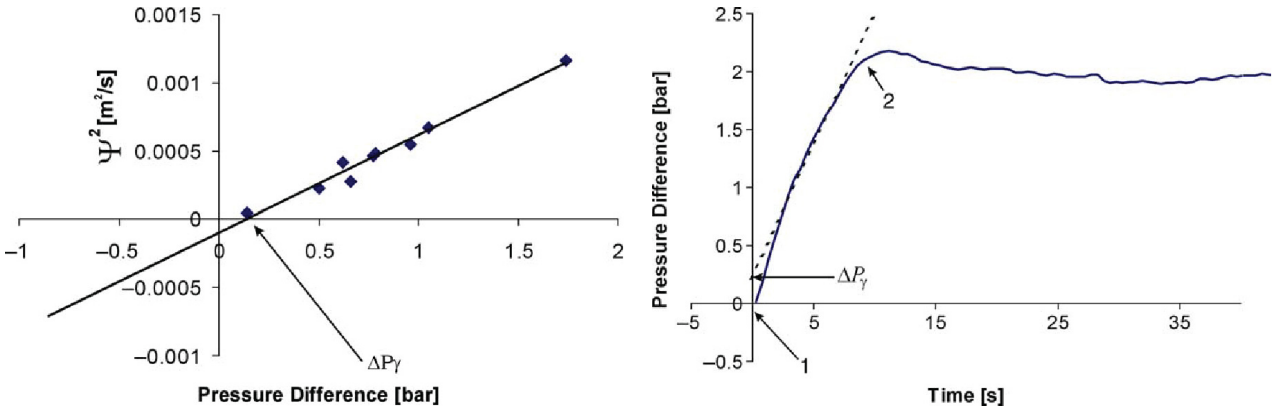

Figure 2.8: Determination of the capillary pressure drop ΔP_γ in (a) constant pressure and (b) constant flow rate experiments. Reproduced with permission from [42].

When the resin is applied under constant flow rate, dL/dt from equation 2.18 remains constant and is equal to L_f/t. The flow front position moves forward linearly with time and can be written as follows:

$$L(t) = \frac{Q}{A(1-V_f)}t \tag{2.21}$$

And thus,

$$\Delta Papp = -\frac{Q^2\eta}{A^2 K_{uns}(1-V_f)}t - \Delta P_\gamma \tag{2.22}$$

In this case, ΔP_γ can be obtained in a single measurement, inversely to constant pressure experiments. As shown in Fig. 2.8b, the pressure versus time curve presents a nonlinear profile at the beginning of the impregnation corresponding to a transient phase (point 1). Later, the resin progressively saturates the preform, the flow reaches a steady-state regime and the curve becomes linear (point 2). A linear regression can be performed and ΔP_γ corresponds to the value obtained at time zero.

Verrey et al. [42] proved that it is more suitable to measure ΔP_γ in a constant flow experiment rather than constant pressure experiment, since the velocity changes significantly during the impregnation resulting in a range of capillary numbers. In addition, they concluded that it is possible to measure the dynamic contact angle realizing different experiments at constant flow rate injections as the capillary number remains constant all along the test (Fig. 2.9).

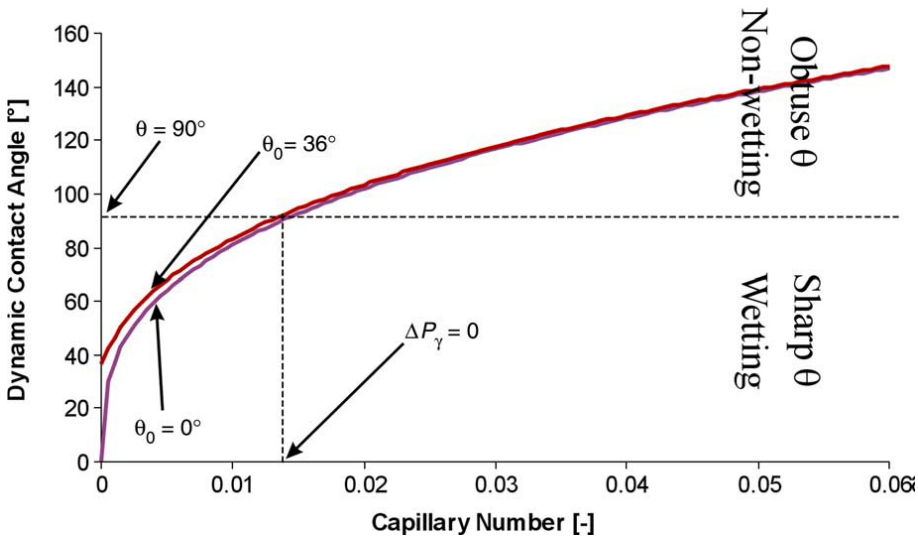

Figure 2.9: Dynamic contact angle as a function of the capillary number for a carbon-epoxy system. Reproduced with permission from [42].

Theoretically, unsaturated and saturated permeability should be equal as they depend only on the preform structure. However, significant differences between these two values have been reported in literature [80–85]. Intuitively, those differences stem from capillary effects taking place at the flow front which do not affect the saturated permeability measurement. Indeed, capillary effects can alter the fluid velocity leading to erroneous unsaturated permeability measurements if they are not taken into account (Eq. 2.20 and 2.22). Bréard et al. [82] introduced for the first time the unsaturated to saturated permeability ratio R_s which can be linked to the capillary pressure as:

$$R_s = \frac{K_{uns}}{K_{sat}} = 1 + \frac{\Delta P_\gamma}{\Delta P_{app}} \tag{2.23}$$

As already introduced in equations 2.16 and 2.17, ΔP_γ depends on the capillary number and the dynamic wettability of the system. Hence, K_{unsat} relies on the fluid-fabric wettability and does not exclusively depend on the porous medium architecture. If infiltration is carried out under conditions close to the optimal capillary number, capillary effects are negligible and R_s will be close or equal to 1. On the contrary, if ΔP_γ is not negligible, the two permeability values will differ. In particular, if ΔP_γ is negative, the system is wetting and $R_s > 1$ ($K_{uns} > K_{sat}$) (ΔP_{app} is negative, cf. Eq. 2.19) and if ΔP_γ is positive, the system is non-wetting and $R_s < 1$ ($K_{uns} < K_{sat}$).

The ratio R_s was found to be generally below 1, considering that the fluid acts with a non-wetting behavior [82] even though values above 1 have been also been observed [81]. Salvatori et al. [44] showed for a classic woven fabric, that R_s is greater than 1 at low capillary numbers, below 1 for high capillary numbers and around 1 close to the optimal conditions. For a fabric with large meso-channels, R_s was found to be close to 1 for a wide range of capillary numbers since inter-tow flow dominates the overall flow kinetics. Caglar et al. [86], studied the effect of corona treatment on glass fibers and found a R_s value higher for treated fabrics indicating an increasingly wetting dynamic behavior. Recently, Staal et al. [87] investigated the effect of grafted aligned carbon nanotubes (CNT) on alumina fiber woven

fabrics and found R_s values to be higher than 1 arising from a strong capillary wicking happening in forest areas created by CNTs.

2.4.2 Unsaturated flow

Notwithstanding the extensive use of the slug-flow assumption, many authors found significant deviations from this fully saturated state together with a nonlinear pressure profile along the infiltrated preform [32, 88–94]. As shown in Fig. 2.7, three regions can be identified during an impregnation: the dry preform, a transition zone where the saturation is less than one, and a fully saturated area. To tackle unsaturated flow phenomena two main strategies are commonly adopted. The first one is more specific to the polymer composite processing field and considers the preform as a dual-scale body with flows in intra- and inter-tow regions. The second approach is inspired from soil science and relies on traditional multiphase flow equations for porous media.

Dual-phase approach

This method separates intra- and inter-tow impregnations introducing a sink term into fully saturated methods [28, 30, 82, 95–103]. It assumes that viscous forces dominate the infiltration and the system is thus non-wetting. During infiltration, the flow preferentially fills the macro spaces and fluid flow in bundles is delayed, thus altering the local pressure. The delayed secondary flux fills gradually the pores inside the bundles as shown in Fig. 2.10. Generally, the length of the delayed zone with unsaturated tows is assumed to be constant. Then, the pressure drop creates an apparent change in the permeability and this delayed effect is considered by adding a sink term into the flow equations which represents the liquid volume rate into the fiber tow over time (which also corresponds to the rate of degree of saturation).

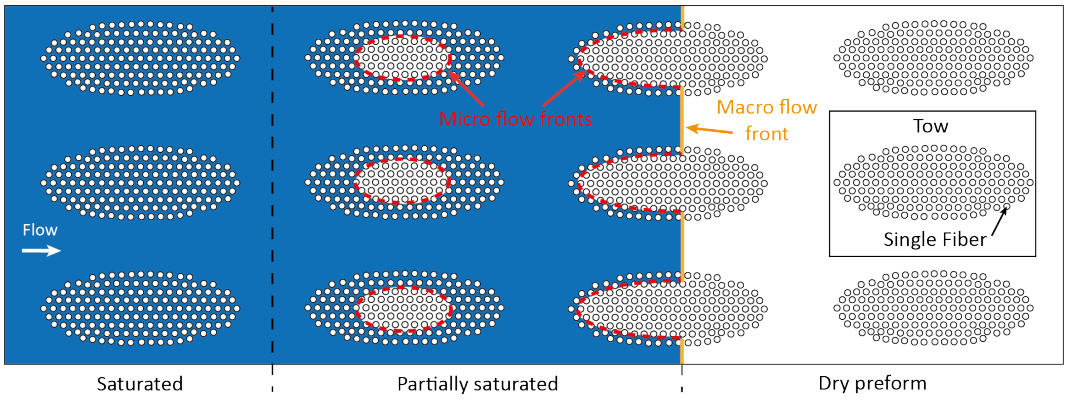

Figure 2.10: Schematic of the dual-phase approach with delayed impregnation of the tows.

In this approach, tow and overall fabric permeability are usually measured in saturated mode, however, for more accuracy, some researchers proposed to model the permeability in terms of degree of saturation or void content ($K(S)$) [100, 101]. The mass conservation equation, is thus written integrating a sink

term, as [28]:

$$\nabla \left(\frac{K(S)}{\eta} \nabla P \right) = \phi \frac{\partial S}{\partial t} \tag{2.24}$$

with $\partial S/\partial t$ the saturation rate representing the delay in tow saturation. Consequently, the delayed saturation results in a non-linear pressure profile $P(z)$, which proved to be convex and/or concave, depending on how capillary effects manifest themselves during flow kinetics [28].

Multiphase flow approach

Although this approach is commonly used in other branches of engineering such as petroleum engineering, agriculture, biological engineering or hydrology among others, researchers applied it seldom to model polymeric resin infiltration processes [82, 104–108]. Several references can be found for metal matrix impregnation which can serve as a basis for polymer-based composites [6, 51, 94, 109–111]. This approach relies on the displacement of two different immiscible fluids inside a porous medium in which permeability and pressure are dependent on the infiltrating fluid saturation.

In the case of polymer infiltration, the resin invades the porous medium (fabric), displacing and expelling the fluid which saturates the porous medium (air). As already discussed, depending on the fiber/matrix system and the impregnation conditions (mainly fluid velocity), resin and air can be either wetting and non-wetting, or inversely. Considering the common high processing speeds, the resin is generally considered to be non-wetting phase. Thus, since in static conditions, resins wet fibers, a capillary driven flow can be assimilated to an imbibition process and inversely a viscous driven flow to drainage process. Based on that, the fluid progression in drainage and imbibition systems is schematically presented in Fig. 2.11.

Two-phase flow problems are commonly solved by finite element method given their appealing advantages in terms of numerical robustness. The system of equations consists of: partial differential equations (PDE) describing the transport of the phases in the model and some auxiliary equations describing for example hydraulic properties and coupling the wetting (w) and non-wetting (nw) phases [112, 113]. Mass balance and momentum equations are linked through the saturation as:

$$S_w + S_{nw} = 1 \tag{2.25}$$

In multiphase studies, the capillary pressure is considered at the macroscopic level. If the porous medium is assimilated to a random assembly of tubes of various radii, the macroscopic capillary pressure will thus depend on an average of several radii of menisci. Each of these tubes will drain the fluid differently and a strong relationship is created between the saturation and the capillary pressure. Analogously to what was presented before, the macroscopic capillary pressure P_c is defined as the

pressure difference between the two phases as:

$$P_c(S_\alpha) = P_{nw} - P_w \tag{2.26}$$

with α refering either to w of nw and P_{nw} and P_w the averaged pressures respectively of the wetting and non-wetting phases within the REV. There are five formulations to tackle two-phase fluid flow, and their differences mainly come from the variables that are solved. The two main formulations are: the two-pressure (or partial pressure, solved for P_{nw} and P_w) and the fractional flow (solved for (P_s, S_w) or (P_s, S_{nw}) with $P_s = P_{nw} + P_w$) formulations.

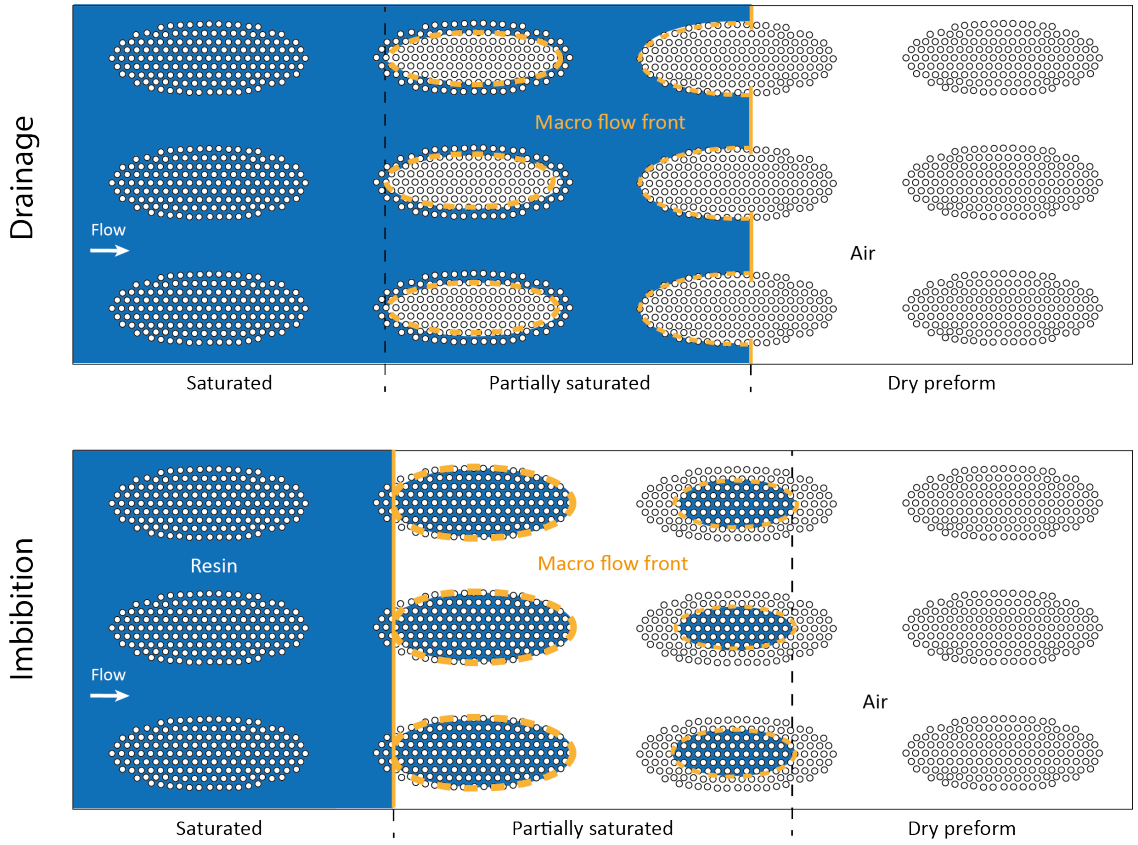

Figure 2.11: Schematic of drainage and imbibition in fibrous preforms.

The two-pressure formulation uses mass balance equations and the single-phase Darcy's law to describe the velocity of the two fluids through the same porous material. This approach has separate equations for wetting and non-wetting phases and uses the fluid capacity C. If the air pressure is assumed to be relatively low, the mass balance equation for the resin can be solved independently and is reduced to Richard's equation [114] as used by Nordlund et al. [105]. The fractional flow method treats the multi-phase flow as a total mixed fluid and the individual phases are described as fractions of the total flow. This approach considers the saturation of one of the two phases and a global pressure as independent variables [115]. Two equations stem from this approach: the global pressure equation and the saturation equation using a diffusive coefficient due to capillary effects [106, 107].

To solve multiphase flow equations, the definition of some constitutive relationships for pressure and permeability versus saturation are also required, known as hydraulic functions. The permeability is divided in two terms $k_r K_{sat}$, k_r being the relative permeability, a dimensionless value between 0 and 1 and function of S. The relative permeability is defined for both phases as $k_{r,nw}$ and $k_{r,w}$, and describes how fluid and air phases flows in respect to each other into the porous media. The saturation as a function of pressure curve $S(P_c)$ is known as the imbibition-drainage curve [116]. Many mathematical descriptions for k_r and $S(P_c)$ have been proposed, but the most employed ones are the ones developed by Brooks and Corey [117] and the ones from van Genuchten and Mualem [118–120] which exhibit a power law dependence. Their equations are presented in Table 2.1, where λ, β, L, M and N are fitting parameters and H_b and H_p the bubbling and capillary pressure heads respectively.

Table 2.1: Hydraulic functions descriptions.

Hydraulic function	Brooks and Corey	Van Genuchten-Mualem
Conductivity $k_r(S)$	$k_{r,w} = (S_w)^{\frac{2+3}{\lambda}}$	$k_{r,w} = (S_w)^L \left(1 - \left(1 - S_w^{\frac{1}{M}}\right)^M\right)^2$
	$k_{r,nw} = S_{nw}^2 \left(1 - (1 - S_{nw})^{\frac{2+\lambda}{\lambda}}\right)$	$k_{r,nw} = S_{nw}^L \left(1 - (1 - S_{nw})^{\frac{1}{M}}\right)^{2M}$
Retention $S(P_c)$	$S_w = (H_b/H_p)^\lambda$	$S_w = \left(1 + \lvert\beta H_p\rvert^N\right)^{-M}$
	$S_{nw} = 1 - (H_b/H_p)^\lambda$	$S_{nw} = 1 - \left(1 + \lvert\beta H_p\rvert^N\right)^{-M}$

For example, Nordlund et al. [105] used the Van Genuchten-Mualem semi-empirical expressions to model the impregnation of a glass preform by a resin in non-wetting conditions and Gascón et al. [106, 107], the Brooks and Corey formulation with $\lambda = 2$ to model the saturation in a glass fiber reinforcement to predict void formation and transport mechanisms.

It should be noted that those models are generally employed for rather homogeneous porous media, which do not exhibit a dual scale porosity distribution. Nevertheless, since natural porous media (for which these models are highly employed), may also exhibit a variety of heterogeneities such as cracks, fractures or an assembly of porous aggregates, researchers proposed to adapt these models to dual-scale architectures. Gerke and van Genuchten [121] proposed to superpose two saturation curves: one for the highly permeable fractured system and one for the less permeable matrix or aggregate system. The resulting hydraulic functions, thus show an inflexion point typical of dual scale media. This approach, however, requires the identification of a large number of fitting parameters, which make the identification very challenging. In the present work, the single scale multiphase approach presented in Fig. 2.11 is adopted to model unsaturated flow since the fabric employed is sufficiently uniform that we did not see any strong separation of scales in the saturation profiles. Nevertheless, the dual-scale description developed in the frame of soil science is encouraging to further investigate the application of multiphase models to describe LCM processes, in particular with highly permeable fabrics [44].

2.4.3 Additional challenges in flow kinetics

So far, attempts to model the simple case of a resin flowing through a porous medium have been presented. In section 2.1.2, the existence of more complex composite systems has been highlighted, which further increase the challenge of describing and understanding infiltration phenomena. In this small section, some of the strategies formulated by researchers to model more complex systems are summarized.

Natural fiber reinforced composites still present a large amount of porosity and processing defects mainly due to an incomplete understanding of the role of initial humidity level in fibers, surface characteristics and their complex geometry. Moreover the impregnation kinetics is altered by fiber intrinsic absorption and swelling mechanisms. During impregnation, fibers first absorb the resin, removing liquid from the main stream, acting as a sink component and decreasing the velocity at the flow front. Then, fibers swell, inducing a change on fiber diameter and as a result on the overall microstructure. These coupled effects have a large impact on permeability measurements, and thus on R_s. In particular, absorption influences K_{sat} and swelling the K_{uns} [11]. Several authors proposed to model these effects during infiltration by introducing modifications to the conventional fluid models, by adapting the permeability as a function of time and fiber radius, for example [17, 122–127]. As a remark, fibers are highly sensitive to polar fluids, highly affecting permeability measurements when water-based model fluid are employed [124].

In systems including additional phases, the new material is either placed in between the fabric layers or mixed to the resin and infiltrated depending on its size and shape. In the first case, it modifies and adds complexity to the porous media architecture and should overcome the impregnation step [45, 128]. It has been observed that third phases generally decrease unsaturated permeability by exacerbating capillary effects. In the second case, particles should be homogeneously mixed to the resin and uniformly distributed in the final composite [129–137]. However, the introduction of particles can lead to undesired filtration effects even with nano-scale particles flowing through a preform of 40% volume fraction [138].

In order to ensure a strong interface region between fiber and polymers, commercial fibers are coated with sizings [139]. Sizings are generally made to functionalize fibers and increase their compatibility with specific monomer types. As a result, they alter the surface chemistry of the fiber, thus affecting its wettability and thereby capillary effects. Commercial sizings' wettability is reported to vary strongly due to differences in the sizing composition but the confidential nature of commercial sizing compositions has impeded further investigations into the role of sizing compositions on the (intra-yarn) flow behavior. Besides, some surface treatments (such as physical or chemical) can be applied onto sized fibers, to further improve and control resin-fiber interactions [140].

2.5 Physics of voids

In section 2.3.3, micro and meso-voids formation by air entrapment arising from the strong dual porosity of textile architectures has been tackled. Nevertheless, a discrepancy between the void content stemming from a non-uniform impregnation and the final one is often observed. As a matter of fact, trapped voids can still change their shape and size and move with the flow throughout the impregnation before consolidation [28, 56], as depicted in Fig. 2.12. Just after formation, voids rearrange themselves to reach a lower surface tension and can be subsequently deform depending on surrounding forces and pore geometry. For example, Kang and Kurt [141] showed that the void deformation increases with its size but when the void diameter is too large, the force balance is lost and the void breaks up. Then, voids can also shrink by compression due to a surrounding pressure change or by dissolution into the resin and grow because of the diffusion taking place at the void-resin interface [142].

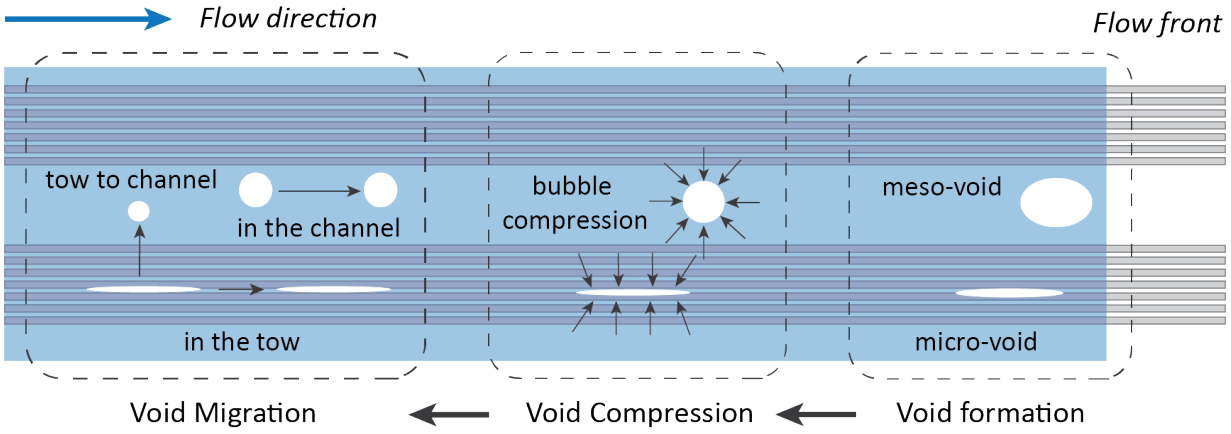

Figure 2.12: Stages of void life during resin infiltration in LCM. Figure adapted from Refs. [26, 56].

The void mobility is governed by a force balance between the drag force stemming from the pressure drop across the void and the interfacial adhesion due to surface tension as well as the advancing and receding contact angles [143]. In general, adhesion forces are smaller than hydrodynamic pressure resulting in the free movement of voids with the flow. However, this becomes more complex when voids are constricted into channels and particularly when they face geometrical constrictions [143, 144]. Gardescu [145] applied the Young Laplace equation to calculate the pressure required for a bubble to pass through a circular tube. He showed that when an horizontal fluid drag force is applied to the void, the adhesion force is lowered due to a change of the receding contact angle stemming from a void local deformation enhancing the fluid displacement. The equation he proposed can also be extrapolated to describe the force balance arising when a void faces a channel size reduction, in which the gap radius plays a crucial role [79, 146].

As a result, two main parameters are crucial to characterize void mobility: the main radii (channel and/or void), highly dependent on the fabric architecture and the pressure gradient between the void ends, strictly connected to the resin velocity and thus the capillary number Ca. Researchers

[92, 141, 147–149] defined a critical capillary number Ca_{mob}, defined from the competition between dynamic capillary forces and viscous shear forces, above which voids start to become mobile for a given system and can be expressed as [52]:

$$Ca_{mob} = \frac{4K_{sat}k_r}{l_{void}\cos\Omega}\left(\frac{\cos\theta_r}{D_e} - \frac{\cos\theta_a}{D}\right) \tag{2.27}$$

where l_{void}, D_e, D are respectively, the void length, pore throat (corresponding to the smallest pore) diameter and the averaged pore diameter. The angle Ω corresponds to the angle between the void length direction and the average flow direction and θ_r and θ_a are the dynamic receding and advancing contact angles between the fluid and the fibers.

Researchers found that it is more difficult to remove micro-voids inside the tows while meso-voids can easily be evacuated with the resin. For example, Rohatgi et al. [150] state that in the smaller gaps in between the fibers as compared to meso-gaps in between the tows, the drag force is not high enough, preventing micro-voids to move. Lundström et al. [144] claimed that micro-voids could be removed by compression and diffusion, subsequently, migrating to inter-tow areas and become inter-tow voids when merging with other micro-voids albeit this step is not so easy to carry out in some LCM processes.

In the present work, void formation and migration mechanisms stemming from the fluid displacement into a fibrous preform as well as the resulting void location and morphology as a function of the wettability and the porous medium architecture will be addressed.

2.6 Impregnation assessment

To accurately assess flow and void phenomena, the impregnation is usually studied by coupling post-mortem or in-situ observations of the flow to the mathematical models previously presented. Nevertheless, although several methods have been proposed, no agreement has been reached on the preferred technique since each specific method brings its own advantages and trade-offs between spatial resolution, recording speed and ease of implementation.

2.6.1 Post-mortem measurements

Post-mortem measurements were the first proposed method to analyze the final composite part quality resulting in varying process parameters, by determining the residual void content after consolidation. Composite parts were observed by performing a micrograph of the cross-section [103, 105, 150–152], burn-off [52], Archimedes method [151], non-destructive ultrasonic C-scan [153–155], active thermography [156] or micro-CT [157, 158]. However, while bringing the advantage of being an easy method with low equipment costs, post-mortem analysis could lead to large inaccuracies. In addition, since the void content is also affected by phenomena occurring after passing of the flow front, post-mortem measurements are not fully representative to describe flow mechanisms.

2.6.2 In-situ flow visualization practices

Direct flow visualization techniques offer a more accurate way to assess the flow morphology, enabling a better understanding of flow kinetics. Many experimental methods have been proposed over the years, for the sake of elucidating flow patterns either very locally at the scale of a few fiber tows, or through the macroscopic analysis of the porous medium progressive saturation by the flowing fluid. However, seldom techniques have been developed for non-translucent fabrics such as glass and rare studies tackled the impregnation through non-translucent fabrics such as carbon.

Flow through translucent preforms

The most widespread and simple approach relies on optical techniques to record impregnation in a non-intrusive manner and at a relatively high spatial and time resolution [52]. The recorded images are thereafter analysed to extract the required information [48, 60, 100, 102, 105, 142, 159–161]. In order to enhance the fluid/fabric visual contrast, colorants compatible with the test fluid can be added [44, 162–164]. For example, Nordlund and Michaud [105] and Faccioto et al. [48] employed optical methods to record the linear flow with a conventional camera and estimate the width of the unsaturated region over time in glass preforms. An increase in spatial resolution can be achieved with optical microscopes, though at the cost of a smaller field of view [60, 159, 165]. For instance, Yoshiara et al. [60] observed the dual-scale flow and void formation on single woven pristine and fluorine coated fabric layers at the micron-scale. They found that the void formation is drastically affected by a change in the static contact and the dynamic contact angle is a critical parameter controlling the impregnation and meso-void formation processes.

These techniques however allow the capture of flow patterns only at the surface (in contact with the mold) and wall-effects, race-tracking as well as nesting effects which are known to highly influence the flow might be neglected [166]. This is why they are often reserved to single layer experiments and are not fully representative of real fibrous preforms impregnation. To overcome this issue, some authors proposed to use Visible Light Transmission (VLT) to observe the through-thickness flow [100]. The principle is to place a diffuse light below the transparent mold and a camera above to record the light intensity averaged over the preform thickness. The addition of fluorophores, employed by Refs. [52, 54, 72, 106, 107, 167], provided an improved contrast to assess the progressive saturation of glass fibrous preforms and characterize the local void content to estimate the optimum capillary number.

Alternatively, Caglar et al. [86] recently proposed a novel approach based on UV-photocurable resins, where infiltrating flows are in-situ UV-frozen to be analyzed afterwards. Neitzel et al. [168] employed the same technique to observe dual-scale flows and void formation. One single layer was used in both studies but Caglar et al. [86] concluded that this technique can be extrapolated to multilayer systems. Although there is no time resolution constraint with this approach, allowing the visualization of a large range of flow regimes, the use of specially designed resin systems is required as well as thin and transparent samples to avoid inhibiting the cure reaction that is highly dependent on the penetration

of UV light.

Indirect recording of the flow

Some researchers were also able to extract the flow front location and saturation without directly visualizing the flow. For instance, Villière et al. [108] developed an experimental methodology to build the saturation curve taking advantage of the strong sensitivity of the thermal properties between wet and dry glass preforms recorded by several heat flux sensors placed along the mold. Alternatively, Guéroult et al. [169] infused a non-conductive glass fabric with an electrically conductive liquid and recorded in-situ the voltage which increased with liquid saturation. Similarly, Carlone et al. [97, 98, 170] used dielectric sensors to monitor the capacitance variations induced by the fluid movement while impregnating a glass preform, this method allowed to use less conductive resins. Recently, Neitzel et al. [171] used the same technique to automatically adjust the injection pressure with the aim of controlling and uniforming the flow front velocity to obtain specimens with reduced void content.

However, the requirement of a non-conductive preform limits the previous techniques to other conventional fabrics. To overcome this, recent studies proposed to insulate the sensor or use novel sensors for increased characteristics [172–175]. To-date these novel sensors have not been employed to study unsaturated flows. The discrete nature of sensor limits the observations that can be made with optical techniques while the spatial resolution of these techniques remains relatively low.

Flow through non-translucent preforms

The aforementioned techniques are generally only suitable for translucent glass preforms and infiltration through many commercially available fibers, which are opaque, such as carbon, flax or Kevlar, has seldom been addressed in literature. Few methods have been proposed and are hereunder outlined.

Some researchers were able to optically visualize flow fronts in carbon, for example Lystrup et al. [176], by means of fluorescent dyes, but as previously discussed those are limited to single layers or a top view [177, 178]. Ravey et al. [77] proved the feasibility of tracking the flow front position of glass and carbon fabrics during wicking experiments by Infrared Thermography (IRT) but again, the single ply limitation arises.

Ultrasound techniques, known for their high acquisition rates, have been tested as alternative to track resin flows in fibrous preforms. Thomas et al. [179] tracked through-thickness resin flow via acoustic C-scan measurements giving a planar view of the sample. While this method gives an indication of through-thickness saturation of the preform, the limited spatial resolution does not allow for distinction of capillary effects such as localized saturation and void formation. Alternatively, Liu et al. [180] were able to visualize the advancement of a resin flow impregnating into one and two layers of carbon fabric using an ultrasound imaging system. However, the scale resolution and the detecting depth are presented as the main limitations of the approach. Ultrasounds were also used as an indirect measure-

ment to track the front position and characterize the unsaturated permeability in carbon preforms in Refs [181–183].

Endruweit et al. [184] investigated the use of Magnetic Resonance Imaging (MRI) to in-situ map the local fluid concentration and distribution at the meso-scale during the impregnation of several layers of glass and carbon fabrics. However, the authors pointed out two main drawbacks when using this imaging technique: the scanning times were between 7 and 20 minutes, far away from conventional infiltration speeds and the spatial resolution was limited by signal relaxation effects.

2.6.3 Flow visualization by means of X-ray techniques

X-ray imaging relies on the ability of the electromagnatic waves (with wavelengths ranging from 0.01 to 10 nm) to penetrate matter allowing high speed measurements (over 20 frames per second). It is possible to study dynamic processes with 2D radiographic tools or carry out more complex processes with 3D tomographic reconstruction methods although more complex equipment is needed [185]. As a result, X-ray visualization techniques proved to be potentially very powerful techniques to observe materials with an increased spatial and temporal resolution with thickness averaged information. Their ability to pass through objects and provide photographic reconstruction of the transmitted signal makes them an attractive alternative for non-destructive inspection as well as for the study of dynamic transport phenomena. In the particular case of composites, given the low density of both resins and fibers leading to low absorption properties, the observation via conventional radiography is not simple and request high beam energies or the use of contrasting agents.

Bréard et al. [186] were pioneers in applying X-ray techniques by tracking through-thickness the flow through a random mat by X-ray radiography. Resulting images had a sufficient resolution to capture the flow path whereas the geometry of the fibrous preforms was not elucidated. The use of X-ray Computed Tomography (XCT) has allowed to assess dual-scale flows at an unprecedented resolution (features up to the sub-micron scale can be reached). However, it remains more suitable for static or very slow processes since blurring effects can appear due to the flow movement, lowering the image resolution [79]. To solve this, the acquisition time should be fast enough to limit the movement to less than 1 voxel per scan. Owing to the scanning time limitation, some studies employed XCT to indirectly assess the dual-scale behavior, e.g. by evaluating fiber stack thickness changes [187] or use the preform 3D scan to carry out computational fluid dynamics simulations [188].

All the same, the swift development in X-ray imaging tools has allowed recent researchers to image in-situ dual-scale flow behavior. Vilà et al. [146] were the firsts to use XCT to image the intra-tow impregnation of a glass bundle using a synchrotron beamline. Fluid front speeds were very slow to reproduce capillary flows and the injection was stopped to perform the imaging recording, since the 3D scan (with voxel size 2.5 μm) took about 120 min. Then, Larson et al. [189, 190] drastically reduced the imaging time to 1.5 min at the cost of resolution, and recorded the flow through fibers

bundles at higher speeds, more representative to processing speeds used in LCM. Vilà et al. [146] and Larson et al. [189, 190] exploited the progressive saturation of glass fiber bundles from the recorded images and related it to local capillary pressure and relatives. In the same vein, Castro et al. [70], imaged capillary wicking in a fiber bundle with increased resolution to study 3D local contact angles by means of synchrotron radiation.

Recently, Castro et al. [79] made use of so-called synchrotron radiation computed laminography and were able to significantly gain in field of view as well as in acquisition times (1.8 min) per tomogram to image planar samples, being the first to in-situ image dual-scale flow behavior in woven textiles with micron-scale resolution as shown in Fig. 2.13. They analyzed equilibrated and capillary flows and segmented both inter- and intra-yarn void distributions, gaining novel insights in void formation mechanisms. Interestingly, Gayot et al. [191] just published a proof-of-concept study to in-situ dynamically monitor the void formation and curing with a lab-based XCT method (also referred to as 4D-XCT) at a scan time of 2 min 15 s per scan. Nevertheless, the temporal resolution of XCT technologies remains low when compared to impregnation speeds used in LCM processes [192].

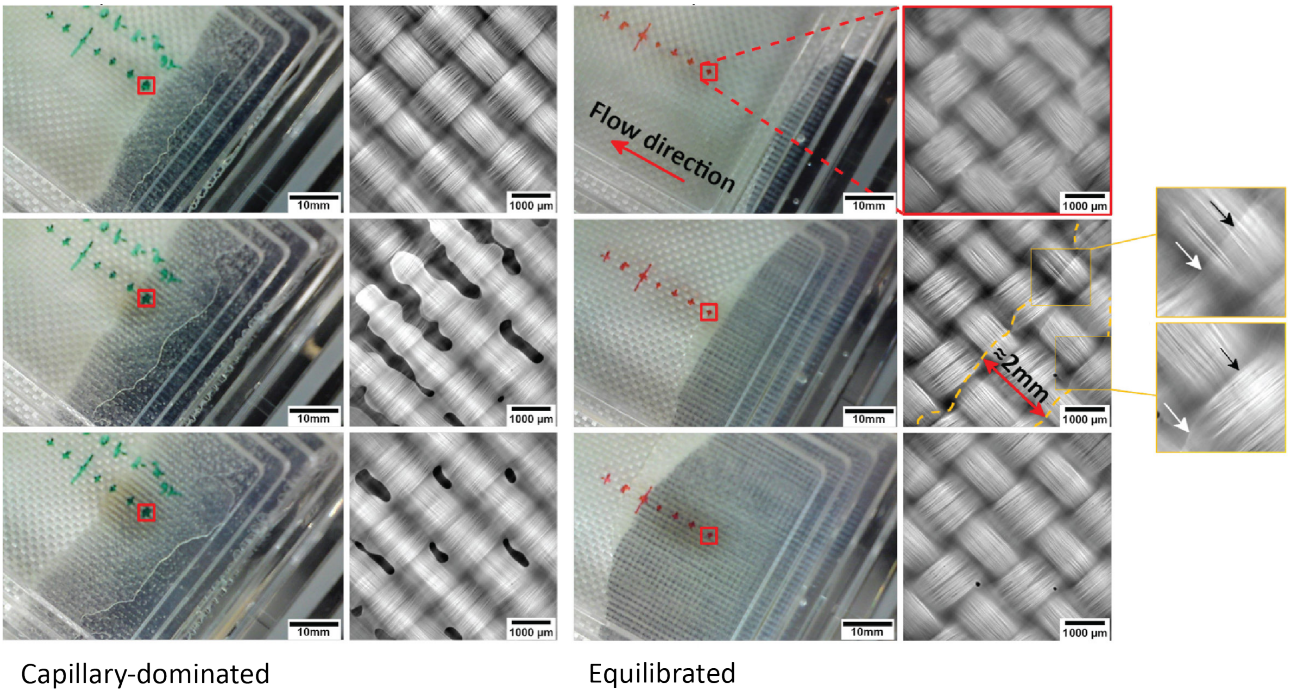

Figure 2.13: Flow progression recorded by synchrotron radiation computed laminography. Reproduced with permission from [79].

2.7 X-ray phase contrast imaging

Conventional X-ray techniques based on X-ray attenuation can be limiting when a contrast between low density materials, which weakly absorb X-rays such as composites, is sought. A novel technique named X-ray phase contrast combining grating interferometry [193–199] has enabled to overcome this limitation, enhancing the contrast between materials that present similar densities and features such as boundaries between similar materials, by using the refraction and scattering ability of X-rays [200]. Furthermore, this technique allows to image large samples and can be adapted to conventional X-ray laboratory sources instead of synchrotron sources [201–203].

2.7.1 X-ray Talbot-Lau interferometry

The typical configuration of a Talbot-Lau interferometry is shown in Fig. 2.14 and consists of a conventional X-ray source, three gratings (G_0, G_1 and G_2) and an X-ray detector. Grating based imaging uses periodic structures to diffract the incident waves. These gratings act as a dispersive element and every fractional distance, the same signal pattern is repeated but appears phase-shifted with a fractional period [194, 195, 204].

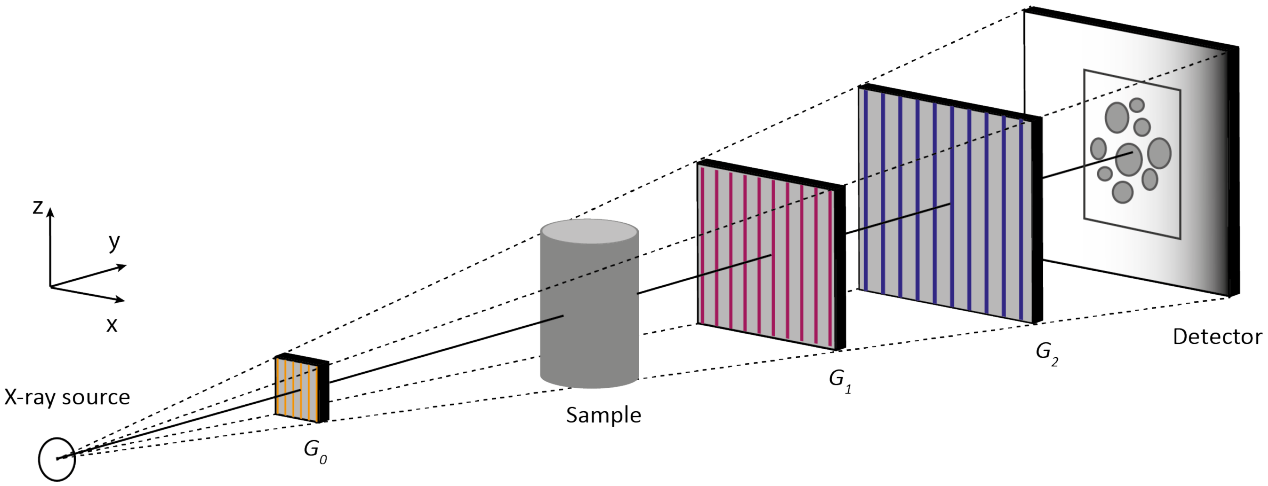

Figure 2.14: Representation of a Talbot-Lau interferometry setup, using three optical gratings.

Thus, the principle of this method is to create an image from the modified structured interference pattern of the grating when a sample is placed in between the source grating G_0 and G_1 and G_2 gratings. In particular, G_0 is an absorbing grating placed close to the beam source and its function is to divide the beam coming from the X-ray source to increase the spatial coherence. G_1 is a phase grating whose mission is to split and divide the incoming beam, thus inducing periodical phase modulations on the X-ray wave front and an intensity pattern I_f is produced in the plane of G_2. The local changes of the interference pattern are thereupon recorded on the detector with the help of G_2 which is an absorption analyzer grating. The changes in the intensity modulation are finally converted into changes in the intensity I_{pix} recorded by the corresponding pixel of the X-ray detector (Fig. 2.15) [195].

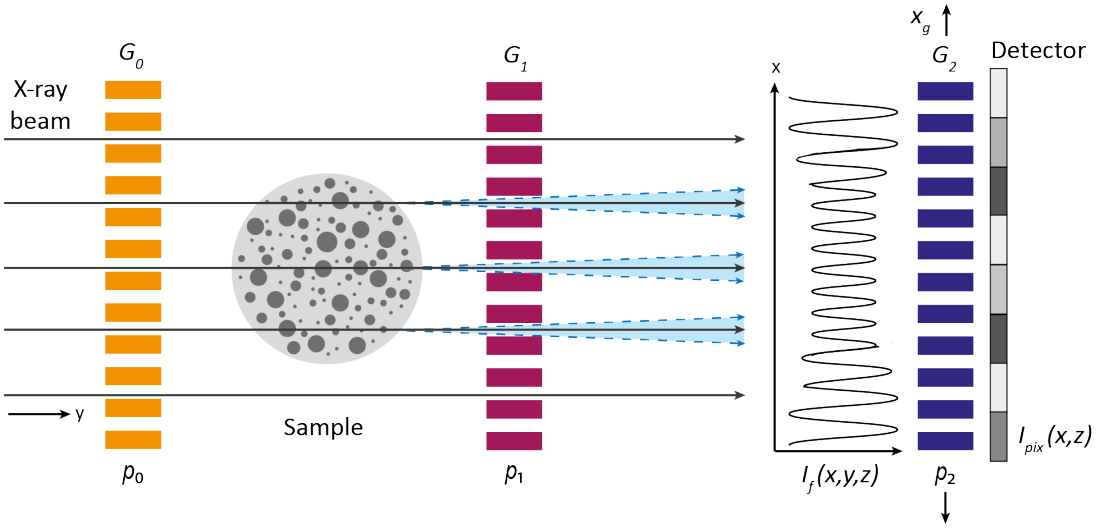

Figure 2.15: Representation of the X-ray wave front perturbations introduced by an object, which are translated into intensity variations and thereafter measured by a detector.

In the presence of an object, the X-ray beam propagation is affected by three phenomena: attenuation, refraction and ultra-small angle scattering, as presented in Figure 2.16. In the case of a pure absorbing object, the intensity curve is decreased due to the absorption of photons that interact with matter mainly in form of photoelectric effect and Compton scattering. Then, a purely phase-shifting object induces a deviation of the X-ray beam by an angle α_s. Finally, a pure scatterer object presents internal inhomogeneities, which will induce fast variations of the wave front by small and ultra-small angle scattering (SAS) (very small angular deflection in the order of arc-seconds) and a beam broadening w. Those inhomogeneities are variations in the electron density at a length scale close or below the grating period of G_1. It should be noted that the refraction angle and the SAS are measured only perpendicular to the grating's lines. As a result, intensity variations parallel to the grid lines are observed and defects in the perpendicular direction to the grating lines might not be identified in the images. For this reason, the gratings can be rotated 90° in order to acquire different images and observe the sample in different direction and try to identify anisotropic defects [205].

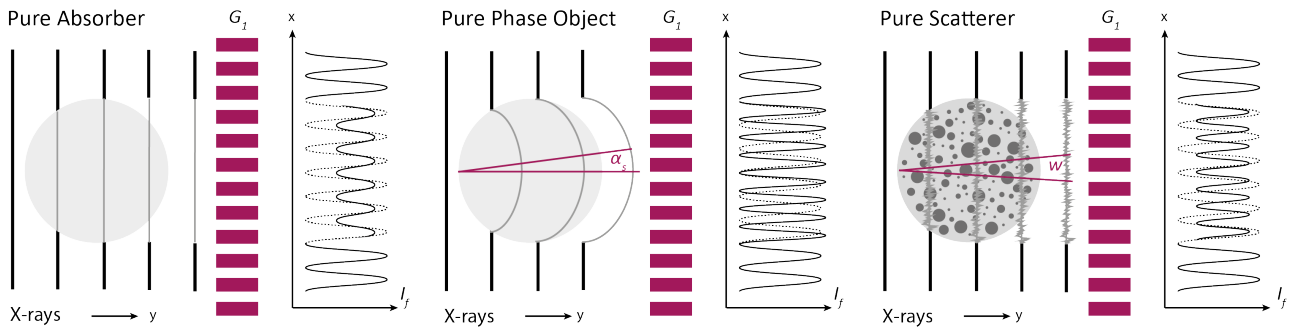

Figure 2.16: Schematic of the X-ray front and the amplitude transmission function (I_f) perturbations induced by a pure absorber, refractive and scatterer objects.

It is possible to decouple the aforementioned different contributions and extract three different images, namely absorption, refraction and scattering images by applying a reconstruction method. The operating principle for image extraction is as follows: the period p_2 of the analyzer grating G_2 and the interference pattern caused by G_1 are matched. For each measurement, the analyzer grating G_2 is moved in small steps in transverse direction over one period of the grating. Then, an intensity curve is recorded for each exposure, the intensity is a function of the grating position x_g and the pixel position (Fig. 2.17).

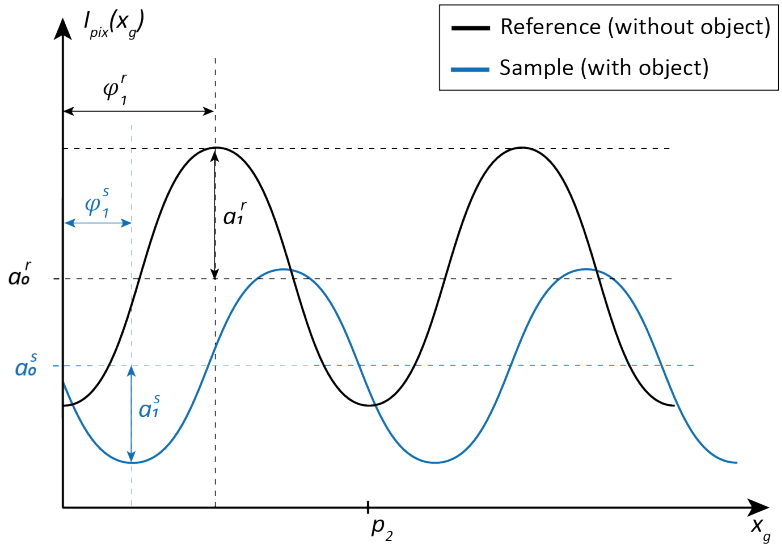

Figure 2.17: Representation of a measured intensity I_{pix} in function of the relative grating position over the pattern period (x_g) by a detector.

To analyze the changes quantitatively, the recorded intensity for each detector pixel $I_{pix}(x, z)$ can be written by means of a Fourier series as follows:

$$I_{pix}(x, z, x_g) = \sum_i a_i(x, z) \cos\left(ik_g x_g + \varphi_i(x, z)\right) \approx a_0(x, z) + a_a(x, z) \cos\left(ikx_g + \varphi_i(x, z)\right) \quad (2.28)$$

where a_i are the amplitude coefficients, k the number of steps ($k = 2\pi/p_2$) and φ_i the corresponding phase coefficients. The absorption image T is given by the normalized average transmission of the specimen for each pixel as $T(x, z) = a_0^s(x, z)/a_0^r(X, z)$, where the subscripts s and r denote "sample" and "reference". The absorption image would be the same as the one measured by conventional X-ray radiography. The differential phase (or refraction) image DP is given by $DP(x, z) = (\varphi_1^s - \varphi_1^r)/2\pi$. The scattering image V is given by the normalized visibility $V(x, z) = (v^s(x, z))/(v^r(x, z))$, where v is the visibility and it is expressed as $v^r(x, z) = a_1^r(x, z)/a_0^r(x, z)$. For samples with negligible small angle scattering, visibility remains unchanged and is equal to 1. Conversely, for samples that present strong internal density variations on the micrometer scale, strong small-angle X-ray scattering signal is produced leading to a decrease of the visibility with values lower than 1 [195, 204].

2.7.2 Applications

X-ray phase contrast technique is mainly used in the medical imaging field [206–217], but it is gaining interest in other sectors as a non-destructive evaluation techniques to observe for example, natural samples [218], elucidate hidden features in archaeological findings [219] or for materials science to detect porosity [220, 221]. In particular, this technique turns out to be very interesting to assess the internal structure of composite materials.

Gresil et al. [205] compared traditional non-destructive methods with grating based X-ray phase contrast imaging for the detection of defects such as porosity, foreign objects, cracks, resin rich areas, cut fibres, wavy fibres in carbon composite structures for aerospace applications showing the interest of this technique to provide unique features in terms of reliability and detailed insight. Similarly, Hannesschläger et al. [222] studied the main fiber orientation of injected short glass fiber reinforced polymer, Revol et al. [223–225] evaluated the size of fiber bundles, the resin content and the fabrics weave pattern, Gusenbauer et al. [226] made an extensive study to determine the porosity in carbon and glass composites and Senck et al. [227, 228] determined the fiber lay-up and characterized micro-craks in loaded carbon fiber laminated in 2D and 3D among others [229]. Pathak et al. [230] observed in-situ the dynamic failure mechanisms of carbon composites in tensile mode.

Nevertheless, all those studies were based on observations of cured samples. So far, no studies have been focused on observing the processing of composites materials by means of X-ray phase contrast imaging. Some researchers nonetheless succeeded in observing with clarity the presence and distribution of a liquid in gas or liquid phases. This is mostly the case in medical applications, but a first application in cementitious materials was successfully proposed. Yang et al. [231] worked on the visualization of unsaturated water transport in mortar and they manage to track a fast transport process which can be compared to LCM process in terms of speed. They found that capillary water uptake leads to a decrease in scattering which is produces a high contrast between wetted and non-wetted zones. Then, Prade et al. [232] visualized the transport of water during the hardening of a cementitious sample which is a slow dynamic process on the micrometer scale which can be interesting in the case of LCM to understand slow phenomena such as void migration.

2.8 Conclusions

Impregnation of fibrous preforms by a liquid resin is a key step in LCM processes that should be controlled to avoid flaws and achieve manufactured parts with outstanding properties. Since infiltration falls in the wide class of phenomena wherein a fluid displaces another within a porous media, it is found in several natural and engineering processes and an extensive literature exists on the subject. Nevertheless, a clear understanding of flow kinetics and the interplay between different physical phenomena taking place from micro to macro scales has never been reached so far.

Engineering textiles present a hierarchical architecture, with densely packed fiber tows, leading to strong capillary effects. During infiltration, the fluid flow pattern is determined by the extent of viscous and capillary forces and it is commonly assumed that a dual-scale flow arises from the specific architecture of fabrics generating a void entrapment mechanism. Moreover, wettability which is a pore scale property turns out to be dynamically dependent affecting the overall kinetics and thus the behavior of the flow pattern. Researchers found that there is an optimum impregnation speed at which this dual-scale is mitigated and the void content is minimal. However, to date no one has been able to predict this optimum condition according to the system physical parameters and/or processing conditions for instance.

Many efforts have been carried out over the past thirty years, to visualize the flow dynamics and describe its behavior with mathematical models, with the aim to better predict industrial manufacturing processes. Several techniques have been developed for glass preforms given their translucency but few studies have focused on non-translucent preforms such as carbon. Nowadays, X-ray based techniques gain a foothold as non-destructive techniques in many sectors given their increased spatial and temporal resolution. Furthermore, given the sparking interest of these techniques, several technologies are developed around X-rays to extract information from the different signals coming out from their interaction with matter leading to a wide range of materials that can be analyzed. For instance, the novel X-ray phase contrast image, will be exploited in the present work, to bring further insight into the dynamics of fluid flow in carbon based preforms.

Chapter 3

Materials and methods

This chapter first introduces the selected materials for this work: porous preforms and infiltrating liquids. Then, the design of the impregnation experiments and flow assessment methodology are presented. Finally, the flow modelling approach is detailed.

3.1 Materials

3.1.1 Porous materials

A glass fabric supplied by Suter Kunststoffe AG (Switzerland) was selected as translucent reference material. The glass fabric (Fig. 3.1 is a woven 2 × 2 twill made out of E-glass with an areal weight $A_w = 390$ gsm and previously used by Caglar et al. [45, 86]. The glass fiber density is 2.61 g/cm^3 and its diameter 9 µm.

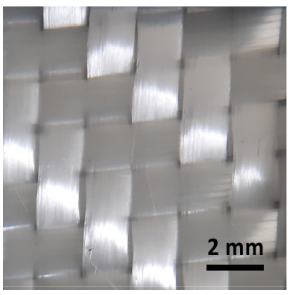

Figure 3.1: Reference twill glass translucent fabric.

Two carbon fabrics were employed: a unidirectional and a twill, both supplied by Suter Kunststoffe AG (Switzerland) as well. The unidirectional fabric (Fig. 3.2a) was selected as non-translucent reference material. Actually, is a quasi-unidirectional fabric with thin E-glass threads in the weft direction to maintain the position of the carbon tows, with a total areal weight of 270 gsm (with 96.3 wt.% of carbon). The 2 × 2 twill fabric (Fig. 3.2b) was used as alternative fabric given its strong dual-scale; its areal weight is $A_w = 285$ gsm. According to the datasheet, the carbon fibers for both fabrics are

sized Tenax HTA 3151 fibers from Teijin with a density of 1.77 g/cm^3 and diameter of 7 µm.

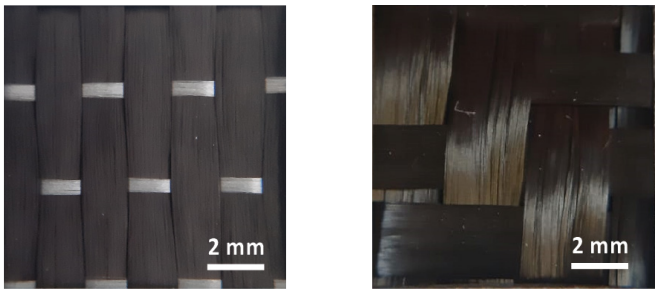

(a) **(b)**

Figure 3.2: Pictures of the (a) reference non-translucent unidirectional and (b) twill carbon fabrics.

Two flax fabrics supplied by Bcomp (Switzerland) were chosen as alternative non-translucent preforms. One is a 2 × 2 twill fabric (ampliTexTM5040) with an areal weight of 300 gsm (Fig. 3.3a). The other one is a unidirectional fabric (ampliTexTM5057) with a polyester thread in the weft direction to maintain the structure, its areal weight is 150 gsm (Fig. 3.3b). Flax fibers' diameter varies from 20 to 40 µm.

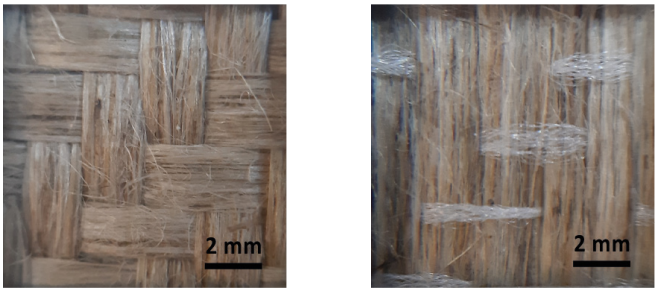

(a) **(b)**

Figure 3.3: Pictures of (a) the twill and (b) the unidirectional flax fabrics.

Finally, the 3D printed structure designed by Morren et al. [233, 234] was used to visualize impregnation of a polymeric based porous structure. The structure is a grid of 3 mm thickness, with macro-spaces interconnected with micro-channels to mimic a textile-like solid as shown in Fig. 3.4. Initially, the purpose of this porous structure was to produce a reference textile-like solid specimen with anisotropic permeability, for calibration of permeability measurement set-ups and validation of permeability modelling. The porous grid was reproduced by a FlashForge Hunter Digital Light Processing (DLP) 3D printer with the resin FlashForge FH110 (density about 1.1 g/ml) and had a dimension of 5 cm × 12 cm and 3 mm thick, the length was limited by the maximal printing size of the 3D printer.

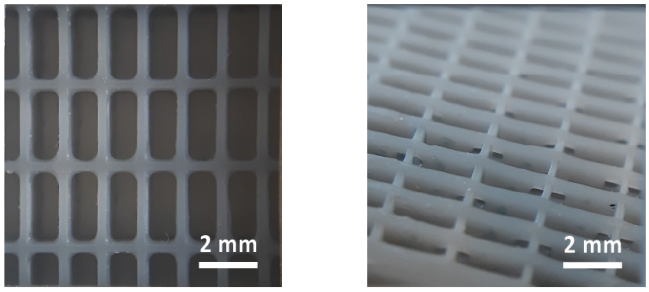

(a) (b)

Figure 3.4: Pictures of the 3D printed structure (a) from above and (b) from the side showing the interconnected porosity.

3.1.2 Fluids

As a reference test fluid, a water based solution of poly(ethylene glycol) (PEG) (M_w = 35 kDa, Sigma Aldrich) at a concentration of 16.7 wt.% was prepared, previously employed and also characterized by Salvatori et al. [44], to obtain a viscosity similar to those of thermosetting resins typically used in composites manufacturing. For optical experiments a small amount of Rhodamine B colorant from Carl Roth, was added to the fluid, without altering the solution properties.

With the aim of increasing fluid-fabric contrast in X-ray absorption, a zinc iodide-based contrasting agent solution was prepared following the recipe of Sket et al. [235]: by mixing 60 g of ZnI_2 (M_w = 319.19, Fluorochem) to 20 ml of water and 10 ml of surfactant Kodak Photo-Flo 200. Then, the reference PEG solution was mixed to 20 vol.% of the contrasting solution leading to a final composition of: 62.5 wt.% of water, 22.6 wt.% of ZnI_2, 11.0 wt.% of PEG and 3.9 wt.% of surfactant.

Then, it was sought to design a fluid with similar properties to the previous PEG-ZnI_2-based solution, i.e. viscosity and X-ray attenuation, but different wetting properties. To this end, a water-based solution of glycerol (99.5%, M_w = 92.09, Sigma Aldrich) at a concentration of 87 wt.% was prepared and was mixed to 20 vol.% of a second contrasting agent prepared avoiding the surfactant to not modify the wetting properties of the fluid, in which 60 g of ZnI_2 were mixed to 30 ml of water. The final composition of this mix was: 62.5 wt.% of glycerol, 20.1 wt.% of ZnI_2 and 17.4 wt.% of water.

Another fluid with similar viscosity and X-ray attenuation properties was also developed but finally not used in the frame of the thesis. The fluid was an epoxy blend with ZnI_2 also as contrasting agent. Its properties are presented in *Chapter 9* section 9.1.1.

The fluids were characterized by measuring their density, surface tension and viscosity-temperature dependence in order to be able to measure the permeability from Darcy's law (Eq. 2.5) and calculate the capillary number (Eq. 2.13). The density was simply measured with an analytical balance Mettler Toledo XSR204. The surface tension in air (γ_{la}) at ambient temperature was measured through of the pendant drop method on a Drop Shape Analyzer (DSA30, Krüss). The viscosity measurement

was assessed in a concentric cylinder rheometer (AR2000ex, TA Instruments), by means of a Peltier Couette setup with a temperature ramp ranging from 15 °C to 30 °C at a heating rate of 0.1 °C/min and constant shear rate of 10 s^{-1}. The viscosity vs. temperature curve $\eta(T)$ was fitted with an Arrhenius law:

$$\eta(T) = B \exp\left[-\frac{E_a}{RT}\right] \tag{3.1}$$

where B and E_a are the fitted pre-exponential and activation energy parameters and R the gas constant. The Newtonian behavior of fluids was verified by performing a shear logarithmic sweep ramp from 0.1 s^{-1} to 100 s^{-1}. Table 3.1 summarizes the properties of the test fluids used in the current thesis.

Table 3.1: Properties of test fluids.

Fluid	Density* [g/ml]	Surface tension* [mN/m]	Viscosity* [Pa · s]	E_a [kJ · mol^{-1}]	B [Pa · s]
PEG 16.67%	1.026	57.3	0.089	-20.39	$2.39 \cdot 10^{-5}$
PEG 16.67% + CA1	1.276	32.7	0.075	-20.79	$1.72 \cdot 10^{-5}$
Glycerol 87% + CA2	1.400	65.5	0.074	-40.96	$4.90 \cdot 10^{-9}$

* Values at 25 °C.

3.2 Impregnation experiments

3.2.1 Wettability characterization

The static contact angle θ_e between liquid and fabric was measured by means of the drop-on-fiber method following the geometrical analysis proposed by Carroll [236]. For that, a single fiber was carefully separated from the fabric, taped straight on a metal frame and the liquid was sprayed manually onto the fibers. The droplets were analyzed by a Keyence VHX-7000 microscope equipped with a zoom lens (100× to 1000×) and imaged at a resolution of 1600 × 1200 pixels.

3.2.2 Impregnation setup

A mold for flow experiments was designed to perform impregnations on fabrics of maximum size of 50 mm × 150 mm. The mold is composed of two aluminum external frames, two poly(methyl methacrylate) plates of 15 mm thick with one of the two perforated with tubes fittings for the fluid entry and exit, a stainless steel spacer (interchangeable spacers of different thickness were built to adapt the mold cavity thickness), a joint made out of silicon to prevent and minimize race-tracking, and fourteen bolts to close the overall setup. PMMA was chosen as transparent mold halves as it does not scatter X-rays and the thickness was optimized to reach a compromise between minimum noise in the X-rays which results from the PMMA absorption and maximum rigidity to avoid the setup deflection

from the fabric compaction.

Impregnation experiments were carried out as follows: fabrics layers were cut to a width of 4.95 ± 0.05 cm and desired length up to 15 cm and were fitted in the mold cavity. The fluid was injected either at constant flow rate or constant pressure, an injection unit R-100E syringe pump from Razel Scientific Instruments and a pressure pot were used respectively. Reinforcements were impregnated vertically from bottom to top (z-direction) and contribution of the hydrostatic pressure buildup due to the vertical position, was neglected (and assumed to be maximum of few kPa) since it was limited due to the fluid low density and short impregnation length. Then, a sensor Keller Series 35XHTT was employed to monitor the fluid pressure and temperature all along the impregnation. The overall setup is shown in Fig. 3.5. Optical observation of flow progression was performed through the transparent mold by a digital camera Canon EOS700D the video acquisition was set to 30 frames per second with a resolution of 1920 × 1080 pixels.

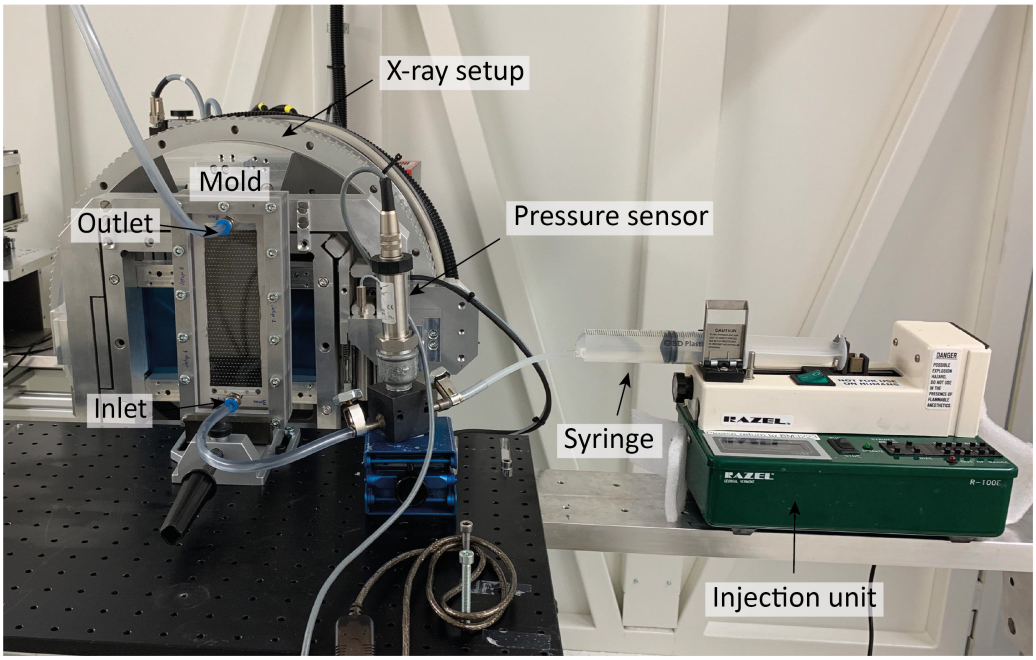

Figure 3.5: Impregnation setup.

3.3 Flow assessment

3.3.1 Visualization by means of X-ray phase contrast

The phase contrast X-ray imaging apparatus developed within the EVITA project (Non-Destructive Evaluation, Inspection and Testing of Primary Aeronautical Composite Structures Using Phase Contrast X-Ray Imaging) was used in the frame of this thesis [205]. The system is a Talbot-Lau grating interferometer based on the principles presented in *Chapter 2* and allows imaging an area of approximately 70 mm × 70 mm per acquisition. Moreover, the setup incorporates a moving platform (in x and z-directions) for large parts scanning and whose movement can be synchronized with the image

acquisition. The resulting images have a resolution of 1334 × 1331 pixels. The X-ray setup is the same as shown in Fig. 2.14 and includes a conventional X-ray source, three X-ray gratings and a X-ray detector. In the current setup, the grating lines of G_1 and G_2 are positioned along the z-direction and the gratings move in the x-direction as represented in Fig. 2.14.

As already introduced, this methodology allows to obtain three different images, namely absorption, refraction and scattering images. Preliminary experiments were performed to qualitatively assess the contrast between a stack of 8 layers of the reference carbon fabric and some drops of PEG-based solution embedded in two PMMA plates. An example is shown in Fig. 3.6 elucidating a clear contrast obtained in scattering images.

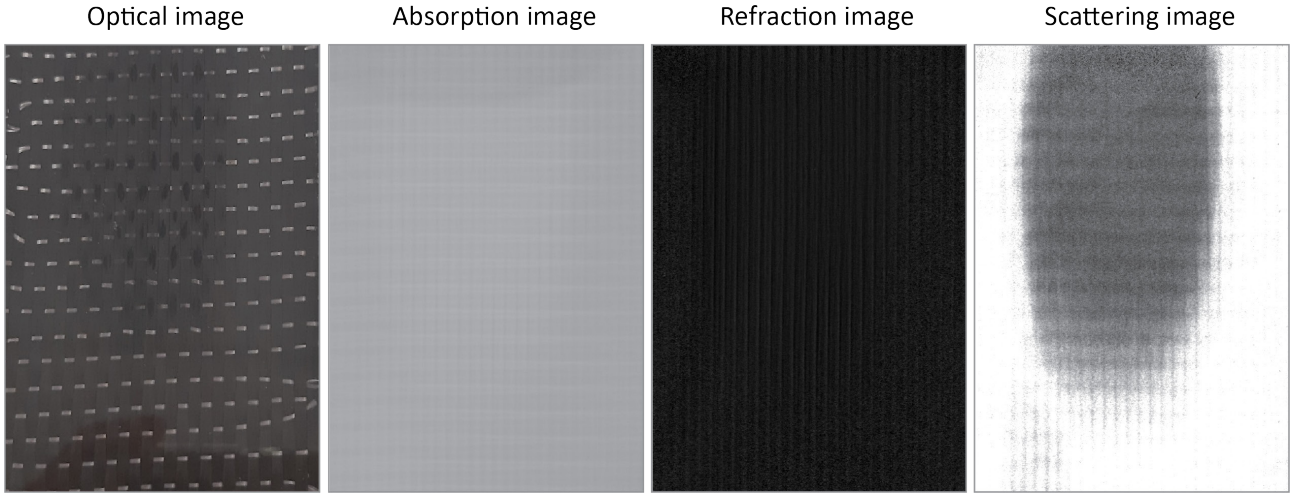

Figure 3.6: Images obtained with X-ray phase contrast imaging of a drop of liquid into a carbon fiber.

3.3.2 Acquisition methodology

After performing preliminary tests to define the required X-ray setup parameters to obtain scattering images with a satisfactory resolution and a good fluid/fabric contrast at a minimum time, it was set to acquire images from a series of 7 phase steps with an exposure time of 700 ms resulting in an averaged acquisition time of 9.2 s. There is an additional time (9.2 s - 7 × 700 ms) corresponding to the duration required to transfer data between phase steps. The acceleration voltage of the X-ray tube was 60 kV.

An acquisition methodology was conceived to track the impregnation along the preform length by synchronizing the X-ray stage movement in the z-direction and the flow speed. First, the impregnation mold was carefully positioned and centered in front of the acquisition window. The procedure was developed to center the flow front in the resulting images. As shown in Fig. 3.7, six different positions were defined, corresponding to five vertical platform movements of 25 mm. Then, the following steps were performed:

i. before launching the impregnation, the dry perform was scanned at one acquisition per position;

ii. the dynamic impregnation was tracked by adjusting for each experiment the number of acquisitions per positions, which was predefined, according to the flow front speed previously measured. It should be noted that it is possible to run constant pressure experiments, by defining a different number of acquisitions for each position;

iii. once the fluid reached the outlet, the impregnation was continued for a certain time (the time was set according to the flow conditions) ensuring a complete saturation of the fabric and a third scan was performed at one acquisition per position.

At the beginning of each of the three steps, a calibration routine was performed because the system calibration is sensitive to changes in ambient conditions. Finally, after each experiment, a data base file with the different acquisition times was generated and was used to couple the flow front spatial and temporal positions.

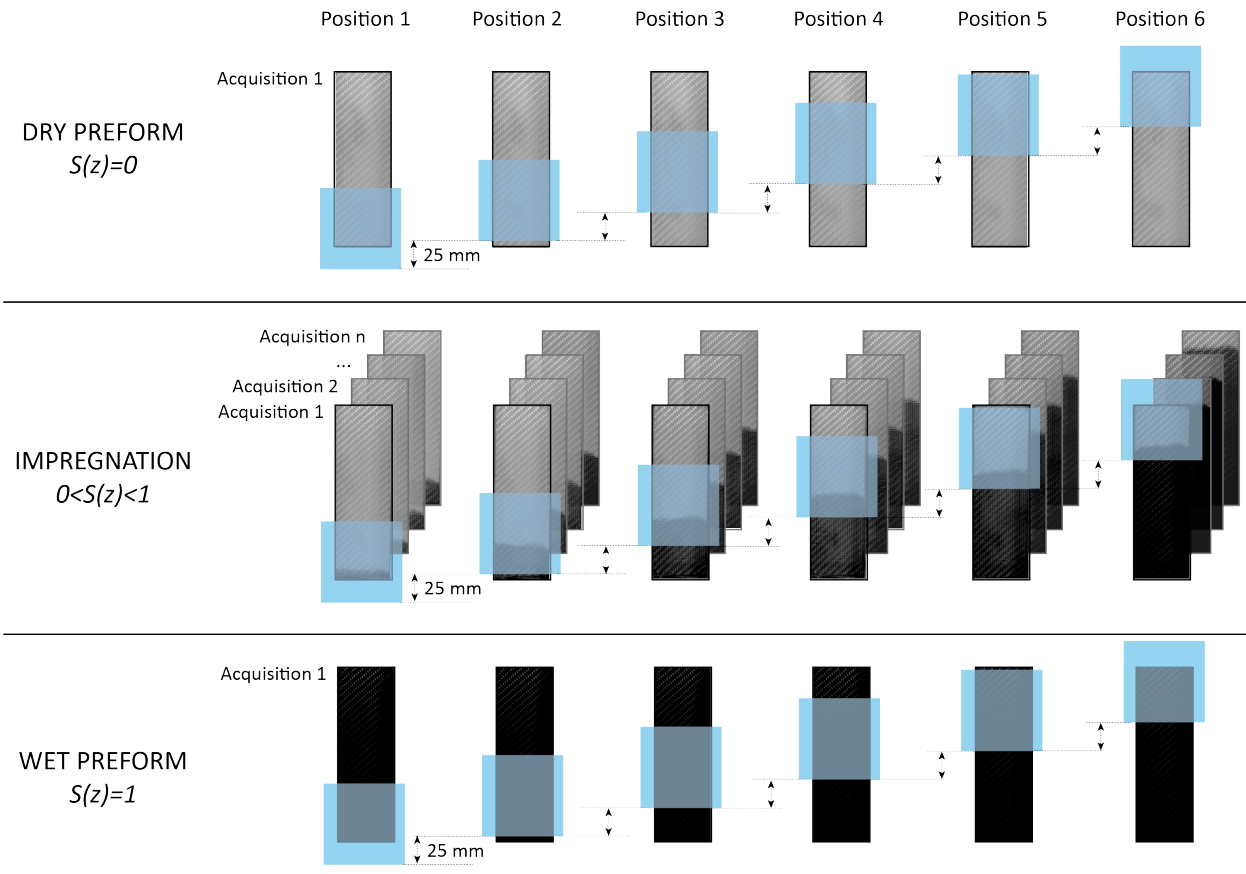

Figure 3.7: Representation of the acquisition procedure.

3.3.3 Saturation curve construction

A methodology was developed to extract the saturation curve versus the position $S(z)$ from the grayscale analysis of X-ray images, in particular for absorption and scattering images. An image processing routine was applied for each set of images to correct the verticality, cropping the selected

area of the impregnation for the saturation analysis (e.g. to remove flow edge effects) and smoothing the image if needed with an averaging filter. The saturation assessment was based on defining the deviation of the grayscale values of images acquired during impregnation from those of images from dry and wet states as illustrated in Fig. 3.8, where the light area corresponds to the dry fabric and the dark one to the fabric wet with fluid. It is assumed that the pixel intensity of the wetted fabric scans corresponds to a saturation equal to 1.

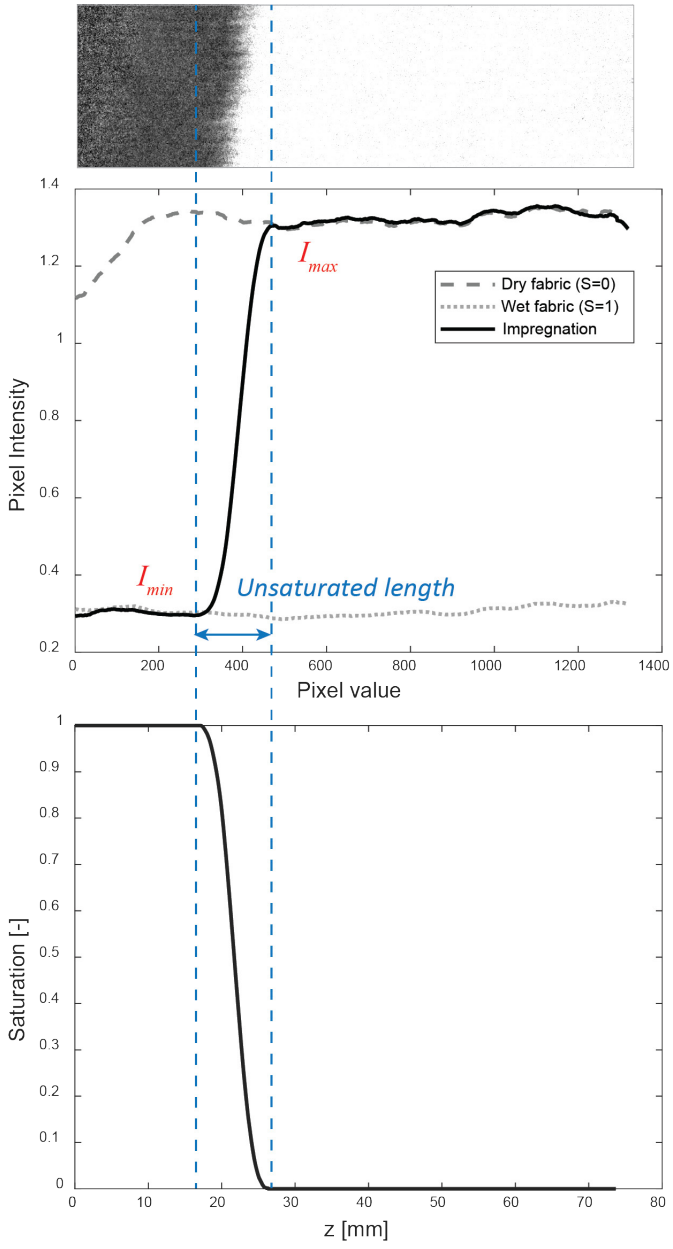

Figure 3.8: Methodology for the construction of $S(z)$ curve form the grayscale of X-ray acquisition images from an example of a scattering image of an impregnation in a carbon fabric.

For each image, the averaged pixel intensity value over each column, i.e. along the part width, was calculated. Then, for each position of X-ray setup acquisition, the pixel intensity versus pixel position curves of the dry and wetted fabric were generated and compared to the impregnation curves of that position. Three zones were thereafter distinguished: fully wet, unsaturated and dry fabric. The pixel intensity value I_{min} defines the transition between fully and partially saturated zones and I_{max} between the unsaturated area and the dry fabric. Finally, each pixel intensity value was converted into a saturation value by linear interpolation and the position z in pixels into millimeters by using the corresponding pixel size (between 50 and 55 µm). As all the instances linked to the image acquisition are recorded by the X-ray system and the stage displacement is known, $S(z,t)$ curves can be easily extracted.

3.3.4 Three-dimensional measurements

In the last stage of the project, infiltration experiments were performed and visualized in 2D and 3D by X-ray radiography and X-ray computed tomography respectively with the setup shown in Fig. 3.9. The same impregnation configuration as presented in Fig. 3.5 was employed but the mold was modified in order to remove the metal parts that would interfere in the 3D tomographic scans. For that, the inner steel spacer was replaced by one made out of PMMA and the external aluminium frames were removed. The setup was closed with twelve metal screws, leaving the 3D scan are free of high-density materials. From the 3D scans, the mold deflection was measured to be less than 2%. The impregnation mold and the pressure sensor were placed in a rotating stage for the 3D scans acquisition.

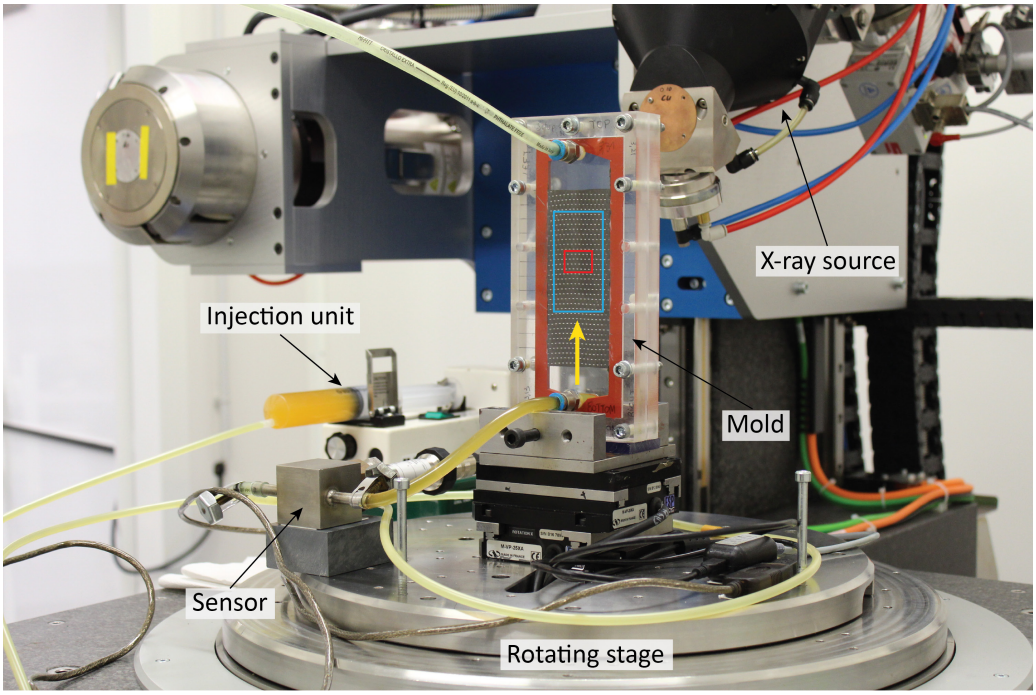

Figure 3.9: Impregnation setup adapted for X-ray tomographic scans. The yellow arrow shows the impregnation direction, the blue rectangle the total 2D scan area and the red the 3D scan area.

The flow progression was visualized by X-ray absorption using a laboratory X-ray microtomograph (RX Solutions Ultratom, PIXE Platform, EPFL, Switzerland) at 80 kV and 230 µA and an imaging rate of 2 images per second. Images were acquired at a pixel size of 15 µm and the flow front was tracked for an area of approximately 5.5 cm long and 3 cm width (blue area in Fig. 3.9). The location of the scanning area was the same for all experiments, more or less centered, in the middle of the fabric length and width. For that, three different positions were defined corresponding to three vertical movements of the X-ray source of 12 mm following a similar procedure as the one presented in section 3.3.2. A dry scan was performed followed by the progressive acquisition of the impregnation (the number of acquisitions per experiment was set according to the flow speed) and finally by a wet scan. Then, to evaluate dry and wet states of the preform, before and after each impregnation a tomographic 3D scan was performed at 3 images per second at a voxel size of 10 µm using the same X-ray facility. The 3D scans were performed in the middle position of the 2D scans as illustrated in Fig. 3.9 with the red rectangle.

3.3.5 Segmentation of 3D reconstructions

Scanned volumes were cropped to 1650 pixels × 310 pixels and 1200 slices, resulting in a volume size of 16.5 × 12.0 × 3.1 mm^3. The stack thickness was set to get rid of the mold and facilitate the segmentation analysis. An averaging filter was applied to the original data in the three x, y and z directions in Fiji [237]. Then, dry and wet scans were segmented by means of Ilastik [238], a machine-learning-based image analysis tool for pixel classification in which the user manually labels several regions corresponding to the different phases.

Three segmentation training algorithms were developed, each using a volume of 100 consecutive slices that were manually labelled to generate training data: one for the dry unidirectional fabric with “carbon”, “glass” and “pores” as labels; another for the dry twill with only two labels, namely “carbon” and “pores”; and one to treat the wet images with two phases “liquid” and “void”. An example of segmentation for dry and wet states for the UD fabric is illustrated in Fig. 3.10. The corresponding training algorithm is thereafter applied for each scanned volume and segmented images were then assembled in Avizo software to analyze the void content, location, and geometry.

In addition, a pore network model (PNM) construction was applied to the 3D segmented images, by using the PNM module from Avizo, to quantitatively assess the geometry and topology of the meso-pore space. The segmented pore label, corresponding only to the meso-space in between bundles, was separated into different objects which were automatically assimilated to pores connected with pore-throats [239, 240].

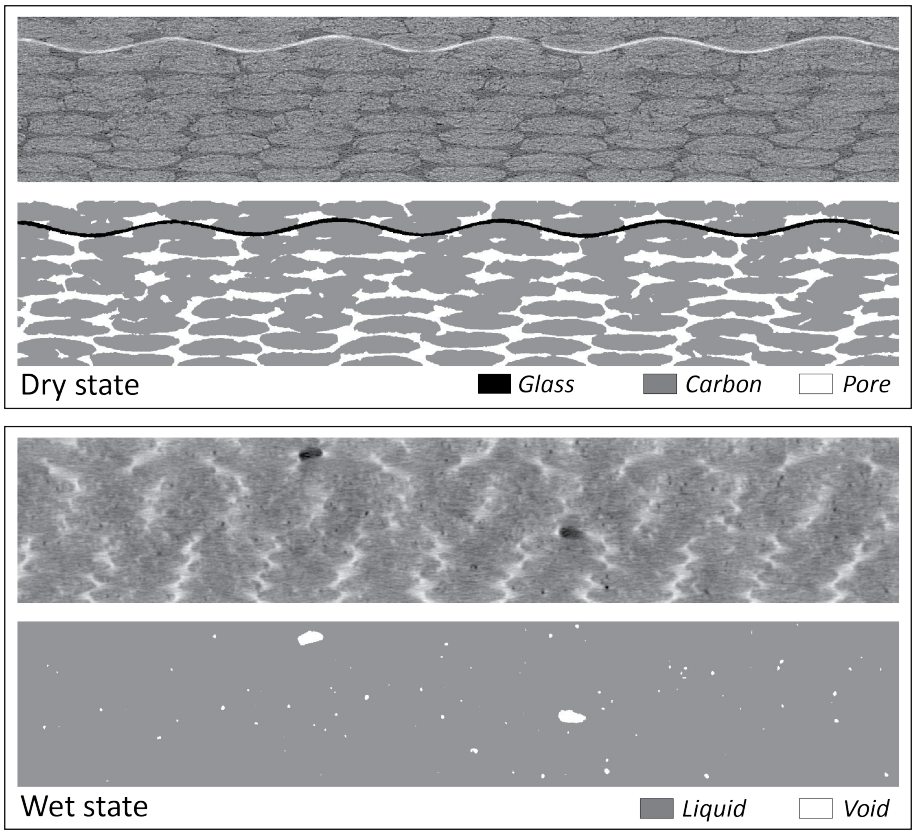

Figure 3.10: Segmentation of two-dimensional cross-sections for dry and wet states of the UD carbon fabric.

3.4 Flow modelling

3.4.1 Two-phase flow approach

In this thesis we chose to describe the dynamic displacement of the resin flow at the macroscopic scale by a two-phase flow model adapted from soil-science as previously proposed in Refs. [104, 105]. The flow behavior of two immiscible fluids inside complex porous media is affected by several factors such as wettability, viscosity ratio, heterogeneities of the pore geometry among others. This widely used approach encompasses all fluid-solid surface effects through the capillary pressure and the relative permeability descriptions.

The medium is defined by a representative elementary volume (REV) with three phases, namely air, resin and fibers. Even though the UD carbon fabric employed for the modelling has a bimodal pore size distribution, we assume here that the separation of scales in the textile considered is small enough that a dual porosity approach is not necessary [121, 241], which will be further confirmed. In addition, as already suggested in previous work (Ref. [105]), and considering the rather high viscosity of the fluid as compared to water (as the fluid of consideration in soil science studies), we consider that flow takes place far from equilibrium conditions, and so that the capillary pressure acting at the fluid/air interface depends on the flow rate conditions. Thus, the resin phase will be considered either wetting or non-wetting depending on the Ca value, and the air phase takes the opposite wetting properties. The two phases are thus defined by their wetting behavior, wetting or non-wetting and their respective

contents are θ_w and θ_{nw} and their sum is equal to the available pore space ϕ:

$$\phi = \theta_w + \theta_{nw} \tag{3.2}$$

Before impregnation, the porous preform is fully saturated with air and no resin phase is contained. Unlike soil media which can be initially partially saturated, in liquid composite molding, there is no residual resin. The degree of effective saturation S_α for each phase is thus defined as the ratio between the phase volume and the total free space:

$$S_\alpha = \frac{\theta_\alpha}{\phi} \tag{3.3}$$

with α denoting either the wetting (w) or the non-wetting (nw) phase. S varies between 0 and 1, 0 and 1 corresponding respectively to a dry and fully saturated preforms. Consequently, their effective saturations are coupled as:

$$S_w + S_{nw} = 1 \tag{3.4}$$

The macroscopic capillary pressure description P_c, combines the two phases through their pressures with the relation:

$$P_c(S_\alpha) = P_{nw} - P_w \tag{3.5}$$

In LCM, the air pressure is generally atmospheric, and for simplicity it is set to zero as a baseline. The specific capacity C_α of each phase is also defined as:

$$C_\alpha = \theta_\alpha \frac{\partial S_\alpha}{\partial P_c} \tag{3.6}$$

The capacity of both phases is the same but with opposite sign and thus related as: $C_w = -C_{nw}$. Resin infiltration is modelled with a continuum mechanics approach and it is assumed that air and fluid are incompressible Newtonian fluids and that infiltration takes place without any heat exchange (for non-isothermal cases, an equation for thermal transport can also be added). For each phase, the mass conservation equation is written as:

$$\frac{\partial \theta_\alpha}{\partial t} + \nabla \cdot (\theta_\alpha \vec{u}_\alpha) = \frac{\partial \phi S_\alpha}{\partial t} + \nabla \cdot (\phi S_\alpha \vec{u}_\alpha) = 0 \tag{3.7}$$

with u_α the average fluid velocity. It should be noted that equation 3.7 neglects gravitational or other momentum transfer between bodies and is only valid for a Reynolds number less than one, defined in relation to the average fluid velocity and the pore diameter. Darcy's law is applied to write the momentum equation for the liquid [29] (the mass balance equation is null for the solid since it is a rigid preform):

$$\phi S_\alpha \vec{u}_\alpha = -\frac{K_{sat} k_{r,\alpha}}{\eta_\alpha} \nabla P_\alpha \tag{3.8}$$

with K_{sat} is the preform saturated permeability, $K_{sat}k_{r,\alpha}$ the relative permeability, η_α the phase viscosity (considered to be constant along the impregnation) and ∇P_α the pressure gradient in the phase α. The term $\phi S_\alpha \vec{u}_\alpha$ from Eq. 3.8 is known as the superficial or infiltration velocity. Then, since air pressure is assumed to be null, the governing equation for the liquid phase is reduced to Richards' equation as [114, 242]:

$$C_\alpha \frac{\partial p_\alpha}{\partial t} + \nabla \cdot \left[-\frac{K_{sat}k_{r,\alpha}}{\eta_\alpha} \nabla P_\alpha \right] = 0 \tag{3.9}$$

To solve the whole set of equations describing a non-linear problem, initial and boundary conditions need to be defined as well as the retention and permeability relationships, $S_\alpha(P_c)$ and $k_{r,\alpha}(S_\alpha)$ respectively. Those hydraulic functions are generally not known and need to be identified experimentally. For simplicity in a numerical point of view, van Genuchten and Mualem relationships have been chosen [118–120].

$$S_w = \begin{cases} \frac{1}{\left(1+|\beta H_p|^N\right)^M} & \text{for} \quad H_p > 0 \\ 1 & \text{for} \quad H_p \leqslant 0 \end{cases} \tag{3.10}$$

$$S_{nw} = 1 - S_w \tag{3.11}$$

$$k_{r,w} = \begin{cases} S_w^L \left[1 - \left(1 - S_w^{1/M}\right)^M\right]^2 & \text{for} \quad H_p > 0 \\ 1 & \text{for} \quad H_p \leqslant 0 \end{cases} \tag{3.12}$$

$$k_{r,nw} = \begin{cases} S_{nw}^L \left[1 - (1 - S_{nw})^{1/M}\right]^{2M} & \text{for} \quad H_p > 0 \\ 1 & \text{for} \quad H_p \leqslant 0 \end{cases} \tag{3.13}$$

where $H_p = P_c/(\rho_\alpha g)$ is the pressure head and L, N, M and β the van Genuchten parameters, which all depend on Ca, with $M = 1 - 1/N$.

In literature, hydraulic properties and the relation of these parameters are generally assumed to be of static nature. In particular, β is inversely related to the "bubbling" or "entry" pressure which represents the pressure that a non-wetting fluid must overcome to displace a wetting fluid, specific for a fluid/solid pair and its value is close to the capillary pressure for homogeneous and isotropic media [109, 117] and

N and M are related to the distribution of particle sizes in the porous medium. The parameter L is usually set to 0.5 and it is related to the tortuosity and connectivity of the medium according to the original work of Mualem [118]. However, its physical meaning have been questioned and since it often takes a negative value, most of the times it is just regarded as a free fitting parameter [105, 243, 244]. Thus, these parameters are essentially shape parameters without a clear physical meaning and it is crucial to correctly constrain them to obtain parameters with reasonable meaning [244]. In our pressure driven flow case, depending on the fluid kinetics, the resin may be either the wetting or non-wetting phase, and the respective descriptions for saturation and permeability will be adapted accordingly. Hence, it is expected that hydraulic functions are unique for a given injection condition, namely the imposed flow rate, and that all parameters are functions of Ca.

3.4.2 Numerical modelling

Richards' differential equation is non-linear and requires the definition of hydraulic properties as function of the saturation. Its solutions were numerically approximated thanks to a 1D model which was implemented to simulate the unidirectional flow in COMSOL Multiphysics 5.6. In particular, equations 3.9 to 3.13 were solved by a finite element method (FEM) with quadratic shape functions to find the resulting pressure field for the resin. It should be noted that quadratic shapes functions were used for simplicity as they are defined by default and computation times were very short, nevertheless, linear shape functions can also be used and might be interesting for more complex geometries. A requirement of the developed model is to know in advance if the fluid progresses with a wetting or a non-wetting behavior.

Two models were thus developed to solve Eq. 3.9: one where the infiltrating resin is the wetting phase ($\alpha = w$) and the other, the non-wetting phase ($\alpha = nw$). Since air pressure is assumed to be zero, for the wetting case, the fluid pressure is defined by P_w thus $P_c = -P_w$. Analogously for the non-wetting case, the fluid pressure is P_{nw} and $P_c = P_{nw}$. The retention equations 3.10 and 3.12 define the fluid behavior in the wetting case and equations 3.11 and 3.13 the non-wetting case. To completely define the problem, initial and boundary conditions were set. Following a convergence study, the geometry was spatially discretized into a mesh with an element size of $5 \cdot 10^{-4}$ m resulting in 300 domain elements. An implicit backward differentiation formula method was used as stepping method for the time-dependent solver and a maximum time step of 0.1 s was set.

3.4.3 Parameters identification

Retention equations are defined by the empirical parameters β, L and N, that need to be found to solve the whole model. However, those cannot be directly measured and they were thus identified by solving an inverse problem. Building on the pythonic scripting interface for COMSOL, Mph (version 1.1.6) [245], a Python optimization procedure was implemented to fit the model over the experimental data. To perform the optimization, $S(z,t)$ training curves should be selected per experiment and then, the following four steps were carried out:

1. Numerical results were extracted by evaluating the model at experimental times and saturation at experimental points was computed with a cubic spline interpolation.

2. The Weighted Mean Squared Error (WMSE) was calculated for each time and the error E for all curves was aggregated with the mean of the individual errors as:

$$E = \frac{1}{k} \sum_{i}^{k} \frac{\sum_{j}^{a} w_j \left(S(z_j, t_i)_{sim} - S(z_j, t_i)_{exp} \right)^2}{\sum_{j}^{a} w_j} \tag{3.14}$$

   where k is the number of selected times, a the number of data points, w_j the user defined weight (equal to 1 for the linear part of the curve, between $S = 0.1$ and $S = 0.9$ and 10 for the rest), $S(z_j, t_i)_{sim}$ and $S(z_j, t_i)_{exp}$ are respectively modeled and experimental saturation data of the i^{th} time at j^{th} position. The error E was measured for more than 15000 combinations of β, L and N over a large range of values (β = [1, 100], L = [-2, 0] and N = [1, 30]) to build a surface response plot.

3. The combinations of parameters giving an error value up to 20% of the lowest error were selected as initial inputs for the optimization routine. Eq. 3.14 was set as objective function and minimized. However, it is crucial to notice that the saturation $S(z_j, t_i)_{sim}$ is the output of the FEM. Therefore, it is impossible to obtain the objective function derivatives directly with respect to the input parameters. Furthermore, the response is not linear and exhibits several local minima. The optimization was thus performed with one of the Nelder-Mead, Powell, Dual Annealing, or Differential Evolution algorithms implemented in Scipy (version 1) [246], to overcome these limitations. The Nelder-Mead algorithm based on an heuristic (and evolutionary) search [247, 248] was found to offer the best compromise between result quality and convergence speed and the Differential Evolution to better minimize the error at the expense of long convergence times.

4. The quality of the fitting was checked by computing the error E for additional validation curves that were not used in the optimization. Finally, the problem was constrained by setting upper and lower boundaries for the different parameters as well as a maximum number of iterations [243, 249].

Chapter 4

Visualization of dynamic flows with X-ray phase contrast imaging

Direct visualization of resin infiltration is often sought to elucidate flow patterns and validate models to predict the filling kinetics during liquid composite model processes. In this chapter, we evaluate the use of X-ray phase contrast interferometry as an imaging technique to visualize fluid progression through different translucent and non-translucent preforms. To that end, constant flow rate experiments were performed with a model fluid into glass, carbon and flax fabrics and a 3D printed structure. Moreover, by taking advantage of the increased contrast between fluid and fabric in scattering images, we build the dynamic saturation curve in which the pixel intensity values are transformed into saturation level versus position and time. The results prove the suitability of this technique to observe the progressive saturation averaged through the thickness of translucent and non translucent porous preforms even with conventional resins. The porosity network formed by the layers of fabric, the refractive properties of the material, the fabric geometry and its position relative to the X-ray setup are reported to be the main parameters affecting image contrast.

Part of this chapter has been published as:

Helena Teixidó, Baris Caglar, Vincent Revol, Véronique Michaud. "In-operando dynamic visualization of flow through porous preforms based on X-ray phase contrast imaging", Composites Part A: Applied Science and Manufacturing, Volume 149, 106560, 2021 [250].

4.1 Introduction

In this chapter, an in-operando experimental method based on X-ray phase contrast imaging is proposed for the visualization of fluid flow through translucent and non-translucent textile preforms using standard test fluids, at an image acquisition rate of less than 10 seconds with the aim of studying the progressive saturation during infiltration of fibrous preforms by polymeric resins. After validating this novel method through flow experiments with translucent glass fiber fabrics against traditional video imaging methods, the thickness-averaged flow evolution in non-translucent carbon fabrics was assessed. Impregnation conditions were varied through the imposed flow rate, the number of layers and the volume fraction, analyzed the resulting effect on image contrast and resolution, and taking advantage of the increased contrast, the saturation curve was built from the grayscale analysis of scattering images. Finally, the potential and limits of the method are discussed towards the study of impregnation of natural fibers and a polymeric pore network produced by 3D printing.

4.2 Materials and methods

4.2.1 Materials

Four fibrous reinforcements (which properties are summarized in Table 4.1) and a polymeric structure were employed. The twill glass fabric and the unidirectional carbon fabric were selected as reference translucent and non-translucent fabrics respectively. The twill and unidirectional flax fabrics were used as alternative non-translucent preforms. The orientation of fabric reinforcements was 0° for all experiments. The 3D printed structure was based on the geometry designed by Morren et al. [233, 234].

Table 4.1: Fibrous reinforcement properties.

Fiber type	Structure	A_w [g/m^2]	Fiber density [g/m^2]	Fiber diameter [µm]
E-glass	2 x 2 Twill	390	2.6	9
Carbon	Unidirectional	270	1.8	7
Flax	2 x 2 Twill	300	1.3	20 - 40
Flax	Unidirectional	150	1.3	20 - 40

The test fluid was the aqueous solution of PEG (M_w=35 kDa, Sigma Aldrich) at a concentration of 16.7 wt%. For optical experiments around 0.08 wt.% of Rhodamine B colorant (Carl Roth), which provides a strong coloration, was added to the fluid. Given the small amount of colorant, the properties of the PEG solution are considered to be equal to those of the solution containing a colorant and in the frame of this work, a viscosity of 0.11 Pa $\cdot$ s (value at 20 °C) was considered.

4.2.2 Methods

Flow experiments were carried out with the setup shown in Fig. 3.5, from *Chapter 3* section 3.3.1. Fabrics were cut to a width of 4.95 ± 0.05 cm and a length of 15 cm. Porous structures were fitted in the cavity of a metal spacer with an inner silicon joint to minimize race tracking, then enclosed in between transparent PMMA top and bottom parts placed in between metal frames and fastened with screws. Metal spacers of different thicknesses were employed to vary the mold cavity thickness.

The setup was placed in the EVITA imaging facility, in front of the grating G_1 and impregnation was performed vertically from bottom to top (z-direction) at constant flow rate. The progressive impregnation was recorded with the acquisition procedure presented in *Chapter 3* section 3.3.2, at an imaging rate of 9.2 seconds approximately. Then, from scattering images, the saturation $S(z,t)$ curves were built for the experiments of interest following the procedure described in section 3.3.3, using a study area with a width of 400 pixels (roughly corresponding to a width of 2.2 cm) and a pixel size of 54 µm. An overview of the experimental campaign is given in Table 4.2, with n the number of layers employed, h the spacer thickness and resulting volume fractions V_f, flow front speeds u and capillary numbers Ca.

Table 4.2: Impregnation experiments visualized by X-ray phase contrast.

Test #	Fabric	n [-]	h [mm]	V_f [%]	u [mm/s]	Ca (10^{-4})
1	Twill Glass	9	3	45	0.13	1.37
2	Twill Glass	9	3	45	0.23	2.42
3	Twill Glass	9	3	45	0.48	5.04
4	UD Carbon	9	3	45	0.26	2.73
5	UD Carbon	9	2.5	54	0.22	1.93
6	UD Carbon	9	3.5	39	0.23	2.68
7	UD Carbon	6	2	45	0.25	2.63
8	UD Carbon	3	1	45	0.22	2.31
9	UD Carbon	12	4	45	0.27	2.84
10	UD Carbon	15	5	45	0.27	2.84
11	UD Carbon	18	6	45	0.27	2.84
12	Twill Flax	3	2	35	0.16	1.99
13	Twill Flax	9	6	35	0.16	1.99
14	UD Flax	6	2	35	0.12	1.49
15	UD Flax	12	4	35	0.10	1.24
16	Polymeric structure	1	3	48	0.15	1.51

Impregnation of the twill glass fabric (with constant n and V_f) was carried out at three flow rates and conducted under X-ray phase contrast imaging and repeated under conventional optical methods to provide a validation of the proposed visualization method. The flow front advancement was recorded by a digital camera through the transparent mold and corresponding dynamic saturation curves were built adapting the methodology of Nordlund et al. [105] and were thereafter compared with the curves obtained by X-ray image analysis.

Then, as the aim of this work is to demonstrate the potential of the method for non-translucent fabrics, different tests were performed with the carbon fabric, in particular to analyze the effect of the number of layers and the volume fraction on scattering images' contrast. Finally, the two flax fabrics were impregnated with the same volume fraction, varying the number of layers and one impregnation was carried out for the 3D printed structure.

4.3 Results

An example of absorption, refraction and scattering images obtained for each porous structure type is shown in Fig. 4.1. Contrasts and features obtained for each type of image are thereafter discussed and explained based on physical properties.

4.3.1 Validation with a glass fabric

A good contrast between fabric and fluid is revealed by the scattering image for the glass fabric (Fig. 4.1a), whereas the absorption and refraction images exhibit very low contrast, with a barely visible flow front. Nevertheless, the dry and wet areas of the preform can also be differentiated in the refraction image since the structural pattern disappears when the fabric is fully saturated. Compared to absorption images, in which the fabric structure is highlighted and can be assimilated to a square grid, in scattering and refraction images, the fabric structure was only identified in the vertical direction and probably related to the grating orientation in the X-ray setup [223].

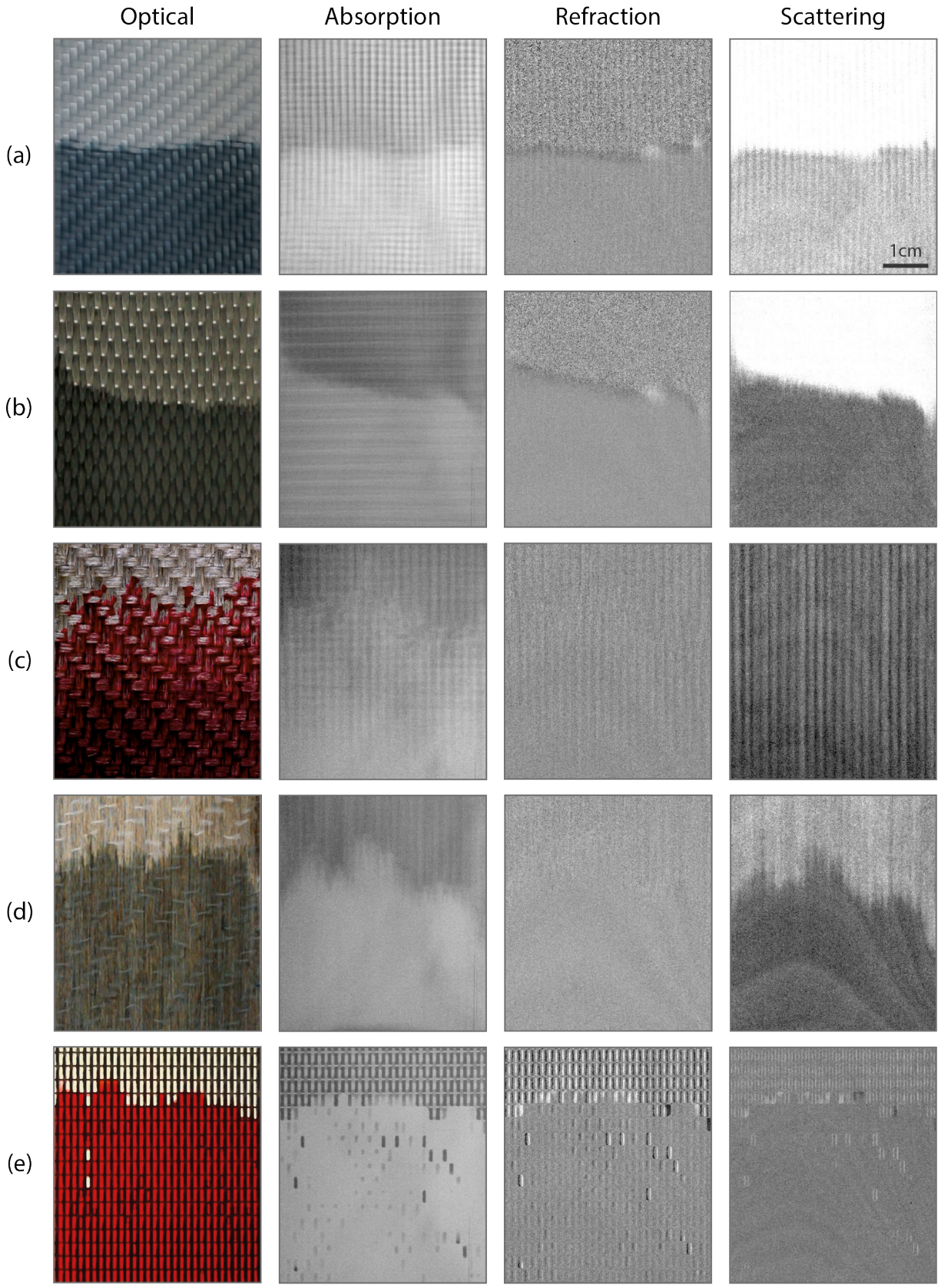

Figure 4.1: Example of flow patterns observed in optical, absorption, refraction and scattering images obtained for the different reinforcements (a) Twill Glass (test #2), (b) UD Carbon (test #4), (c) Twill Flax (test #12), (d) UD Flax (test #14) fabrics and (e) the 3D printed structure (test #16). The image of the optical view does not correspond to the flow shown in X-ray images as the X-ray infrastructure did not allow capturing videos during the measurements. The scale is the same for all pictures.

For the sake of elucidating the flow front patterns, the three glass fabric impregnations were performed under a Keyence VHX-7000 digital microscope equipped with a zoom lens 10×. The resulting images, displayed in Fig. 4.2, revealed that the unsaturated zone increases with the flow speed. At the low capillary number, $Ca = 1.37 \cdot 10^{-4}$ (test #1, Fig. 4.2a), a narrow unsaturated zone is observed, corresponding to a rather balanced flow, nonetheless with a slight predominance of capillary driven fluid flow in the tows. For the medium capillary number $Ca = 2.42 \cdot 10^{-4}$, (test #2, Fig. 4.2b), the fluid first fills the inter-tow spaces; the tows behind the flow front are not completely saturated thus indicated a viscous flow. The fastest flow with a higher capillary number $Ca = 5.04 \cdot 10^{-4}$, (test #3, Fig. 4.2c), presents the same trend as the medium impregnation case (test #2) but with a large unsaturated zone and has thus a more viscous behavior.

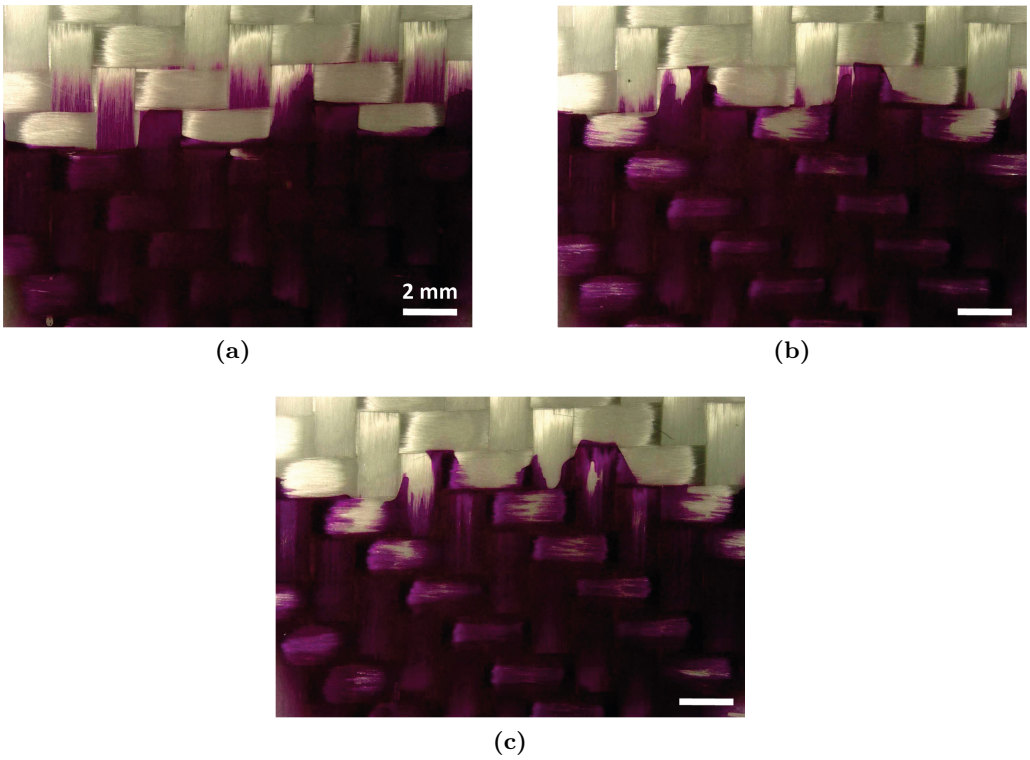

Figure 4.2: Flow patterns in the twill glass fabric imaged by a digital microscope for impregnation conditions (a) #1 (b) #2 and (c) #3.

Dynamic saturation curves $S(z,t)$ were constructed for the three glass impregnations for similar times, from optical and X-ray image methods. The results are shown in Fig. 4.3 and prove a clear agreement between the two methods. The slight differences in unsaturated areas between the two methods can derive from the fact that the flow is observed only from the surface in the video acquisition where wall effects take place [251] whereas the flow is thickness averaged in X-ray acquisition. In addition, we calculated flow displacements of the three tests during one single image acquisition for both imaging methods (Table 4.3). A phase-dependent anticipation or delay of the flow was observed during fast impregnation resulting in a lower precision on the saturation measurement by the X-ray approach. This effect could be minimized in improved setups by reducing the acquisition time with a more pow-

erful X-ray source and/or optimizing the grating geometry which was initially developed for static measurements. Considering the curve shapes, the steeper curve with the narrower unsaturated zone corresponds to the more balanced flow (test #1), while with increasing flow speed, the saturation curves become less steep (tests #2 and #3). These findings are in good agreement with observations from Fig. 4.2.

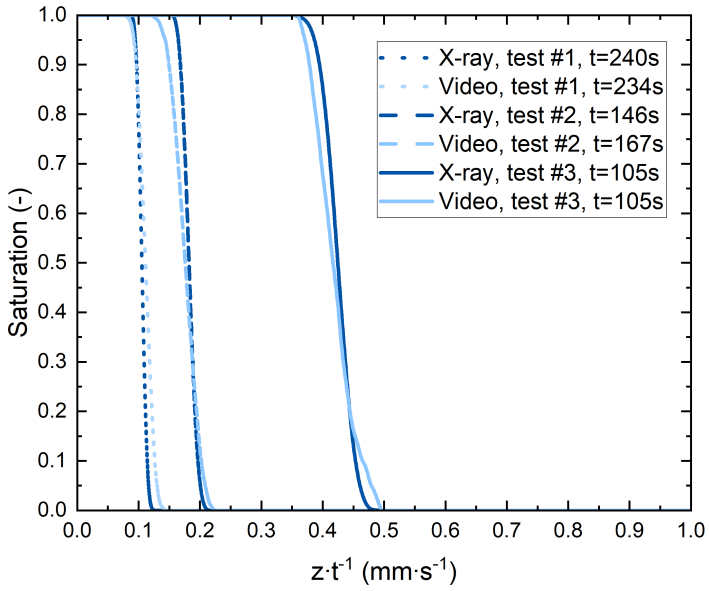

Figure 4.3: Comparison of $S(z,t)$ curves built from optical and X-ray acquisitions.

Table 4.3: Comparison of flow progression during in-situ flow imaging.

Acquisition method	Acquisition time [s]	Flow displacement per image acquisition [mm]		
		Test #1	Test #2	Test #3
X-ray	9.2	1.20	2.12	4.42
Video	0.04	0.005	0.01	0.02

As the thickness averaged flow front location for glass preforms was successfully captured via X-ray phase contrast imaging and the method was validated, the current aim is to extend the technique towards the visualization of fluid flow through non-translucent preforms, in particular carbon fabrics.

4.3.2 Carbon fabric

Test #4 was defined as reference and its corresponding X-ray images are displayed in Fig. 4.1b. Interestingly, the scattering image for carbon fabric revealed a better fluid-fabric contrast as compared to glass fabric. As expected, the carbon preform did not show much contrast in absorption images

and horizontal glass stitches appeared better since the density of glass is higher than that of carbon. It should be noted that, in scattering images, glass stitches were also identified by the pixel intensity, which was slightly lower in the zones where the glass stitches were present, compared to areas with only carbon. This observation proves the convenience of the proposed technique for the study of flow through preforms made up of different materials. Finally, as for the glass fabric, no significant contrast was obtained from the refraction image apart from the loss of pattern in the region with liquid. Spaces between the tows were visible in scattering and refraction images in the form of vertical lines, albeit thinner as compared to those of the glass fabric as the structure is more compact.

The saturation curve $S(z)$ for each acquisition for impregnation #4 was constructed. A subset of collected curves and three image reconstructions for different times illustrating the impregnation along the fabric length are shown in Fig. 4.4. Based on the graph, the saturation decreases almost linearly over the unsaturated region and for all curves, the slope is nearly identical as expected since the fluid was injected at a constant flow rate and the impregnation conditions were invariable along the fabric length and time.

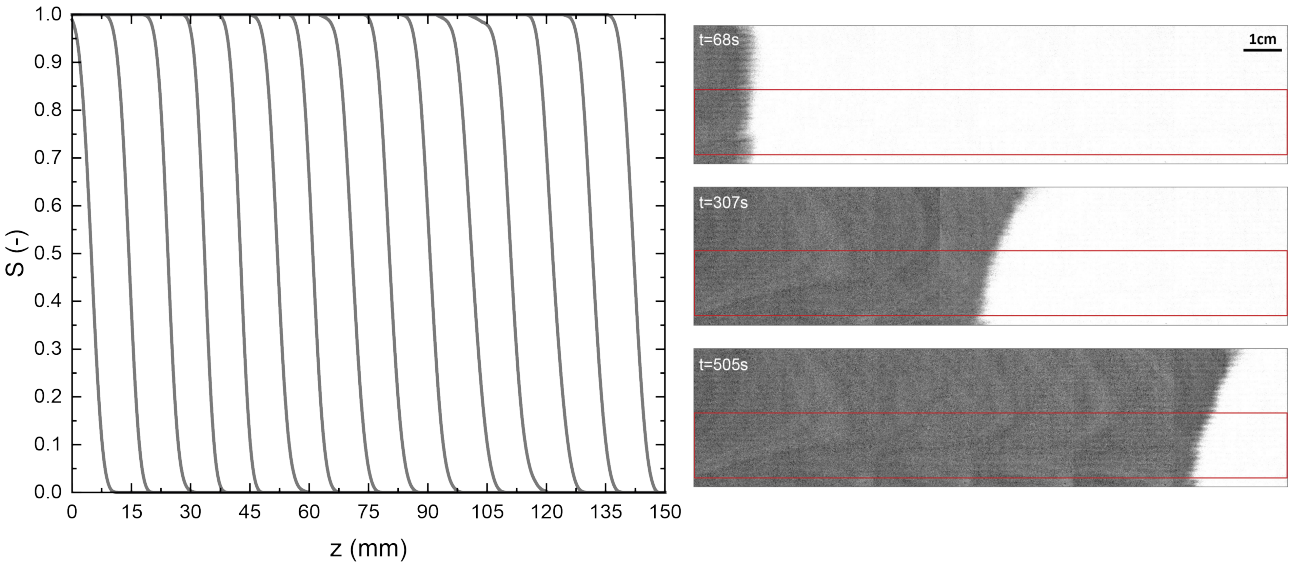

Figure 4.4: $S(z)$ curves for test #4 taken every 4 acquisitions (corresponding to approximately 37 s) (right) and three reconstructions of the impregnation along the fabric length at three instants with the measurement zone highlighted in red.

Then, the role of fiber volume fraction on scattering images contrast was investigated, by compressing a pre-determined number of layers to different thicknesses, and also the role of the number of layers, by compressing several numbers of layers leading to the same fiber volume fraction at different thicknesses. Fig. 4.5 depicts an increase of the contrast (as well as the signal-to-noise ratio) with the number of layers. The low value peak of the histograms corresponds to the dark area (wetted fabric) and the high value peak to the white area (dry fabric), the contrast can be simply visualized by the separation of these two peaks. According to literature, the scattering signal increases with the porosity level as well as the pore size [205, 206, 221, 252]. Indeed, considering that transitions

between air and material act as the X-ray scattering inhomogenities and that the number of scattering events increases with the number of layers, the current observations are thus well aligned with the underlying physical phenomena. On the other hand, the change in number of scattering transitions due to change in volume fraction (while having same number of fabric layers) is limited since the same number of fibers are present in the cavity and this is why, experiments #4, #5 and #6 resulted in similar contrast. Therefore, the majority of scattering events arise from the fiber-pore transitions and the change in the size of pores created between the fibers is not significant enough to contribute to the scattering signal.

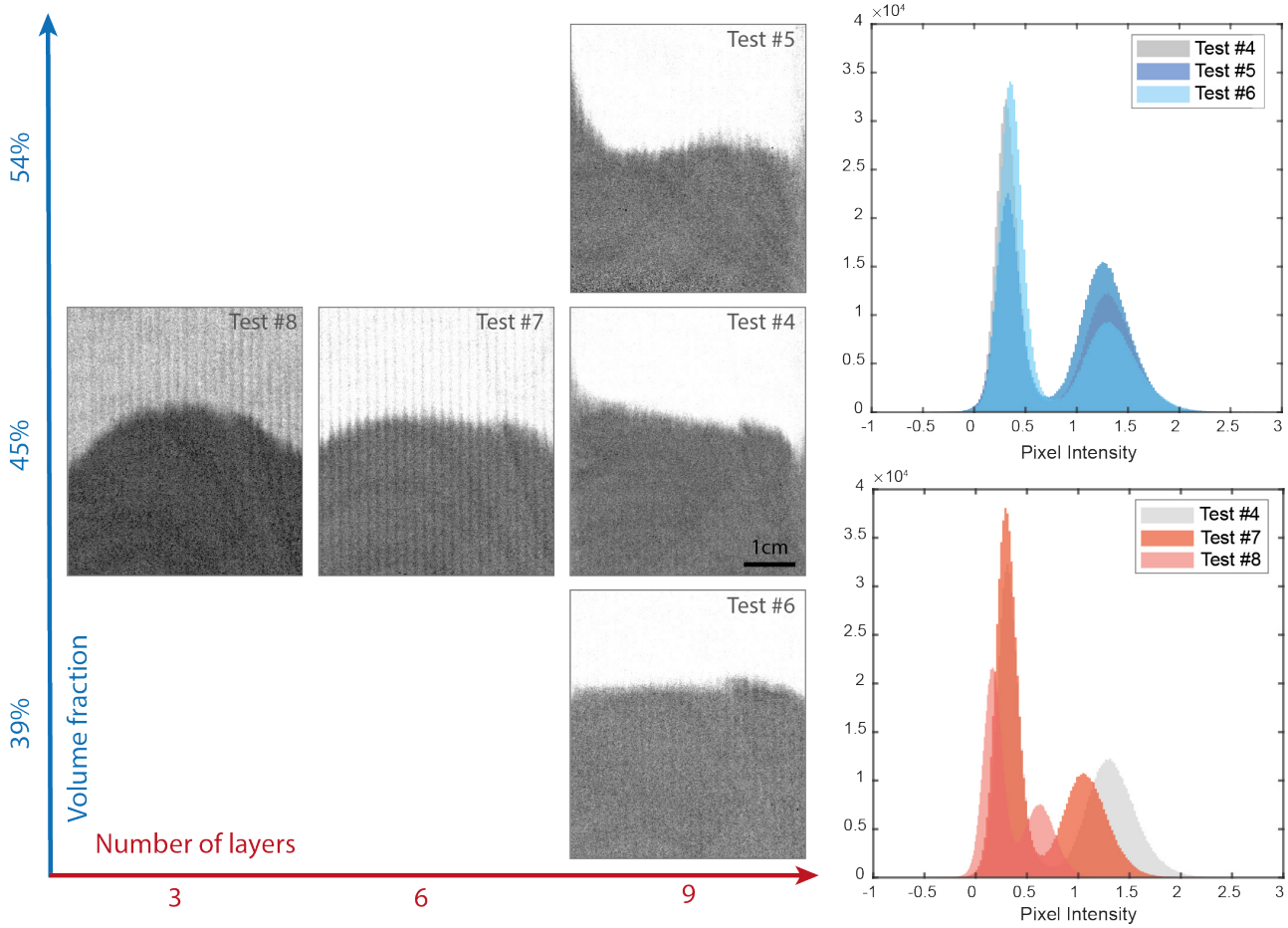

Figure 4.5: Comparison of scattering images obtained for the different impregnation configurations for the carbon preform (tests #4 to #8) with the corresponding histograms.

Three additional tests (#9, #10 and #11) in which the number of layers was increased to 12, 15 and 18 were performed to further investigate the effect of the number of layers on the pixel intensity. From scattering images in Fig. 4.6, an apparent change in the contrast between the two phases (fluid and fabric) is not observed. Increasing the number of layers from 9 to 12 (tests #4 and #9) results in a greater separation between the two peaks in the histogram and thus more contrast. However, for 15 and 18 layers (tests #10 and #11), histograms are almost superposed and contrast cannot be further enhanced by increasing the number of layers.

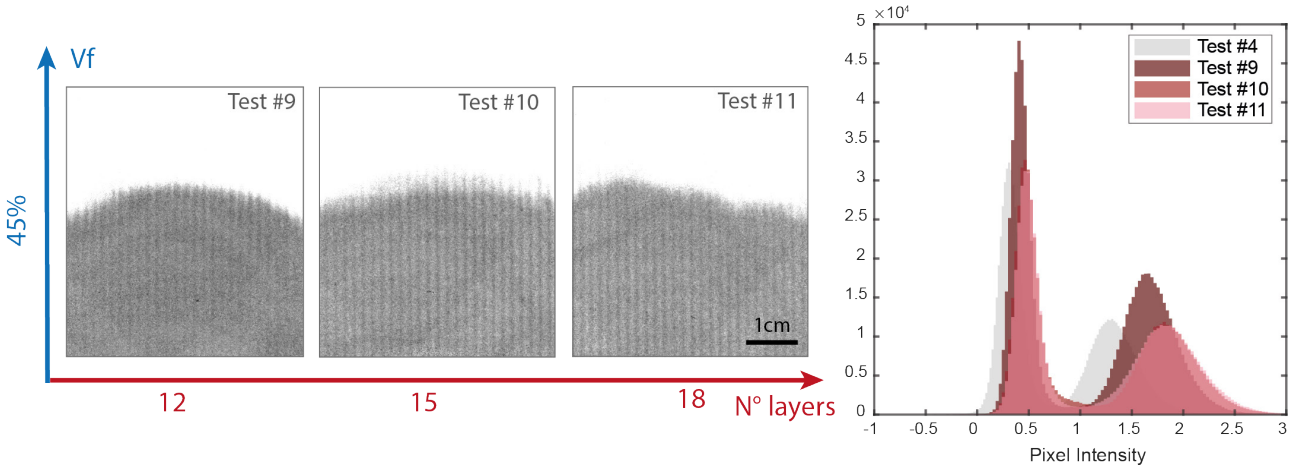

Figure 4.6: Comparison of scattering images obtained for tests #9, #10 and #11 with the corresponding histograms which are compared to the one of test #4.

4.3.3 Flax fabrics

Fig. 4.1c and d show respectively, the images obtained for test #12 with the twill flax and test #14 with the unidirectional flax fabrics. In scattering images, the flow front is barely visible for the twill whereas it is clearly observed for the UD. Based on our previous results with carbon fabric, this difference in contrast can be related to the number of layers used. This is why, tests #13 and #14 (Fig. 4.7), were performed with the aim to evaluate the increase of contrast by increasing the number of fabric layers. For both cases the contrast slightly improved. For the twill case (Fig. 4.7a), the flow front starts to appear when the number of layers was increased from 3 to 9 and for the UD case (Fig. 4.7b), the contrast between fabric and liquids is increased. However, despite the increased contrast by increasing the number of layers for the two flax fabrics, the contrast was far from reaching a level comparable to that observed in glass or carbon fabrics. Moreover, there is still a significant difference between the two fabric configurations twill and UD, that is potentially linked to the resolution of the flow front rather than the contrast (e.g. contrast in tests #13 and #14 seems very close in Fig. 4.7, but the flow front outline hardly recognized for the twill case). Thus, the fabric structure is suspected to play a major role in the imaging principle.

Then, for both samples (Fig. 4.1c and d), the absorption image brought the flow pattern out for the two cases. A flow pattern directly linked to the fabric structure is depicted: in the weave case, the unsaturated zone is larger because large pores created by the weft and warp tows enhance viscous flow between tows while intra-tow spaces require longer time scales for impregnation; conversely, the unidirectional fabric presents a more compact structure with more evenly distributed pores in which the fluid cannot easily progress in between the tows and the boundary is crisper. The present results provide a stimulus for further investigation of flow through natural preforms and in order to better visualize impregnation of natural fiber preforms with the present technique, other solutions can be explored such as changing the fluid nature, changing the orientation of the gratings or increasing the X-ray source power.

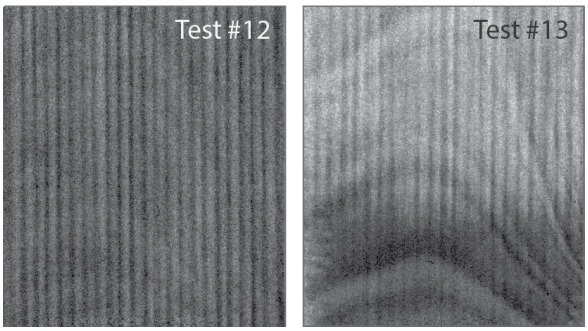

(a) Twill flax

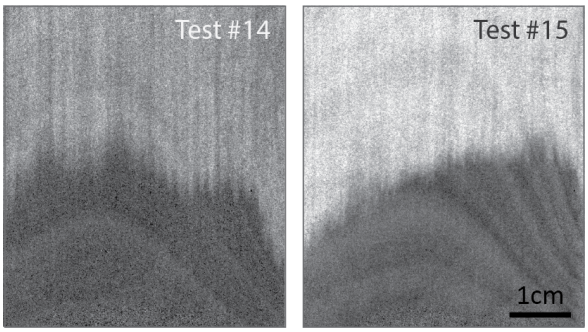

(b) UD flax

Figure 4.7: Comparison of contrast in scattering images through the (a) twill (using 3 and 9 layers) and (b) UD (using 6 and 12 layers) flax fabrics with an increase of fabric layers. An interference pattern strongly affects images of tests #13 and #15, this was due to a default in a piezoelectric cable throughout the testing day.

4.3.4 Polymeric structure

The obtained images corresponding to the polymeric structure impregnation (test #16) are shown in Fig. 4.1e. No significant contrast was obtained for the scattering image between the grid and the fluid since the grid is a homogeneous material and the porosities are in the range of a millimeter. In addition, the fluid path in between the small pores of the structure was hidden by the polymeric structure. Vertical lines corresponding to the edges of the large cavities were the only elements that were barely visible. Absorption images revealed more interesting results: the location of the small cavities was distinguished, corresponding to less dense zones where the grid appeared lighter, the fluid path was easily tracked and empty, partially-filled and filled cells were clearly highlighted. Thus, the observation of flow through the 3D printed polymeric porous preform under X-ray techniques is enhanced by attenuation rather than scattering. Interestingly, this approach could be extended to more complex networks for fluid dynamics studies. This example shows at the same time the limitation and versatility of the presented technique.

4.4 Discussion

The increased contrast obtained in scattering images mainly arises from the difference between the very heterogeneous internal structure of fabrics that scatters X-ray and the homogeneous medium that the fabric becomes once it is impregnated with liquid. It is thus expected that this technique will be equally suitable to observe specific thermoset resins used for LCM. However, different contrast was obtained for the different materials and test conditions. In order to quantitatively compare the contrast achieved in scattering images for the studied fibrous reinforcements, an intensity range value was defined for each sample by the subtraction of I_{min} from I_{max} (*Chapter 3* section 3.3.3). An overview of the contrast values obtained for all experiments is illustrated in Fig. 4.8 where the intensity range was plotted versus the number of layers. The three main factors responsible for the contrast are presented hereunder.

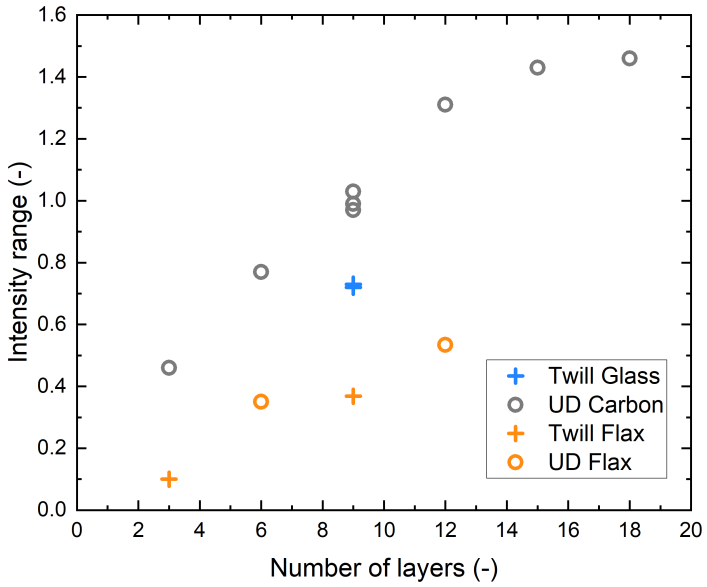

Figure 4.8: Intensity range of scattering images versus the fabric number of layers.

4.4.1 Effect of the number of layers and fiber diameter

From previous findings, the volume fraction has a minimal effect on the scattering contrast. However, the contrast strongly depends on the number of layers since fibers act as main scatterers. Fig. 4.8 illustrates this observation for the UD carbon fabric, since the signal intensity versus the number of layers a follows a linear trend till it reaches a saturation value as we previously suggested.

Moreover, fibers with larger diameters have lower specific surface area per volume compared to fibers with smaller diameters and thus will create fewer scattering events. Indeed, fibers with a diameter comparable to the grating size (4 µm), are in the "sensitive size window" [253] and scatter the X-ray

signal better, resulting in an enhanced contrasts. By referring to Table 4.1, fiber diameters are in line with the obtained contrast. Glass and carbon fabrics which have fibers with diameters of less than 10 µm gave better contrast compared to flax fabrics which possess fibers with significantly larger diameters. As carbon and glass fabrics have similar diameters, the contrast difference between them in the scattering images arises mostly from their refraction coefficients.

4.4.2 Effect of the material composition

The highest fluid/reinforcement contrast was achieved with carbon fabric, thereupon glass and finally flax (Fig. 4.8). According to the literature, inhomogeneities that create scattering refer to variations in the electron density which are related to the materials' refraction coefficient δ [204]. In Table 4.4, linear absorption μ and refraction δ coefficients from tabulated databases are presented for the different materials at the X-ray intensity used in this work, assuming that water is the main element of the fluid mixture, carbon, silica and cellulose those of carbon, glass and flax fibers respectively.

Evidently, the refraction coefficient has a direct impact on refraction images, indeed, the flow front was pinpointed for glass and carbon samples because their refraction coefficients are high enough compared to that of the fluid whereas for flax fabrics, the front was hardly detected given the proximity of the cellulose and fluid refraction coefficients. In addition, it can be highlighted that refraction coefficients prove to be also directly linked to the scattering ability of each material, since carbon and glass have higher values, they gave better contrast in scattering images when compared to flax. Then, the absorption coefficient (related to the ability to attenuate X-ray) is directly linked to the material density and this is why glass showed higher contrast in absorption.

Table 4.4: Absorption and refraction properties of carbon, silica and cellulose at 60 keV from [254, 255].

Material	Formula	μ [m^{-1}]	δ (10^{-7}) [-]
Water	H_2O	0.21	0.6
Glass	C	0.32	2.0
Carbon	SiO_2	0.63	1.5
Flax	$C_{12}H_{10}O_5$	0.24	0.8

4.4.3 Effect of the structure

The fabric configuration also influences the scattering contrast. For a given material, more compact and homogeneous fabric layers with fibers parallel to the grating lines provided a higher contrast, the phenomena is clearly illustrated by twill and UD flax fabrics experiments (Fig. 4.1c and d). For unidirectional fabric configurations, where fibers were parallel to the grating lines we obtained a stronger signal with respect to the twill configuration. Indeed, in refraction and scattering images, variations

on the x-direction (perpendicular to the grating lines) are only measured and thus variations on the z-direction such as the horizontal bundles of the twill fabrics do not appear on those images.

By rotating the fabric and thus creating an angle between the gratings and vertical/horizontal bundles, it would be possible to observe weft and warp directions of twill fabrics. We repeated test #4 by rotating the setup around the y-axis by 45° for a glimpse of the influence of the fabric orientation: an example of scattering image is shown in Fig. 4.9. As expected, the fabric weave patterns are observed in x and z directions, the contrast, though, is decreased at 45°.

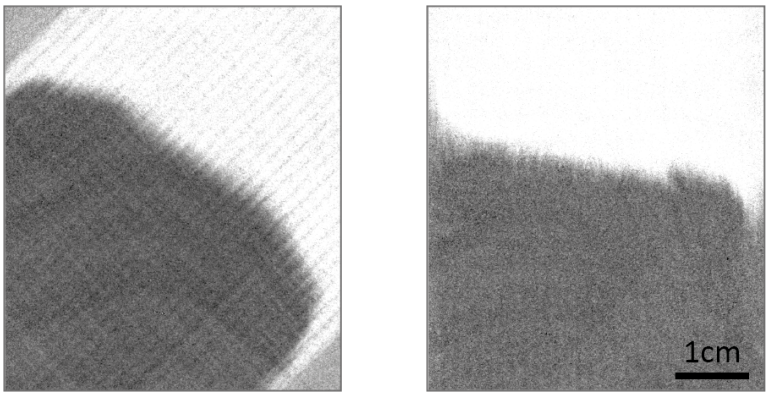

(a) **(b)**

Figure 4.9: Scattering images (a) resulting of a rotating the setup 45° and (b) reference at 0°.

4.5 Conclusions

X-ray phase contrast imaging proved to be a powerful tool to visualize in-operando dynamic fluid flows across the thickness of translucent and non-translucent fibrous preforms. In particular, we observed the progressive saturation of carbon fabric preforms by collecting images with an acquisition time of less than 10 s, transcending previously reported approaches, and on a relatively large sample size window of 7 cm × 7 cm. Moreover, given the enhanced contrast between fabric and liquid, progressive saturation curves were built from a grayscale image analysis.

Then, taking advantage of the wide range of materials that this technique can visualize, glass preforms were used for validating the current method by comparing the resulting progressive saturation through glass preforms by X-ray and conventional optical techniques. The visualization method was then extended to carbon and flax fabrics and a 3D printed preform.

By comparing different geometric and flow velocity configurations, we identified the main parameters affecting the scattering contrast, including the number of layers, the fiber diameter, the refraction properties of the material as well as the fabric structure. This provides guidelines for the in-depth analysis of flow patterns, in particular in non-transparent carbon fabrics, with model fluids or reac-

tive resins, for model validation and identification of the relevant parameters governing flow in liquid composite molding processes.

Finally, once the factors affecting the image resolution have been evaluated, in *Chapter 5*, it is sought to explore the potential of X-ray phase contrast technique to elucidate and study dual-scale flow patterns.

Chapter 5

Assessment of dual-scale flows for impregnation studies

In infiltration studies, it is sought to assess the flow front progression with as much accuracy and detail as possible, since it is there that many phenomena take place. Concretely, the dual-scale geometry characteristic of fibrous media triggers a dual-scale fluid pattern, inducing subsequently, a void formation mechanism which directly impacts the final part properties. Depending on the extent of viscous and capillary forces, the fluid adopts different preferential paths. Besides, the transition from capillary to viscous dominated flows is linked to the dynamic wettability in which the fluid switches from wetting to non-wetting states. Here, conventional X-ray radiography is compared to X-ray phase contrast technique to image in-situ constant flow rate impregnation of a non-translucent unidirectional carbon fabric. X-ray attenuation of the fluid phase was increased by using a ZnI_2-based contrasting agent, leading to enough contrast between the liquid and the low density fibers. We proved the suitability of conventional X-ray transmission to visualize fluid paths by elucidating different flow patterns, spanning from capillary to viscous regimes and a meso-void entrapment phenomenon. The versatility of the technique was strengthened by visualizing flow through two flax and a twill carbon fabrics.

Part of this chapter has been published as:

Helena Teixidó, Baris Caglar, Véronique Michaud. "Dual-scale visualization of resin flow for liquid composite molding processes", Proceedings of the 20^{th} European Conference on Composite Materials, ECCM20, Lausanne, Switzerland, 2022 [256].

5.1 Introduction

In the previous chapter, we proposed to use an X-ray phase contrast device to assess the progressive saturation of several distinct fibrous preforms even with conventional resins with acquisition rates below 10 seconds per acquisition. This technique is sensitive to the ultra-small angle scattering and allows to enhance the contrast between materials with low density but with enough micro-scale heterogeneities such as fabrics and resins. In this chapter, the potential of this technique to evidence dual-scale flow patterns is explored. We found out that sometimes, a sufficient resolution was not achieved and to to overcome this limitation, we investigated the use of contrasting agents added to the fluid phase to enhance the fluid/fabric contrast in conventional absorption images. The benefits and limitations between the two methods for elucidation of dynamic patterns in different fibrous preforms and entry data for mathematical models are addressed.

5.2 Materials and methods

5.2.1 Materials

The unidirectional carbon fiber reinforcement (Fig. 3.2a) was selected for the dual-scale visualization assessment. The twill and unidirectional flax fabrics (Fig. 3.3) and the twill carbon fabric (Fig. 3.2b) were used for the final method validation.

Two PEG-based solutions were used as tests fluids. One is the aqueous solution of PEG at 16.67 wt.% and the second one is the same PEG-solution but with the ZnI_2-based contrasting solution (CA1) added to the first solution. The properties of the mixtures assumed for this chapter are listed in Table 5.1.

Table 5.1: Considered fluids properties.

Fluid	Viscosity [Pa · s]	Density [g/ml]	Surface tension [mN/m]
PEG 16.7 wt.%	0.103	1.026	56.5
PEG 16.7 wt.% + CA	0.087	1.276	32.7

5.2.2 Methods

Flow experiments were performed with the setup and procedure from *Chapter 3* sections 3.3.1 and 3.2.2. Fabric layers were accurately hand-cut to a dimension of 4.95 ± 0.05 cm x 15 ± 0.10 cm and fitted into the PMMA mold with the desired cavity thickness. Vertical constant flow rate experiments were carried out, the capillary number thus stays constant along the test and the fluid velocity was estimated by measuring the average front velocity.

Three experiments were conducted at different flow rates to obtain a range of flow regimes spanning from capillary to viscous dominated with the PEG 16.7 wt.% solution (tests #1, #2 and #3) and were repeated with the solution with contrasting agent (tests #4, #5 and #6). Two additional experiments were performed with the two flax fabrics (tests #7 and #8) and one with the twill carbon fabric (test #9) with the fluid containing ZnI_2. A summary of the experimental campaign is given in Table 5.2.

Table 5.2: Impregnation experiments.

Test #	Fluid	Fabric	n [-]	h [mm]	V_f [%]	u [mm/s]	Ca (10^{-4})
1	PEG 16.7 wt.%	UD Carbon	9	3	45.0	0.08	0.80
2	PEG 16.7wt.%	UD Carbon	9	3	45.0	0.26	2.61
3	PEG 16.7wt.%	UD Carbon	9	3	45.0	0.38	3.81
4	PEG 16.7wt.% + CA1	UD Carbon	9	3	45.0	0.08	1.17
5	PEG 16.7wt.% + CA1	UD Carbon	9	3	45.0	0.26	3.80
6	PEG 16.7wt.% + CA1	UD Carbon	9	3	45.0	0.38	5.56
7	PEG 16.7wt.% + CA1	Twill Flax	9	6	34.6	0.17	2.96
8	PEG 16.7wt.% + CA1	UD Flax	12	4	34.6	0.10	1.74
9	PEG 16.7wt.% + CA1	Twill Carbon	8	3	42.2	0.25	3.84

5.3 Results and discussion

5.3.1 Observation of flow regimes by X-ray phase contrast

Tests #1, #2 and #3 correspond respectively to capillary, balanced and viscous flows and the images recorded by X-ray-phase contrast are shown Figure 5.1. As already reported in *Chapter 4*, the higher fabric/fluid contrast is obtained in scattering images, when conventional fabrics and impregnation liquids are employed.

Viscous fingering and unsaturated length are depicted in the scattering images for test #3, when compared to absorption and refraction images. It should be noted that the unsaturated length can be also extracted from the refraction image even though not through the contrast obtained but rather from the homogeneity of the signal. In absorption images, viscous fingering in between the tows can be recognized but the intensity is very weak and disturbed by horizontal glass stitches that gave a strong signal. Results for test #2, showed a rather balanced flow as expected with a flat and sharp flow front, similarly observed for the three images. However, for capillary flows (experiment #1), the scattering image appears to underestimate the flow pattern. Although the flow front position is identified, the intra-tow capillary fingering is not elucidated in the scattering image. Absorption and

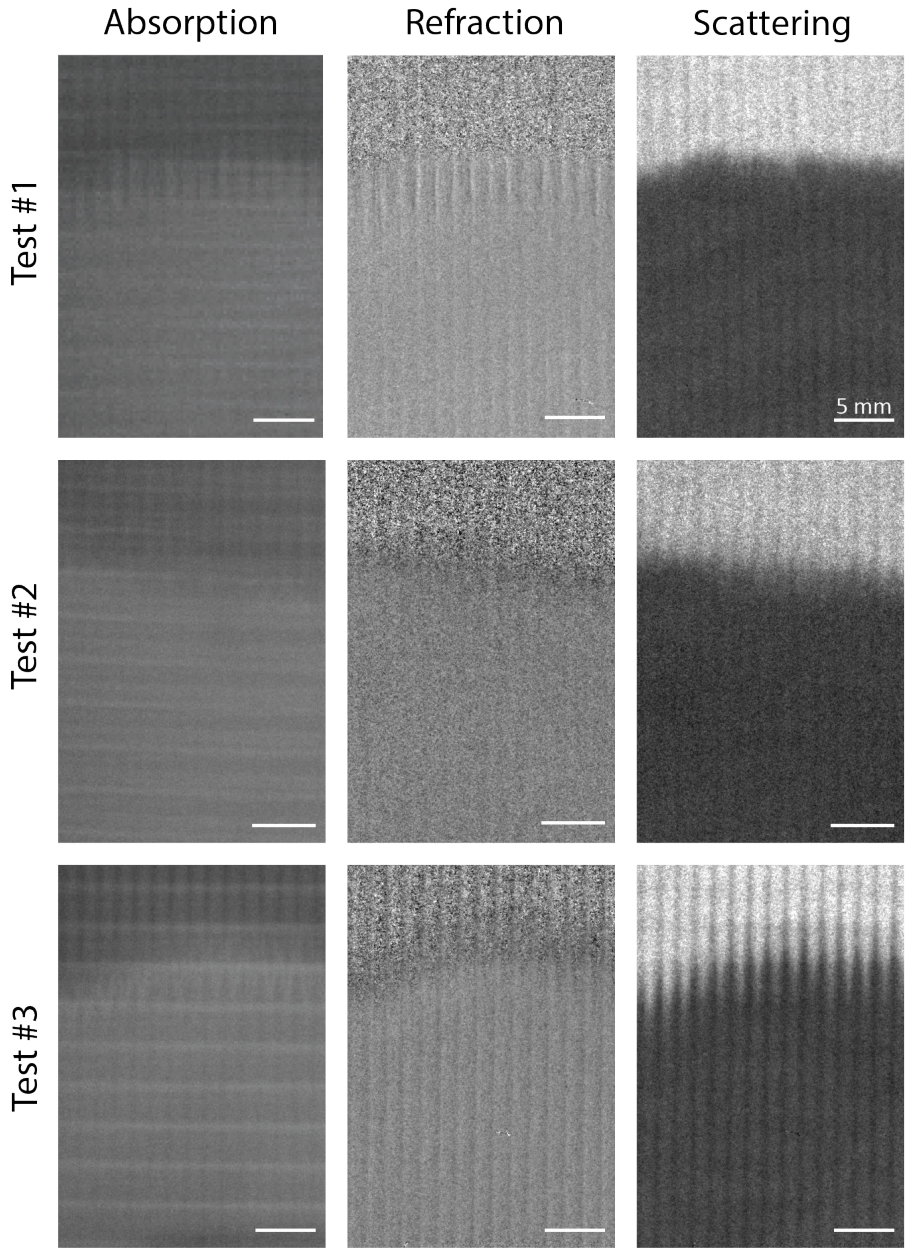

Figure 5.1: Absorption, refraction and scattering images obtained for the UD carbon impregnated with the PEG 16.67% solution (tests #1, #2 and #3).

refraction images, nonetheless, show a large unsaturated area and a flow preferentially filling the tows. The interpretation of the flow front in these images is unfortunately hampered by the low contrast obtained.

This is why, to further explore the potential of X-ray phase contrast imaging to observe dual-scale flow patterns, it was sought to combine these images to strengthen the signal and better draw the flow front contour. Analogously to what was done by Senck et al. [227] for dual-scale characterization of cracks in fiber reinforced composites, the combination of absorption and scattering images was tried. The idea is to create a superimposed image by using the power of each technique as the dark field image is sensitive to subpixel variations and thus the fabric porosity, while the absorption image depends on the

material density and elucidates the fabric macrostructure. Since, it was observed that the unsaturated area was visible in refraction images, it was used as well. For the three flow conditions, a Gaussian filter was applied to the scattering image and refraction and absorption images were combined by calculating their absolute difference. Then, by using the Red-Green-Blue (RGB) coding, the B and R channels were attributed to the absorption-refraction and scattering images respectively to construct the superimposed images shown in Fig. 5.2.

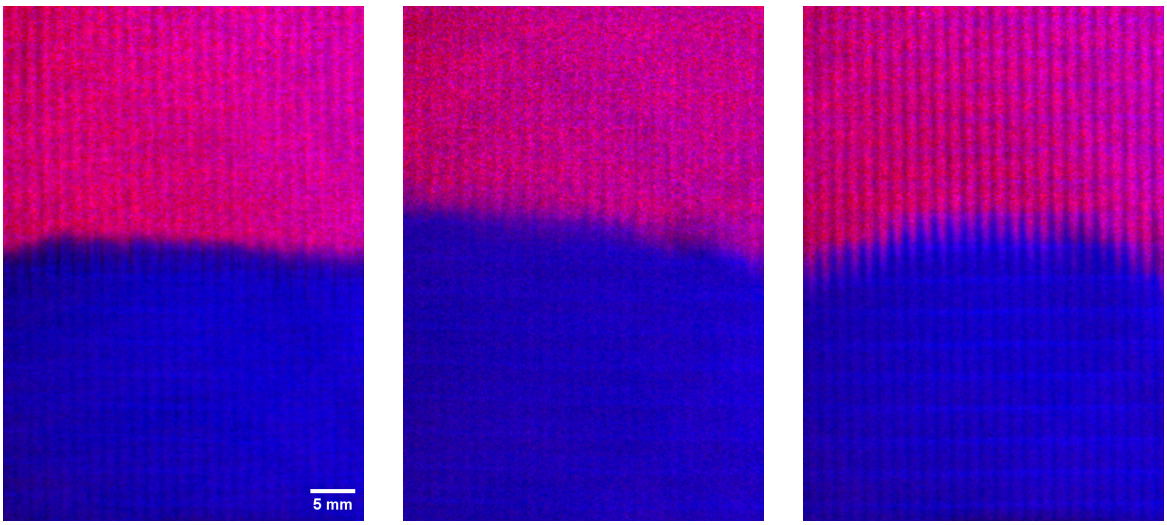

Figure 5.2: Superimposed absorption, refraction and scattering images for visualization of flow patterns. Acquisition corresponding to tests (a) #1, (b) #2 and (c) #3.

The different patterns are highlighted for all cases and the fabric structure appears clearly in the impregnated length. However, the mathematical analysis of these images is limited to extract quantitative information such as the saturation ratio. To overcome this limit, and since in absorption images the flow front line is neat, the potential benefit of a contrasting agent in the solution to increase the effect of the fluid on the attenuation signal is investigated thereafter.

5.3.2 Observation of flow regimes by X-ray radiography

Flow front images obtained for experiments employing the ZnI_2-based contrasting solution (tests #4, #5 and #6) are shown in Figure 5.3. With this approach, a high resolution and fluid/fabric contrast is obtained in absorption images whereas little information can be extracted from refraction and scattering images in which the flow front is disturbed by the fluid composition, affecting its refraction properties.

In this set of impregnations, the different flow domains are distinctly identified in absorption images: capillary and viscous fingering are observed for tests #4 and #6 respectively with a large unsaturated area and as expected, test #5 is a rather balanced flow with a small unsaturated zone. Moreover, inter-tow meso-voids resulting from strong capillary effects are apparent for test #4, as shown with

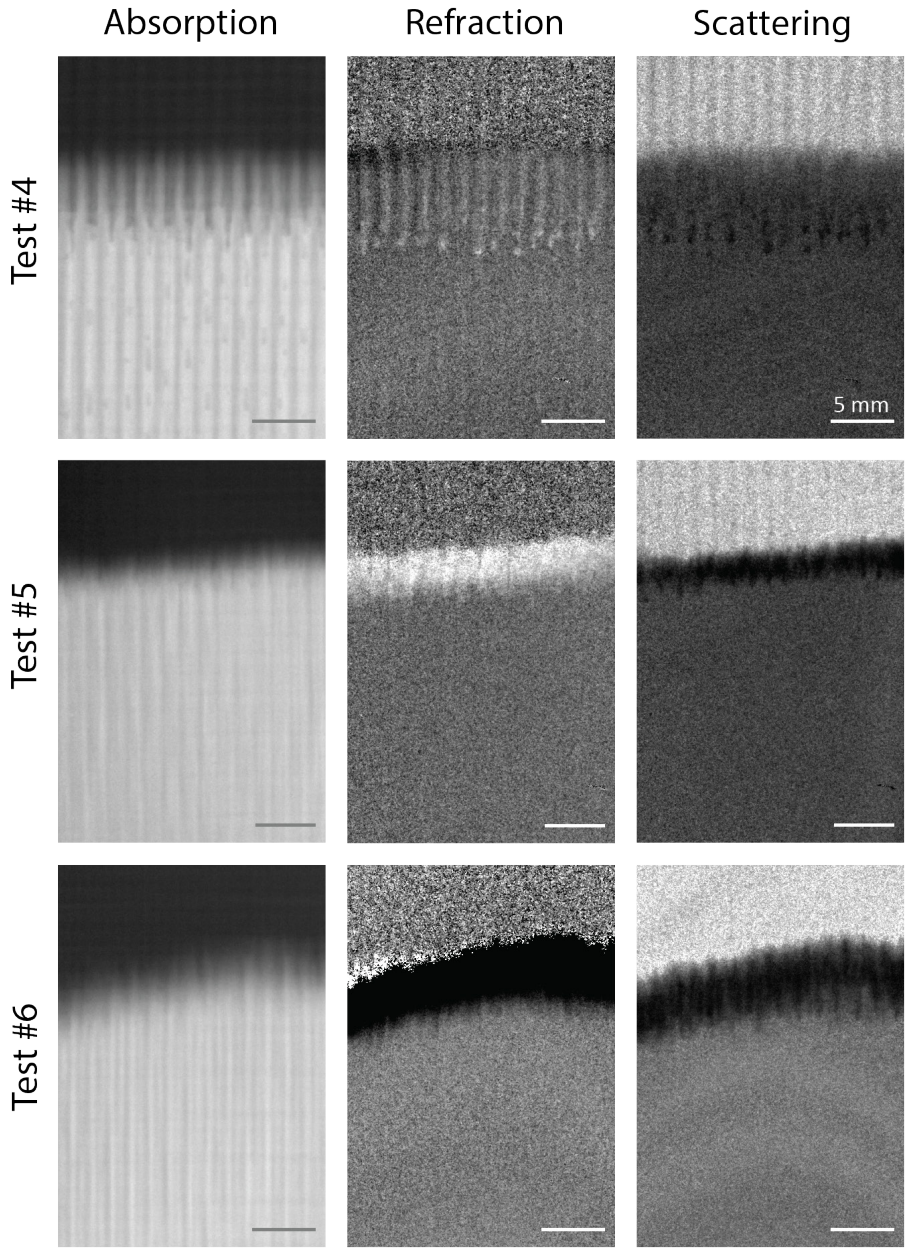

Figure 5.3: Absorption, refraction and scattering images obtained for the UD carbon impregnated with the PEG 16.67% + CA1 (tests #4, #5 and #6).

more detail in Fig. 5.4. It can be observed that for the capillary case (test #4), the flow front is almost flat due to the domination of homogeneous diffusion inside the tows whereas for the viscous dominated flow (test #6), it is less sharp since it is highly influenced by fabrics layup resulting in an irregular meso-porosity network.

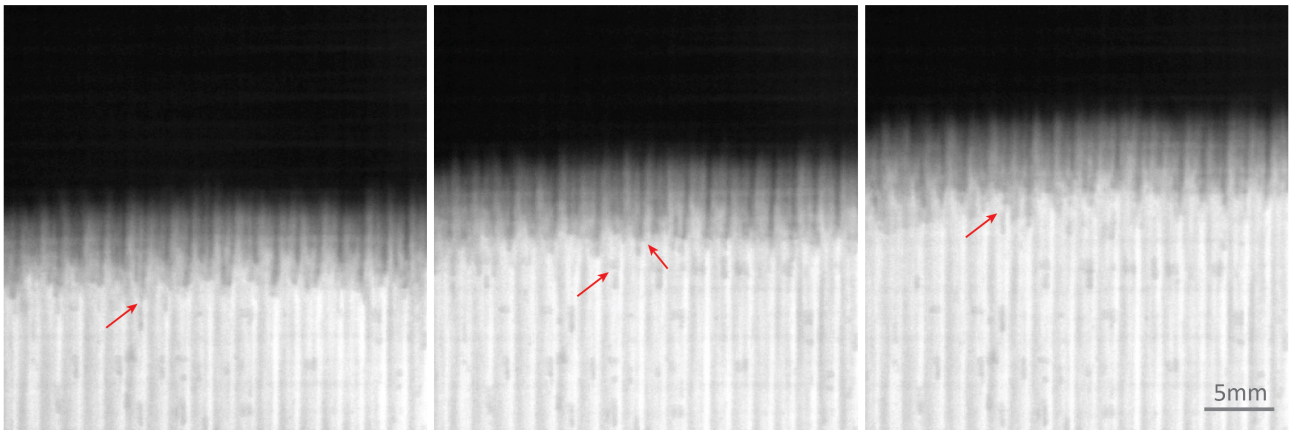

Figure 5.4: Meso-void formation observed in absorption images (test #4). From left to right the images spaced of 36.8 seconds. Red arrows show some examples of void entrapment due to the horizontal stitches.

The fabric architecture and in particular the presence of the horizontal stitches were found to be the major factor affecting the flow pattern. In the capillary-driven case, fiber bundles create "pools" in the upstream areas which lead to meso-void entrapment as shown in the sequence of images in Fig. 5.4 and explained in Fig. 5.5a. In the viscous case, they form large empty areas within the fibrous preform leading to a stabilization of the flow as shown in Fig. 5.5b. As a result, the saturation as a function of position will result in an almost linear decrease over the unsaturated area for all cases.

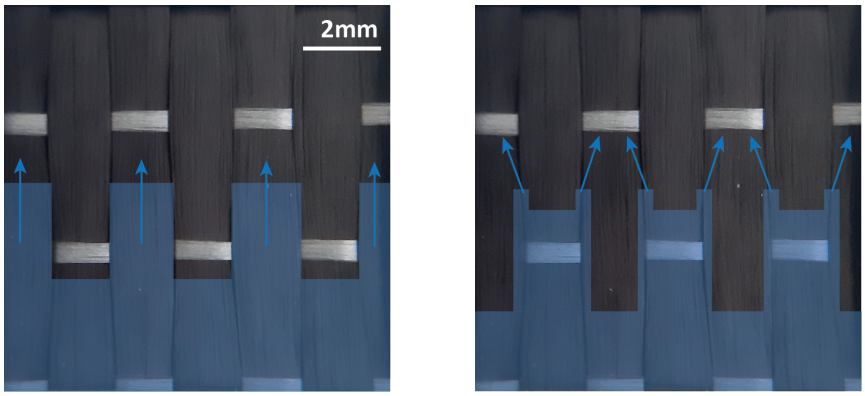

(a) **(b)**

Figure 5.5: Schematic of the influence of the fabric architecture on (a) capillary and (b) viscous flow patterns.

5.3.3 Visualization methods comparison

With the aim of comparing the two visualization methods to assess the flow front pattern and saturation rate, histograms of absorption, refraction and scattering images for tests #2 (Fig. 5.1) and #5 (Fig. 5.3) were built and are grouped in Fig. 5.6.

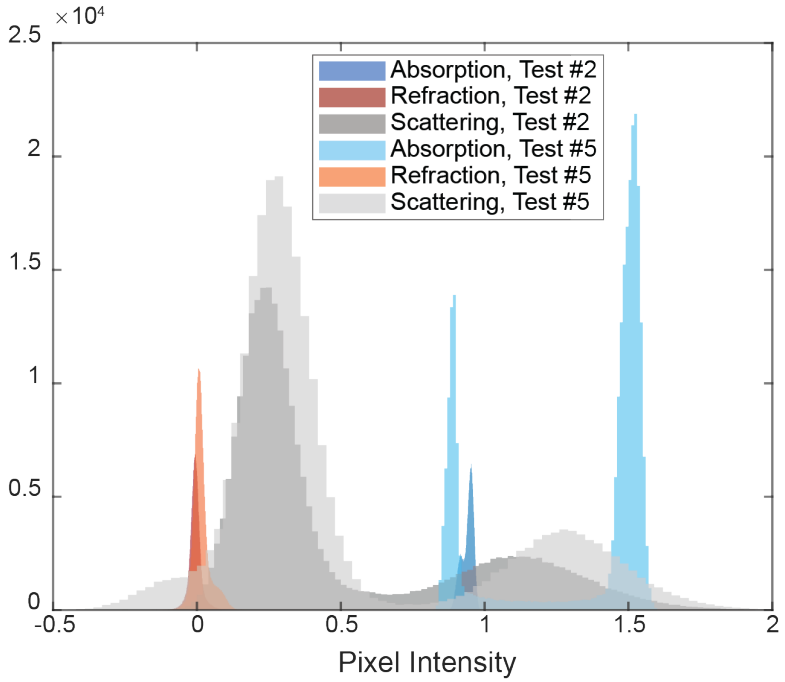

Figure 5.6: Comparison of histograms for absorption, refraction and scattering images of tests #2 and #5.

The absorption image discloses differentiated peaks of dark and light grays when the contrasting agent is added, whereas without it, nearly only one peak appears. Moreover, when compared to scattering images that display separated peaks as well, the pixel intensity range per peak (i.e. for fluid and fabric) is narrower for absorption images. This leads to better differentiation between the two materials, simplifying the image interpretation and analysis since the objective is to build the dynamic saturation curve for each experiment following the grayscale analysis method presented in *Chapter 3* section 3.3.3. Refraction image histograms were very similar for both techniques and with a single peak, since as already mentioned, information is transmitted through the texture (or signal homogeneity) rather than through the contrast.

Table 5.3 summarizes the main advantages and disadvantages of the two approaches. As a matter of fact, conventional radiography by means of contrasting agents seems to be a powerful technique to observe flow patterns with satisfying resolution of the flow front, allowing to elucidate preferential flow paths and void formation mechanisms. Even though, some hurdles need to be overcome to carry a thorough flow analysis: (i) for viscous flows, the flow displacement per image acquisition can be too significant leading to a slight error when building the saturation curve, to overcome this, it is sought to reduce the time of acquisition; (ii) a complete analysis of the final saturation state (accurate mea-

surement of the residual porosity) is needed to properly describe the flow behavior for the modelling; (iii) micro-void formation and location is hardly identified with this method.

Table 5.3: Advantages and disadvantages between the studied visualization methods.

	Advantages	Disadvantages
X-ray phase contrast imaging	• Scattering image gives a good fluid/fabric contrast to track flow progression at a real scale • Conventional resins can be used • Additional information about the flow can be extracted from the refraction image	• Scaterring image resolution is not sufficient to extract flow patterns, in particular, intra-tow flow. • Grating orientation can conceal some features • Time of acquisition can be too long for fast flows
X-ray transmission	• Fine detail is obtained • Flow patterns are highlighted for all impregnation speeds • Since the grating movement is not needed, the acquisition time can be reduced • Meso-void formation can be observed	• Need of contrasting agents to visualize flow patterns, modifying fluid properties

5.3.4 Examples with other systems

In this section, the visualization of flow through other preforms rather than the unidirectional carbon fabric with conventional radiography is evaluated. Impregnation of the two flax preforms is shown in Fig. 5.7 and 5.8. Interestingly, an unsaturated area varying over time is observed for both cases, even though the phenomenon is more pronounced for the twill fabric due to the pronounced dual-scale porosity of this medium (larger meso-pores when compared to the UD). This was attributed to absorption and swelling effects happening behind the flow front as introduced in *Chapter 2* section 2.4.3. Hence, this approach can be extended to study the impregnation of natural preforms. However, it should be noted that the test fluid employed is water-based, thus swelling and absorption are expected to be significant.

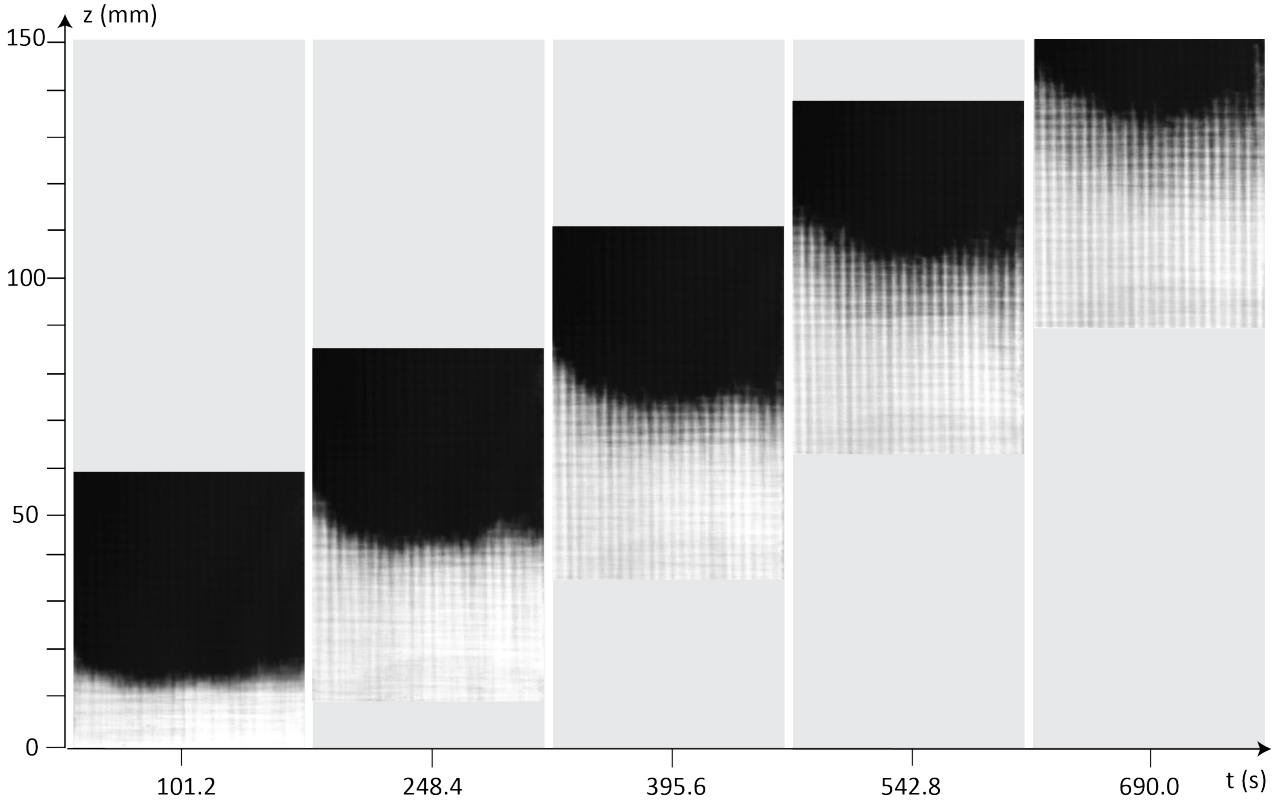

Figure 5.7: Representative absorption images of the twill flax fabric impregnation (test #7).

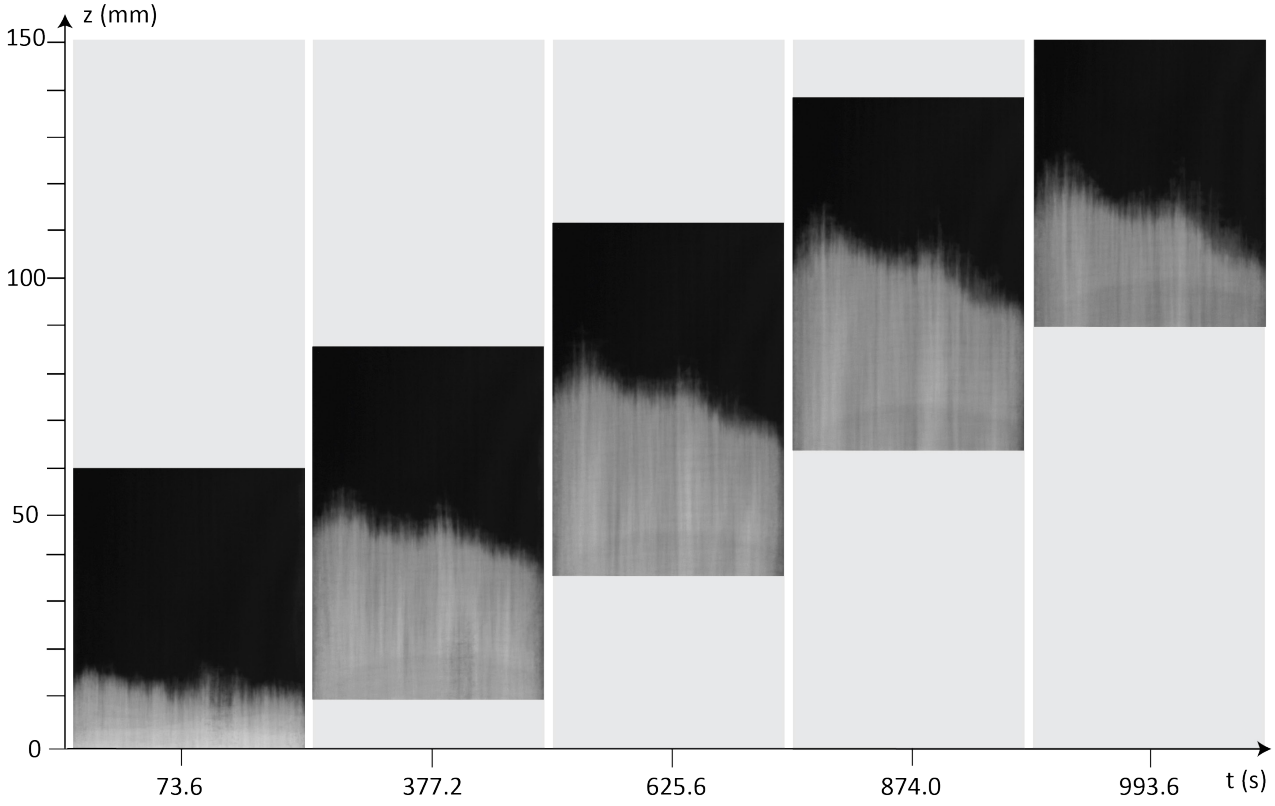

Figure 5.8: Representative absorption images of the unidirectional flax fabric impregnation (test #8).

Finally, an impregnation in the twill carbon preform was carried out and the flow front behavior is shown in Fig. 5.9 with a sequence of three images. A small unsaturated area is observed depicting a rather balanced flow. A lot of meso-voids were formed, those stemming from the highly heterogeneous geometry, with large meso-spaces in between the tows and large horizontal bundles, perpendicular to the flow direction. Moreover, the interconnected meso-pore structure led to void migration events throughout the impregnation.

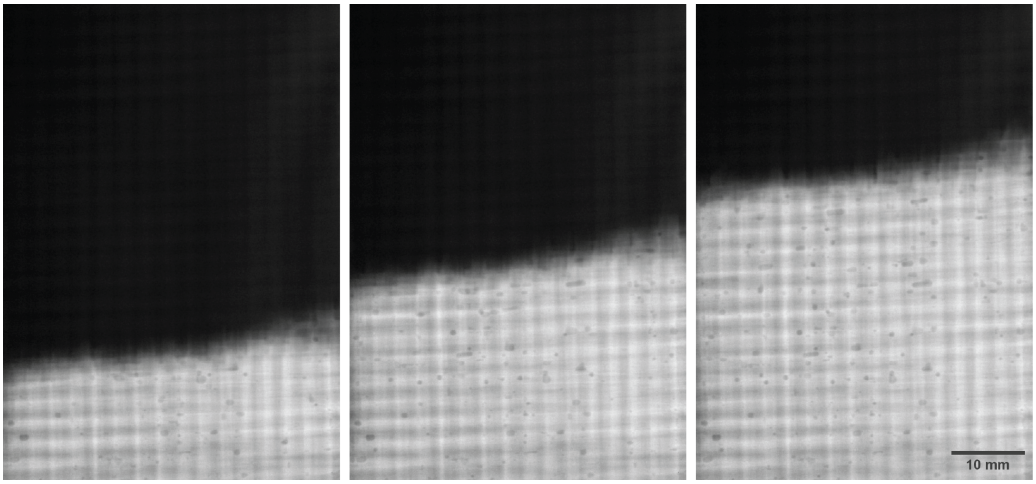

Figure 5.9: Visualization of the twill carbon fabric impregnation (test #9). Absorption images correspond to an acquisition position visualizing roughly the middle position of the fabric. Each image is separated by 46 seconds.

5.4 Conclusion

The present results show that scattering images obtained by X-ray phase contrast imaging were not able to elucidate flow front patterns with enough detail. In particular, capillary fingering happening in slow flows was hindered by an inter-tow signal close to that of partially saturated tows. A combination of absorption, refraction and scattering images was proposed to obtain images in which the flow regime was depicted. However, those images do not allow to build the saturation curve from a simple mathematical analysis, e.g. from the grayscale analysis as done in the previous chapter with scattering images.

To overcome these drawbacks, we proposed to use conventional X-ray radiography and proved that it can be a suitable technique for in-situ flow analysis for LCM studies and in particular for non-translucent preforms. Despite the low density of carbon and flax fabrics, by adding a ZnI_2-based contrast agent to the model fluid, we were able to enhance the fluid/fabric contrast in absorption images and elucidate fluid path at a real impregnation rate with a satisfactory resolution.

The flow front for different impregnation conditions was successfully tracked for a unidirectional carbon preform. Capillary to viscous fingering regimes were clearly identified and the location and shape

of meso-porosity for the capillary case was even observed. Then, the method was successfully extended to observe flow through unidirectional and twill flax fabrics and a twill carbon. A variable size of the saturated area was observed for the natural fiber preforms and attributed to swelling and absorption phenomena. Void formation and motion in the twill carbon fabric was also depicted revealing the versatility of the technique to study different phenomena taking place during infiltration.

Chapter 6

Modelling of dynamic fluid saturation in carbon reinforcements

A methodology is proposed to monitor and model the progressive saturation of a non-translucent unidirectional carbon fabric stack through its thickness making use of the approach presented in the previous chapter to assess the progressive saturation by means of X-ray radiography and extract the dynamic saturation curves using image analysis. Four constant flow rate injections with increasing flow speed were carried out. These were simulated by a numerical two-phase flow model for both capillary and viscous leading flow conditions. The hydraulic functions describing pressure and relative permeability versus saturation were determined by fitting the saturation curves using a heuristic optimization routine. As the fluid velocity increases and the flow regime at the flow front shifts from capillary to hydrodynamically driven, the resulting capillary pressure curves for a given saturation level are shifted to higher values, from negative to positive. These as well as the capillary pressure calculated from the pressure drop within the unsaturated region of the fabric correlate well with a corresponding change in the averaged dynamic contact angle.

Part of this chapter has been published as:

Helena Teixidó, Guillaume Broggi, Baris Caglar, Véronique Michaud. "Measurement and modelling of dynamic fluid saturation in carbon reinforcements", Composites Part A: Applied Science and Manufacturing, 107520, 2023 [257].

6.1 Introduction

Modelling fluid flow through fibrous reinforcements at the processing macro-scale has received much attention in the past decades with the aim of predicting the preform filling step to manufacture composite parts [7, 8]. For simplicity, infiltration studies often assume a fully saturated flow front progression. However, approaches considering multiphase flows taking place at different scales seem to be more realistic and are increasingly proposed.

One method is the two-phase flow initially developed in soil-science and used in liquid composite molding in the frame of metal-based matrix materials [109, 110, 258, 259] but still seldom applied for polymeric composites [104–108]. A continuum mechanics framework in which a resin phase displaces air (second phase) contained in a porous medium is applied. Then, in order to solve mass and momentum conservation equations for each phase within a representative volume element, constitutive relationships for pressure and relative permeability vs saturation are defined. Nevertheless, those relationships are not straightforward to directly measure experimentally and rely thus on the fitting of semi-empirical equations which are subsequently inserted into multiphase flow equations [117, 120].

The modelling of fluid flow in carbon fabrics has been barely addressed given the few available experimental setups to observe flow through non-translucent preforms. In this chapter, we employ the methodology developed in previous chapters: we observe the progressive saturation of the unidirectional carbon fabric via radiography and enhance the fluid/fabric contrast by means of contrasting agents added to the model fluid, gaining further details in the impregnation of a unidirectional carbon preform, thus with a rather uniformly bi-modal pore size distribution. The progressive saturation is then analyzed for injection conditions covering various flow regimes and modelled with a two-phase flow model as developed in Ref. [105], further extended to account for both capillary and viscous leading flow scenarios each related to a given value of the capillary number. An optimization procedure is proposed to extract the relevant constituting parameters from the experimental drainage-imbibition curves. Finally, we propose to link the results of the two-phase flow model with the mesoscopic capillary pressure drop approach, based on saturated flow assumptions, through the dynamic contact angle dependency on the capillary number.

The terminology presented in Fig. 6.1 is employed in this chapter; when the flow progresses ahead inside the tows, we will describe it as capillary leading flow and it is modelled with an imbibition model in which the displacement phase, the liquid, is wetting; conversely, when the flow progresses at the front in meso-spaces (in between the layers and the tows), we will describe it as viscous leading flow and it is modelled with the drainage model in which the liquid is the non-wetting phase.

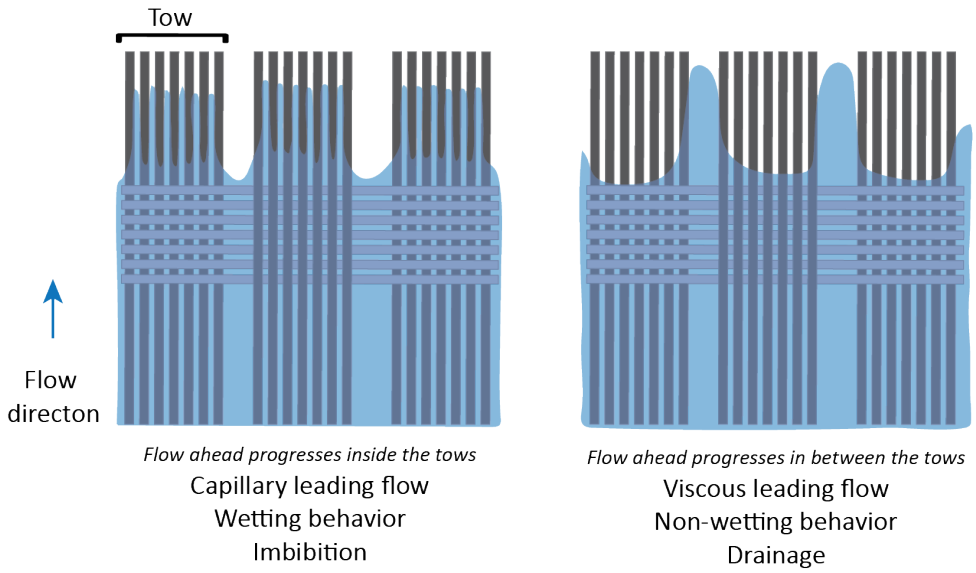

Figure 6.1: Schematic of the terminology employed in the current chapter.

6.2 Materials and methods

6.2.1 Materials

The quasi unidirectional carbon fabric with $A_w = 270$ gsm. According to the description of the fabric on section 3.1.1, the fabric is uniformly bi-modal and we do not expect this fabric to show extreme dual-scale effects as observed in other textiles where large flow channels are present [44]. We thus expect flow patterns to mostly relate to dynamic wetting effects.

The UD fabric impregnated with the aqueous solution of polyethylene glycol including the contrasting agent with formulation: 62.5 wt.% of water, 11.0 wt.% of PEG (M_w = 35kDa, Sigma Aldrich), 22.6 wt.% of ZnI_2 (M_w = 319.19, Fluorochem) and 3.9 wt.% of Kodak Photo-Flo 200. A surface tension value of a value of 32.7 ± 0.2 mN/m was obtained, averaging four measurements and since the fluid is water based, we estimated that the change in surface tension between experimental conditions varied by not more than 1% [260].

For the permeability study, the water-based solution of PEG at 16.67 wt% was employed.

6.2.2 Flow experiments

Flow experiments were performed with the X-ray phase contrast imaging setup presented in *Chapter 3* section 3.3.1 and acquired with the methodology from section 3.3.2. Only absorption images were used in this study, since according to *Chapter 5* an optimal flow front resolution was not achieved with the scattering images. It should be noted that the grayscale is thus inverted in the present work, the liquid being the dark phase and the fluid the light one.

Nine fabric layers with a dimension of 4.95 ± 0.05 cm × 15 cm were fitted in a 3 mm thick metal

spacer enclosed in the PMMA based mold, leading to a fiber volume fraction of $V_f \approx 45$ %. In-plane injections at four different constant flow rates were performed in the vertical position, obtaining a range of flow regimes spanning from capillary to viscous driven.

The approximate fluid front flow velocity was adjusted by controlling the pump settings and the actual one was then measured by averaging the front speed from the saturation curves. In particular, the position z at $S = 0.5$ was plotted versus time and the resulting curve was fitted with a linear function, the average velocity corresponding to the slope. All along the infiltration, the fluid pressure and temperature were measured. The flow front u and superficial U velocities, the average fluid temperature T with the respective viscosity μ and capillary numbers Ca are listed in Table 6.1.

Table 6.1: Impregnation experiments.

Test #	u [mm/s]	U [mm/s]	T [°C]	μ [Pa · s]	Ca (10^{-4})
1	0.082	0.045	25.4	0.074	1.02
2	0.213	0.117	26.7	0.072	2.58
3	0.258	0.142	22.8	0.082	3.47
4	0.429	0.236	25.0	0.075	5.41

6.2.3 Dynamic saturation assessment

For each experiment, the saturation curve $S(z, t)$ was built as a function of location z in the fabric and impregnation time t. The same routine to build the saturation curve from the grayscale analysis of X-ray images as described in *Chapter 3* section 3.3.3 and validated in *Chapter 4* was employed.

A region of interest of 500 pixels was selected, corresponding to a width of 2.5 cm approximately located in the middle of the sample to get rid of flow edge effects. The averaged pixel intensity value over fabric width was calculated and converted into saturation value by comparing the pixel intensity values to those corresponding to fully wet and fully dry states. Saturation value extraction was calibrated to ensure that the value always remained between 0 (fully dry state) and 1 (final state after flushing the resin for several minutes).

6.2.4 Numerical modelling

Flow experiments were modelled with a two-phase flow approach, whose equations are developed in *Chapter 3* section 3.4.1 and implemented in a 1D model in COMSOL Multiphysics 5.6 as introduced in section 3.4.2. At the inlet ($z = 0$ m), a normal inflow velocity equal to the superficial velocity U, representing the constant flow rate was set and at the outlet ($z = 0.15$ m), a no-flow condition

(ensuring that no flow is entering at this point).

Infiltration experiments were all carried out with the same fluid and fibrous preform. As introduced in section 3.4.2, a requirement for the developed model is to know in advance if the fluid progresses with a wetting or a non-wetting behavior. This was visually determined by observation of the dynamic flow front: if flow within the tows led the overall flow front, the fluid was considered as wetting for this range of flow rates, whereas if flow within the tows lagged, the fluid was considered as the non-wetting phase (and air the wetting phase).

In the present macroscopic approach, all effects and processes that will influence the equilibrium between the two fluid phases (such as surface tension, wettability of the solid, porosity distribution) are lumped into $P_c - S - k_r$ relationships for a given value of Ca. Moreover, since P_c is determined under different injection conditions in this work (the desaturation rate $\dot{S} = \partial S/\partial t$ is not equal to 0), it is regarded as a dynamic capillary pressure. Consequently, the difference between non-wetting and wetting pressures is not only due to capillarity but also depends on the flow dynamics (such as the pressure gradient needed to overcome viscous forces) [261]. Even if saturation curves are generally determined in literature under static conditions (and thus only dependent on the system properties), researchers proved that they lead to a poor prediction of two-phase flow kinetics in real non-steady cases.

Dynamic effects manifest themselves, notably as differences in hydraulic functions descriptions [262, 263]. Thus a dynamic capillary pressure, $P_{c,d}(S, \dot{S})$ with a more general thermodynamic definition, is increasingly employed and is related to the static one $P_{c,e}(S)$ by introducing a dynamic term dependent on the temporal rate of saturation change τ, such that $P_{c,d}(S, \dot{S}) = P_{c,e}(S) - \tau(\dot{S})$. This term τ, also called the capillarity coefficient, is a measure of the fluid speed to reach an equilibrium state. Even though some studies showed a dependence between τ and S, the functional relationship is still unclear [264–266]. Experimentally, the dynamic capillary pressure is observed to be greater than the static one in drainage and lower in imbibition, and their discrepancy is suggested to arise from the change of static to dynamic contact angles [263, 267–271]. This arises from the fact that capillary pressure (in a saturated slug-flow assumption) is related to the contact angle θ by Eq. 2.15 as previously introduced in *Chapter 2* section 2.4.1.

The link between dynamic contact angle (which in this case corresponds to an averaged contact angle, as it is averaged over the whole REV) and capillary pressure obtained from the multiphase flow approach is however not often directly made in the literature, in part because fluids used in soil science have a much lower viscosity than organic resins, hence less marked dependency of the contact angle on flow velocity.

6.2.5 Permeability measurement

To solve equation 3.9, a proper measurement of the saturated permeability K_{sat} is first sought. Permeability experiments were performed with the same mold and setup configuration as the flow experiments, thus with an aspect ratio of 3 between length and width. At the outlet, a beaker and a scale were added to record the outcoming mass after full impregnation of the preform related to the outcoming flow rate Q_{out} with the fluid density. Before each experiment, the fabric stack was weighed to accurately estimate the fabric volume fraction. In an in-plane impregnation, K_{sat} can be easily calculated from the relation derived from Darcy's law (Eq. 2.7), with ΔP_{app}, the average pressure difference during the saturated flow.

Since in a constant flow rate, the pressure increases first linearly during the saturation of the preform and then becomes stable once the preform is saturated, the fluid was let to flow enough so the pressure was constant (varying $\pm$ 0.001 bar) to measure the saturated permeability. Three experiments per constant flow rate condition (same as tests #1 to #4) were carried out to elucidate if the K_{sat} was somehow dependent on the flow rate. The twelve permeability results as a function of the superficial velocity are shown in Fig. 6.2 and as no trend was observed, a mean value of the K_{sat} was calculated resulting in an averaged value of $8.63 \cdot 10^{-11} \pm 1.33 \cdot 10^{-11}$ m^2 which is highlighted in red.

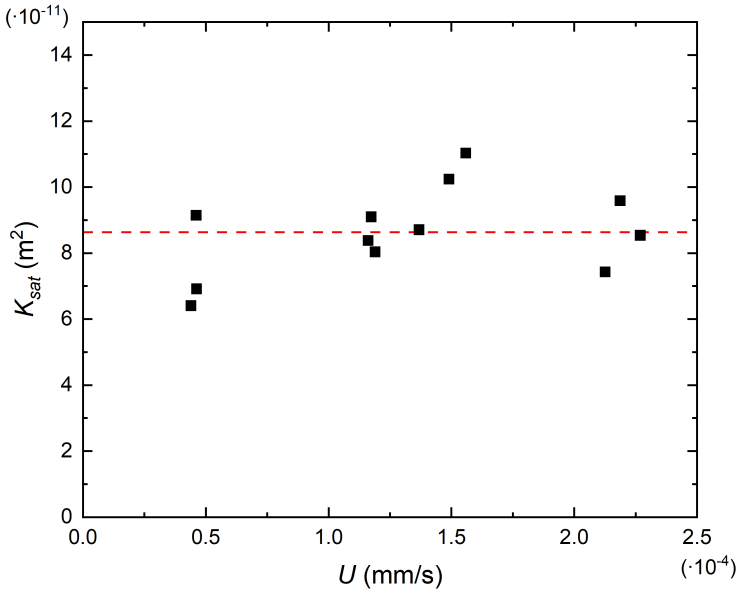

Figure 6.2: Saturated permeability results.

6.2.6 Parameters identification

To perform the optimization, eleven $S(z,t)$ training curves were selected per experiment with the aim of representing various instances throughout the mold-filling. The optimization routine presented in *Chapter 3* section 3.4.3 was employed to identify β, L and N parameters that better fit the experimental data. As the saturation curves are almost self-similar over the position z and linear over a large domain, the error minimization resulted in the fitting of the average linear region. Thus, the WMSE was used to increase the weight of the non-linear region, namely below 0.1 and over 0.9 saturation by assigning the value of w_j accordingly. The problem was constrained by choosing upper and lower boundaries for the different parameters and the maximum number of iterations was set to 1000.

Since, the Nelder-Mead algorithm [247, 248] based on an heuristic was found to offer the best compromise between result quality and convergence speed and the Differential Evolution to better minimize the error at the expense of long convergence times, they were employed to run the optimization computations.

6.3 Results

6.3.1 Flow experiments

An example of a sequence of three images per experiment taken at different times is shown in Fig. 6.3, for the four experiments with resulting flow regimes elucidated with this approach.

Capillary fingering is clearly observed for test #1, with flow leading within the tows, resulting in an unsaturated length up to 20 mm. Test #2 shows a slight capillary behavior and test #3 turned out to be a rather balanced flow with a small unsaturated zone. For both experiments, the unsaturated length was close to 10 mm. Viscous fingering is observed for test #4 with a larger unsaturated area (up to 15 mm), and flow leading between the tows. In this last case, the front is slightly more blurred due to the nesting induced changes in the meso-porosity network. Thus, for experiments #1 and #2, the resin is considered wetting and for #3 and #4 non-wetting.

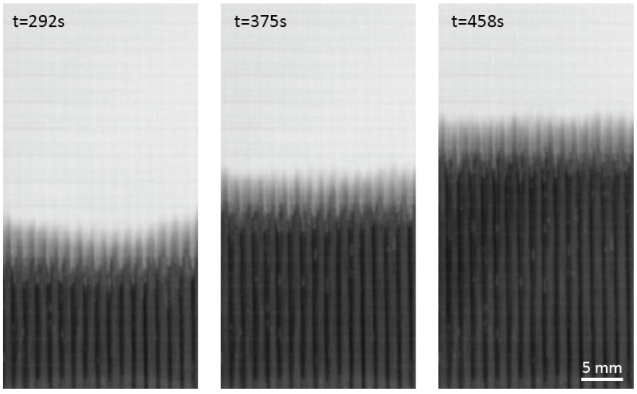

(a) $Ca_1 = 1.02 \cdot 10^{-4}$

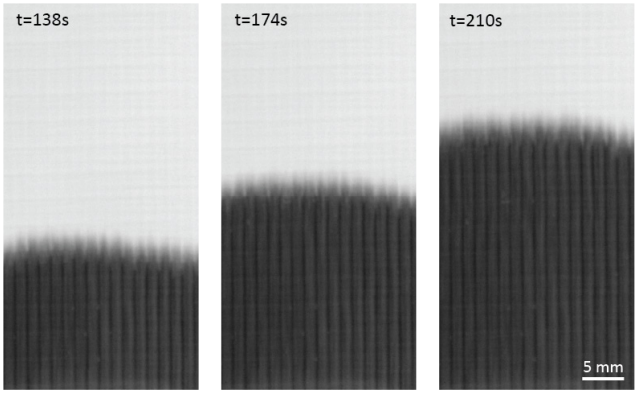

(b) $Ca_2 = 2.58 \cdot 10^{-4}$

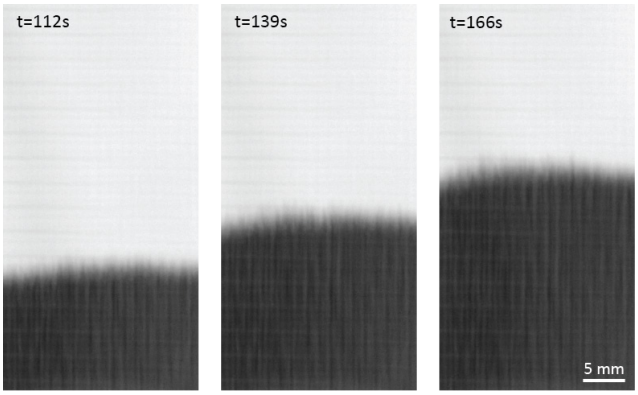

(c) $Ca_3 = 3.47 \cdot 10^{-4}$

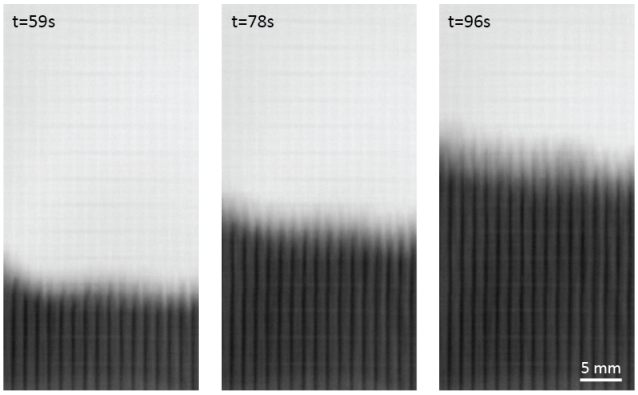

(d) $Ca_4 = 5.41 \cdot 10^{-4}$

Figure 6.3: X-ray absorption images showing the flow progression at three different times for the four injection conditions.

The pressure difference between the inlet and the outlet ΔP shows a linear behavior with time in all cases as expected, as illustrated in Fig. 6.4. Moreover, for tests #3 and #4, the pressure does not increase immediately because no pressure builds up at the inlet in the early phases of flow due to capillary wicking, which confirms our previous visual observations [42]. However, due to the low pressure values of the current experiments, these could not be exploited to directly evaluate a capillary pressure drop, as was done in Ref. [42].

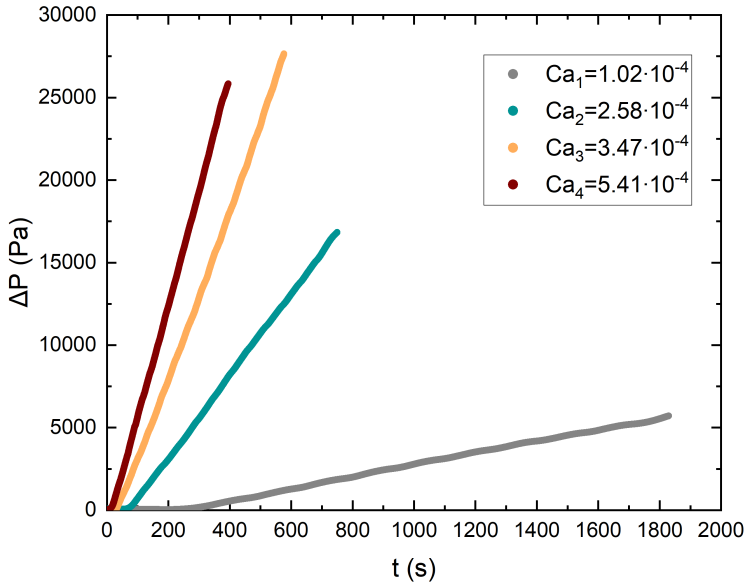

Figure 6.4: ΔP pressure measurements.

6.3.2 Numerical simulation and optimization

The numerical simulations were carried out for the four injection conditions with the aim of exploiting $S(z,t)$ curves to extract $S(P_c)$ and $k_r(S)$. According to the previous observations, tests #1 and #2 were modelled as a wetting infiltrating fluid displacing non-wetting air and conversely, #3 and #4 as a non-wetting fluid displacing wetting air. Table 6.2 lists the times t_i used for the optimization of $S(z,t)$ curves. Those were selected so that the flow front was between 20 and 130 mm from the inlet with an increment of 10 mm approximately, giving a representative section of almost the entire steady fabric impregnation.

Table 6.2: Selected instances for optimization.

Times (s)	Test #1	Test #2	Test #3	Test #4
t_1	236.9	91.5	76.1	49.3
t_2	347.1	138.1	121.3	68.1
t_3	467.1	183.4	156.9	96.4
t_4	577.0	228.8	195.5	116.0
t_5	697.9	275.9	231.9	143.4
t_6	825.5	330.6	278.0	161.8
t_7	960.2	377.9	313.9	180.8
t_8	1087.0	422.6	349.6	207.4
t_9	1204.4	468.1	395.0	234.6
t_{10}	1332.4	514.1	431.4	252.8
t_{11}	1442.8	560.3	466.7	280.0

With the aim of determining the fitting parameters with accuracy, the error E (Eq. 3.14) between experimental and numerical data was calculated for several combinations of β, L, N and then the best candidates (giving smaller error) were used as inputs to the optimization routine. Details of the optimization procedure are provided in *Chapter 9*, section 9.2.1.

The minimized aggregated error E as well as the optimized β, L, N and resulting M values are presented in Table 6.3. A general trend was observed for β that increases as Ca decreases as Nordlund et al. [105] previously observed and the inverse for N that increases with Ca, even though values of N for drainage experiments were very close. Finally, L was found negative in all cases similarly to Refs. [105, 243, 244].

Table 6.3: Parameters identification results.

Test #	Model	β	L	N	M	E (10^{-3})
1	Wetting	26.79	-1.09	3.00	0.67	2.36
2	Wetting	14.39	-1.07	5.04	0.80	0.20
3	Non-wetting	4.70	-0.78	19.41	0.95	0.22
4	Non-wetting	2.43	-0.90	20.85	0.95	0.78

The numerical simulations using the optimized parameters are compared with the experimental data in Fig. 6.5. For flow regimes close to a balance between capillary and viscous forces (tests #2 and #3), the saturation curves are very similar and the curve fitting matches almost perfectly. For viscous and capillary flows, since the flow front is slightly time-variant due to potential slight fiber rearrangements and more pronounced dual-scale effects, saturation curve shapes differ more along the fabric length and experimental times.

For all cases, the saturation curves were quite steep due to a relatively small and rather stable unsaturated area, as previously introduced in *Chapter 5*, a characteristic dictated by the fabric geometry more specifically by the transverse stitches that limits extensive capillary flow before filling the larger gaps around themselves.

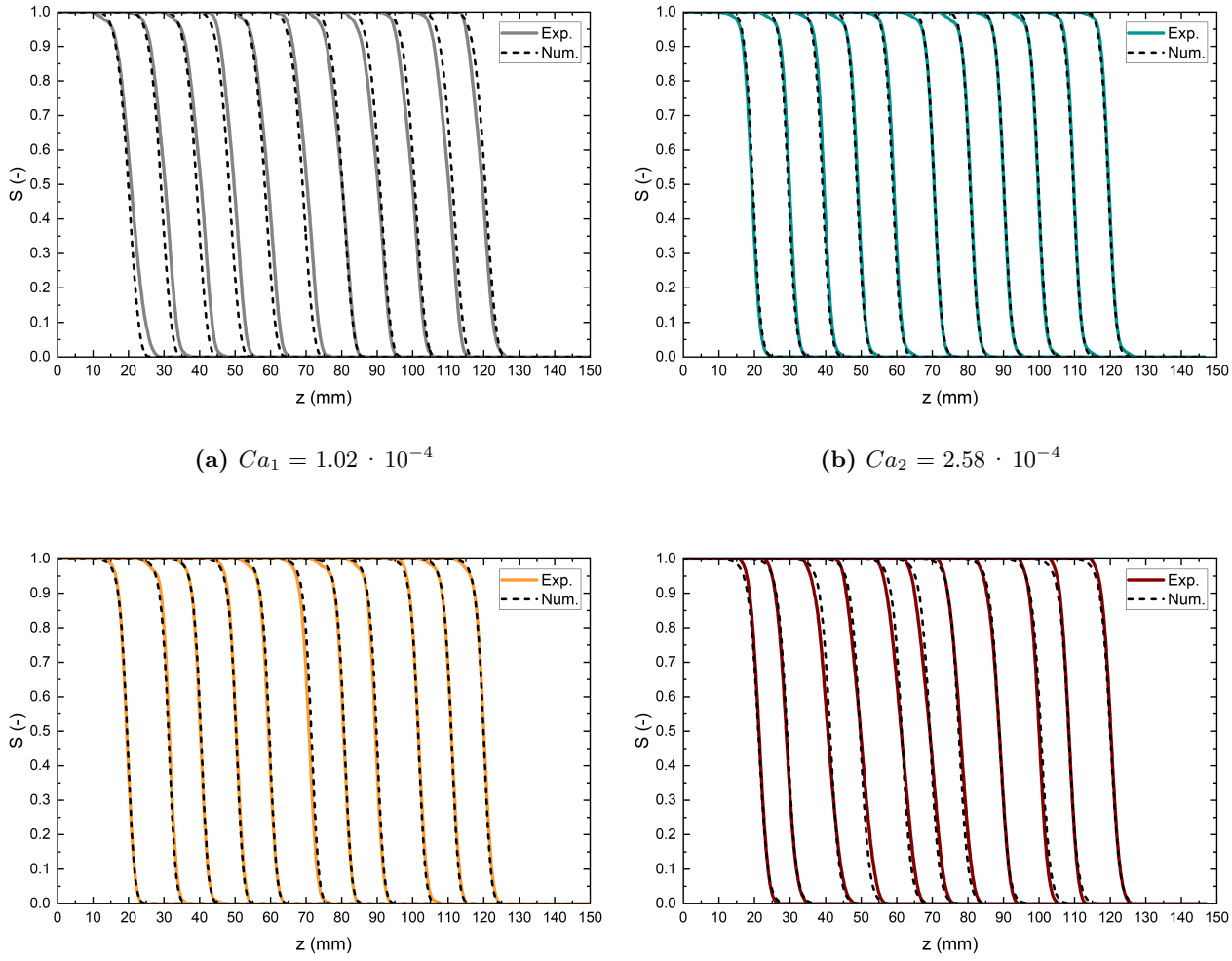

(a) $Ca_1 = 1.02 \cdot 10^{-4}$ **(b)** $Ca_2 = 2.58 \cdot 10^{-4}$

(c) $Ca_3 = 3.47 \cdot 10^{-4}$ **(d)** $Ca_4 = 5.41 \cdot 10^{-4}$

Figure 6.5: Experimental and numerical $S(z, t_i)$ curves.

6.3.3 Hydraulic functions as function of capillary regime

Previous results allowed to build the hydraulic functions describing the unsaturated flow behavior for the experimental injections. The relative permeability versus the liquid saturation functions $k_r(S)$ obtained by modelling the different flow regimes with the optimized parameters from Table 6.3 are given in Fig. 6.6. The shape of the curve differs when fluid is treated either as non-wetting (increasing concave) or wetting (increasing convex) even though this is more pronounced for capillary leading cases compared to viscous leading cases where curves present almost a linear profile as already suggested by Nordlund et al. [105].

Moreover, it is observed that the relative permeability is an increasing function of flow rate (and consequently of the Ca) for a given saturation level. Current results agree with published data since concave to convex shapes for wetting and non-wetting fluids as well as the displacement rate and wettability effects on the relative permeability have already largely been reported in literature for non-fibrous media [272–275]. This result can also be intuitively understood in our case, since we expect that fluid fills mostly the intra-tow region in the low Ca case, leading to a low value of relative permeability, whereas the fluid fills mostly the inter-tow regions in the high Ca case, leading to a higher value of relative permeability, since the large spaces between tows mostly govern the permeability.

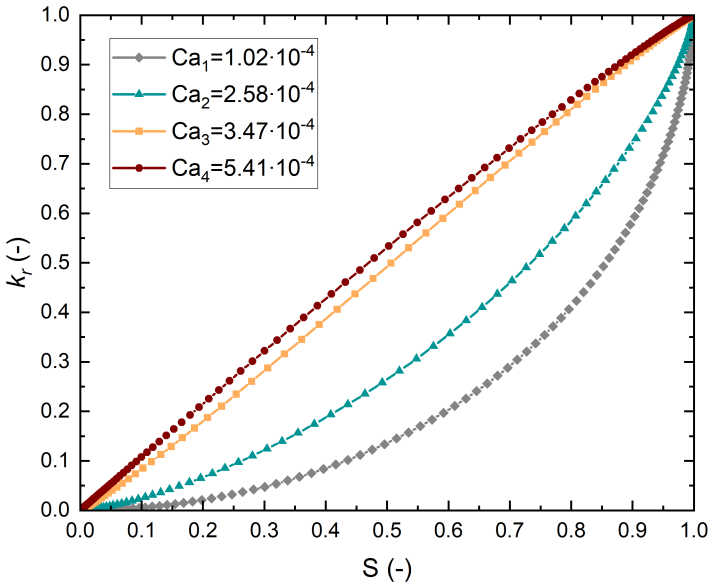

Figure 6.6: Hydraulic relative permeability function $k_r(S)$.

Similarly, the respective retention functions $S(P_c)$ were obtained and are presented in Fig. 6.7. Drainage curves (describing tests #3 and #4) were found to be rate dependent: for the fastest flow rate (test #4), the unsaturated region is spread over of a wider range of capillary pressures when compared to the lower flow rate (test #3). Thus, increasing the flow rate results in a less steep drainage curve, indicating a larger unsaturated zone with a large distribution of capillary pressures. The drainage curve dependency on the flow rate to describe unsaturated flow in dual-scale fabrics was already observed by Nordlund et al. [105] and related to the dynamic wetting conditions.

However, the same trend was not observed in imbibition curves (describing tests #1 and #2) which were very similar for both injection cases even though the pressure at smaller saturation rates was found to be higher for the slower case (test #1) as suction in the tows is higher. The imbibition curve of test #1 is in fact very close to spontaneous imbibition in static conditions (which corresponds to a wicking experiment), since the pressure increase is very low, as shown in Fig. 6.4. Conversely, in drainage, narrow pores between bundles massively affect the $S(P_c)$ curve and the entrance pressure effect shifts the curve to higher positive values. This was also observed by Smiles et al. [276], who found retention curves to be non-unique during drainage (dynamic drainage curves present higher suction than static ones) whereas dynamics effects are not observable during imbibition and the retention description is unique. In other words, since the dynamic effects depend on the pressure change, the retention curve is also influenced by the pressure head caused by viscous effects, which is more important at high flow rates [277].

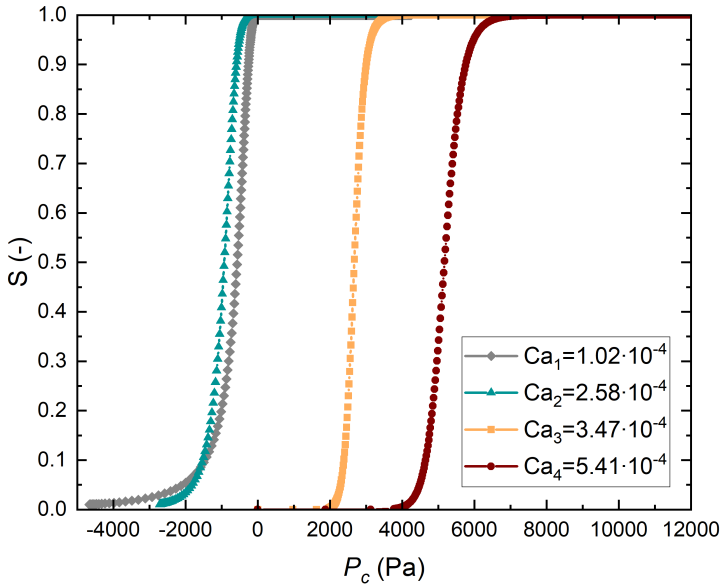

Figure 6.7: Hydraulic retention function $S(P_c)$.

Finally, it is of interest to point out that the attribution of the liquid phase to a wetting or a non-wetting phase was made here based on our observation of the flow front. As a result, tests #2 and #3 show very similar saturation curves $S(z,t)$ because they are close to the balanced regime but the $k_r(S)$ and $S(P_c)$ descriptions are very different, since one is considered an imbibition whereas the other one was considered as a drainage experiment. For intermediate flows, capillary and viscous fingering are hardly discernable in the unsaturated length and in addition, the unsaturated length is even more sensitive to the flow front shape when compared to viscous or capillary dominated flows. Thus, it is tricky for intermediate flows to define sharp boundaries between the two wetting conditions since there is not a given speed at which a fluid pass from wetting to non-wetting behavior but rather an interval of speeds at which both coexist, regarded in literature as crossover pattern [278]. This is why the multiphase approach can be limiting when considering the capillary to viscous leading flows transition state. Nevertheless, Foroughi et al. [279] very recently proposed a saturation-capillary pressure relationship taking into account dynamic wetting. Encouragingly, this equation might be implemented in the current model to define for example constant pressure driven impregnation in which the dynamic wetting switches from a non-wetting to a wetting state.

The determination of P_c–S–k_r relationships is essential to model unsaturated flows with a two-phase flow approach. These parameters are affected by fluid and porous media properties but how is still a subject of intense research [275]. Commonly, they are fitted to experimental data based on stationary measurements and the non-uniqueness of these relationships, in particular in dynamic conditions, is well acknowledged in soil science literature for both drainage and imbibition phenomena [280]. In particular, the dynamic effect was shown to be more significant for low permeability porous media [281] and was proven to be impacted by several factors such as porous medium and fluid properties as well as some external factors [267]. In soil science, the averaged pore throat size has been shown to have the greatest impact leading to a constant redistribution of fluid flow at the pore scale.

In our case, where liquid resins flow through fibrous porous media, with rather stable pore sizes over the length of the preform, wetting phenomena proved to be a dynamic property highly influencing the relative movement and distribution of fluid inside the porous medium at the macro-scale and thus the flow descriptions P_c and k_r [7, 42, 282]. Current results show that dynamic wetting results in a change of the hydraulic descriptions. Concerning the relative permeability curve, a decrease of Ca corresponding to an increasingly capillary dominated flow pattern led to a decrease of the relative permeability for a given saturation value. Since the relative permeability reflects the connected pathway of flow based on saturation distribution, it seems logical that viscous flow dominated cases present high k_r values at the Darcy scale when compared to capillary dominated flows (permeability values far from K_{sat}). For the drainage cases, the relative permeability function is almost linear; this can be attributed to the dominant flow taking place in meso-spaces, so that the overall permeability is expected to be close to the saturated permeability, as was already noted in previous work [44, 283–285]. It should be noted that some authors questioned the use of the saturated permeability for the definition of the Darcy's permeability since the K_{sat} is sensitive to the flow in meso-pores and unsaturated flows occur across

all the pore scale range [243].

Although capillary pressure plays a major role in the description of fluid flow in unsaturated porous media, the theoretical basis and practical implications of it remain poorly understood [263]. In static conditions, there is only one capillary pressure P_c which depends on the system and is described as the pressure difference between the wetting and non-wetting phases as described earlier. However, in dynamic conditions, P_c also depends on the saturation speed $\dot{S}$ and the difference between pressures is not only due to capillary effects close to equilibrium but also to the pressure gradient needed to overcome the viscous forces. In the present work, we show that the dynamic wetting also influences the $S(P_c)$ relationship. In drainage processes, we observed that a higher flow rate results in a decrease of the system wettability and thus a higher capillary pressure is observed for a given saturation. Conversely, in imbibition processes, a higher wettability has a small impact on the capillary pressure description [263, 264, 280, 286, 287]. Dynamic forces are highly scale dependent and although several studies agreed on the influence of the dynamic effects in drainage processes, a consensus on how dynamic effects affect imbibition processes at large scales has not been reached so far given the interplay of physical phenomena happening at the microscale [287–289].

6.3.4 Comparison with the slug-flow approach

In fully saturated flow studies, following a slug-flow approach, capillary effects are lumped into a capillary pressure drop at the flow front ΔP_γ, defined as the pressure difference between the local pressure in the fully saturated fluid phase just behind the infiltration front and the pressure in the preform ahead of the infiltration front [6, 86]. With this approach, Verrey et al. [42] showed the velocity dependence of the capillary pressure drop and the dynamic contact angle using the Hoffman-Voinov-Tanner law (Eq. 2.17).

With the aim of evaluating the difference between a capillary pressure drop evaluated using the slug flow approach and our approach, and characterizing the relationship between capillary effects and wetting changes, the capillary pressure drop ΔP_γ was estimated in our four experiments. Since we could not make use of the pressure curves (as performed in Ref. [42]), due to the relatively low precision of the injection pump impacting the pressure readings at very low pressure regime, we evaluated the pressure difference between the beginning and end of the unsaturated region from the simulation results as $\Delta P_\gamma = P(S = 0.99) - P(S = 0.01)$, with P the pressure in the fluid phase, as illustrated in Fig. 6.8 for test #1 case at time t_4.

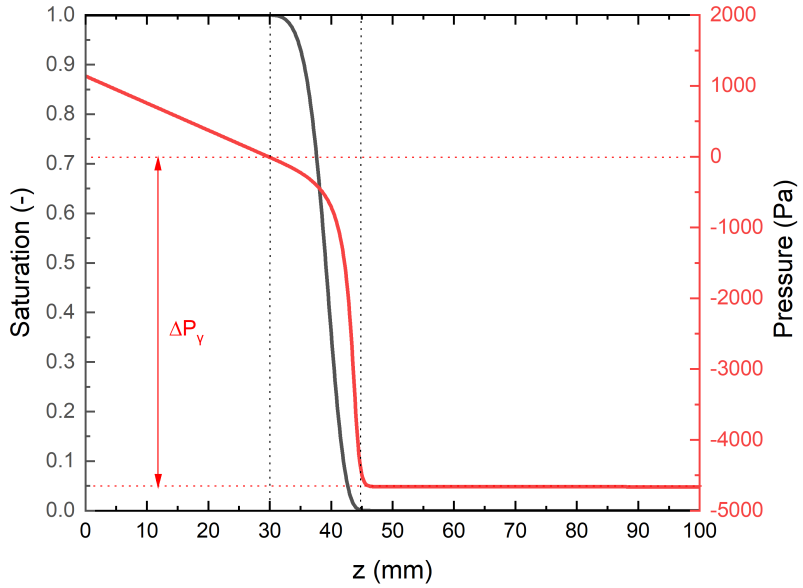

Figure 6.8: Schematic representation of ΔP_γ determination from the saturation and pressure of the fluid phase versus the position z. Example from test #1.

The values are then correlated to the capillary pressure curves found using the multiscale flow approach as shown in Fig. 6.9. The capillary pressure drop ΔP_γ corresponds indeed to the distance between $P_c = 0$ and $P_c(S = 0.01)$ for imbibition and $P_c(S = 0.99)$ for drainage. It can be remarked that for imbibition curves, the overall ΔP_γ is equal to the capillary pressure curve since the flow in the unsaturated region progresses only due to capillary effects whereas on the drainage case, ΔP_γ corresponds to a pressure P_e (or entry pressure) that should be overcome so the non-wetting liquid starts displacing the wetting fluid plus the capillary pressure needed to fill all the pores as previously suggested.

This approach can be directly related to the relative position of the flow fronts within the tows and in the meso-space region: indeed, this approach means that locally, the local pressure in the tows is lower, or higher as compared to the local pressure between the tows, which must be closer to atmospheric pressure, since the wetted perimeter is small as compared to the air-fluid surface in these areas. Thus, the resulting average pressure close to the flow front is negative or positive and is related to the dynamic capillary pressure identified in this work. We explore the idea to compare this to a dynamic wetting angle to find out if it is possible to make the link between the multiphase flow approach and the usual slug-flow approach often used in composite processing. We nonetheless keep in mind that a more detailed, local scale analysis would be required to explore the limits of this approach, in particular when the separation of scales between inter- and intra-tow regions becomes large.

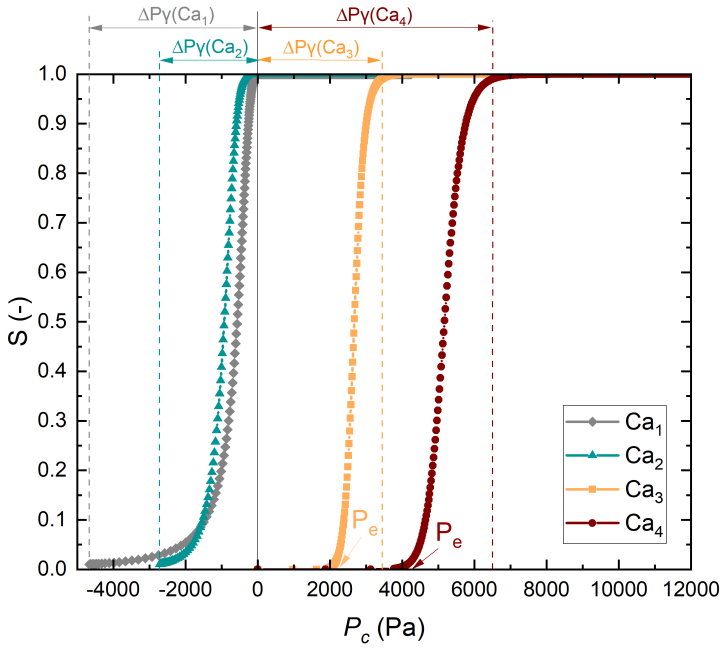

Figure 6.9: Representation of ΔP_γ determination from drainage-imbibition curves.

Thus, the liquid-fiber interface per unit of liquid volume, S_f was calculated assuming fibers as perfect cylinders of radius r_f with Eq. 2.8, leading to an estimated value of $S_f = 467{,}532\ \mathrm{m}^{-1}$. However, as suggested in Ref. [42], the use of equation 2.17 is very sensitive to the value of S_f and a more accurate measurement could be necessary. Figure 7.2 shows a representative drop of fluid onto a carbon fiber extracted from the fabric following the methodology from *Chapter 3* section 3.2.1. A static contact angle θ_e value of $23.4° \pm 4.6°$ was obtained by averaging the measurements for about 50 drops.

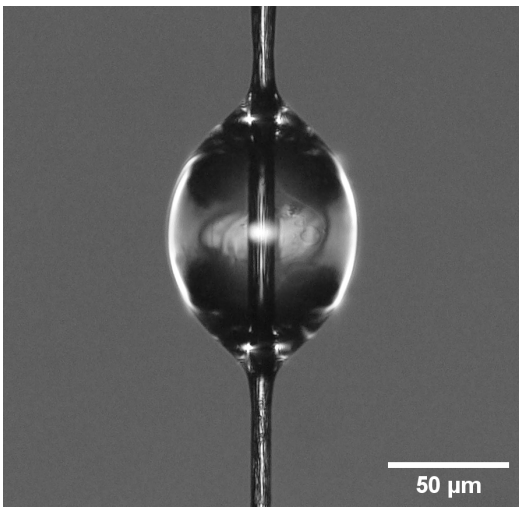

Figure 6.10: Drop analysis on a carbon fiber.

Analogously to Verrey's work, the experimental values of capillary pressure drop were plotted against the capillary number to illustrate the influence of the fluid velocity on capillary effects and fitted to Eq. 2.17, and c_T was found to be equal to 14510 (Fig. 6.11). The evolution of the capillary pressure drop is directly linked to the dynamic contact angle θ which can be easily determined by Tanner's law (Eq. 2.16, Fig. 6.11).

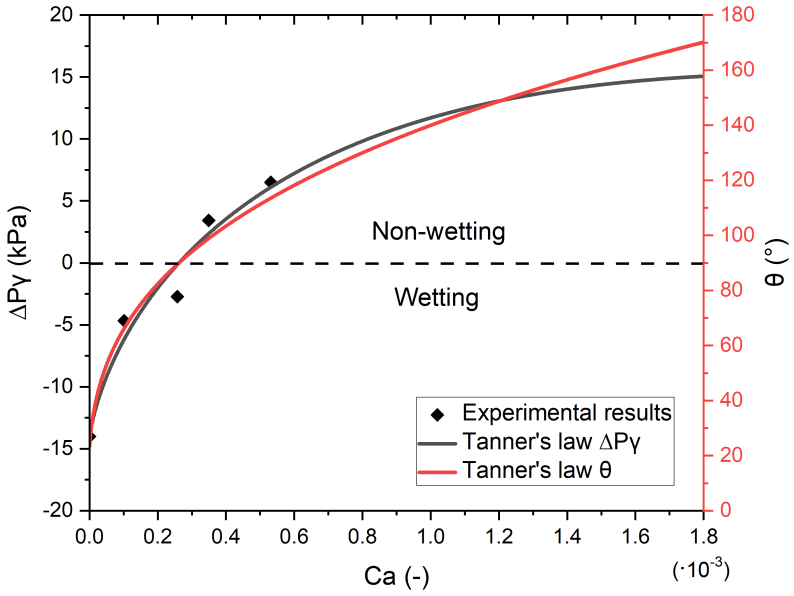

Figure 6.11: Influence of the fluid velocity on the capillary pressure drop and the resulting $\theta(Ca)$ curve.

Despite the differences in original assumptions between slug-flow and two-phase flow approaches, the results revealed to align well when converged with the definition of the dynamic contact angle, which can be considered here as an averaged contact angle, since it is extracted from a volume averaged measurement. Current capillary pressure values (and the location of the optimal capillary number, when the dynamic contact angle is 90°) were found to be rather low when compared to literature [42, 105]; this was attributed to the volume fraction which was less than 50% in our case and the strong wettability of our liquid (with low surface tension and contact angle). This methodology is however not restricted to the use of model fluids, in particular when using X-ray phase contrast which does not require the addition of contrasting agents, and further tests can be carried out following this methodology with epoxy resins and higher volume fractions.

6.4 Conclusions

A methodology was presented to analyze the progressive saturation of a carbon fabric preform. Impregnation under constant flow rate was visualized by means of conventional X-ray radiography. Taking advantage of an enhanced absorption contrast between the low-density fibers and the high intensity signal of a model fluid containing contrasting agents, the corresponding dynamic saturation curves were built. Then, a two-phase flow model inspired from soil-science was applied to numerically describe the infiltration of the fluid into the dry preform for wetting and non-wetting systems. Hydraulic functions $S(P_c)$ and $k_r(S)$ were obtained by fitting experimental and numerical $S(z,t)$ curves and finding van Genuchten and Mualem's parameters with a heuristic optimization algorithm. The effect of the capillary number on hydraulic functions was elucidated and found to be in accordance with the literature from soil science.

In the current work, simple 1D models have been developed but can be easily extrapolated to 2D or 3D simulations in COMSOL or other numerical codes, to represent impregnation of parts with more complex geometries. Moreover, a simple correlation was found between the multiscale flow approach and the slug-flow assumption allowing to build the dynamic contact angle and capillary pressure versus the capillary number from the progressive saturation analysis. Those results emphasize the validity and usefulness of the slug-flow assumption employed in previous works [42, 44, 86] and give new insights on the multiphase flow method.

Two-phase flow models are used in many engineering branches leading to a very well-documented topic but unfortunately barely developed in the frame of LCM infiltration where the meso and microstructure exhibits rather anisotropic features unlike other domains. Moreover, some observed natural phenomena such as the effect of swelling media [290–293] or the significant air entrapment mechanism happening during imbibition (since the pore scale invasion mechanisms are more complex) when compared to drainage [294, 295], can be extrapolated to impregnation studies that would encourage the use of this approach. For that purpose, this work has gone some way towards promoting the application of two-phase models in the frame of LCM infiltration. In case of textiles with larger meso-channels, leading to a very clear dual-scale morphology, the use of a superposition of saturation curves could be investigated, as proposed in fractured porous media, and a more local approach, considering flow in inter- and intra-tow regions separately would be of interest. In addition, since hydraulic functions are directly linked to flow kinetics happening at the pore-scale, it is sought in the next chapter, to investigate the effects of wettability and porous medium configuration on the flow invasion patterns and consequently on these continuous descriptions at the macro-scale, with a deep insight on intermediate states at which a fluid potentially switches from a wetting to a non-wetting state.

Chapter 7

Effect of wettability and textile architecture on fluid displacement and pore formation

Void formation arising from an irregular resin flow has been shown to be the most common flow-induced defect during LCM. In this chapter, we seek to address how air entrapment mechanisms are influenced by the wetting characteristics of the fluid and by the pore architecture. To this end, we evaluate the behavior of two model fluids with different surface tensions flowing through three carbon fiber reinforcements by means of X-ray radiography and we assess initial and final states for each experiment by performing X-ray computed tomography scans. The scan of the dry preform is used to describe the pore space geometry employing a pore network model and that of the wet preform to quantify the void content, location, and morphology. We found that the fluid characteristics strongly affect the flow front patterns and pore filling events for a given fabric architecture, and that two main promoters of snap-off events resulting in meso-void formation are involved in capillary dominated flows: a very wetting system leading to corner flows and the fabric bundles oriented perpendicular to the flow acting as obstacles.

This chapter is based on an article in preparation for submission to a peer reviewed journal:

Helena Teixidó, Baris Caglar, Véronique Michaud. "Effect of wettability and textile architecture on fluid displacement and pore formation during infiltration of carbon fibrous preforms".

7.1 Introduction

Fluid transport in porous media can be described at the scale of a pore (micro-scale) in which parameters such as pore connectivity, roughness, and fluid/solid interfacial properties govern the fluid movement or at the meso- or Darcy-scale in which the flow is defined by a continuum mechanics approach in a representative volume element characterized by the medium porosity, permeability and saturation. The relationship between the physical phenomena taking place in these two scales remains unclear particularly because the pore-scale spatial heterogeneity highly affects the flow at the macro-scale [296–298]. For example, the wettability is known to affect micro-displacement events and pore connectivity, exerting a powerful impact at the Darcy-scale, i.e. on the invasion pattern related to capillary effects and the efficiency of the fluid displacement and consequently air entrapment [282]. Hence, the dynamic effect of wettability on infiltration behavior in a confined porous medium with a given spatial distribution of pores and this topic remains to this day a major scientific challenge [61, 299–302].

In composites, a good wetting between matrix and fibers is sought to ensure good interfacial adhesion. Commonly, static and dynamic wetting are characterized at the microscale with single fiber measurements techniques (and extended to the meso-tow scale in Ref. [66]) by direct optical visualization and the Wilhelmy method [68, 303–306], and at the meso-tow and macro-layer scales with wicking experiments and the Washburn method [63, 73, 74, 177]. The influence of wetting on the overall pressure driven flow kinetics has still seldom been addressed in LCM. Recently, Caglar et al. [86] showed an increased dynamic wetting behavior for corona treated glass fabrics and characterized the related change of the flow front morphology for a similar flow rate. Similarly, Yoshihara et al. [60], showed that wetting exerts a strong effect on the impregnation behavior and the void processes in a single layer of pristine and fluorine coated woven glass fabrics.

Flow studies also rely on a good description of the pore space geometry and topology. Nowadays, X-ray techniques have allowed to image and reconstruct in 3D the porosity of fibrous preforms with unprecedented spatial resolution [44, 307, 308]. An improved description of the pore-network has enabled to perform numerical models to simulate, predict and gain a better insight on flow kinetics (in LCM processes, mainly to assess the permeability). For porous media made out of soil or rocks, a pore network model (PNM) is frequently employed to simply characterize the architectural features of the porous media, such as tortuosity, pore size distribution and connectivity. The principle is to describe the available volume as a set of pores linked with throats that describe the connectivity [239, 309]. Nevertheless, this approach is still seldom applied in the frame of composite systems [240, 310, 311].

In the previous chapter, we modelled the displacement of a model fluid into a carbon preform by means of macroscopic saturation profiles and the two-phase flow extension of Darcy's law. However, these descriptions give very little insight on the flow regimes at the pore scale, where local capillary forces play a major role. In the present chapter, we investigate the effect of a change in the fluid wetting characteristics on the flow morphology, and the fluid displacement events taking place in the

unsaturated area close behind the flow front, for three woven architectures. For this, we performed constant flow rate experiments with two fluids of different static surface tensions but similar viscosity, both containing contrasting agents, that we observe in-situ, in 2D averaged over the thickness with X-ray radiography. We then assessed the pore network geometry by using a pore network model and carried out a void analysis stemming from capillary/viscous phenomena by performing 3D tomographic scans of the dry and wet preform states, in order to better elucidate the role of wetting and fiber architecture on the flow and porosity patterns.

7.2 Materials and methods

7.2.1 Materials

The three fabrics are shown in Fig. 7.1: the quasi-unidirectional carbon fabric (A_w = 270 g/m^2) was employed as a reference fabric (called UD); then, the original fabric structure was modified by removing two over three horizontal glass bundles, and its areal weight was then estimated to 263 g/m^2 (called UDM); and the twill carbon fabric (A_w = 285 g/m^2, called TW).

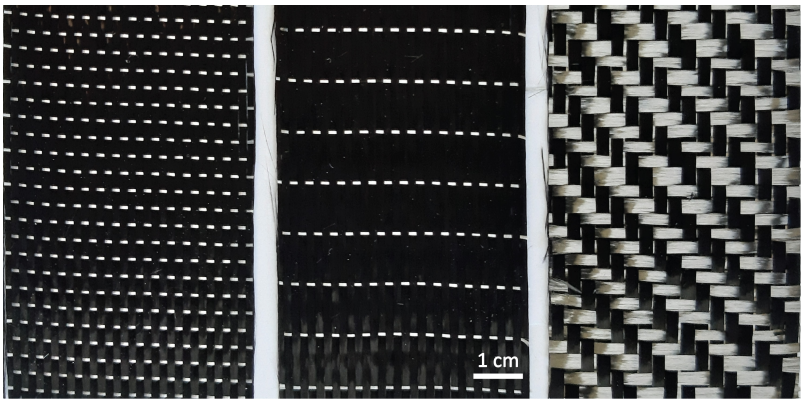

Figure 7.1: Form left to right: original unidirectional (UD), modified unidirectional (UDM) and twill (TW) carbon fabrics.

Two model fluids were employed: the water-based solution of polyethylene glycol (PEG, Sigma Aldrich, 35 kDa) with contrasting agent CA1 and the water-based solution of glycerol (99.5%, M_w = 92.09, Sigma Aldrich) with the contrasting solution CA2. The properties of each fluid are presented in *Chapter 3* section 3.1.2.

7.2.2 Flow experiments

Flow experiments were performed with the setup described in *Chapter 3* section 3.3.4. Fibrous preforms were prepared by stacking 9 layers of accurately hand-cut fabric with a dimension of 4.95 ± 0.05 cm × 10 cm. To accurately measure the volume fraction, the fabric stack was weighed with a scale (with a repeatability of ± 0.001 g). Then, layers were fitted in the cavity of a PMMA spacer of 3.2 mm with an inner silicon joint and enclosed in between two thick PMMA halves. To prevent from bending, outer PMMA plates were fastened with twelve metal screws, leaving the 3D scan area

free of high-density material. In-plane injections at a constant flow rate were performed vertically (from bottom to top, z-position) thanks to a syringe pump and the pressure and temperature were monitored along the test. The fluid velocity was adjusted by controlling the pump setting and was estimated by measuring the averaged front progression from the 2D scans. A summary of the experimental campaign is given in Table 7.1, with the resulting fiber volume fraction V_f, flow front velocity u, average fluid temperature T with respective viscosity μ and capillary number Ca.

Table 7.1: Impregnation experiments.

Test #	Fabric	Fluid	V_f	T [°C]	μ [Pa · s]	u [mm/s]	Ca (10^{-4})
1	UD	PEG + CA1	43.1	25.8	0.074	0.708	9.06
2	UD	PEG + CA1	42.9	26.6	0.072	0.244	3.06
3	UD	PEG + CA1	43.0	26.2	0.073	0.074	0.94
3 bis	UD	PEG + CA1	43.1	26.5	0.072	0.074	0.93
4	UDM	PEG + CA1	42.2	26.1	0.073	0.077	0.99
5	TW	PEG + CA1	44.5	24.1	0.077	0.087	1.14
6	UD	Glycerol + CA2	42.9	24.0	0.078	0.626	4.24
7	UD	Glycerol + CA2	42.9	23.7	0.079	0.270	1.19
8	UD	Glycerol + CA2	43.2	24.1	0.077	0.070	0.47
9	UDM	Glycerol + CA2	41.6	24.0	0.078	0.073	0.51
10	TW	Glycerol + CA2	44.5	23.9	0.078	0.083	0.55

The flow progression was visualized following the procedure from *Chapter 3* section 3.3.4. 2D X-ray radiography was employed to track the flow front as well as the dry and wet states and images were acquired at a rate of 2 images per second and a pixel size of 15 µm. 3D tomographic scans of the dry and wet states were performed in the middle position of the 2D scan and acquired at 3 images per seconds with a voxel size of 10 µm. The resulting 3D scans were segmented by employing the methodology developed in *Chapter 3* section 3.3.5.

7.2.3 Unsaturated length measurement

From the 2D scans, a mean unsaturated length was measured for each experiment: images were cropped at three different locations with a width of 110 pixels for the UD fabric and 210 pixels for the twill, corresponding roughly to three bundles located in the middle and right and left sides of the image. Separate bundles were selected instead of a larger fabric width in order to only capture the unsaturated length arising from the capillary versus viscous forces competition and avoid effects such as race-tracking that would lead to non-flat fronts. Then, similarly to the procedure developed in *Chapter 3* section 3.3.3, the average pixel intensity value was calculated over the cropped area width

and plotted versus the fabric length for each impregnation state as well as for the wet and dry states. By comparing the curves, two boundaries are set to define the unsaturated length as shown in Fig. 3.8.

7.3 Results

7.3.1 Static contact angle measurement

In order to assess the static contact angle between carbon and glass fibers and the two model fluids, 20 to 25 droplets were analyzed for each condition following the methodology presented in *Chapter 3* section 3.2.1. An example for each fiber/fluid system is shown in Fig. 7.2. For the model fluid with PEG, a static contact angle of 23.42° ± 4.36° was obtained for carbon, and for glass 10.25° ± 5.61° (Fig. 7.2a). For the glycerol solution, a static contact angle of 52.54° ± 4.66° was obtained for carbon, and 41.35° ± 5.07° for glass (Fig. 7.2b). Hence, the PEG solution has a stronger static wetting behavior when compared to the glycerol towards the fiber surfaces.

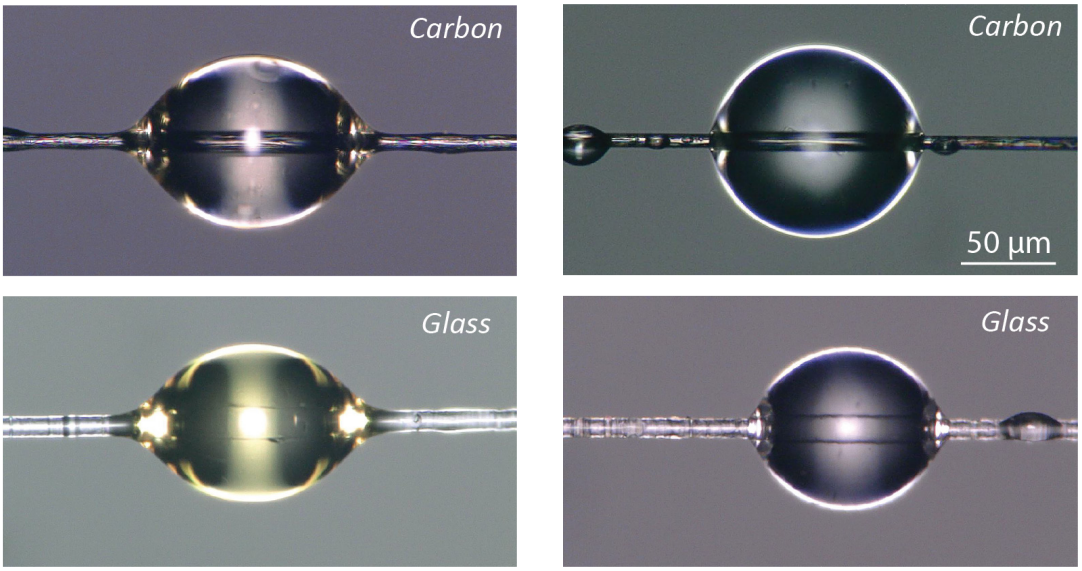

(a) PEG-based solution **(b)** Glycerol-based solution

Figure 7.2: Droplets of the (a) PEG-based and (b) glycerol-based model fluids on carbon and glass fibers.

7.3.2 Front displacement behavior in the UD carbon fabric

The morphological characteristics of the two model fluids displacement inside the unidirectional carbon preform under the different injection conditions were carefully explored. A sequence of four snapshots per experiment illustrating the flow patterns are depicted in Fig. 7.3 for the impregnation with the PEG solution and Fig. 7.4 with the glycerol solution. Corresponding movies can be dowloaded after obtaining permission, following the link provided in the figure caption.

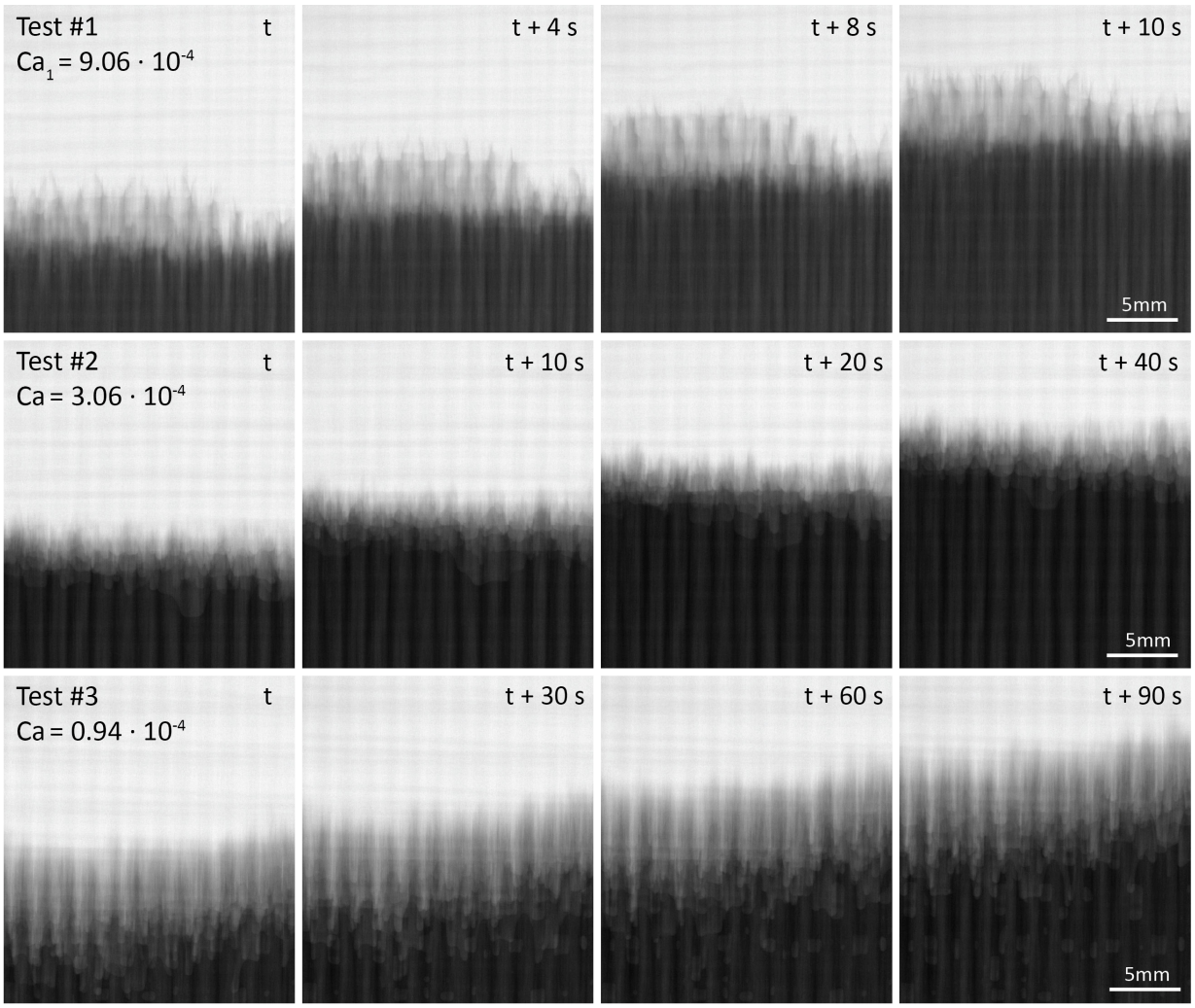

Figure 7.3: Sequence of images showing the PEG-based fluid distribution in the unidirectional carbon reinforcement for decreasing capillary number, thus from viscous to capillary dominated flows for the PEG-based solution (tests #1 to #3). The videos are available online in Ref.[312].

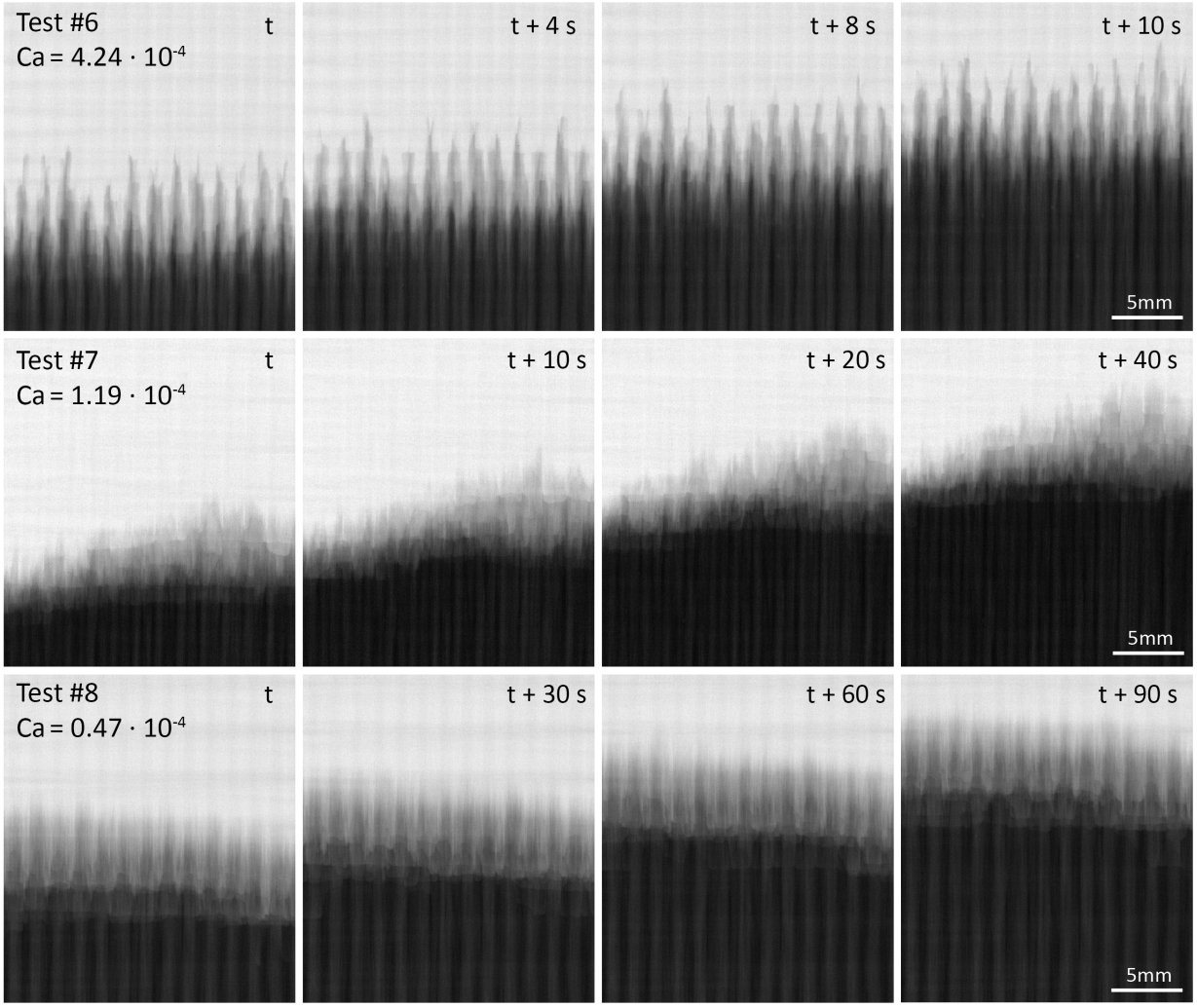

Figure 7.4: Sequence of images showing the fluid distribution in the unidirectional carbon reinforcement for decreasing capillary number, thus from viscous to capillary dominated flows for the glycerol-based solution (tests #6 to #8). The videos are available online in Ref. [312].

For the fastest injections (tests #1 and #6), the flow leads in between the tows, and thus is similar to drainage, in which the fluid has a non-wetting behavior, and the porous medium has a better affinity to the defending fluid (air) when compared to the invading fluid (liquid). The flow progresses along the center of the largest pores as the fluid attempts to minimize the contact with the fibers, resulting in a viscous flow elucidated by the dominance of well-connected longitudinal paths in between the tows. This follows a piston-like advancement and the corresponding dominant pore-scale invasion mechanism under drainage condition is known in soil science as burst (or Haines jump) [313, 314]. Moreover, where horizontal bundles are present, these longitudinal paths converge. The viscous fingering is as expected more significant for the less wetting fluid (Fig. 7.4), where a clear domination of positive curvatures over negatives is clearly observed, whereas for test #1 (Fig. 7.3), fingering is less pronounced, and the unsaturated area is more compact.

For the intermediate cases, a rather balanced displacement is captured for both experiments #2 and #7. Capillary and viscous flows are hardly distinguished in the unsaturated length, and it is difficult to define sharp boundaries between the two displacement patterns. As matter of fact, we observe that there is an intermediate flow rate condition for which the fluid adopts both wetting behaviors at the same time depending on the displacement location. This can be linked to the variability in the pore distribution and the local heterogeneity with meso and micro-pores, which lead to the coexistence of different displacement mechanisms, regarded as a crossover pattern [278].

Finally, for capillary dominated cases (tests #3 and #8), the fluid invasion pattern is assimilated to an imbibition type. The flow progresses with a corner flow behavior, by filling pores with smaller cross section located inside the tows; the flow front is hence led by capillary wicking. As described by Bico et al. [315], two macroscopic fronts can be identified: ahead, a thin flow that propagates using the thin pore structure (capillary flow leading the flow) and at the bottom, a main flow which saturates the medium. For the strong wetting conditions (test #3, Fig. 7.3), the unsaturated area is larger and the flow progresses less homogeneously as compared to test #8 (Fig. 7.4). As observed in the literature, a high wetting together with a low surface tension makes the air/fluid interfaces very easy to deform and stretch resulting in very unstable interfaces, resulting either in local fluid fast advance to re-equilibrate itself or in snap-off events, resulting in air entrapment [316–318]. Moreover, meso-void formation was not observed in the delayed front and took place where horizontal stitches were present, demonstrating that the porous medium geometry also plays an important role on the location and shape of entrapped voids. Then, test #8 falls in a less wetting condition, and even if capillary wicking is significant in the tows, the flow progresses backwards with a rather cooperative behavior and no snap-off events occur. The horizontal stitches were found to act as barriers, leveling and redistributing the delayed viscous flow.

The different patterns were better elucidated by applying a variance filter and subsequently adding the filtered and original images. An overview of the different flow fronts for tests #1 to #3 and #6 to #9 is presented in Fig. 7.5. Strong capillary and viscous fingering from test #3 and #6 respectively as well as the simultaneous flow fronts are highlighted. As a summary, the pore-scale displacements for drainage and imbibition descriptions differ and these cannot be considered as "symmetric" phenomena. This difference stems from the pore-scale wetting. For drainage, the pore size distribution is the main geometrical factor dominating flow according to literature, which results in the present case to a vertical viscous fingering since meso-pores in the UD fabric are found along the flow direction. Conversely, for imbibition cases, the corner flow pattern impedes viscous fingering and the fluid front progresses inside the tows. Thus, the fluid front is in addition to the pore structure also influenced by the pore corner characteristics, and their specific surface area as shown in Ref. [282].

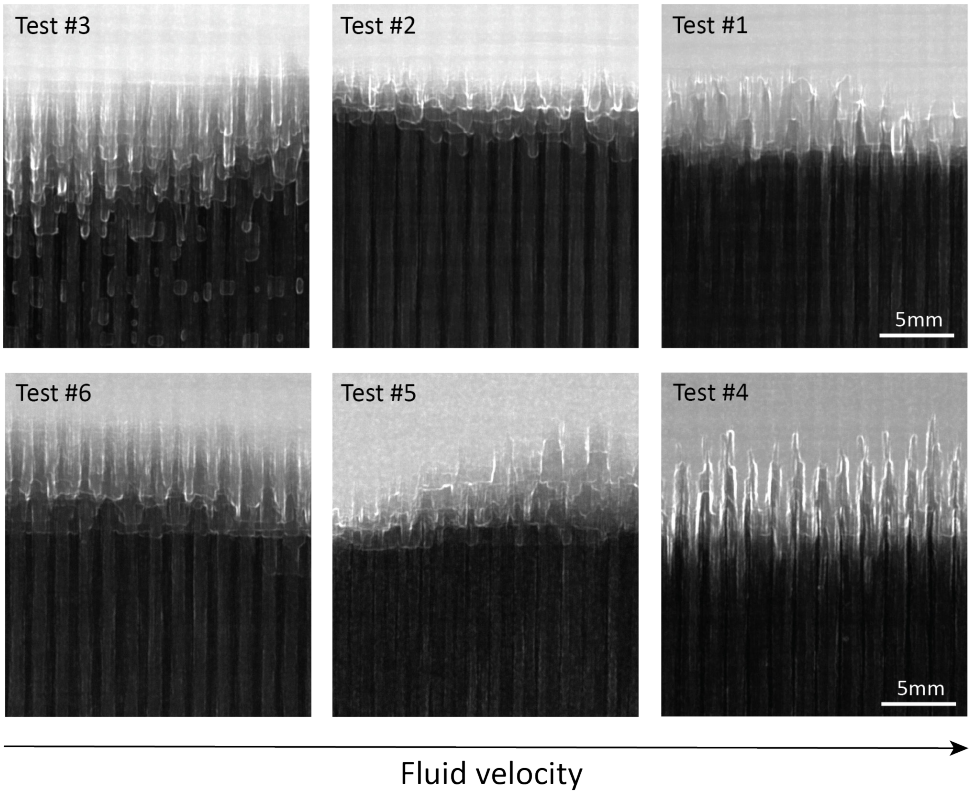

Figure 7.5: Flow paths elucidated with a variance filter for tests #1 to #3 and #6 to #8.

The pressure difference ΔP measured at the inlet for the six tests performed with the UD fabric are presented in Fig. 7.6. As expected, the pressure curves versus time are very similar per flow rate conditions since the viscosity values are practically the same. Experiments for the intermediate condition (tests #2 and #7) gave slightly different trends but this is attributed to scattering of experimental measurements.

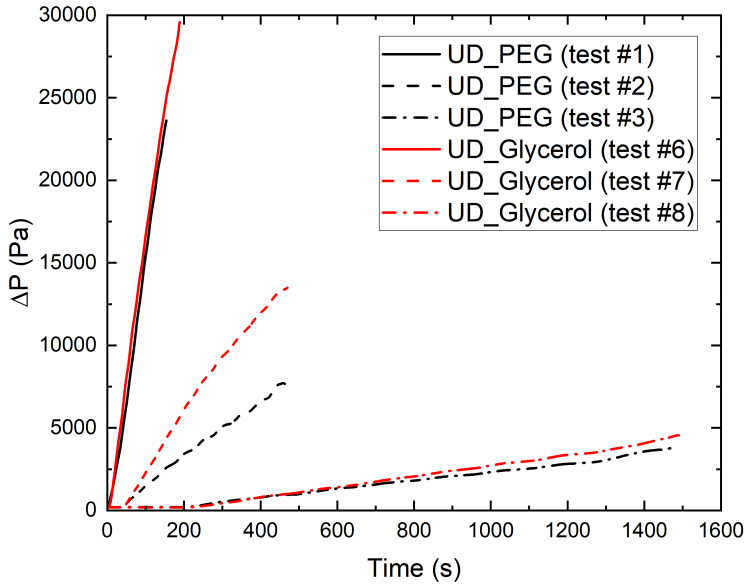

Figure 7.6: ΔP measurements of UD fabric impregnation experiments.

7.3.3 Comparison of front displacements in the UD modified and the twill fabrics

Since previous results proved that horizontal bundles significantly affect the flow pattern and increase the occurrence of snap-off events, the effect of the fabric geometry on the flow progression and void entrapment in wetting conditions was investigated. For that, two approaches were selected: the structure of the UD carbon was modified to observe the effect of the transverse glass tows and a twill fabric was selected to highlight the influence of a more balanced geometry.

The flow patterns obtained by impregnating the UDM with the two fluids (tests #4 and #9) are shown in Fig. 7.7. The UDM impregnations confirmed that horizontal bundles act as obstacles, blocking temporarily the vertical flow taking place in the meso-spaces. Then, once the flow overcomes the stitches, the delayed flow front speeds up locally to find stability, resulting in a large saturation gradient along the bundles. Thus, as already observed for the UD fabric (tests #3 and #8), the transverse yarns contribute to locally redistribute the fluid. Just behind the flow front, both cases exhibit a similar unsaturated area which as expected is longer when compared to simple UD impregnations since the distance between transverse stitches was increased, while the flow patterns and fluid distribution differ. For the strong wetting fluid (test #4), concave menisci in between the tows are observed. In addition, when the fluid arrives to the horizontal glass bundles, those start to be impregnated increasing the probability of snap-off events. This is similar to what happened in test #3 with pristine UD but less frequently. For the less wetting fluid (test #9), the delayed front, behind the capillary wicking, progresses also with concave menisci while with a more "U" shape, indicating a larger contact angle. The overall flow progression seems to be more cooperative whereas for test #4 the fluid front seems to be made up of individual fronts confirming previous observations.

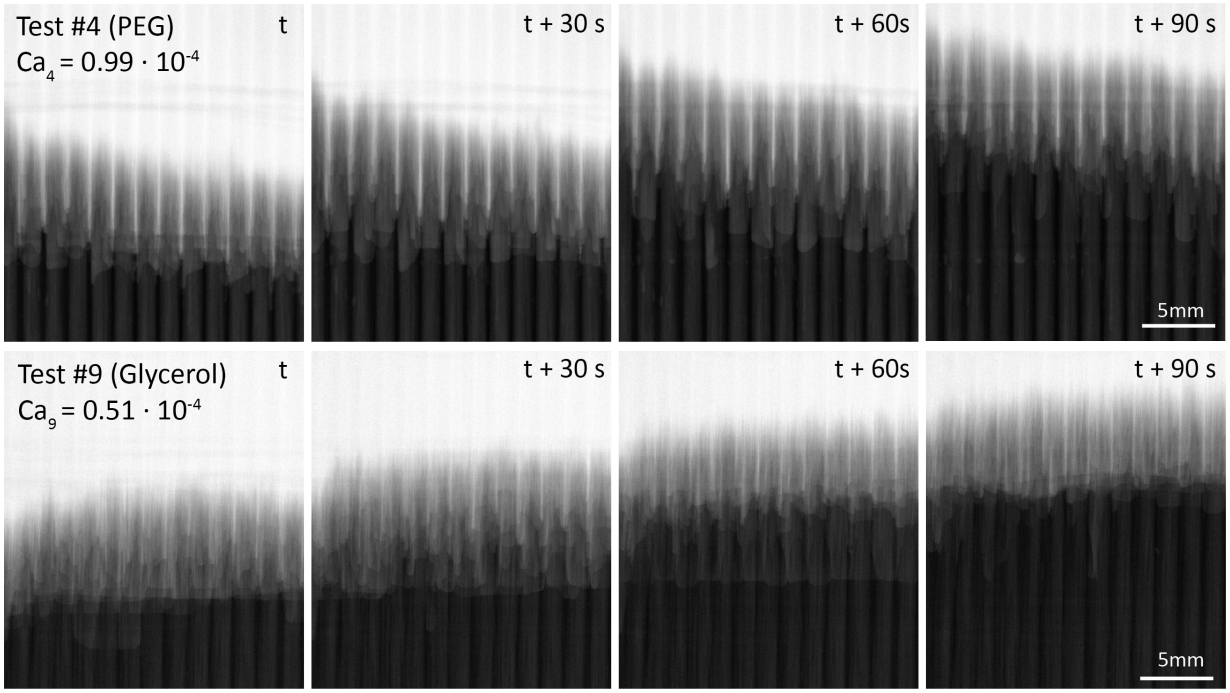

Figure 7.7: Sequence of images showing the fluid distribution in the modified unidirectional carbon reinforcement (tests #4 and #9) for capillary dominated flows. The videos are available online in Ref. [312].

Impregnation of the twill fabric was also performed with both fluids under capillary dominated flow (tests #5 and #10), and the obtained flow patterns are shown in Fig. 7.8.

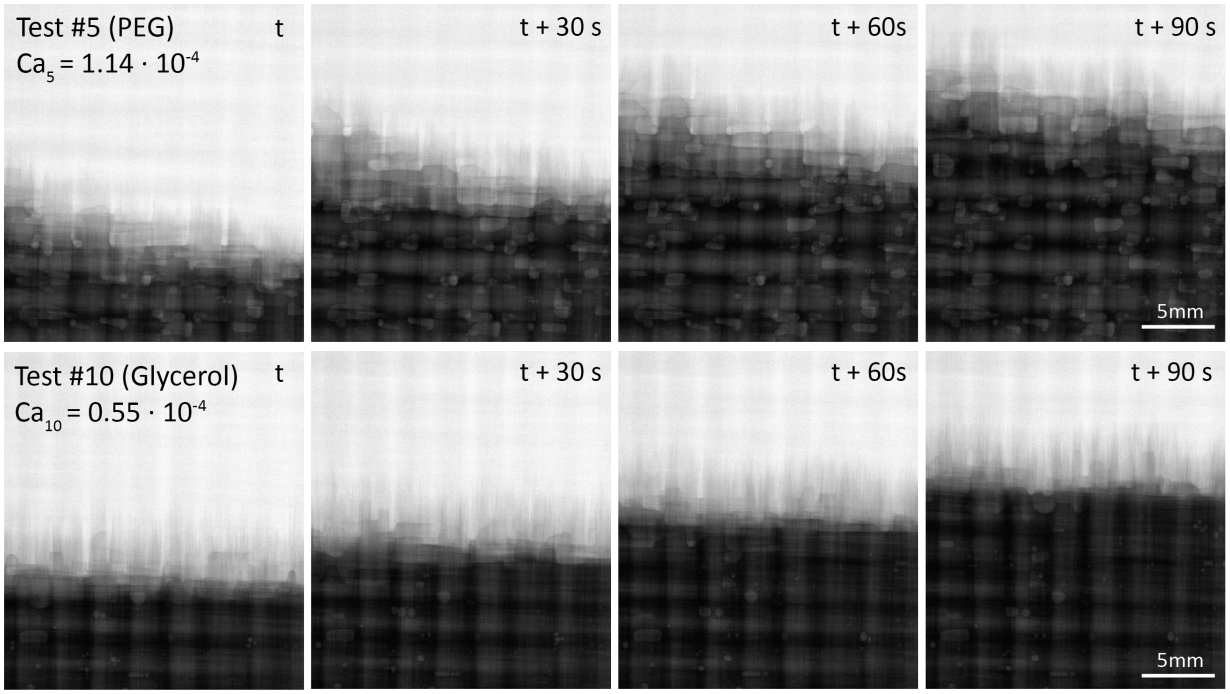

Figure 7.8: Sequence of images showing the fluid distribution in the twill carbon reinforcement (tests #5 and #10) for capillary dominated flows. The videos are available online in Ref. [312].

This fabric was chosen for its strong bi-directionality and its different meso-porosity (bundles are less compact leading to larger inter-tow space when compared to the UD). Evidently, this fabric architecture led to an increased void formation for both experiments, with a higher void fraction for the strongly wetting fluid (test #5). Snap-off events were found to arise from the early liquid progression inside the horizontal bundles, leading to an encirclement of air as represented in Fig. 7.9. The void shape differs between the two wetting conditions, namely, more elongated for the very wetting fluid, given the low surface tension and more round for the less wetting case.

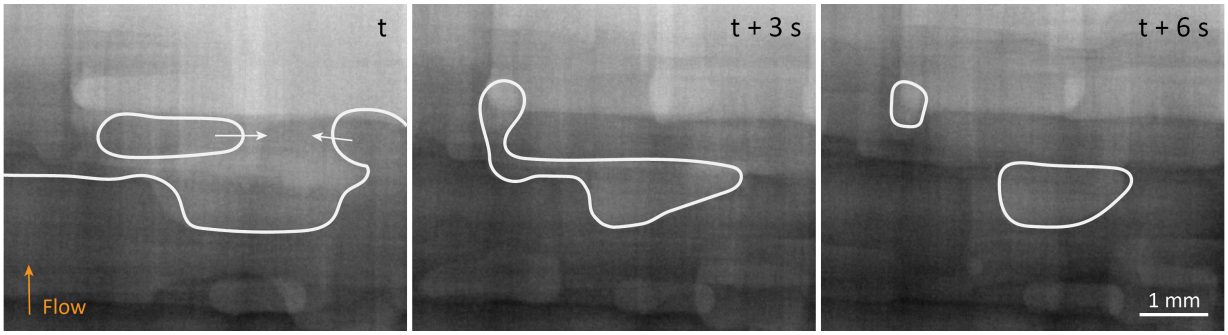

Figure 7.9: Example of snap-off and break up from three pictures taken at successive times (from test #5). The arrows at time t indicate the local flow direction.

7.3.4 Void motion phenomena

During the capillary dominated flows experiments, void motion (e.g. a change of void shape and size as well as void migration) was observed, in particular, with high frequency for the TW fabric and almost null for the two UD fabrics. An example of the different phenomena observed is presented in Fig. 7.10, in which the displacement of different bubbles has been tracked.

The evolution of pink, red and brown (1, 2 and 3 respectively) bubbles is illustrated just after their formation at the flow front; in this case, the void rearranges itself and shrinks to minimize the surface tension. The white (4) void undergoes a change of shape and size due to two consecutive splitting occurrences. Given its position and shape, this bubble seems to be not very stable, and the vertical fraction of the bubble along the fluid direction exerts a pressure on the bubbles that promotes the deformation and then break up. The blue (5) and yellow (6) voids illustrate a vertical migration through the preform in the fluid direction which are displaced thanks to the increasing fluid pressure with time in the constant flow rate experiments [26]. The blue (5) one, reaches the flow front and disappears whereas the yellow (6) one stays entrapped probably due to a channel constriction as illustrated in Fig. 7.11. Similarly, the orange (7) void migrates over a small distance and interestingly in an opposite direction to the flow, it ends trapped with a different shape from the initial one. Finally, green (8) bubbles show the formation of several rather small bubbles that are positioned first side by side, and with time end up coalescing.

As a conclusion of this observation, several concomitant phenomena are observed during the same slow flow experiment, depending on the initial size of the bubble, its shape and location with respect to the transverse bundles.

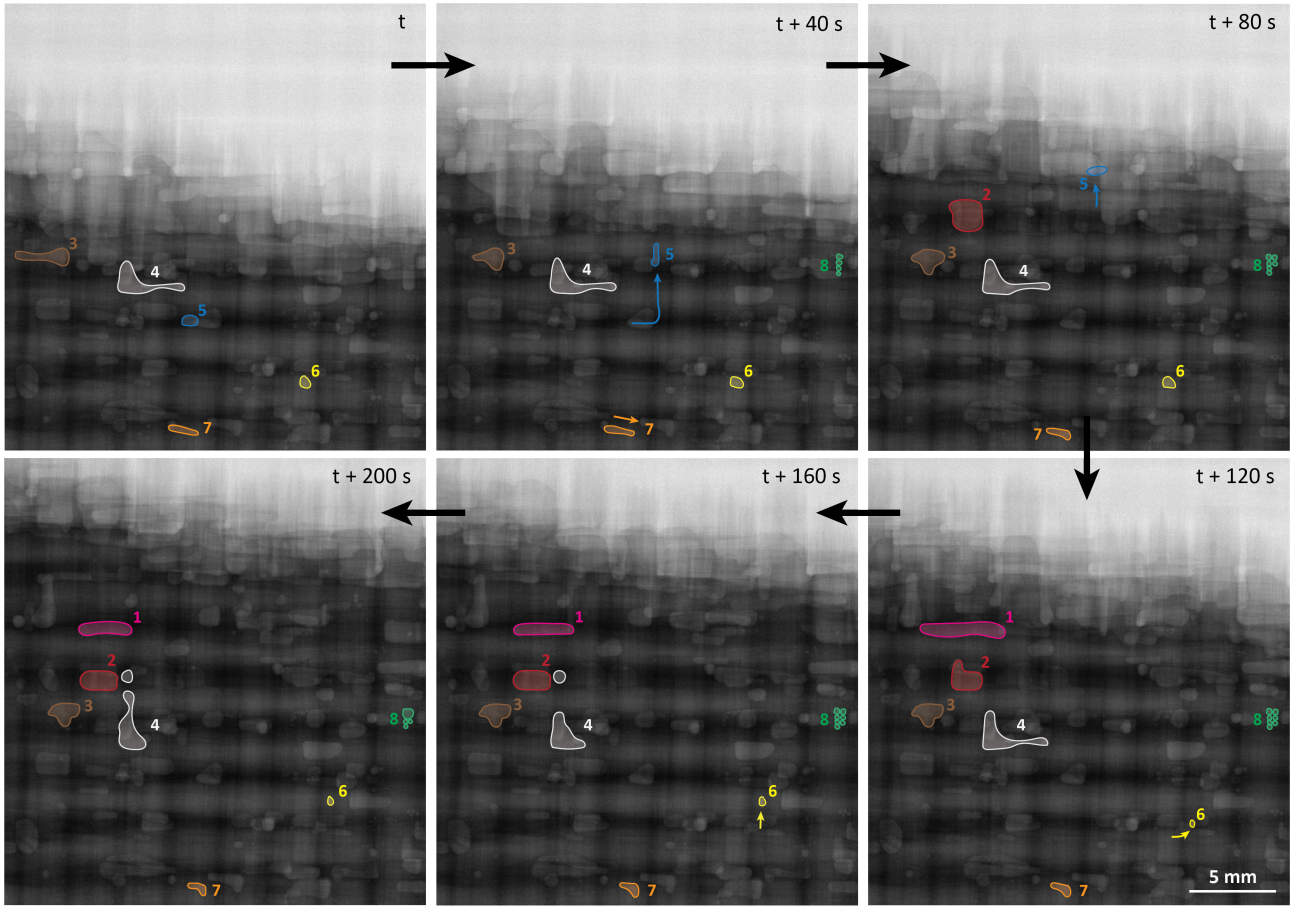

Figure 7.10: Void motion in the TW fabric under capillary dominated flows (from test #5).

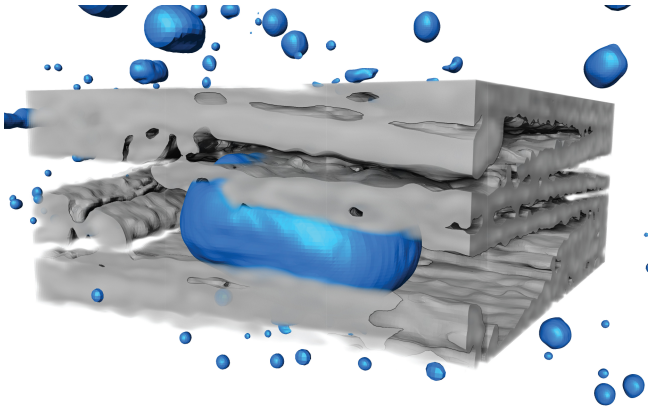

Figure 7.11: 3D view of an entrapped void in a channel constriction (from test #10).

7.3.5 Void morphology and location

The porosity was segmented from the 3D wet scans. For all cases of capillary driven impregnation, meso-voids with a volume higher than 0.007 mm^3 are presented in Fig. 7.12. For tests #3, #4, #5 and #10, the figures of meso-voids were combined with the 3D scans of the dry states, to illustrate their location and morphology within the pore space and are provided as movies in the link provided in the figure caption.

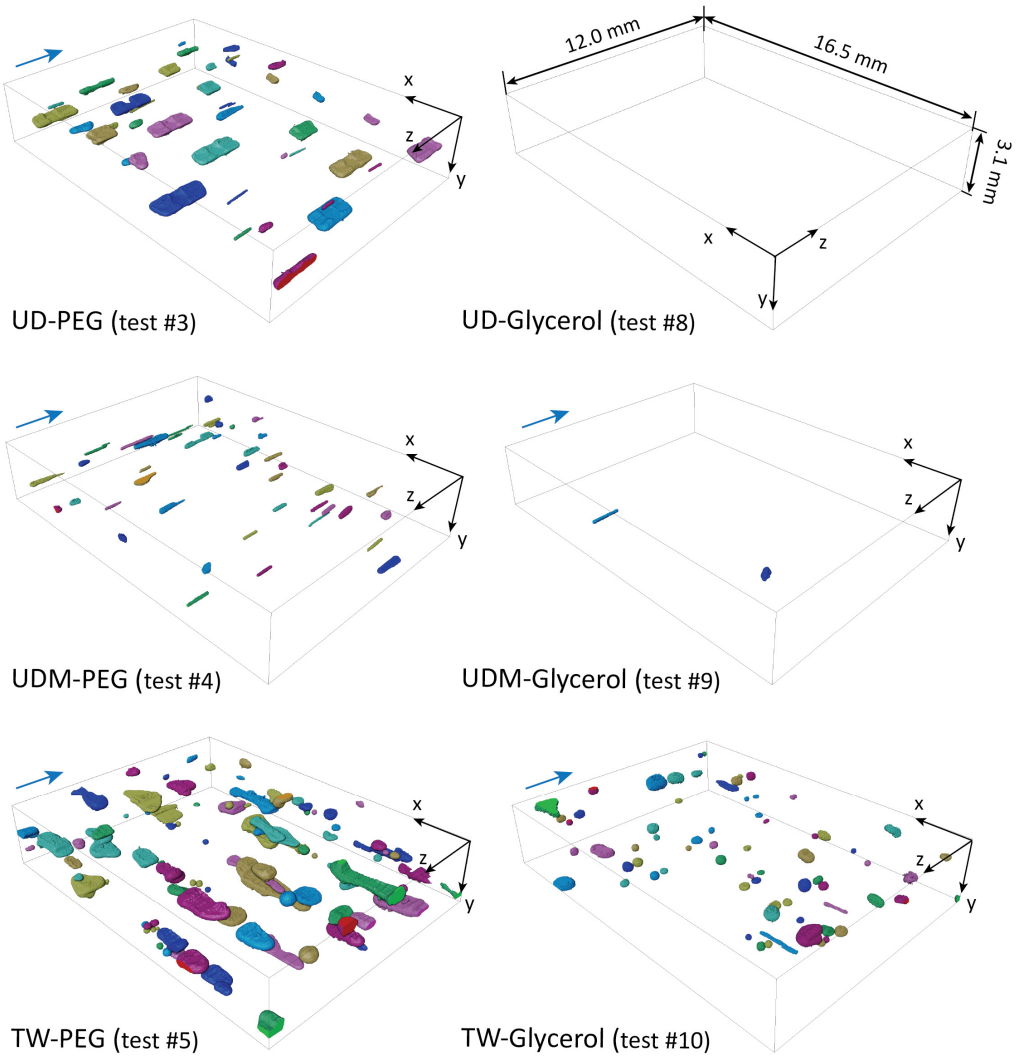

Figure 7.12: 3D volume rendering of meso-void distribution for capillary driven tests. The flow direction is indicated with the blue arrows. The colors were used to differentiate and label the voids. The videos are available online in Ref. [319].

From Fig. 7.12, it is clear that highly wetting conditions (PEG solution) were more prone to create meso-voids when compared to the impregnations carried out with the less wetting glycerol fluid. Comparing the UD-PEG and the UDM-PEG experiments, all voids were longitudinally aligned with the flow direction, with an obvious decrease of void content and size for the UDM. Comparing TW samples, the voids showed a different shape, very elongated in the very wetting case (test #5) and more spherical for the less wetting case (test #10) as expected given the different static contact an-

gles. For both experiments, the residual voids remained oriented perpendicular to the flow in between horizontal bundles showing that they mainly arise from the presence of these obstacles at 90°, and formed by air encirclement as shown in Fig. 7.9.

From the void analysis, it was found that meso-voids for the UD fabric (test #3), were suprisingly located in between two specific layers as shown in Fig. 7.13a; this was caused by the location and superposition of horizontal bundles. In particular, meso-voids were observed to be clamped by two glass bundles which created a channel constriction that promoted the snap-off events. This particular geometry resulted from a specific stacking of fabric layers that led to this pore configuration hindering the flow. To verify this, experiment #3 was repeated by varying the stack procedure (test #3bis), to specifically avoid the superposition of two glass bundles facing each other. The lower resulting void content is shown in Fig. 7.13b.

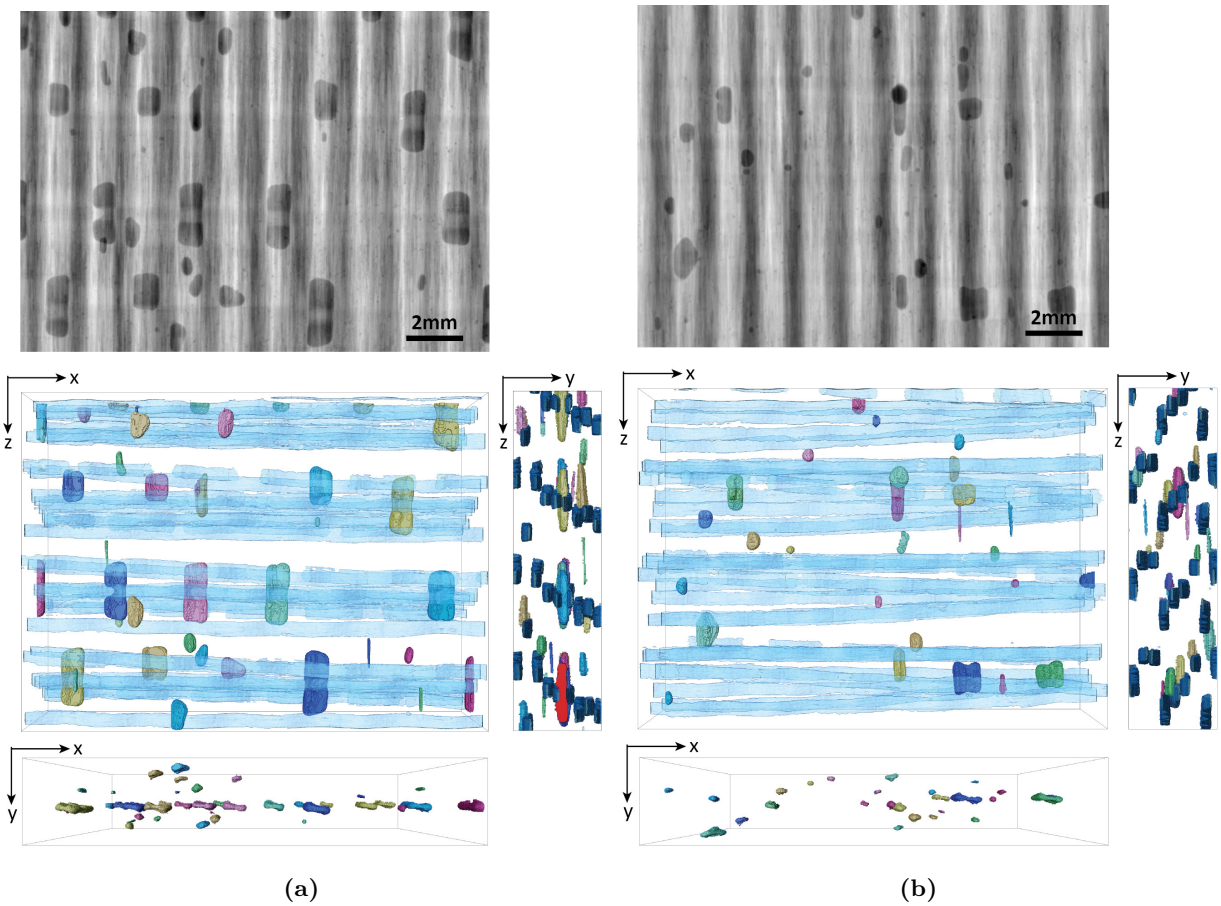

Figure 7.13: Meso-void location in two UD fabric layers stacking configurations, 2D mean projection from the 3D scan of the wet state and segmented meso-voids and glass bundles (in blue): results from (a) test #3 and (b) test #3bis.

This finding underlines the importance of studying flow displacements in real systems containing several layers, and the risks created by increased constrictions created by a very regular lay-up. Moreover, these results show the careful attention that should be paid in manual labor parts of composite

processing such as fabric stacking.

7.3.6 Relation between void content and unsaturated length

For experiments carried out with the UD fabric at different injection conditions (tests #1 to #3 and #6 to #8), the total void content extracted from the wet state 3D scans as well as the unsaturated length measured on the 2D impregnations are plotted as a function of the capillary number (Fig. 7.14). It should be noted that, even though the superficial velocity was very close for each pair of experiments, namely slow (tests #1 and #6), intermediate (tests #2 and #7) and fast (tests #3 and #8), the Ca differed significantly between fluid types (as expected given the different surface tension values between fluids). In both cases, a drop in unsaturated length is observed when flow is more balanced, however the trend of void fraction is not so clear. Nonetheless, what is clearly observed is that the nature of the fluid strongly affects the void content (Fig. 7.14, gray color).

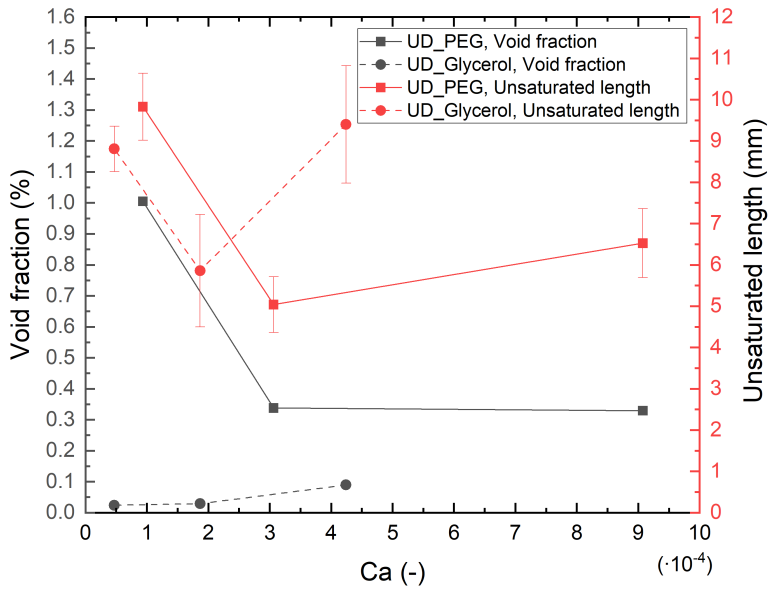

Figure 7.14: Void fraction and unsaturated length resulting from the UD fabric impregnation with PEG and glycerol-based fluids as a function of capillary number.

Overall, the void content is higher for all the experiments performed with the PEG-based liquid. In particular, this liquid led to an increased number of micro-voids in the impregnated preforms for all conditions, with a baseline amount around 0.3%. In addition, impregnation with PEG solution led to an increased void content for the low-speed case due to the formation of meso-voids, whereas intermediate and viscous flow cases led to a similar void content. For the fastest flow (test #3), the viscous fingering was indeed not prominent, the flow displacement being thus classified as a rather low drainage or even cross-flow pattern. For impregnation with the glycerol solution, the number of voids is very low for both slow and intermediate speeds and voids start to appear when the velocity is increased, in the form of micro-voids due to the pronounced viscous fingering and delayed flow in the

tows. As already observed optically in pristine and fluorine coated glass fabrics by Yoshiara et al. [60], by increasing the static contact angle (in our case from PEG to glycerol), the meso-void formation is suppressed for small Ca.

A direct relation between the void content and the unsaturated length is not so simple to establish apart from the fact that the smallest unsaturated area corresponds to a reduced void content as flow speeds in inter- and intra-tow regions are close. Then, for both cases of slow impregnation (low Ca value), the unsaturated lengths were very similar (around 9.5 mm $\pm$ 1 mm), however, an increased void content was obtained with the PEG solution as a corner flow, stemming from its low surface tension enhanced the formation of meso-voids as already discussed. This shows the importance of pore-scale kinetics and its influence at Darcy's scale.

Similarly, the unsaturated length was plotted versus void content as a function of the capillary number for the UD, UDM and TW fabric impregnations, in Fig. 7.15.

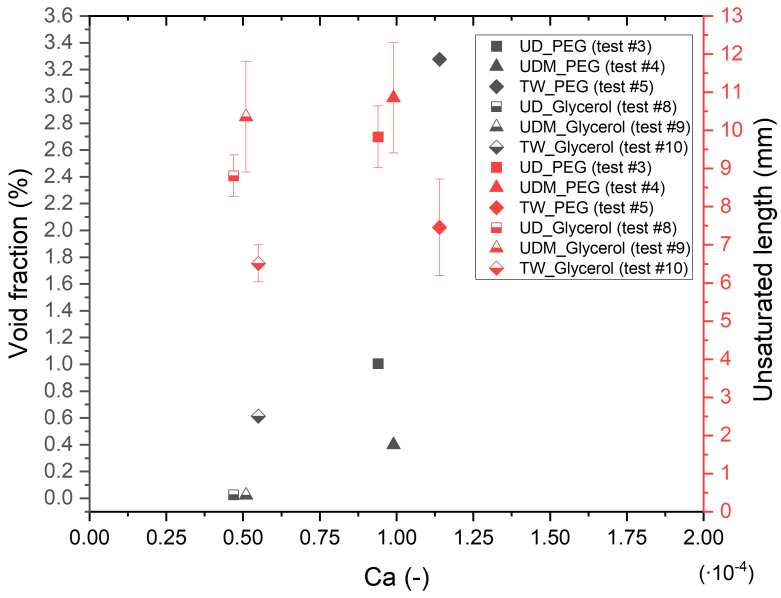

Figure 7.15: Void fraction and unsaturated length resulting from the UD, UDM and TW fabrics for capillary dominated flows impregnations with PEG and glycerol-based fluids as a function of capillary number.

With the aim of investigating the effect of the fabric geometry on the flow kinetics, a dimensionless number was defined for each fabric type to account for the crossover events describing potential obstacles to the flow. The bundle width (W) over the average distance between successive transverse yarns (D) was calculated as illustrated in Fig. 7.16. The ratio W/D gives a value between 0 and 1: if W/D is close to 0, the fabric is more unidirectional with thin horizontal bundles, and conversely, if W/D is close to 1, the fabric shows a bidirectional architecture with thick perpendicular bundles.

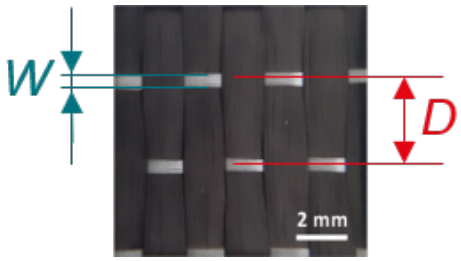

Figure 7.16: Example of inter-bundle distance (D) and bundle width (W) measurement on the UD fabric.

The inter-bundle distance (D) and bundle width (W) were measured on a fabric over an average of 15 measurements performed by a caliper and under an optical microscope respectively. The results are presented in Table 7.2 and the ratio W/D was plotted versus void content and unsaturated length in Fig. 7.17 (for an easier interpretation, the data projection was also plotted).

Table 7.2: Inter-bundle over bundle width results.

Fabric	D [mm]	W [mm]	W/D [-]
UD	3.37 ± 0.10	0.53 ± 0.03	0.16
UDM	10.07 ± 0.28	0.53 ± 0.03	0.05
TW	2.97 ± 0.42	2.37 ± 0.37	0.80

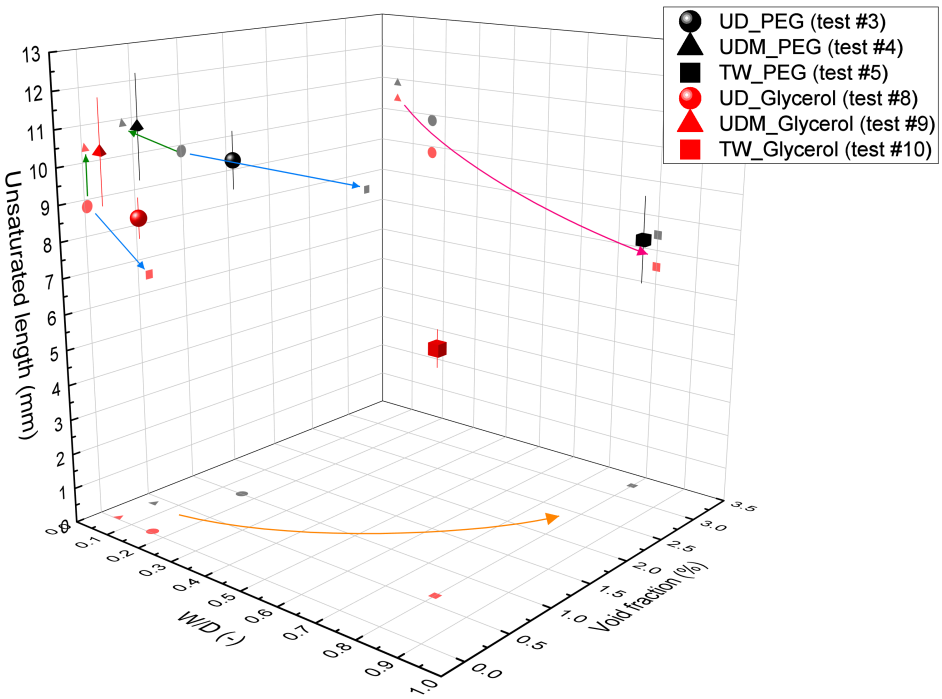

Figure 7.17: Unsaturated length versus void fraction and the W/D ratio for the low speed impregnation of the UD, UDM and TW fabrics.

Analyzing the unsaturated length versus void content, taking the UD fabric as reference (dots in Fig. 7.17), when the preferential bundle direction was increased by removing some horizontal stitches (UDM), less voids were entrapped, and a larger unsaturated length and standard deviation is observed on account of the larger space between horizontal bundles (Fig. 7.17, green arrow). Thus, in a more unidirectional fabric (with fibers and tows aligned with the flow direction), even though the flow does not progress with the same speed in intra and inter-tow regions, few voids are created because the flow is not hampered by any obstacles such as transverse bundles or notable channel constrictions. Conversely, fiber bundles oriented with an angle to the flow direction triggered more voids and a smaller unsaturated area, as illustrated with the TW fabric (Fig. 7.17, blue arrow). In this case, horizontal bundles act as flow barriers, responsible for snap-off events and leveling the flow front thus reducing the unsaturated length. Hence, the results confirm that the topology of the porous medium plays a major role in governing flow and influencing void entrapment events and the extent of unsaturated pore space. It is thus observed that a larger unsaturated area is not strictly linked to an increased void content.

An increase of the W/D ratio results in a decrease of the unsaturated length (Fig. 7.17, pink arrow) and an increase of the void content (Fig. 7.17, orange arrow). This trend shows that thick bundle widths horizontal to the flow direction are determinant to the void formation mechanisms. By comparing values of Table 7.2, UD and TW fabrics have a similar inter-bundle width, but since the horizontal tow is thicker for the TW, this makes a higher obstacle and barrier for the flow which creates abrupt path changes (90° from the unidirectional flow direction to the horizontal tow), promoting the number of snap-off events. Moreover, increasing the number of horizontal bundles makes longitudinal tows to be wavier, influencing the nesting and having a direct effect on the meso-pore connection in between layers.

7.3.7 Pore network modelling

Owing to the fabric architecture impact on void entrapment events in particular for capillary driven flows, a pore network model, characterizing the connectivity and pores size, is applied to better describe the meso-pore space in 3D for preforms of tests #3 to #5 and #8 to #10. The statistical results for the different properties of the pore-network, namely the pore-body and pore-throat radii, the pore-throat length and pore network connectivity for all samples are presented in Table 7.3 [239, 320].

Similar results were obtained for the same fabric types (UD, UDM and TW) as expected. For this reason, only one example of pore network construction per fabric configuration is shown in Fig. 7.18 as well as the corresponding histograms of the pore-body and pore-throat radii and the pore-throat length distribution. The predominance of unidirectional throats is observed in both UD and UDM, while TW presents a grid type topological description of the medium, with several horizontal throats. The pore-body histogram is very similar for both UD and UDM samples, indicating that the pore size did not change much by modifying the fabric, whereas the twill configuration led to a higher mean

Table 7.3: Pore network model results.

Test #	Fabric/Fluid	Number of pores	Number of throats	Pore-body eq. radius [mm]	Pore-throat eq. radius [mm]	Pore-throat length [mm]	Coordination number
3	UD/PEG	763	1869	0.31 ± 0.11	0.11 ± 0.06	1.57 ± 0.89	4.91 ± 2.44
3bis	UD/PEG	712	1775	0.32 ± 0.10	0.11 ± 0.06	1.58 ± 0.87	4.99 ± 2.22
4	UDM/PEG	534	1208	0.31 ± 0.11	0.11 ± 0.07	2.11 ± 1.47	4.52 ± 2.01
5	TW/PEG	405	887	0.40 ± 0.14	0.15 ± 0.09	1.78 ± 0.77	4.38 ± 2.13
8	UD/Glycerol	896	2046	0.28 ± 0.09	0.10 ± 0.05	1.49 ± 0.89	3.57 ± 2.11
9	UDM/Glycerol	467	895	0.32 ± 0.10	0.11 ± 0.07	2.14 ± 1.33	3.83 ± 2.01
10	TW/Glycerol	399	902	0.40 ± 0.05	0.14 ± 0.08	1.80 ± 0.78	4.52 ± 1.15

value of pore-radius as well as a wider distribution. Then, the pore-throat distribution is very similar for the three fabrics but the pore-length differed, in particular, for the UDM fabric for which the throats were longer when compared to UD or TW fabrics.

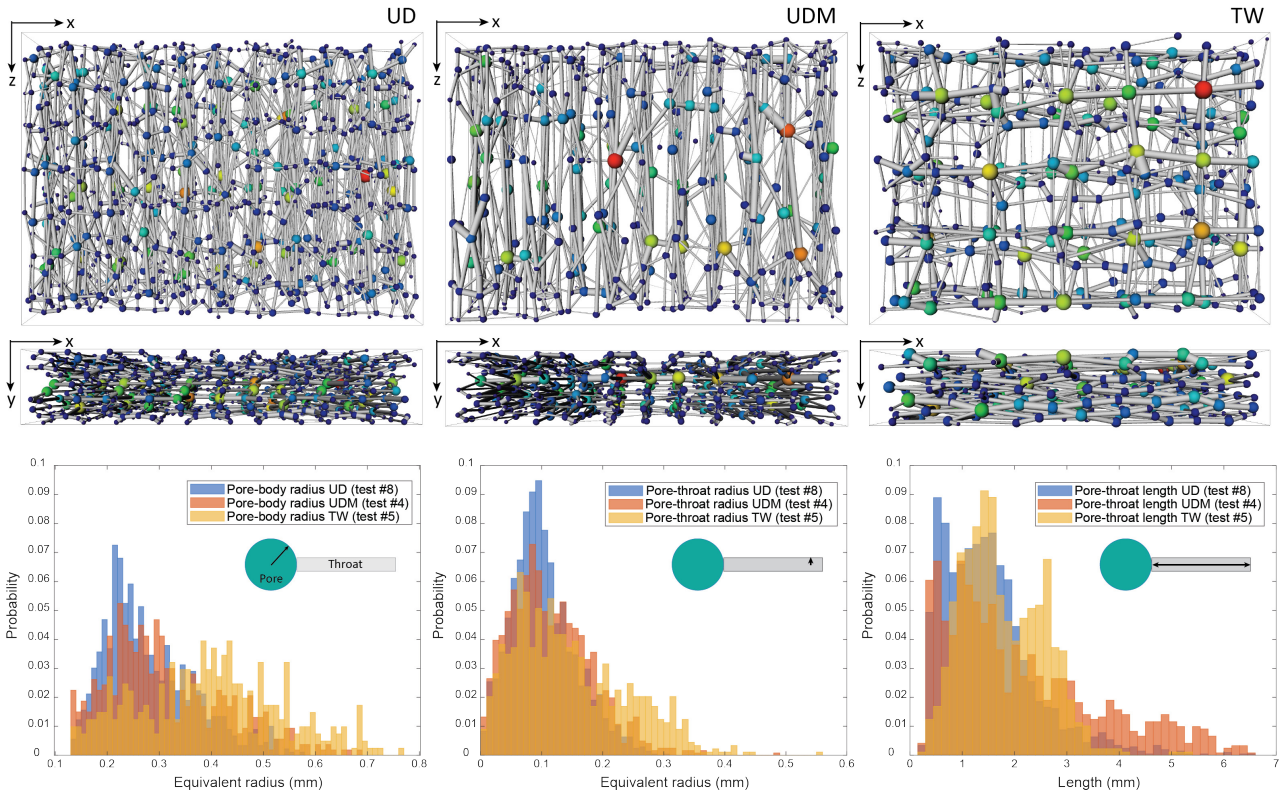

Figure 7.18: 3D views of the pore-network of the scanned fabrics (UD (test #8), UDM (test #4), TW (test #5) and corresponding histograms for the pore-body and pore-throat radii as well as pore-throat lengths. The pore bodies and pore throats are respectively rendered as colored spheres and gray cylinders that are smaller than their actual sizes to improve visualization. For both pores and throats, the size is related to the equivalent pore size (scale factor 0.5) and for the pores, the color distribution is in relation to the pore volume (from dark red corresponding to large pores and dark blue smaller pores).

The twill fabric has a pore size distribution that is shifted to the larger sizes, triggering a more heterogeneous pore architecture influencing the spatial scaling effects and increasing the probability of trapping events which is in line with our previous results. Conversely, UD and UDM show a more homogeneous architecture, resulting in less trapping as observed in the experiments and it is expected that this pore topology would facilitate the upscaling from pore description to macro flows in a modelling point of view. For the UD fabric, it is interesting to note that the pore radius is around 300 microns (pore body equivalent radius from the PNM, Table 7.18), whereas the distance between tows as observed from the surface is about 60 microns (measured from a micrograph). This indicates that the fabric meso-spaces are dominated by the spaces between layers, in regions where the glass stitches create locally more compressed tows.

Similarly to the descriptor W/D ratio in 2D, we explored to describe the 3D configuration in terms of crossover events. In particular, the quantitative analysis of the throat geometry and distribution illustrates the capacity of fluid transport into the pore network [321]. This is why, on one side, the throat volume was calculated, as the throat area times the throat length, since it will be proportional to the volumetric rate of fluid that the throats will drain and on the other side, the orientation of the throats with respect to the flow direction was measured by calculating the angle between the z-direction and each single throat in the xz plane. In Fig. 7.19, the 3D histogram of the throat volume and the resulting angle is plotted for each fabric type. Between the UD and UDM fabrics, the main orientation in the 0° is demonstrated by a wider distribution of throat volume close to the 0° for the UDM as expected. For these fabrics, above 20°, there is a more or less constant distribution of throat volumes. TW fabric with similar proportion of throat volume at 0° and 90° confirm the strong bi-directionality. Moreover, for this type of fabric there are really no throats oriented around 45°, when compared to the other fabrics, proving the abrupt corners that the flow will have to face.

The PNM proves to be an interesting approach to describe the meso-porosity of fibrous porous media with the aim of predicting fluid patterns and susceptible locations for void entrapment events. For example, according to literature [322], entrapped voids are located where body-to-throat ratios are rather large (in fact representing a pore constriction). In other words, the snap-off event occurs in narrow throats whereby a capillary instability splits the non-wetting phase which then retracts into the pore bodies and the void stays stable against further displacement. Interestingly, de Vries et al. [323] also employed pore-scale models to describe the multi-scale fluid transport in an aggregated dual porosity pore structure which can be inspiring to further use this type of descriptions for fibrous materials.

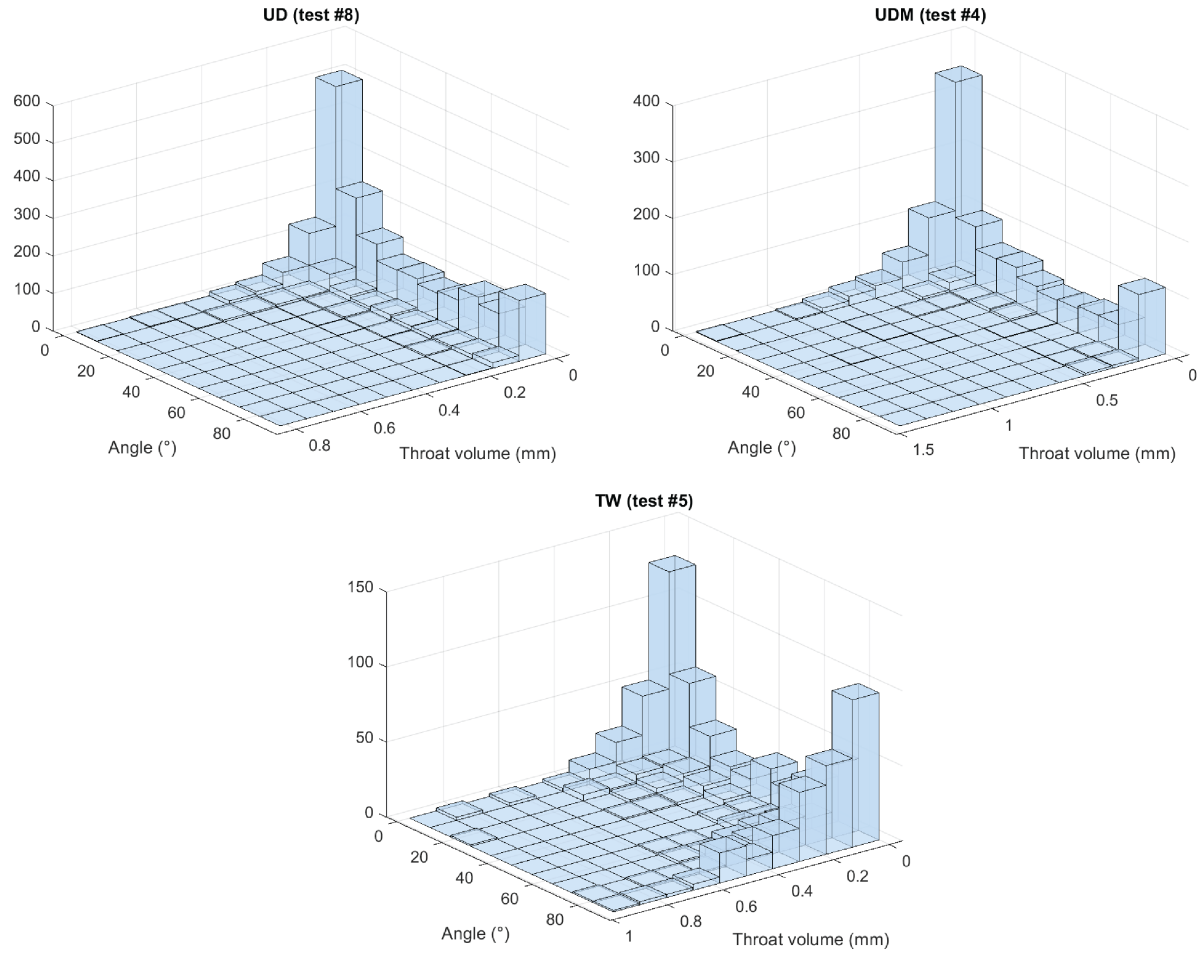

Figure 7.19: 3D histograms of the angle of throats with respect to the z-direction and the throat volume for UD, UDM and TW fabrics.

7.4 Conclusions

Although resin infiltration is controlled by the porous medium permeability, the infiltration speed and viscosity, according to Darcy's law, it is known that the wettability also plays an important role in multiphase flows since it controls the location and spatial distribution of flow patterns inside the porous media. In this study, we combined X-ray radiography and X-ray computed tomography to elucidate the link between dynamic fluid patterns, pore geometry and void entrapment mechanisms and proved the role of wettability in carbon fibrous preforms infiltration through experimental results enriched by advanced imaging techniques. In particular, we observed in-situ imbibition and drainage displacements in a UD fabric and imbibition displacements in a UD modified and a twill fabrics employing two liquids with different static contact angles.

Pore-scale displacements, observed by 2D scans, differed between drainage and imbibition. In drainage, a piston like displacement in the meso-pores located between the tows leads the flow and vertical viscous fingering is observed. In imbibition, though, where fluid displacement is very slow, the wettability was found to play a crucial role in the progression of the flow front and void entrapment mechanisms.

In particular, a very strong wetting system results in a strong corner fluid flow type triggering a less cooperative progressive flow front, enhancing the probability of snap-off events [324].

The 3D scan of the wet state allowed measurement of the void content and segmentation of the meso-porosity to investigate and compare the void morphology (highly influenced by the contact angle) and location in space. We were able to bring out that the UD fabric stack led to a particular porous morphology that influenced void entrapment in between 2 layers that present a specific pore configuration. Then, by comparing the void content for the capillary impregnations of the UD, UDM, and TW fabrics, the pore space configuration showed to significantly influence the amount of air trapping events. Moreover, it was found that bundles oriented perpendicular to the flow act as "obstacles" that can increase the probability for snap-off events as well as "stoppers" leveling off the flow and decreasing the unsaturated length. A dimensionless number was calculated in 2D in a single fabric layer to account for the bundle width over the inter-bundle distance. A pore network model (PNM) was in addition applied to the segmented 3D scans of the dry state, to better describe these three meso-pore architectures and two major geometrical parameters were found to affect capillary trapping: a wide pore (body and throat) size distribution together with and throat angle farther from the flow direction. The PNM approach could be further exploited to predict fluid patterns and susceptible locations for void entrapment events even though this would require a more localised analysis, and a higher resolution 3D scan to fully capture the intra-tow flow [322].

This work presents a complete methodology to assess fluid kinetics in fibrous porous media and leaves the door open to perform deeper analysis on the effect of wettability and pore geometry to void formation mechanisms. Next steps would be to determine how the Ca versus void content curve evolves as a function of the wettability and to further investigate the link between the fabric geometry and void entrapment mechanisms with the PNM approach by studying other fabric types for example (i.e. non-crimp or knitted fabrics among others) with the aim of quantitatively describing the optimal capillary number Ca_{opt}.

Chapter 8

Conclusions and perspectives

8.1 Conclusions

This study assesses the visualization of flow progression in fibrous reinforcements in particular for non-translucent fabrics by means of X-ray imaging with the aim of understanding and modelling the resin flow behavior in liquid composite molding processes.

In the first part, a novel tool was evaluated to observe in-situ the flow of a model fluid through translucent and non-translucent preforms. The tool is based on X-ray phase contrast imaging, which special feature resides in its high sensitivity to the small-angle scattering, thus elucidating features in low density materials but with enough microscale heterogeneities. Five different porous media were tested: a twill glass fabric, a unidirectional carbon fabric, a twill and a unidirectional flax fabrics and a 3D printed polymeric grid. We were able to successfully track the progressive saturation of the carbon preform at an acquisition time less than 10 s on a sample size window of 7 cm $\times$ 7 cm and the increased fluid/fabric contrast enabled us to extract the saturation curve $S(z,t)$ from the grayscale analysis. Then, we evaluated the main parameters affecting the contrast by comparing the different geometric configurations of different nature and we identified the main parameters affecting the contrast, which are the number of layers employed, the fiber diameters, the refraction properties of the material and the fabric structure. Carbon UD preforms resulted in the best contrast due to the small diameter of carbon fibers and their undirectional configuration in line with the gratings. Glass fabrics also gave a good contrast and were used for the method validation. The two flax fabrics provided less contrast given their larger diameter as well as lower refraction properties when compared to the previous fibers. Finally, this technique was not suitable for the polymeric structure, for which conventional absorption images were sufficient to depict the flow pattern.

Once the method was validated, we sought to evaluate the potential of X-ray phase contrast imaging to elucidate dual-scale flows. We found that scattering images did not lead to a very precise observation of capillary fingering, as the contrast between partially impregnated tows and inter-tow areas was very similar. Although it is possible to combine the different images obtained by X-ray phase contrast

imaging and highlight the different patterns, the pixel intensity analysis from those images could not be achieved with a simple mathematical operation (e.q. a mean value of the grayscale) to build the saturation curve. To overcome this, we conducted impregnations with a model fluid containing a ZnI_2 based contrasting solution and we succeeded in enhancing fluid/fabric contrast in conventional absorption images. We then depicted capillary and viscous dominated fluid paths in the UD carbon fabric with increased resolution and extrapolated the method to visualize flow through a twill carbon and UD and twill flax fabrics.

In light of these results, we carried out injections of the UD carbon fabric at different constant flow rates spanning from capillary to viscous driven flow patterns and extracted the respective dynamic saturation curves. A unidirectional two-phase flow model was developed in COMSOL and applied to numerically describe the infiltration for wetting and non-wetting systems. Then, experimental and numerical $S(z,t)$ curves were fitted using an optimization algorithm based on an heuristic computation allowing to determine the van Genuchten and Mualem's parameters β, N and L. Those permitted to extract the hydraulic functions $S(P_c)$ and $k_r(S)$ for each flow velocity. The relative permeability was found to be related to the capillary number and the shape of the permeability versus saturation curve differed between drainage and imbibition cases. This was attributed to the domination of flow in either intra- or inter-tow spaces: in drainage, a linear trend was observed since the flow dominates in the meso-pores and the relative permeability is thus defined as $k_r = S$ whereas in imbibition, the function is defined by a concave shape, showing a greater flow restriction when the saturation takes place first in the bundles, which have themselves a low permeability. Then, a simple correlation was made between the multiscale flow description of the capillary pressure $S(P_c)$ and the slug-flow assumption enabling to build the dynamic contact angle and capillary pressure versus the capillary number from the progressive saturation analysis. Our results emphasized the validity and usefulness of the slug-flow assumption and gave new insights on the two-phase flow method.

To further investigate flow kinetics, an improved visualization method was proposed. We performed X-ray radiography for the 2D flow visualization at the faster rate of 2 images per second and pixel size of 15 µm and performed 3D tomographic images (with voxel size of 10 µm) of the initial dry and final wet states. The flow progression of two fluids with different surface tension into three carbon fabrics with different pore architectures was investigated. Flow patterns at the pore scale were found to differ for imbibition and drainage cases. Drainage was found to be dominated by a piston-like progression following a displacement pattern regulated by meso-pores whereas imbibition was led by a corner flow type in the tows. In imbibition, the wettability turned out to play a major role in the progression of the flow front and void entrapment mechanisms and a very strong wetting system resulted in a less cooperative progressive flow front, enhancing the probability of snap-off events. Then, the fabric geometry, described by means of a pore network model (PNM), also proved to play an important role in controlling the fluid displacement and void formation. More precisely, two main parameters were highlighted: a wide pore (body and throat) size distribution together with an orientation of the pore throats making a large angle with the flow direction increased the probability of snap-off events and

reduced the unsaturated length (for capillary dominated flows).

In summary, the following statements can be made:

1. X-ray phase contrast imaging is a powerful and versatile technique to observe fluid flow at a real processing scale in translucent and non-translucent preforms even with conventional resins. Even though dual-scale patterns can be discerned with this method, they do not clearly appear in scattering images in particular cases such as capillary driven flows which impedes the grays scale image analysis to build the saturation curve.

2. Conventional X-ray radiography appears to be an interesting alternative since it can bring enough resolution and detail to depict capillary and viscous flows and even void entrapment mechanisms, although contrasting agents should be added to the infiltrating fluid, limiting the use of resins. Zinc iodide, though, proved to be very suitable as X-ray attenuating element as it can be easily mixed to water based model fluids and even with epoxy mixed to alcohol based solutions.

3. A two-phase flow model can be used to describe and model resin flow infiltration in fibrous preforms for wetting and non-wetting cases. By fitting experimental progressive saturation curves $S(z,t)$, obtained from the 2D thickness averaged X-ray images to simulation data with a heuristic algorithm, it is possible to extract the hydraulic descriptions $k_r(S)$ and $S(P_c)$ per system and impregnation condition.

4. The capillary pressure extracted with the two-phase flow model reveal to be in good agreement with the definition of the capillary pressure from the slug-flow assumption and could be also used to describe the dynamic $P_c(Ca)$ and $\theta(Ca)$ curves.

5. To gain a better insight on the effect of dynamic flow displacements and void formation mechanisms as well as their relation to the fabric preform geometry and topology, X-ray radiography can be coupled to 3D XCT scans to assess pre- and post-impregnation states.

6. Pore network models (PNM) were found to be a well adapted method to describe the meso-pore space geometry and topology of fibrous porous media.

7. Infiltrating a textile preform with a strongly wetting fluid results in a rather non-cooperative flow that enhances snap-off events triggering entrapped meso-voids, in the case of capillary driven flows.

8. The pore space geometry plays an important role on fluid displacement and void entrapment mechanisms. It was found that bundles oriented perpendicular to the flow act as "obstacles" that can increase the probability for snap-off events as well as "stoppers" leveling off the flow and decreasing the unsaturated length.

8.2 Perspectives

8.2.1 Flow kinetics in porous media

In the current work, we developed a two-phase flow model approach to describe the hydraulic properties of an impregnated porous media from the experimental progressive saturation curves $S(z,t)$. The interest of multiphase flow models is that they are massively employed in many engineering branches and have witnessed an extensive literature dedication. Researchers though seldom extrapolated this method to describe liquid composite processes mainly because of the strong dual-scale poral space of textile preforms. A requirement of the developed method is to know in advance the fluid wetting behavior, either wetting or non-wetting which was assimilated to capillary or viscous driven flows respectively and was determined visually. As a result, the proposed approach relies on an optical and subjective evaluation of the flow and besides, this choice is sometimes not so trivial to make. In addition, this can also be limiting when describing constant pressure driven cases in which the wettability can switch from non-wetting to wetting. An improvement of the numerical description should be thus made, for example, by building a single two-phase flow model in which the dynamic wettability can be defined as separate variable and does not need to be determined visually. In literature, researchers also faced the same challenge and started to develop descriptions of $S(P_c)$ taking into account the wettability which could be inspiring for our case [279].

Additionally, we presented a complete methodology to assess fluid kinetics in fibrous porous media and we leave the door open to perform deeper analysis on the effect of wettability and pore geometry to void formation mechanisms. Since the developed model was only carried out for a single type of fabric, with a given V_f, it would be interesting to run the model and find the different hydraulic properties for a given system with some variations and set how $k_r(S)$ and $S(P_c)$ vary with a change of wettability, change of V_f, change of fabric type as well as the effect of those parameters on the Ca versus void content curve.

We hope that our research will serve as a base for future studies on flow kinetics in the frame of LCM processes and could be extended to more complex systems such as: multifunctional composites including third phases (for which 3D tomographic scans will allow to assess the degree of filtration or movement of the third phase with the flow for example); hybrid preforms with different fiber nature compositions; or plant based fiber preforms (for which it is expected that swelling and absorption will highly influence the hydraulic properties). In particular, for experiments with natural fibers, we can take advantage of the formulated fluids with contrasting agents (PEG, glycerol and epoxy based solutions), that contain different water contents and could be used to analyze the dimensional changes of the fabrics and fibers during infiltration.

8.2.2 Imaging method

X-ray techniques proved to be very powerful to observe in-situ the flow progression through fibrous preforms. Although X-ray phase contrast imaging could be used for low density carbon fabrics and with conventional resins the spatial and temporal resolution were slightly limiting when accurate dual-scale flows are targeted. X-ray conventional radiography allows to overcome these hurdles and to depict the 3D porous geometry by tomographic reconstructions. It should be noted, that in the frame of this thesis relatively fast 3D scans were performed (30 min) but if required, the resolution can be enhanced by increasing the number of acquired images as well as the voxel size to assess the effects of flow at a smaller scale (the employed X-ray machine can perform scans up to a voxel size of 0.4 μm). Similarly, the voxel size can be also be reduced for 2D scans to visualize micro-flows and the scanning time can be lowered to capture fast flow trajectories (the employed X-ray machine can perform acquisitions up to 9 fps). However, the main inconvenient of the presented approach is that contrasting agents should be added to the fluid that would change its physical properties, thus limiting to observe real impregnation cases.

Even though the design and development of visualization techniques is still challenging, our results were very encouraging and further work is required to validate them by performing infiltration experiments in 4D (3D image + real time) in a synchrotron beamline [325–327]. A large infrastructure is however needed in this case with high X-ray source energies to perform very fast scans but in return enables to capture flow dynamics in-situ in the 3D space to identify fluid transport processes at the pore scale as well as void formation and motion mechanisms with an outstanding resolution. Encouragingly, this method has already been employed to observe multiphase flow in geoscience for example to investigate the effect of flow dynamics on spatially and temporally heterogeneous pore networks [328].

Another alternative would be to employ neutron imaging which has similar spatial and temporal resolution when compared to X-ray imaging [329], with the particularity that neutron interaction with hydrogen is very high due to the increased scattering probability as shown in Fig 8.1. For instance, a 1 cm thick layer of water is almost opaque when imaged with this technique [330]. In literature, some researchers already reported the observation of two-phase flow fluid distribution in porous media such as sandstone, rocks, concrete and porous asphalt by neutron imaging [331–334]. In the case of composite materials, this technique will allow to even observe impregnation with conventional fabrics and resins through metal closed molds and asses final filling stated by performing 3D tomographic reconstructions.

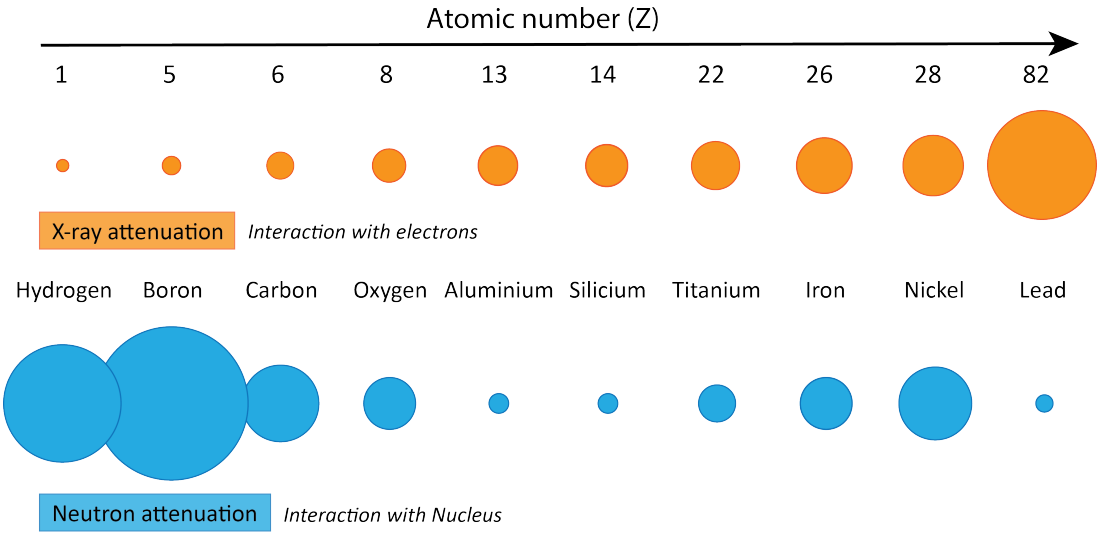

Figure 8.1: Comparison between X-ray and neutron attenuation, adapted from [330, 331, 335].

Chapter 9

Annexes

9.1 Annexes - Materials and Methods

9.1.1 Infiltrating liquids

An extra fluid epoxy-based (without hardener) was developed with similar properties, in particular, viscosity and X-ray attenuation, to those of the PEG and glycerol based solutions containing ZnI_2. The composition of the mix was: 20 wt.% of epoxy resin Sika Biresin TD150, 58 wt.% of alcohol benzyl (99.8%, $M_w = 108.14$, Honeywell) and 22 wt.% ZnI_2 ($M_w = 319.19$, Fluorochem). The alcohol benzyl was used to decrease the epoxy viscosity, initially of 0.5 Pa $\cdot$ s. In order to get an homogeneous mix, the ZnI_2 was previously mix to the alcohol benzyl before adding the epoxy.

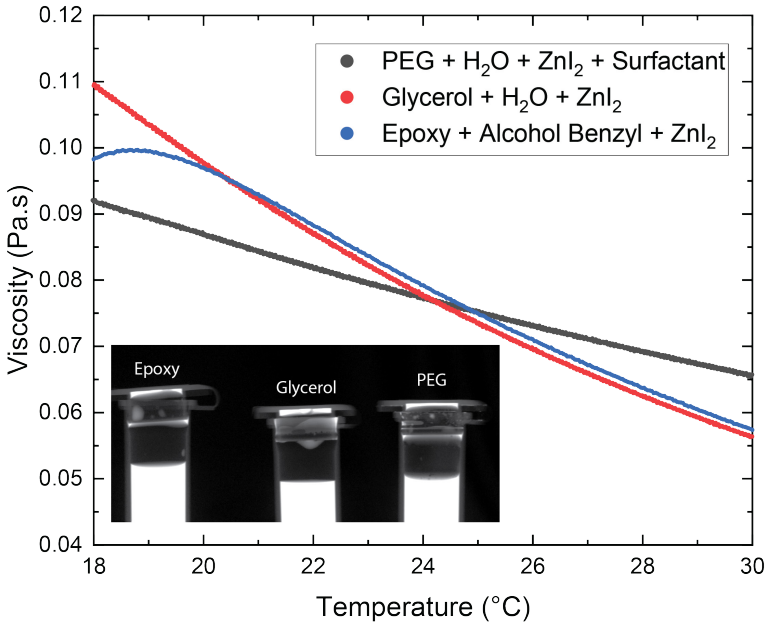

Figure 9.1: Viscosity-temperature curve of the designed fluids and their X-ray attenuation.

In Fig. 9.1 are shown the visocsity-temperature dependence curves for the different fluids containing contrasting agents designed as well as the evaluation of the X-ray attenuation. The intensity of the signal was assessed by comparing the histograms of each liquid contained in the small test-tube of same volume. The density of the mixture was measured to be 1.276 g/ml and the surface tension in air 36.2 mN/m.

9.2 Annexes - Modelling of dynamic fluid saturation in carbon reinforcements

9.2.1 Optimization procedure to find β, L and N

To explore the relationship between the different fitting parameters, the error E between experimental and numerical data for several combinations of , L and N was calculated. A 2D matrix plot was built to visualize at once the screening results of the fitting parameters combinations and the respecting error, $E_{\beta,L,N}$. Per experiment, the difference D between each error $E_{\beta,L,N}$ and the minimum error E_{min} was calculated and values up to the 100% are plotted in Fig. 9.2:

$$D = \frac{E_{\beta,L,N} - E_{min}}{E_{min}} \cdot 100 \tag{9.1}$$

Since β, N and L are shape parameters, for experimental curves which are less self-similar (concept explained in Fig. 9.3), namely for tests #1 and #4 which have less stable flow fronts over time, a large number of parameter combinations gave a small error when compared to results for curves in tests #2 and #3. In order to reduce this "self-similarity effect" on the parameters' search, another approach to the curve fitting method could be to build a master curve that would be the average from all the measured curves. Nevertheless, tests #2 and #3 still gave different parameter combinations leading to a very small error, which can even be increased by enlarging the research domain, proving the high sensitivity of the model to these parameters which leads to a non-unique solution for the description of hydraulic curves. In literature this is well known, and researchers propose to carry out statistical analysis to better establish porous media characteristics [336, 337]. Moreover, the inferred distributions of the different pairs of parameters show a strong correlation between β and L for the wetting cases and between β and N for the non-wetting cases. The parameters β and N exhibit a power-law like relationship that has also been observed in literature [336, 337].

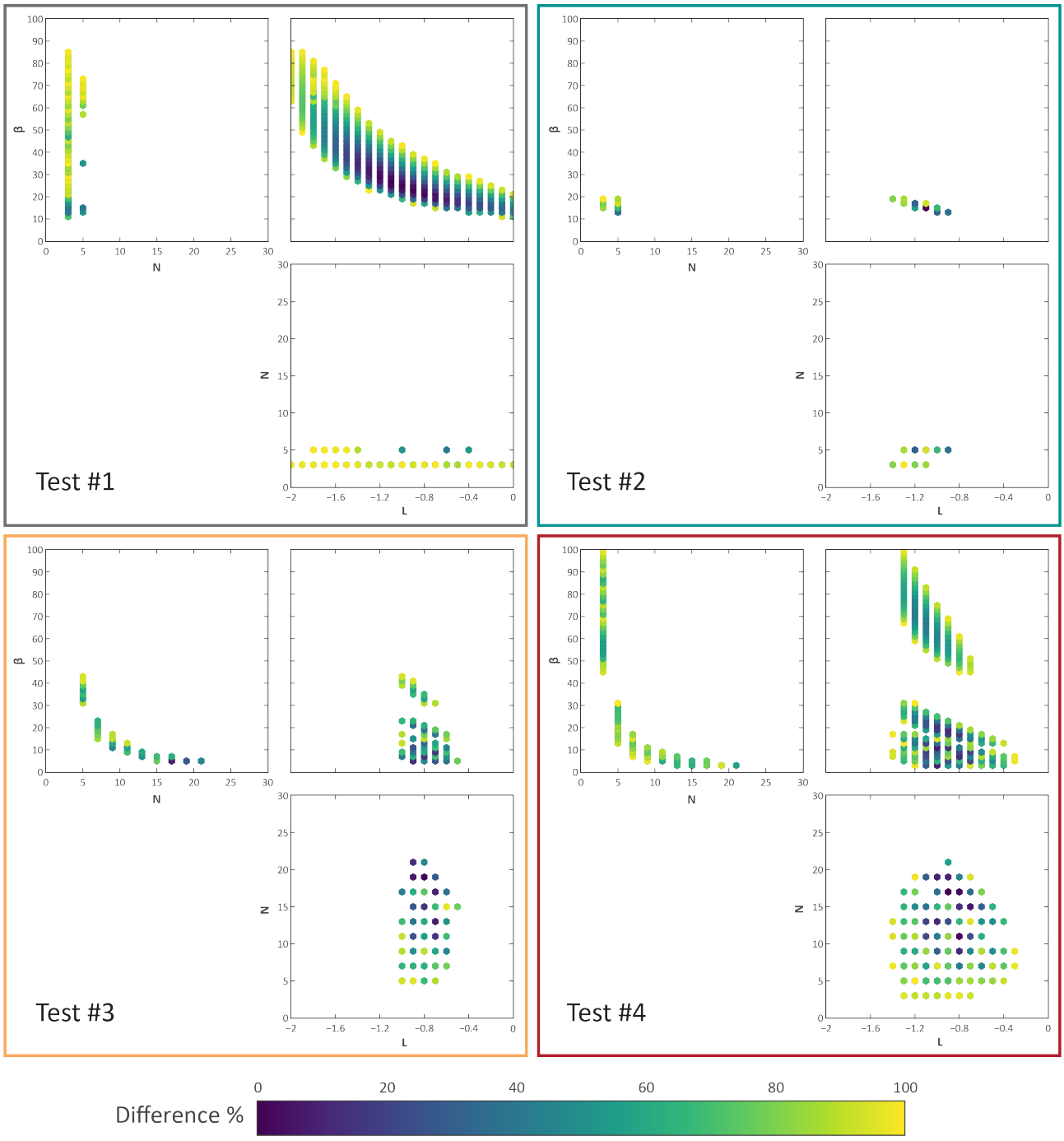

Figure 9.2: Scatter plot matrix of the minimal error difference as a function of β, L and N fitting parameters.

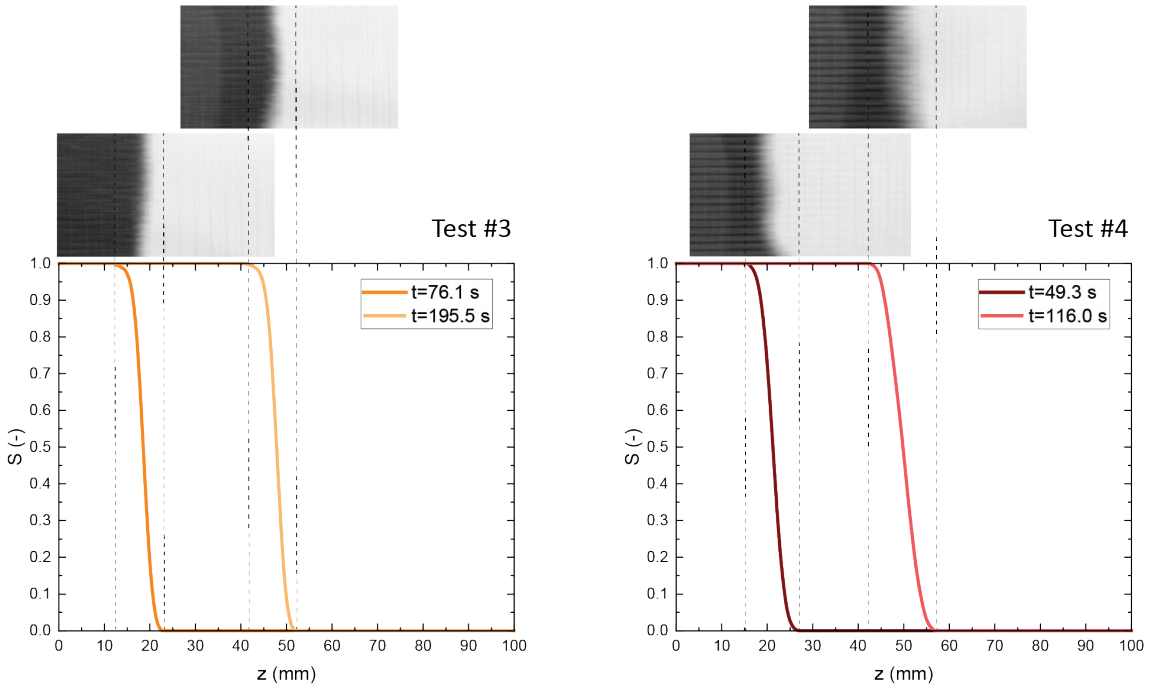

Figure 9.3: Example of saturation curves for test #3, showing self-similar curves and test #4 with curves with more different shapes over time.

Bibliography

[1] Amaël Cohades, Nathan Hostettler, Malvina Pauchard, Christopher J.G. Plummer, and Véronique Michaud. Stitched shape memory alloy wires enhance damage recovery in self-healing fibre-reinforced polymer composites. *Composites Science and Technology*, 161:22–31, 2018. ISSN 02663538. doi: 10.1016/j.compscitech.2018.03.040.

[2] Amaël Cohades, Callum Branfoot, Steven Rae, Ian Bond, and Véronique Michaud. Progress in self-healing fiber-reinforced polymer composites. *Advanced Materials Interfaces*, 5(17):1800177, 2018. ISSN 21967350. doi: 10.1557/mrs2008.164.

[3] J. Fan and J. Njuguna. An Introduction to Lightweight Composite Materials and Their Use in Transport Structures. In *Lightweight Composite Structures in Transport: Design, Manufacturing, Analysis and Performance*, pages 3–34. Elsevier Inc., 2 2016. ISBN 9781782423430. doi: 10.1016/B978-1-78242-325-6.00001-3.

[4] João M. P. Q. Delgado, Antonio Gilson Barbosa De Lima, Mariana Julie, and Nascimento Santos. *Transport Phenomena in Liquid Composite Molding Processes*. SpringerBriefs in Applied Sciencesand Technology, Cham, Switzerland, 2019. ISBN 978-3-030-12715-2. doi: https://doi.org/10.1007/978-3-030-12716-9.

[5] Spiridon Konstantopoulos, Christian Hueber, Ioannis Antoniadis, John Summerscales, and Ralf Schledjewski. Liquid composite molding reproducibility in real-world production of fiber reinforced polymeric composites: a review of challenges and solutions. *Advanced Manufacturing: Polymer and Composites Science*, 5(3):85–99, 7 2019. ISSN 20550359. doi: 10.1080/20550340.2019.1635778.

[6] Véronique Michaud and Andreas Mortensen. Infiltration processing of fibre reinforced composites : governing phenomena. *Composites Part A: Applied Science and Manufacturing*, 32(8):981–996, 2001. ISSN 1359-835X. doi: 10.1016/S1359-835X(01)00015-X.

[7] Véronique Michaud. A review of non-saturated resin flow in liquid composite moulding processes. *Transport in Porous Media*, 115(3):581–601, 2016. ISSN 15731634. doi: 10.1007/s11242-016-0629-7.

[8] Helena Teixidó, Jeroen Staal, Baris Caglar, and Véronique Michaud. Capillary effects in fiber reinforced polymer composite processing : A review. *Frontiers in Materials*, 9:809226, 2022. ISSN 2296-8016. doi: 10.3389/fmats.2022.809226.

[9] Aliakbar Gholampour and Togay Ozbakkaloglu. A review of natural fiber composites: properties, modification and processing techniques, characterization, applications. *Journal of Materials Science*, 55:829–892, 1 2020. ISSN 15734803. doi: 10.1007/s10853-019-03990-y.

[10] François Boussu, Irina Cristian, and Saad Nauman. General definition of 3D warp interlock fabric architecture. *Composites Part B: Engineering*, 81:171–188, 2015. ISSN 13598368. doi: 10.1016/j.compositesb.2015.07.013.

[11] Abdul Moudood, Anisur Rahman, Andreas Öchsner, Mainul Islam, and Gaston Francucci. Flax fiber and its composites: An overview of water and moisture absorption impact on their performance. *Journal of Reinforced Plastics and Composites*, 38(7):323–339, 2019. ISSN 15307964. doi: 10.1177/0731684418818893.

[12] Jinchun Zhu, Huijun Zhu, James Njuguna, and Hrushikesh Abhyankar. Recent development of flax fibres and their reinforced composites based on different polymeric matrices. *Materials*, 6(11):5171–5198, 2013. ISSN 19961944. doi: 10.3390/ma6115171.

[13] Heura Ventura, Josep Claramunt, Antonio Navarro, Miguel A Rodriguez-Perez, and Monica Ardanuy. Effects of Wet / Dry-Cycling and Plasma Treatments on the Properties of Flax Nonwovens Intended for Composite Reinforcing. *Materials*, 9(2):93, 2016. ISSN 19961944. doi: 10.3390/ma9020093.

[14] E. Sinha and S. Panigrahi. Effect of plasma treatment on structure, wettability of jute fiber and flexural strength of its composite. *Journal of Composite Materials*, 43(17):1791–1802, 2009. ISSN 00219983. doi: 10.1177/0021998309338078.

[15] B. Koohestani, A. K. Darban, P. Mokhtari, E. Yilmaz, and E. Darezereshki. Comparison of different natural fiber treatments: a literature review. *International Journal of Environmental Science and Technology*, 16(1):629–642, 2019. ISSN 17352630. doi: 10.1007/s13762-018-1890-9.

[16] Maria Carolina Seghini, Fabienne Touchard, Fabrizio Sarasini, Laurence Chocinski-Arnault, Jacopo Tirillò, Maria Paola Bracciale, Milan Zvonek, and Vladimir Cech. Effects of oxygen and tetravinylsilane plasma treatments on mechanical and interfacial properties of flax yarns in thermoset matrix composites. *Cellulose*, 27(1):511–530, 2020. ISSN 1572882X. doi: 10.1007/s10570-019-02785-3.

[17] Delphin Pantaloni, Alain Bourmaud, Christophe Baley, Mike J. Clifford, Michael H. Ramage, and Darshil U. Shah. A review of permeability and flow simulation for liquid composite moulding of plant fibre composites. *Materials*, 13(21):1–23, 11 2020. ISSN 19961944. doi: 10.3390/ma13214811.

[18] Alessia Melelli, Olivier Arnould, Johnny Beaugrand, and Alain Bourmaud. The middle lamella of plant fibers used as composite reinforcement: Investigation by atomic force microscopy. *Molecules*, 25(3), 2 2020. ISSN 14203049. doi: 10.3390/molecules25030632.

[19] B. Ravishankar, Sanjay K. Nayak, and M. Abdul Kader. Hybrid composites for automotive applications – A review. *Journal of Reinforced Plastics and Composites*, 38(18):835–845, 2019. ISSN 15307964. doi: 10.1177/0731684419849708.

[20] Christophe Binetruy and Véronique Michaud. Emerging, hybrid & smart composites. *Functional Composite Materials*, 2(1), 2021. ISSN 2522-5774. doi: 10.1186/s42252-021-00028-y.

[21] Jagath Narayana and Ramesh Gupta. A review of recent research on multifunctional composite materials and structures with their applications. *Materials Today: Proceedings*, 5(2):5580–5590, 2018. ISSN 2214-7853. doi: 10.1016/j.matpr.2017.12.149.

[22] J. Verrey, M. D. Wakeman, V. Michaud, and J.-A. E. Månson. Manufacturing cost comparison of thermoplastic and thermoset RTM for an automotive floor pan. *Composites Part A: Applied Science and Manufacturing*, 37:9–22, 2006. ISSN 1359-835. doi: 10.1016/j.compositesa.2005.05.048.

[23] L. Zingraff, V. Michaud, P. E. Bourban, and J.-A. E. Månson. Resin transfer moulding of anionically polymerised polyamide 12. *Composites Part A: Applied Science and Manufacturing*, 36(12):1675–1686, 2005. ISSN 1359835X. doi: 10.1016/j.compositesa.2005.03.023.

[24] Colin Gomez, Damiano Salvatori, Baris Caglar, Robin Trigueira, Gilles Orange, and Véronique Michaud. Resin transfer molding of high-fluidity polyamide-6 with modified glass-fabric preforms. *Composites Part A: Applied Science and Manufacturing*, 147, 2021. ISSN 1359835X. doi: 10.1016/j.compositesa.2021.106448.

[25] Paolo Ermanni, Claudio Di Fratta, and François Trochu. Molding: Liquid Composite Molding (LCM). In Luigi Nicolais, editor, *Wiley Encyclopedia of Composites*. John Wiley & Sons, Ltd, 2012. ISBN 9781118097298. doi: 10.1002/9781118097298.weoc153.

[26] Mahoor Mehdikhani, Larissa Gorbatikh, Ignaas Verpoest, and Stepan V. Lomov. Voids in fiber-reinforced polymer composites: A review on their formation, characteristics, and effects on mechanical performance. *Journal of Composite Materials*, 53(12):1579–1669, 2019. ISSN 1530793X. doi: 10.1177/0021998318772152.

[27] Y. K. Hamidi and M. C. Altan. Process induced defects in liquid molding processes of composites. *International Polymer Processing*, 32(5):527–544, 2017. ISSN 0930777X. doi: 10.3139/217.3444.

[28] Chung Hae Park and Woo Il Lee. Modeling void formation and unsaturated flow in liquid composite molding processes: A survey and review. *Journal of Reinforced Plastics and Composites*, 30(11):957–977, 2011. ISSN 07316844. doi: 10.1177/0731684411411338.

[29] Henry Darcy. *Les fontaines publiques de la ville de Dijon*. Paris, 1856.

[30] J. Wolfrath, V. Michaud, A. Modaressi, and J.-A. E. Månson. Unsaturated flow in compressible fibre preforms. *Composites Part A: Applied Science and Manufacturing*, 37:881–889, 2006. ISSN 1359835X. doi: 10.1016/j.compositesa.2005.01.008.

[31] Véronique Michaud. Permeability properties of reinforcements in composites. In *Composite Reinforcements for Optimum Performance*, chapter 14, pages 443–472. Woodhead Publishing Series in Composites Science and Engineering, second edition edition, 2021. doi: 10.1016/B978-0-12-819005-0.00014-9.

[32] Richard S. Parnas, Andrew J. Salem, Thomas A. K. Sadiq, Hsin-peng Wang, and Suresh G. Advani. The interaction between micro- and macro-scopic flow in RTM preforms. *Composite Structures*, 27(1-2):93–107, 1994. doi: 10.1016/0263-8223(94)90071-X.

[33] R. Arbter, J. M. Beraud, C. Binetruy, L. Bizet, J. Bréard, S. Comas-Cardona, C. Demaria, A. Endruweit, P. Ermanni, F. Gommer, S. Hasanovic, P. Henrat, F. Klunker, B. Laine, S. Lavanchy, S. V. Lomov, A. Long, V. Michaud, G. Morren, E. Ruiz, H. Sol, F. Trochu, B. Verleye, M. Wietgrefe, W. Wu, and G. Ziegmann. Experimental determination of the permeability of textiles: A benchmark exercise. *Composites Part A: Applied Science and Manufacturing*, 42(9):1157–1168, 2011. ISSN 1359835X. doi: 10.1016/j.compositesa.2011.04.021.

[34] N. Vernet, E. Ruiz, S. Advani, J. B. Alms, M. Aubert, M. Barburski, B. Barari, J. M. Beraud, D. C. Berg, N. Correia, M. Danzi, T. Delavière, M. Dickert, C. Di Fratta, A. Endruweit, P. Ermanni, G. Francucci, J. A. Garcia, A. George, C. Hahn, F. Klunker, S. V. Lomov, A. Long, B. Louis, J. Maldonado, R. Meier, V. Michaud, H. Perrin, K. Pillai, E. Rodriguez, F. Trochu, S. Verheyden, M. Weitgrefe, W. Xiong, S. Zaremba, and G. Ziegmann. Experimental determination of the permeability of engineering textiles: Benchmark II. *Composites Part A: Applied Science and Manufacturing*, 61:172–184, 2014. ISSN 1359835X. doi: 10.1016/j.compositesa.2014.02.010.

[35] D. May, A. Aktas, S. G. Advani, D. C. Berg, A. Endruweit, E. Fauster, S. V. Lomov, A. Long, P. Mitschang, S. Abaimov, D. Abliz, I. Akhatov, M. A. Ali, T. D. Allen, S. Bickerton, M. Bodaghi, B. Caglar, H. Caglar, A. Chiminelli, N. Correia, B. Cosson, M. Danzi, J. Dittmann, P. Ermanni, G. Francucci, A. George, V. Grishaev, M. Hancioglu, M. A. Kabachi, K. Kind, M. Deléglise-Lagardère, M. Laspalas, O. V. Lebedev, M. Lizaranzu, P.-J. Liotier, P. Middendorf, J. Morán, C.-H. Park, R. B. Pipes, M. F. Pucci, J. Raynal, E.S. Rodriguez, R. Schledjewski, R. Schubnel, N. Sharp, G. Sims, E. M. Sozer, P. Sousa, J. Thomas, R. Umer, W. Wijaya, B. Willenbacher, A. Yong, S. Zaremba, and G. Ziegmann. In-plane permeability characterization of engineering textiles based on radial flow experiments : A benchmark exercise. *Composites Part A: Applied Science and Manufacturing*, 121:100–114, 2019. ISSN 1359-835X. doi: 10.1016/j.compositesa.2019.03.006.

[36] T. S. Lundström. The permeability of non-crimp stitched fabrics. *Composites Part A: Applied Science and Manufacturing*, 31:1345–1353, 2000. doi: 10.1016/S1359-835X(00)00037-3.

[37] N. K. Naik, M. Sirisha, and A. Inani. Permeability characterization of polymer matrix composites by RTM / VARTM. *Progress in Aerospace Sciences*, 65:22–40, 2014. ISSN 0376-0421. doi: 10.1016/j.paerosci.2013.09.002. URL `http://dx.doi.org/10.1016/j.paerosci.2013.09.002`.

[38] M. Bodaghi, S. V. Lomov, P. Simacek, N. C. Correia, and S. G. Advani. On the variability of permeability induced by reinforcement distortions and dual scale flow in liquid composite moulding: A review. *Composites Part A: Applied Science and Manufacturing*, 120:188–210, 2019. ISSN 1359835X. doi: 10.1016/j.compositesa.2019.03.004.

[39] A. X. H. Yong, A. Aktas, D. May, A. Endruweit, S. Advani, P. Hubert, S. G. Abaimov, D. Abliz, I. Akhatov, M. A. Ali, T. Allen, D. C. Berg, S. Bickerton, C. Brauner, D. Brütsch, B. Caglar, H. Caglar, P. Causse, A. Chiminelli, A. Cohades, S. Comas-Cardona, M. Danzi, J. Dittmann, C. Dransfeld, P. Ermanni, E. Fauster, J. A. Garcia-Manrique, A. George, R. Graupner, V. Grishaev, A. Guilloux, M. Hancioglu, W. Harizi, T. Herman, W. Huang, M. A. Kabachi, A. Keller, K. Kind, M. Laspalas, O. V. Lebedev, M. Lizaranzu, A. C. Long, K. Masania, V. Michaud, P. Middendorf, D. Salvatori, R. Schubnel, N. Sharp, and M. Sozer. Out-of-plane permeability measurement for reinforcement textiles : A benchmark exercise. *Composites Part A: Applied Science and Manufacturing*, 148:106480, 2021. ISSN 1359-835X. doi: 10.1016/j.compositesa.2021.106480.

[40] Baris Caglar, Guillaume Broggi, Muhammad A. Ali, Laurent Orgéas, and Véronique Michaud. Deep learning accelerated prediction of the permeability of fibrous microstructures. *Composites Part A: Applied Science and Manufacturing*, 158:106973, 2022. ISSN 1359-835X. doi: 10.1016/j.compositesa.2022.106973.

[41] Elena Syerko, Christophe Binetruy, Sébastien Comas-cardona, and Adrien Leygue. A numerical approach to design dual-scale porosity composite reinforcements with enhanced permeability. 131:307–322, 2017. doi: 10.1016/j.matdes.2017.06.035.

[42] J. Verrey, V. Michaud, and J.-A. E. Månson. Dynamic capillary effects in liquid composite moulding with non-crimp fabrics. *Composites Part A: Applied Science and Manufacturing*, 37(1):92–102, 2006. ISSN 1359835X. doi: 10.1016/j.compositesa.2005.04.011.

[43] Viivi Koivu, Maxime Decain, Christian Geindreau, Keijo Mattila, Francis Bloch, and Markku Kataja. Transport properties of heterogeneous materials. Combining computerised X-ray micro-tomography and direct numerical simulations. *International Journal of Computational Fluid Dynamics*, 23(10):713–721, 2010. ISSN 1061-8562. doi: 10.1080/10618561003727512.

[44] Damiano Salvatori, Baris Caglar, Helena Teixidó, and Véronique Michaud. Permeability and capillary effects in a channel-wise non-crimp fabric. *Composites Part A: Applied Science and Manufacturing*, 108:41–52, 2018. ISSN 1359-835X. doi: 10.1016/j.compositesa.2018.02.015.

[45] Baris Caglar, Laurent Orgéas, Sabine Rolland du Roscoat, E. Murat Sozer, and Véronique Michaud. Permeability of textile fabrics with spherical inclusions. *Composites Part A: Applied Science and Manufacturing*, 99:1–14, 2017. ISSN 1359835X. doi: 10.1016/j.compositesa.2017.03.031.

[46] Min Li, Shaokai Wang, Yizhuo Gu, Zuoguang Zhang, Yanxia Li, and Kevin Potter. Dynamic capillary impact on longitudinal micro-flow in vacuum assisted impregnation and the unsaturated permeability of inner fiber tows. *Composites Science and Technology*, 70(11):1628–1636, 2010. ISSN 02663538. doi: 10.1016/j.compscitech.2010.06.004.

[47] Frank Gommer, Andreas Endruweit, and Andrew C. Long. Influence of the micro-structure on saturated transverse flow in fibre arrays. *Journal of Composite Materials*, 52(18):2463–2475, 2018. ISSN 1530793X. doi: 10.1177/0021998317747954.

[48] Silvio Facciotto, Pavel Simacek, Suresh G. Advani, and Peter Middendorf. Modeling of anisotropic dual scale flow in RTM using the finite elements method. *Composites Part B: Engineering*, 214:108735, 2021. ISSN 13598368. doi: 10.1016/j.compositesb.2021.108735.

[49] Maureen E. Foley and John W. Gillespie. Modeling the effect of fiber diameter and fiber bundle count on tow impregnation during liquid molding processes. *Journal of Composite Materials*, 39(12):1045–1065, 2005. ISSN 00219983. doi: 10.1177/0021998305048739.

[50] Jacob Bear. *Theory and Applications of Transport in Porous Media Modeling Phenomena of Flow and Transport in Porous Media*, volume 31. Springer, Cham, Switzerland, 2018. ISBN 9783319728254. doi: doi.org/10.1007/978-3-319-72826-1.

[51] A. Mortensen and T. Wong. Infiltration of fibrous preforms by a pure metal: Part III. Capillary Phenomena. *Metallurgical Transactions A*, 21:2257–2263, 1990. doi: 10.1007/BF02647888.

[52] François LeBel, Édu Ruiz, and François Trochu. Void content analysis and processing issues to minimize defects in liquid composite molding. *Polymer Composites*, 40(1):109–120, 2019. ISSN 15480569. doi: 10.1002/pc.24609.

[53] Beliny Bonnard, Philippe Causse, and François Trochu. Experimental characterization of the pore size distribution in fibrous reinforcements of composite materials. *Journal of Composite Materials*, 51(27):3807–3818, 2017. ISSN 1530793X. doi: 10.1177/0021998317694424.

[54] François LeBel, Amir Ershad Fanaei, Édu Ruiz, and François Trochu. Prediction of optimal flow front velocity to minimize void formation in dual scale fibrous reinforcements. *International Journal of Material Forming*, 7(1):93–116, 2014. ISSN 19606206. doi: 10.1007/s12289-012-1111-x.

[55] Jean Sébastien Leclerc and Edu Ruiz. Porosity reduction using optimized flow velocity in Resin Transfer Molding. *Composites Part A: Applied Science and Manufacturing*, 39(12):1859–1868, 2008. ISSN 1359835X. doi: 10.1016/j.compositesa.2008.09.008.

[56] Chung Hae Park, Aurélie Lebel, Abdelghani Saouab, Joël Bréard, and Woo Il Lee. Modeling and simulation of voids and saturation in liquid composite molding processes. *Composites Part A: Applied Science and Manufacturing*, 42(6):658–668, 2011. ISSN 1359835X. doi: 10.1016/j.compositesa.2011.02.005.

[57] C. Devalve and R. Pitchumani. Simulation of void formation in liquid composite molding processes. *Composites Part A: Applied Science and Manufacturing*, 51:22–32, 2013. ISSN 1359835X. doi: 10.1016/j.compositesa.2013.03.016.

[58] Hu Guo, Kaoping Song, and Rudolf Hilfer. A critical review of capillary number and its application in enhanced oil recovery. *Proceedings - SPE Symposium on Improved Oil Recovery*, 2020. doi: 10.2118/200419-ms.

[59] Hu Guo, Kaoping Song, and R. Hilfer. A brief review of capillary number and its use in capillary desaturation curves. *Transport in Porous Media*, 144:3–31, 2022. ISSN 15731634. doi: 10.1007/s11242-021-01743-7.

[60] Kota Yoshihara, Yo Kamei, Atsuki Mizuno, Haruka Ohgaki, Takuma Hori, and Ichiro Ueno. Effect of wettability on viscous fluid impregnation in single-layer woven-fibre bundles driven by pressure difference. *Composites Part A: Applied Science and Manufacturing*, 138:106049, 2020. ISSN 1359-835X. doi: 10.1016/j.compositesa.2020.106049.

[61] Xiaokang Guo, Runcong Liu, Jiang Wang, Sansan Shuai, Degan Xiong, Shuxin Bai, Nianmei Zhang, Xiufang Gong, and Xiaodong Wang. Pore-scale modeling of wettability effects on infiltration behavior in liquid composite molding. *Physics of Fluids*, 32:093311, 2020. ISSN 10897666. doi: 10.1063/5.0023161.

[62] John C. Berg. *Wettability*, volume 49. Boca Raton, 1993. ISBN 9780429181535. doi: 10.1201/9781482277500.

[63] Monica Francesca Pucci, Pierre Jacques Liotier, and Sylvain Drapier. Capillary wicking in flax fabrics - Effects of swelling in water. *Colloids and Surfaces A: Physicochemical and Engineering Aspects*, 498:176–184, 2016. ISSN 18734359. doi: 10.1016/j.colsurfa.2016.03.050.

[64] Monica Francesca Pucci, Pierre Jacques Liotier, and Sylvain Drapier. Tensiometric method to reliably assess wetting properties of single fibers with resins: Validation on cellulosic reinforcements for composites. *Colloids and Surfaces A: Physicochemical and Engineering Aspects*, 512:26–33, 2017. ISSN 18734359. doi: 10.1016/j.colsurfa.2016.09.047.

[65] Monica Francesca Pucci, Benoît Duchemin, Moussa Gomina, and Joël Bréard. Dynamic wetting of molten polymers on cellulosic substrates: Model prediction for total and partial wetting. *Frontiers in Materials*, 7:143, 2020. ISSN 22968016. doi: 10.3389/fmats.2020.00143.

[66] Jian Wang, Carlos A. Fuentes, Dongxing Zhang, Xungai Wang, Aart Willem Van Vuure, and David Seveno. Wettability of carbon fibres at micro- and mesoscales. *Carbon*, 120:438–446, 2017. ISSN 00086223. doi: 10.1016/j.carbon.2017.05.055.

[67] Daniel Hansen, Niels Bomholt, Jonas Camillus Jeppesen, and Adam Cohen Simonsen. Contact angle goniometry on single micron-scale fibers for composites. *Applied Surface Science*, 392:181–188, 2017. ISSN 01694332. doi: 10.1016/j.apsusc.2016.09.018.

[68] Monica Francesca Pucci, Pierre Jacques Liotier, and Sylvain Drapier. Capillary effects on flax fibers - Modification and characterization of the wetting dynamics. *Composites Part A: Applied Science and Manufacturing*, 77:257–265, 2015. ISSN 1359835X. doi: 10.1016/j.compositesa.2015.03.010.

[69] Mohamed Hamdaoui, Faten Fayala, and Sassi Ben Nasrallah. Dynamics of capillary rise in yarns: Influence of fiber and liquid characteristics. *Journal of Applied Polymer Science*, 104(5):3050–3056, 2007. ISSN 00218995. doi: 10.1002/app.25642.

[70] J. Castro, F. Sket, and C. González. S-XCT experimental determination of local contact angle and meniscus shape in liquid moulding of composites. *Composites Science and Technology*, 199(5):108362, 2020. ISSN 02663538. doi: 10.1016/j.compscitech.2020.108362.

[71] Sana Koubaa, Christian Burtin, and Steven Le Corre. Investigation of capillary impregnation for permeability prediction of fibrous reinforcements. *Journal of Composite Materials*, 50(11):1417–1429, 2016. ISSN 1530793X. doi: 10.1177/0021998315593797.

[72] François Lebel, Amir Ershad Fanaei, Édu Ruiz, and François Trochu. Experimental characterization by fluorescence of capillary flows in the fiber tows of engineering fabrics. *Open Journal of Inorganic Non-metallic Materials*, 2:25–45, 2012. doi: 10.1177/0040517512471742.

[73] Monica Francesca Pucci, Pierre Jacques Liotier, and Sylvain Drapier. Capillary wicking in a fibrous reinforcement - Orthotropic issues to determine the capillary pressure components. *Composites Part A: Applied Science and Manufacturing*, 77:133–141, 2015. ISSN 1359835X. doi: 10.1016/j.compositesa.2015.05.031.

[74] H. N. Vo, M. F. Pucci, S. Corn, N. Le Moigne, W. Garat, S. Drapier, and P. J. Liotier. Capillary wicking in bio-based reinforcements undergoing swelling – Dual scale consideration of porous medium. *Composites Part A: Applied Science and Manufacturing*, 134:105893, 2020. ISSN 1359835X. doi: 10.1016/j.compositesa.2020.105893.

[75] Edward W Washburn. Note on a method of determining the distribution of pore sizes in a porous material. *Proceedings of the National Academy of Sciences of the United States of America*, 7(4):115–116, 1921. doi: 10.1073/pnas.7.4.115.

[76] Jennifer M. Rieser, P. E. Arratia, A. G. Yodh, J. P. Gollub, and D. J. Durian. Tunable capillary-induced attraction between vertical cylinders. *Langmuir*, 31(8):2421–2429, 2015. ISSN 15205827. doi: 10.1021/la5046139.

[77] C. Ravey, E. Ruiz, and F. Trochu. Determination of the optimal impregnation velocity in Resin Transfer Molding by capillary rise experiments and infrared thermography. *Composites Science and Technology*, 99:96–102, 2014. ISSN 02663538. doi: 10.1016/j.compscitech.2014.05.019.

[78] Philippe Causse, Christophe Ravey, and François Trochu. Capillary characterization of fibrous reinforcement and optimization of injection strategy in resin transfer molding. *Journal of Composites Science*, 2(19), 2018. ISSN 2504477X. doi: 10.3390/jcs2020019.

[79] J. Castro, F. Sket, L. Helfen, and C. González. In situ local imaging and analysis of impregnation during liquid moulding of composite materials using synchrotron radiation computed laminography. *Composites Science and Technology*, 215:108999, 2021. ISSN 02663538. doi: 10.1016/j.compscitech.2021.108999.

[80] Thomas L. Luce, Suresh C. Advani, J. Grant Howard, and Richard S. Parnas. Permeability characterization. Part 2: Flow behavior in multiple-layer preforms. *Polymer Composites*, 16(6):446–458, 1995. doi: 10.1002/pc.750160603.

[81] T. S. Lundström, R. Stenberg, R. Bergström, H. Partanen, and P. A. Birkeland. In-plane permeability measurements: a nordic round-robin study. *Composites Part A: Applied Science and Manufacturing*, 31(1):29–43, 2000. ISSN 1359-835X. doi: 10.1016/S1359-835X(99)00058-5.

[82] Joël Bréard, Yann Henzel, François Trochu, and Raymond Gauvin. Analysis of dynamic flows through porous media. Part I: Comparison between saturated and unsaturated flows in fibrous reinforcements. *Polymer Composites*, 24(3):391–408, 2003. ISSN 15480569. doi: 10.1002/pc.10038.

[83] D. A. Steenkamer, S. H. McKnight, D. J. Wilkins, and V. M. Karbhari. Experimental characterization of permeability and fibre wetting for liquid moulding. *Journal of Materials Science*, 30(12):3207–3215, 1995. ISSN 00222461. doi: 10.1007/BF01209239.

[84] F. D. Dungan and A. M. Sastry. Saturated and unsaturated polymer flows: Microphenomena and modeling. *Journal of Composite Materials*, 36(13):1581–1603, 2002. ISSN 00219983. doi: 10.1177/0021998302036013179.

[85] Krishna M. Pillai. Modeling the unsaturated flow in liquid composite molding processes: A review and some thoughts. *Journal of Composite Materials*, 38(23):2097–2118, 2004. ISSN 00219983. doi: 10.1177/0021998304045585.

[86] Baris Caglar, Cem Tekin, Feyza Karasu, and Véronique Michaud. Assessment of capillary phenomena in liquid composite molding. *Composites Part A: Applied Science and Manufacturing*, 120:73–83, 2019. ISSN 1359835X. doi: 10.1016/j.compositesa.2019.02.018.

[87] Jeroen Staal, Baris Caglar, Travis Hank, Brian L. Wardle, Larissa Gorbatikh, Stepan V. Lomov, and Véronique Michaud. In-series sample methodology for permeability characterization demonstrated on carbon nanotube-grafted alumina textiles. *Composites Part A: Applied Science and Manufacturing*, 150:106631, 2021. ISSN 1359835X. doi: 10.1016/j.compositesa.2021.106631.

[88] V. J. Michaud, L. M. Compton, and A. Mortensen. Capillarity in isothermal infiltration of alumina fiber preforms with aluminum. *Metallugical and Materials Transactions A: Physical Metallurgy and Materials Science*, 25A(10):2145–2152, 1994. ISSN 10735623. doi: 10.1007/BF02652315.

[89] Y. De Parseval, K. M. Pillai, and S. G. Advani. A simple model for the variation of permeability due to partial saturation in dual scale porous media. *Transport in Porous Media*, 27(3):243–264, 1997. ISSN 01693913. doi: 10.1023/a:1006544107324.

[90] T. Dopler, A. Modaressi, and V. Michaud. Simulation of metal-matrix composite isothermal infiltration processing. *Metallurgical and Materials Transactions B: Process Metallurgy and Materials Processing Science*, 31(2):225–234, 2000. ISSN 10735615. doi: 10.1007/s11663-000-0041-z.

[91] J. Slade, K. M. Pillai, and S. G. Advani. Investigation of unsaturated flow in woven, braided and stitched fiber mats during mold-filling in resin transfer molding. *Polymer Composites*, 22(4):491–505, 2001. ISSN 02728397. doi: 10.1002/pc.10554.

[92] B. Gourichon, C. Binetruy, and P. Krawczak. Experimental investigation of high fiber tow count fabric unsaturation during RTM. *Composites Science and Technology*, 66(7-8):976–982, 2006. ISSN 02663538. doi: 10.1016/j.compscitech.2005.07.032.

[93] Hua Tan, Tonmoy Roy, and Krishna M Pillai. Variations in unsaturated flow with flow direction in resin transfer molding: An experimental investigation. *Composites Part A: Applied Science and Manufacturing*, 38(8):1872–1892, 2007. doi: 10.1016/j.compositesa.2007.04.002.

[94] Véronique Michaud and Andreas Mortensen. On measuring wettability in infiltration processing. *Scripta Materialia*, 56:859–862, 2007. ISSN 1359-6462. doi: 10.1016/j.scriptamat.2007.02.002.

[95] Hua Tan and Krishna M. Pillai. Multiscale modeling of unsaturated flow in dual-scale fiber preforms of liquid composite molding I: Isothermal flows. *Composites Part A: Applied Science and Manufacturing*, 43(1):1–13, 2012. ISSN 1359835X. doi: 10.1016/j.compositesa.2010.12.013.

[96] John M. Bayldon and Isaac M. Daniel. Flow modeling of the VARTM process including progressive saturation effects. *Composites Part A: Applied Science and Manufacturing*, 40(8):1044–1052, 2009. ISSN 1359835X. doi: 10.1016/j.compositesa.2009.04.008.

[97] P. Carlone and G. S. Palazzo. Unsaturated and saturated flow front tracking in liquid composite molding processes using dielectric sensors. *Applied Composite Materials*, 22(5):543–557, 2015. ISSN 15734897. doi: 10.1007/s10443-014-9422-3.

[98] Pierpaolo Carlone, Felice Rubino, Valentino Paradiso, and Fausto Tucci. Multi-scale modeling and online monitoring of resin flow through dual-scale textiles in liquid composite molding processes. *International Journal of Advanced Manufacturing Technology*, 96:2215–2230, 2018. ISSN 14333015. doi: 10.1007/s00170-018-1703-9.

[99] Joseph Walther, Pavel Simacek, and Suresh G. Advani. The effect of fabric and fiber tow shear on dual scale flow and fiber bundle saturation during liquid molding of textile composites. *International Journal of Material Forming*, 5(1):83–97, 2012. ISSN 19606206. doi: 10.1007/s12289-011-1060-9.

[100] Jeffrey M. Lawrence, Valentin Neacsu, and Suresh G. Advani. Modeling the impact of capillary pressure and air entrapment on fiber tow saturation during resin infusion in LCM. *Composites Part A: Applied Science and Manufacturing*, 40(8): 1053–1064, 2009. ISSN 1359835X. doi: 10.1016/j.compositesa.2009.04.013.

[101] Pavel Simacek, Valentin Neacsu, and Suresh G. Advani. A phenomenological model for fiber tow saturation of dual scale fabrics in liquid composite molding. *Polymer Composites*, 31(11):1881–1889, 2010. ISSN 02728397. doi: 10.1002/pc.20982.

[102] Mathieu Imbert, Sebastien Comas-Cardona, Emmanuelle Abisset-Chavanne, and David Prono. Experimental investigation of intra-tow fluid storage mechanisms in dual-scale fiber reinforcements. *Composites Part A: Applied Science and Manufacturing*, 107:70–82, 2018. ISSN 1359835X. doi: 10.1016/j.compositesa.2017.12.015.

[103] B. Gourichon, C. Binetruy, and P. Krawczak. A new numerical procedure to predict dynamic void content in liquid composite molding. *Composites Part A: Applied Science and Manufacturing*, 37(11):1961–1969, 2006. ISSN 1359835X. doi: 10.1016/j.compositesa.2005.12.017.

[104] Véronique Michaud, Markus Nordlund, T. Staffan Lundström, and Jan-Anders E. Månson. Capillary phenomena in liquid composite moulding. In *16th International Conference on Composite Materials*, Kyoto, Japan, 2007.

[105] Markus Nordlund and Véronique Michaud. Dynamic saturation curve measurement for resin flow in glass fibre reinforcement. *Composites Part A: Applied science and manufacturing*, 43(3):333–343, 2012. ISSN 1359-835X. doi: 10.1016/j.compositesa.2011.12.001.

[106] L. Gascón, J. A. García, F. Lebel, E. Ruiz, and F. Trochu. Numerical prediction of saturation in dual scale fibrous reinforcements during Liquid Composite Molding. *Composites Part A: Applied Science and Manufacturing*, 77:275–284, 2015. ISSN 1359835X. doi: 10.1016/j.compositesa.2015.05.019.

[107] L. Gascón, J. A. García, F. LeBel, E. Ruiz, and F. Trochu. A two-phase flow model to simulate mold filling and saturation in Resin Transfer Molding. *International Journal of Material Forming*, 9(2):229–239, 2016. ISSN 19606214. doi: 10.1007/s12289-015-1225-z.

[108] Maxime Villière, Sébastien Guéroult, Vincent Sobotka, Nicolas Boyard, Joël Bréard, and Didier Delaunay. Dynamic saturation curve measurement in liquid composite molding by heat transfer analysis. *Composites Part A: Applied Science and Manufacturing*, 69:255–265, 2015. ISSN 1359835X. doi: 10.1016/j.compositesa.2014.11.024.

[109] Alain Léger, Ludger Weber, and Andreas Mortensen. Influence of the wetting angle on capillary forces in pressure infiltration. *Acta Materialia*, 91:57–69, 6 2015. ISSN 13596454. doi: 10.1016/j.actamat.2015.03.002.

[110] Gionata Schneider, Ludger Weber, and Andreas Mortensen. Reactive pressure infiltration of Cu-46at.pct. Si into carbon. *Acta Materialia*, 177:9–19, 2019. ISSN 13596454. doi: 10.1016/j.actamat.2019.07.010.

[111] Gionata Schneider, Marta Fornabaio, Ludger Weber, and Andreas Mortensen. Kinetic processes in the high-temperature pressure-infiltration of Al into Al2O3. *Acta Materialia*, 189:105–117, 2020. ISSN 1359-6454/. doi: 10.1016/j.actamat.2020.02.048.

[112] Tore I. Bjørnarå and Eyvind Aker. Comparing Equations for Two-Phase Fluid Flow in Porous Media. In *Proceedings of the COMSOL Conference*, Hannover, 2008.

[113] B. Ataie-Ashtiani and D. Raeesi-Ardekani. Comparison of numerical formulations for Two-phase flow in porous media. *Geotechnical and Geological Engineering*, 28(4):373–389, 2010. ISSN 09603182. doi: 10.1007/s10706-009-9298-4.

[114] L. A. Richards. Capillary conduction of liquids through porous mediums. *Journal of Applied Physics*, 1(5):318–333, 1931. ISSN 01486349. doi: 10.1063/1.1745010.

[115] Brahim Amaziane, Mladen Jurak, and Ana Žgaljić Keko. Modeling and numerical simulations of immiscible compressible two-phase flow in porous media by the concept of global pressure. *Transport in Porous Media*, 84(1):133–152, 2010. ISSN 01693913. doi: 10.1007/s11242-009-9489-8.

[116] Hongjing Gao, Boming Yu, Yonggang Duan, and Quantang Fang. Fractal analysis of dimensionless capillary pressure function. *International Journal of Heat and Mass Transfer*, 69:26–33, 2014. ISSN 00179310. doi: 10.1016/j.ijheatmasstransfer.2013.10.006.

[117] R H Brooks and A T Corey. Hydraulic Properties of Porous Media. In *Hydrology Papers*, volume 3. Colorado State University, Fort Collins, Colorado, 1964.

[118] Yechezkel Mualem. A new model for predicting the hydraulic conductivity of unsaturated porous media. *Water Resources Research*, 12(3):513–522, 1976.

[119] Yechezkel Mualem. Hydraulic conductivity of unsaturated porous media: Generalized macroscopic approach. *Water Resources Research*, 14(2):325–334, 1978. ISSN 19447973. doi: 10.1029/WR014i002p00325.

[120] M. Th. van Genuchten. A closed-form equation for predicting the hydraulic conductivity of unsaturated soils. *Soil Science Society of America Journal*, 44(5):892–898, 1980. ISSN 03615995. doi: 10.2136/sssaj1980.03615995004400050002x.

[121] H. H. Gerke and M. T. van Genuchten. A dual porosity model for simulating the preferential movement of water and solutes in structured porous media. *Water Resources Research*, 29(2):305–319, 1993.

[122] Guilherme Apolinario Testoni, Sihwan Kim, Anurag Pisupati, and Chung Hae Park. Modeling of the capillary wicking of flax fibers by considering the effects of fiber swelling and liquid absorption. *Journal of Colloid and Interface Science*, 525:166–176, 2018. ISSN 10957103. doi: 10.1016/j.jcis.2018.04.064.

[123] Gastón Francucci, Exequiel S. Rodríguez, and Analía Vázquez. Study of saturated and unsaturated permeability in natural fiber fabrics. *Composites Part A: Applied Science and Manufacturing*, 41(1):16–21, 2010. ISSN 1359835X. doi: 10.1016/j.compositesa.2009.07.012.

[124] Van Hau Nguyen, Mylène Lagardère, Chung Hae Park, and Stéphane Panier. Permeability of natural fiber reinforcement for liquid composite molding processes. *Journal of Materials Science*, 49(18):6449–6458, 2014. ISSN 15734803. doi: 10.1007/s10853-014-8374-1.

[125] Monica Francesca Pucci, Pierre Jacques Liotier, David Seveno, Carlos Fuentes, Aart Van Vuure, and Sylvain Drapier. Wetting and swelling property modifications of elementary flax fibres and their effects on the Liquid Composite Molding process. *Composites Part A: Applied Science and Manufacturing*, 97:31–40, 2017. ISSN 1359835X. doi: 10.1016/j.compositesa.2017.02.028.

[126] Reza Masoodi, Krishna M. Pillai, Nick Grahl, and Hua Tan. Numerical simulation of LCM mold-filling during the manufacture of natural fiber composites. *Journal of Reinforced Plastics and Composites*, 31(6):363–378, 2012. ISSN 07316844. doi: 10.1177/0731684412438629.

[127] William Garat, Nicolas Le Moigne, Stephane Corn, Johnny Beaugrand, and Anne Bergeret. Swelling of natural fibre bundles under hygro- and hydrothermal conditions: Determination of hydric expansion coefficients by automated laser scanning. *Composites Part A: Applied Science and Manufacturing*, 131:105803, 2020. ISSN 1359835X. doi: 10.1016/j.compositesa.2020.105803.

[128] E. Manfredi and V. Michaud. Packing and permeability properties of E-glass fibre reinforcements functionalised with capsules for self-healing applications. *Composites Part A: Applied Science and Manufacturing*, 66:94–102, 2014. ISSN 1359835X. doi: 10.1016/j.compositesa.2014.07.006.

[129] Claire Steggall-Murphy, Pavel Simacek, Suresh G. Advani, Shridhar Yarlagadda, and Shawn Walsh. A model for thermoplastic melt impregnation of fiber bundles during consolidation of powder-impregnated continuous fiber composites. *Composites Part A: Applied Science and Manufacturing*, 41(1):93–100, 2010. ISSN 1359835X. doi: 10.1016/j.compositesa.2009.09.026.

[130] M. Nordlund, S. P. Fernberg, and T. S. Lundström. Particle deposition mechanisms during processing of advanced composite materials. *Composites Part A: Applied Science and Manufacturing*, 38(10):2182–2193, 2007. ISSN 1359835X. doi: 10.1016/j.compositesa.2007.06.009.

[131] Delphine Lefevre, Sébastien Comas-Cardona, Christophe Binétruy, and Patricia Krawczak. Modelling the flow of particle-filled resin through a fibrous preform in liquid composite molding technologies. *Composites Part A: Applied Science and Manufacturing*, 38(10):2154–2163, 2007. ISSN 1359835X. doi: 10.1016/j.compositesa.2007.06.008.

[132] D. Lefevre, S. Comas-Cardona, C. Binetruy, and P. Krawczak. Coupling filtration and flow during liquid composite molding: Experimental investigation and simulation. *Composites Science and Technology*, 69(13):2127–2134, 10 2009. ISSN 02663538. doi: 10.1016/j.compscitech.2009.05.008.

[133] Bryan M. Louis, Jesus Maldonado, Florian Klunker, and Paolo Ermanni. Particle distribution from in-plane resin flow in a resin transfer molding process. *Polymer Engineering and Science*, 59(1):22–34, 2019. ISSN 15482634. doi: 10.1002/pen.24860.

[134] Sang Hyuk Yum, Woo Il Lee, and Seung Mo Kim. Particle filtration and distribution during the liquid composite molding process for manufacturing particles containing composite materials. *Composites Part A: Applied Science and Manufacturing*, 90:330–339, 2016. ISSN 1359835X. doi: 10.1016/j.compositesa.2016.07.016.

[135] Hind Haji, Abdelghani Saouab, and Yasir Nawab. Simulation of coupling filtration and flow in a dual scale fibrous media. *Composites Part A: Applied Science and Manufacturing*, 76:272–280, 2015. ISSN 1359835X. doi: 10.1016/j.compositesa.2015.06.004.

[136] Dilmurat Abliz, Benedikt Finke, David C. Berg, Carsten Schilde, and Gerhard Ziegmann. Flow of quasi-spherical nanoparticles in liquid composite molding processes. Part I: Influence of particle size and fiber distance distribution. *Composites Part A: Applied Science and Manufacturing*, 125:105563, 2019. ISSN 1359835X. doi: 10.1016/j.compositesa.2019.105563.

[137] Dilmurat Abliz, David C. Berg, and Gerhard Ziegmann. Flow of quasi-spherical nanoparticles in liquid composite molding processes. Part II: Modeling and simulation. *Composites Part A: Applied Science and Manufacturing*, 125:105562, 2019. ISSN 1359835X. doi: 10.1016/j.compositesa.2019.105562.

[138] B. M. Louis, J. Maldonado, F. Klunker, and P. Ermanni. Measurement of nanoparticles distribution in composite laminates produced by resin transfer molding. In *16th European Conference on Composite Materials*, Seville, Spain, 2014.

[139] James L. Thomason. Sizing Chemistry of Glass Fibers. In Hong Li, editor, *Fiberglass Science and Technology*, chapter 4. Springer, Cham, Switzerland, 2021. ISBN 9783030722005. doi: 10.1007/978-3-030-72200-5{_}4.

[140] Garima Mittal, Kyong Y. Rhee, Vesna Mišković-Stanković, and David Hui. Reinforcements in multi-scale polymer composites: Processing, properties, and applications. *Composites Part B: Engineering*, 138:122–139, 2018. ISSN 13598368. doi: 10.1016/j.compositesb.2017.11.028.

[141] Kai Kang and Kurt Koelling. Void transport in resin transfer molding. *Polymer Composites*, 25(4):417–432, 2004. ISSN 02728397. doi: 10.1002/pc.20035.

[142] Ryosuke Matsuzaki, Daigo Seto, Akira Todoroki, and Yoshihiro Mizutani. In situ void content measurements during resin transfer molding. *Advanced Composite Materials*, 22(4):239–254, 2013. ISSN 09243046. doi: 10.1080/09243046.2013.801822.

[143] Chih Hsin Shih and L. James Lee. Analysis of void removal in liquid composite molding using microflow models. *Polymer Composites*, 23(1):120–131, 2002. ISSN 02728397. doi: 10.1002/pc.10418.

[144] T. Staffan Lundström. Bubble transport through constricted capillary tubes with application to resin transfer molding. *Polymer Composites*, 17(6):770–779, 1996. ISSN 02728397. doi: 10.1002/pc.10669.

[145] Ionel I Gardescu. Behavior of gas bubbles in capillary spaces. *Transactions of the AIME*, 86(01):351–370, 1930. ISSN 0081-1696. doi: 10.2118/930351-G.

[146] Joaquim Vilà, Federico Sket, Fabian Wilde, Guillermo Requena, Carlos González, and Javier LLorca. An in situ investigation of microscopic infusion and void transport during vacuum-assisted infiltration by means of X-ray computed tomography. *Composites Science and Technology*, 119:12–19, 2015. ISSN 02663538. doi: 10.1016/j.compscitech.2015.09.016.

[147] Yunguang Chen, Christopher W Macosko, and H Ted Davis. Wetting of fiber mats for composites manufacturing: II. Air entrapment model. *Aiche Journal*, 41:2274–2281, 1995. doi: 10.1002/aic.690411009.

[148] T. S. Lundström, B. R. Gebart, and C. Y. Lundemo. Void Formation in RTM. *Journal of Reinforced Plastics and Composites*, 12(12):1339–1349, 1993. ISSN 15307964. doi: 10.1177/073168449301201207.

[149] T. Staffan Lundström, Vilnis Frishfelds, and Andris Jakovics. Bubble formation and motion in non-crimp fabrics with perturbed bundle geometry. *Composites Part A: Applied Science and Manufacturing*, 41(1):83–92, 2010. ISSN 1359835X. doi: 10.1016/j.compositesa.2009.05.012.

[150] V. Rohatgi, N. Patel, and L. James Lee. Experimental investigation of flow-induced microvoids during impregnation of unidirectional stitched fiberglass mat. *Polymer Composites*, 17(2):161–170, 1996. ISSN 02728397. doi: 10.1002/pc.10601.

[151] Vishwanath R. Kedari, Basil I. Farah, and Kuang Ting Hsiao. Effects of vacuum pressure, inlet pressure, and mold temperature on the void content, volume fraction of polyester/e-glass fiber composites manufactured with VARTM process. *Journal of Composite Materials*, 45(26):2727–2742, 2011. ISSN 00219983. doi: 10.1177/0021998311415442.

[152] Moon Koo Kang, Woo Il Lee, and H. Thomas Hahn. Formation of microvoids during resin-transfer molding process. *Composites Science and Technology*, 60:2427–2434, 2000. ISSN 02663538/. doi: 10.1016/S0266-3538(00)00036-1.

[153] Sérgio Frascino Müller de Almeida and Zabulon dos Santos Nogueira Neto. Effect of void content on the strength of composite laminates. *Composite Structures*, 28(2):139–148, 1994. ISSN 02638223. doi: 10.1016/0263-8223(94)90044-2.

[154] D. E. W. Stone and B. Clarke. Ultrasonic attenuation as a measure of void content in carbon-fibre reinforced plastics. *Non-Destructive Testing*, 8(3):137–145, 1975. doi: 10.1016/0029-1021(75)90023-7.

[155] Junwei Shi, Songping Liu, Feifei Liu, and Guoli Xun. Multi-mode ultrasonic visualization of porosity in composites using a focused transducer with high sensitivity and near-surface resolution. *Composites Part C: Open Access*, 4:100104, 2021. ISSN 2666-6820. doi: 10.1016/j.jcomc.2020.100104.

[156] G Mayr, B Plank, J Sekelja, and G Hendorfer. Active thermography as a quantitative method for non-destructive evaluation of porous carbon fiber reinforced polymers. *NDT & E International*, 44(7):537–543, 2011. ISSN 0963-8695. doi: 10.1016/j.ndteint.2011.05.012.

[157] Anna Madra, Nemr El Hajj, and Malk Benzeggagh. X-ray microtomography applications for quantitative and qualitative analysis of porosity in woven glass fiber reinforced thermoplastic. *Composites Science and Technology*, 95:50–58, 2014. ISSN 02663538. doi: 10.1016/j.compscitech.2014.02.009.

[158] S. M. Sisodia, S. C. Garcea, A. R. George, D. T. Fullwood, S. M. Spearing, and E. K. Gamstedt. High-resolution computed tomography in resin infused woven carbon fibre composites with voids. *Composites Science and Technology*, 131:12–21, 2016. ISSN 02663538. doi: 10.1016/j.compscitech.2016.05.010.

[159] Ryosuke Matsuzaki, Daigo Seto, Akira Todoroki, and Yoshihiro Mizutani. Void formation in geometry-anisotropic woven fabrics in resin transfer molding. *Advanced Composite Materials*, 23(2):99–114, 2014. ISSN 09243046. doi: 10.1080/09243046.2013.832829.

[160] C. Kracke, A. Nonn, C. Koch, M. Nebe, E. Schmidt, S. Bickerton, T. Gries, and P. Mitschang. Interaction of textile variability and flow channel distribution systems on flow front progression in the RTM process. *Composites Part A: Applied Science and Manufacturing*, 106:70–81, 2018. ISSN 1359835X. doi: 10.1016/j.compositesa.2017.12.010.

[161] M. Bodaghi, C. Cristóvão, R. Gomes, and N. C. Correia. Experimental characterization of voids in high fibre volume fraction composites processed by high injection pressure RTM. *Composites Part A: Applied Science and Manufacturing*, 82:88–99, 2016. ISSN 1359835X. doi: 10.1016/j.compositesa.2015.11.042.

[162] Damiano Salvatori, Baris Caglar, and Véronique Michaud. 3D spacers enhance flow kinetics in resin transfer molding with woven fabrics. *Composites Part A: Applied Science and Manufacturing*, 119:206–216, 2019. ISSN 1359835X. doi: 10.1016/j.compositesa.2019.01.023.

[163] Baris Caglar, Damiano Salvatori, E. Murat Sozer, and Véronique Michaud. In-plane permeability distribution mapping of isotropic mats using flow front detection. *Composites Part A: Applied Science and Manufacturing*, 113:275–286, 2018. ISSN 1359835X. doi: 10.1016/j.compositesa.2018.07.036.

[164] M. A. Kabachi, L. Stettler, S. Arreguin, and P. Ermanni. Concurrent characterization of through-thickness permeability and compaction of fiber reinforcements. *Composites Part A: Applied Science and Manufacturing*, 141:106203, 2021. ISSN 1359835X. doi: 10.1016/j.compositesa.2020.106203.

[165] Chunyang Zhao, Bo Yang, Shilong Wang, Chi Ma, Sibao Wang, and Fengyang Bi. Three-dimensional numerical simulation of meso-scale-void formation during the mold-filling process of LCM. *Applied Composite Materials*, 26(4):1121–1137, 2019. ISSN 15734897. doi: 10.1007/s10443-019-09770-w.

[166] Z. Yousaf, P. Potluri, and P. J. Withers. Influence of Tow Architecture on Compaction and Nesting in Textile Preforms. *Applied Composite Materials*, 24(2):337–350, 2017. ISSN 15734897. doi: 10.1007/s10443-016-9554-8.

[167] F. LeBel, Ruiz, and F. Trochu. Experimental study of saturation by visible light transmission in dual-scale fibrous reinforcements during composite manufacturing. *Journal of Reinforced Plastics and Composites*, 36(23):1693–1711, 2017. ISSN 15307964. doi: 10.1177/0731684417725187.

[168] Benedikt Neitzel and Florian Puch. Optical detection of void formation mechanisms during Impregnation of composites by UV-reactive resin systems. *Journal of Composites Science*, 6(11):351, 2022. ISSN 2504-477X. doi: 10.3390/jcs6110351.

[169] Sébastien Gueroult, Aurélie Lebel-Lavacry, Chung Hae Park, Laurent Bizet, Abdelghani Saouab, and Joël Bréard. Analytical modeling and in situ measurement of void formation in liquid composite molding processes. *Advanced Composite Materials*, 23(1):31–42, 2014. ISSN 09243046. doi: 10.1080/09243046.2013.862383.

[170] Felice Rubino, Fausto Tucci, Vitantonio Esperto, and Pierpaolo Carlone. Filling time reduction in liquid composite molding processes. *Journal of Composites Science*, 6(8), 2022. ISSN 2504477X. doi: 10.3390/jcs6080222.

[171] Benedikt Neitzel and Florian Puch. Application of capacitive sensors and controlled injection pressure to minimize void formation in resin transfer molding. *Polymer Composites*, 2022. ISSN 15480569. doi: 10.1002/pc.27195.

[172] Baris Caglar, William Esposito, Tung Nguyen-Dang, Stella Laperrousaz, Véronique Michaud, and Fabien Sorin. Functionalized fiber reinforced composites via thermally drawn multifunctional fiber sensors. *Advanced Materials Technologies*, 6(3): 2000957, 2021. ISSN 2365709X. doi: 10.1002/admt.202000957.

[173] Athanasios Pouchias, Paul R. Cunningham, Jasmin Stein, and Mihalis Kazilas. Development of a flexible dielectric sensor for flow monitoring of the liquid resin infusion process. *Sensors*, 19(23):5292, 2019. ISSN 14248220. doi: 10.3390/s19235292.

[174] K. I. Tifkitsis and A. A. Skordos. A novel dielectric sensor for process monitoring of carbon fibre composites manufacture. *Composites Part A: Applied Science and Manufacturing*, 123:180–189, 2019. ISSN 1359835X. doi: 10.1016/j.compositesa.2019.05.014.

[175] S. Tiwari, J. Bijwe, and S. Panier. Optimization of surface treatment to enhance fiber – matrix interface and performance of composites. *Wear*, 274-275:326–334, 2012. ISSN 0043-1648. doi: 10.1016/j.wear.2011.09.014.

[176] C. Lystrup, A. George, B. Zobell, K. Boster, C. Childs, H. Girod, and D. Fullwood. Optical measurement of voids in situ during infusion of carbon reinforcements. *Journal of Composite Materials*, 55(6):775–786, 2020. doi: 10.1177/0021998320959820.

[177] Stefan Neunkirchen, Yannick Blössl, and Ralf Schledjewski. A porous capillary tube approach for textile saturation. *Composites Science and Technology*, 230(2):109450, 2022. ISSN 0266-3538. doi: 10.1016/j.compscitech.2022.109450.

[178] Harald Grössing, Natalie Stadlmajer, Ewald Fauster, Martin Fleischmann, and Ralf Schledjewski. Flow front advancement during composite processing: predictions from numerical filling simulation tools in comparison with real-world experiments. *Polymer Composites*, 37(9):2782–2793, 2016. ISSN 15480569. doi: 10.1002/pc.23474.

[179] S. Thomas, C. Bongiovanni, and S. R. Nutt. In situ estimation of through-thickness resin flow using ultrasound. *Composites Science and Technology*, 68(15-16):3093–3098, 2008. ISSN 02663538. doi: 10.1016/j.compscitech.2008.07.012.

[180] Hai Long Liu, Xin-cheng Tu, Joon Oh Lee, and Hyoung-bum Kim. Visualization of resin impregnation through opaque reinforcement textiles during the vacuum-assisted resin transfer molding process using ultrasound. *Journal of Composite Materials*, 48(9):1113–1120, 2014. doi: 10.1177/0021998313482157.

[181] Spiridon Konstantopoulos, Harald Grössing, Patrick Hergan, Markus Weninger, and Ralf Schledjewski. Determination of the unsaturated through-thickness permeability of fibrous preforms based on flow front detection by ultrasound. *Polymer Composites*, 39(2):360–367, 2018. ISSN 15480569. doi: 10.1002/pc.23944.

[182] Francesca Lionetto, Francesco Montagna, and Alfonso Maffezzoli. Out-Of-Plane Permeability Evaluation of Carbon Fiber Preforms by Ultrasonic Wave Propagation. *Materials*, 13(12):2684, 2020. doi: 10.3390/ma13122684.

[183] Francesca Lionetto, Anna Moscatello, Giuseppe Totaro, Marco Raffone, and Alfonso Maffezzoli. Experimental and numerical study of vacuum resin infusion of stiffened carbon fiber reinforced panels. *Materials*, 13(21):4800, 2020. ISSN 19961944. doi: 10.3390/ma13214800.

[184] Andreas Endruweit, Paul Glover, Kay Head, and Andrew C. Long. Mapping of the fluid distribution in impregnated reinforcement textiles using Magnetic Resonance Imaging: Application and discussion. *Composites Part A: Applied Science and Manufacturing*, 42(3):1369–1379, 2011. ISSN 1359835X. doi: 10.1016/j.compositesa.2010.11.012.

[185] Philip J. Withers, Charles Bouman, Simone Carmignato, Veerle Cnudde, David Grimaldi, Charlotte K. Hagen, Eric Maire, Marena Manley, Anton Du Plessis, and Stuart R. Stock. X-ray computed tomography. *Nature Reviews Methods Primers*, 1 (18), 2021. ISSN 2662-8449. doi: 10.1038/s43586-021-00015-4.

[186] J Bréard, A Saouab, and G Bouquet. Dependence of the reinforcement anisotropy on a three dimensional resin flow observed by X-Ray radioscopy. *Journal of Reinforced Plastics and Composites*, 18(9):814–826, 1999. ISSN 0731-6844. doi: 10.1177/073168449901800903.

[187] Julie Hemmer, Christian Burtin, Sébastien Comas-Cardona, Christophe Binetruy, Thibaut Savart, and Arthur Babeau. Unloading during the infusion process: Direct measurement of the dual-scale fibrous microstructure evolution with X-ray computed tomography. *Composites Part A: Applied Science and Manufacturing*, 115:147–156, 2018. ISSN 1359835X. doi: 10.1016/j.compositesa.2018.09.013.

[188] M. A. Ali, R. Umer, K. A. Khan, and W. J. Cantwell. In-plane virtual permeability characterization of 3D woven fabrics using a hybrid experimental and numerical approach. *Composites Science and Technology*, 173:99–109, 2019. ISSN 02663538. doi: 10.1016/j.compscitech.2019.01.030.

[189] Natalie M. Larson and Frank W. Zok. Insights from in-situ X-ray computed tomography during axial impregnation of unidirectional fiber beds. *Composites Part A: Applied Science and Manufacturing*, 107:124–134, 2018. ISSN 1359835X. doi: 10.1016/j.compositesa.2017.12.024.

[190] Natalie M. Larson, Charlene Cuellar, and Frank W. Zok. X-ray computed tomography of microstructure evolution during matrix impregnation and curing in unidirectional fiber beds. *Composites Part A: Applied Science and Manufacturing*, 117: 243–259, 2019. ISSN 1359835X. doi: 10.1016/j.compositesa.2018.11.021.

[191] Sarah F. Gayot, Jeroen Soete, Johan Vanhulst, Christian Bailly, Pierre Gérard, and Thomas Pardoen. Monitoring Void Formation During Liquid Composite Molding by In-Situ X-Ray Computed Tomography. In *Proceedings of the American Society for Composites Thirty Seventh Technical Conference*, 2022.

[192] James Kratz, Pedro Galvez-Hernandez, Laura Rhian Pickard, Jonathan Belnoue, and Kevin Potter. Lab-based in-situ micro-CT observation of gaps in prepreg laminates during consolidation and cure. *Composites Part A: Applied Science and Manufacturing*, 140, 2021. ISSN 1359835X. doi: 10.1016/j.compositesa.2020.106180.

[193] C. David, B. Nöhammer, H. H. Solak, and E. Ziegler. Differential x-ray phase contrast imaging using a shearing interferometer. *Applied Physics Letters*, 81(17):3287–3289, 2002. ISSN 00036951. doi: 10.1063/1.1516611.

[194] Franz Pfeiffer, Timm Weitkamp, Oliver Bunk, and Christian David. Phase retrieval and differential phase-contrast imaging with low-brilliance X-ray sources. *Nature Physics*, 2(4):258–261, 2006. ISSN 17452481. doi: 10.1038/nphys265.

[195] F. Pfeiffer, M. Bech, O. Bunk, P. Kraft, E. F. Eikenberry, CH. Brönnimann, C. Grünzweig, and C. Daivd. Hard-X-ray dark-field imaging using a grating interferometer. *Nature Materials*, 7(2):134–137, 2008. doi: 10.1038/nmat2096.

[196] Atsushi Momose. Phase-sensitive imaging and phase tomography using X-ray interferometers. *Optics Express*, 11(19): 2304–2314, 2003. doi: 10.1364/OE.11.002303.

[197] Atsushi Momose. Development toward high-resolution X-ray phase imaging. *Microscopy*, 66(3):155–166, 2017. ISSN 20505701. doi: 10.1093/jmicro/dfx013.

[198] Timm Weitkamp, Ana Diaz, Christian David, Franz Pfeiffer, Marco Stampanoni, Peter Cloetens, and Eric Ziegler. X-ray phase imaging with a grating interferometer. *Optics Express*, 13(16):6296–6304, 2015. doi: 10.1364/OPEX.13.006296.

[199] Marco Endrizzi. X-ray phase-contrast imaging. *Nuclear Instruments and Methods in Physics Research, Section A: Accelerators, Spectrometers, Detectors and Associated Equipment*, 878:88–98, 2018. ISSN 01689002. doi: 10.1016/j.nima.2017.07.036.

[200] B. L. Henke, E. M. Gullikson, and J. C. Davis. X-ray interactions, photoabsorbtion scattering, transmission and reflection at E=50-30,000 eV, Z=1-92. *Atomic Data and Nuclear Tables*, 54(2):181–342, 1993. doi: 10.1006/adnd.1993.1013.

[201] C. Kottler, F. Pfeiffer, O. Bunk, C. Grünzweig, J. Bruder, R. Kaufmann, L. Tlustos, H. Walt, I. Briod, T. Weitkamp, and C. David. Phase contrast X-ray imaging of large samples using an incoherent laboratory source. *Physica Status Solidi (A) Applications and Materials Science*, 204(8):2728–2733, 2007. ISSN 18626300. doi: 10.1002/pssa.200675659.

[202] Christian Kottler, Vincent Revol, Rolf Kaufmann, and Claus Urban. Dual energy phase contrast x-ray imaging with Talbot-Lau interferometer. *Journal of Applied Physics*, 108:114906, 2010. ISSN 00218979. doi: 10.1063/1.3512871.

[203] Torsten Lauridsen, Erik M. Lauridsen, and Robert Feidenhans'L. Mapping misoriented fibers using X-ray dark field tomography. *Applied Physics A: Materials Science and Processing*, 115(3):741–745, 2014. ISSN 14320630. doi: 10.1007/s00339-014-8398-z.

[204] Vincent Revol. *X-ray phase contrast imaging by grating interferometry*. PhD thesis, University of Zurich, Zurich, 2011.

[205] Matthieu Gresil, Vincent Revol, Konstantinos Kitsianos, Georges Kanderakis, Ilias Koulalis, Marc Olivier Sauer, Hervé Trétout, and Ana Maria Madrigal. EVITA Project: Comparison between traditional non-destructive techniques and Phase Contrast X-ray Imaging applied to aerospace carbon fibre reinforced polymer. *Applied Composite Materials*, 24(2):513–524, 2017. ISSN 15734897. doi: 10.1007/s10443-016-9540-1.

[206] M. Bech, O. Bunk, T. Donath, R. Feidenhans'l, C. David, and F. Pfeiffer. Quantitative x-ray dark-field computed tomography. *Physics in Medicine and Biology*, 55(18):5529–5539, 2010. ISSN 00319155. doi: 10.1088/0031-9155/55/18/017.

[207] Christian Gusenbauer, Elisabeth Leiss-Holzinger, Sascha Senck, Katrin Mathmann, Johann Kastner, Stefan Hunger, and Wolfgang Birkfellner. Characterization of medical and biological samples with a Talbot–Lau grating interferometer μXCT in comparison to reference methods. *Case Studies in Nondestructive Testing and Evaluation*, 6:30–38, 11 2016. ISSN 22146571. doi: 10.1016/j.csndt.2016.02.001.

[208] Shu Ang Zhou and Anders Brahme. Development of phase-contrast X-ray imaging techniques and potential medical applications. *Physica Medica*, 24(3):129–148, 2008. ISSN 11201797. doi: 10.1016/j.ejmp.2008.05.006.

[209] Alberto Bravin, Paola Coan, and Pekka Suortti. X-ray phase-contrast imaging: From pre-clinical applications towards clinics. *Physics in Medicine and Biology*, 58(1):1–35, 2013. ISSN 00319155. doi: 10.1088/0031-9155/58/1/R1.

[210] Maria Seifert, Veronika Ludwig, Sebastian Kaeppler, Florian Horn, Pascal Meyer, Georg Pelzer, Jens Rieger, Daniel Sand, Thilo Michel, Jürgen Mohr, Christian Riess, and Gisela Anton. Talbot-Lau x-ray phase-contrast setup for fast scanning of large samples. *Scientific Reports*, 9(1), 2019. ISSN 20452322. doi: 10.1038/s41598-018-38030-3.

[211] C. Hauke, P. Bartl, M. Leghissa, L. Ritschl, S. M. Sutter, T. Weber, J. Zeidler, J. Freudenberger, T. Mertelmeier, M. Radicke, T. Michel, G. Anton, F. G. Meinel, A. Baehr, S. Auweter, D. Bondesson, T. Gaass, J. Dinkel, M. Reiser, and K. Hellbach. A preclinical Talbot–Lau prototype for x-ray dark-field imaging of human-sized objects. *Medical Physics*, 45(6):2565–2571, 2018. ISSN 00942405. doi: 10.1002/mp.12889.

[212] Regine Gradl, Martin Dierolf, Benedikt Günther, Lorenz Hehn, Winfried Möller, David Kutschke, Lin Yang, Martin Donnelley, Rhiannon Murrie, Alexander Erl, Tobias Stoeger, Bernhard Gleich, Klaus Achterhold, Otmar Schmid, Franz Pfeiffer, and Kaye Susannah Morgan. In vivo Dynamic Phase-Contrast X-ray Imaging using a Compact Light Source. *Scientific Reports*, 8:6788, 2018. ISSN 20452322. doi: 10.1038/s41598-018-24763-8.

[213] Regine Gradl, Martin Dierolf, Lin Yang, Lorenz Hehn, Benedikt Günther, Winfried Möller, David Kutschke, Tobias Stoeger, Bernhard Gleich, Klaus Achterhold, Martin Donnelley, Franz Pfeiffer, Otmar Schmid, and Kaye Susannah Morgan. Visualizing treatment delivery and deposition in mouse lungs using in vivo x-ray imaging. *Journal of Controlled Release*, 307:282–291, 2019. ISSN 18734995. doi: 10.1016/j.jconrel.2019.06.035.

[214] Hiroyuki Yoshioka, Yuho Kadono, Yoon Taek Kim, Hiromi Oda, Takashi Maruyama, Yuji Akiyama, Toshihide Mimura, Junji Tanaka, Mamoru Niitsu, Yoshihide Hoshino, Junko Kiyohara, Satoshi Nishino, Chiho Makifuchi, Atsushi Takahashi, Yuko Shinden, Norihiro Matsusaka, Kazuhiro Kido, and Atsushi Momose. Imaging evaluation of the cartilage in rheumatoid arthritis patients with an x-ray phase imaging apparatus based on Talbot-Lau interferometry. *Scientific Reports*, 10(1), 2020. ISSN 20452322. doi: 10.1038/s41598-020-63155-9.

[215] Christoph Jud, Florian Schaff, Irene Zanette, Johannes Wolf, Andreas Fehringer, and Franz Pfeiffer. Dentinal tubules revealed with X-ray tensor tomography. *Dental Materials*, 32(9):1189–1195, 2016. ISSN 01095641. doi: 10.1016/j.dental.2016.06.021.

[216] F. Horn, K. Gelse, S. Jabari, C. Hauke, S. Kaeppler, V. Ludwig, P. Meyer, T. Michel, J. Mohr, G. Pelzer, J. Rieger, C. Riess, M. Seifert, and G. Anton. High-energy x-ray Talbot-Lau radiography of a human knee. *Physics in Medicine and Biology*, 62 (16):6729–6745, 2017. ISSN 13616560. doi: 10.1088/1361-6560/aa7721.

[217] Sebastian Kaeppler, Jens Rieger, Georg Pelzer, Florian Horn, Thilo Michel, Andreas Maier, Gisela Anton, and Christian Riess. Improved reconstruction of phase-stepping data for Talbot–Lau x-ray imaging. *Journal of Medical Imaging*, 4(3): 034005, 2017. ISSN 23294310. doi: 10.1117/1.jmi.4.3.034005.

[218] Vincent Revol, Carina Hanser, and Michael Krzemnicki. Characterization of pearls by X-ray phase contrast imaging with a grating interferometer. *Case Studies in Nondestructive Testing and Evaluation*, 6:1–7, 2016. ISSN 22146571. doi: 10.1016/j.csndt.2016.06.001.

[219] Veronika Ludwig, Maria Seifert, Tracy Niepold, Georg Pelzer, Jens Rieger, Julia Ziegler, Thilo Michel, and Gisela Anton. Non-destructive testing of archaeological findings by grating-based X-ray phase-contrast and dark-field imaging. *Journal of Imaging*, 4(4):58, 2018. ISSN 2313433X. doi: 10.3390/jimaging4040058.

[220] Shivaji Bachche, Masahiro Nonoguchi, Koichi Kato, Masashi Kageyama, Takafumi Koike, Masaru Kuribayashi, and Atsushi Momose. Laboratory-based X-ray phase-imaging scanner using Talbot-Lau interferometer for non-destructive testing. *Scientific Reports*, 7(1):6711, 2017. ISSN 20452322. doi: 10.1038/s41598-017-07032-y.

[221] V. Revol, I. Jerjen, C. Kottler, P. Schütz, R. Kaufmann, T. Lüthi, U. Sennhauser, U. Straumann, and C. Urban. Sub-pixel porosity revealed by x-ray scatter dark field imaging. 110:044912, 2011. doi: 10.1063/1.3624592.

[222] Christian Hannesschläger, Vincent Revol, Bernhard Plank, Dietmar Salaberger, and Johann Kastner. Fibre structure characterisation of injection moulded short fibre-reinforced polymers by X-ray scatter dark field tomography. *Case Studies in Nondestructive Testing and Evaluation*, 3:34–41, 2015. ISSN 22146571. doi: 10.1016/j.csndt.2015.04.001.

[223] V. Revol, C. Kottler, R. Kaufmann, A. Neels, and A. Dommann. Orientation-selective X-ray dark field imaging of ordered systems. *Journal of Applied Physics*, 112:114903, 2012.

[224] Vincent Revol, Bernhard Plank, Rolf Kaufmann, Johann Kastner, Christian Kottler, and Antonia Neels. Laminate fibre structure characterisation of carbon fibre-reinforced polymers by X-ray scatter dark field imaging with a grating interferometer. *NDT & E International*, 58:64–71, 2013. ISSN 0963-8695. doi: 10.1016/j.ndteint.2013.04.012.

[225] Vincent Revol, Bernhard Plank, Christian Kottler, Johann Kastner, Rolf Kaufmann, Alex Dommann, and Antonia Neels. Laminate fibre structure characterisation by orientation-selective X-ray grating interferometry. In *5th Conference on Industrial Computed Tomography (iCT)*, pages 45–51, Wels, Austria, 2014.

[226] Christian Gusenbauer, Michael Reiter, Bernhard Plank, Dietmar Salaberger, Sascha Senck, and Johann Kastner. Porosity determination of carbon and glass fibre reinforced polymers using Phase-Contrast Imaging. *Journal of Nondestructive Evaluation*, 38:1, 2019. ISSN 15734862. doi: 10.1007/s10921-018-0529-6.

[227] Sascha Senck, Michael Scheerer, Vincent Revol, Bernhard Plank, Christian Hannesschläger, Christian Gusenbauer, and Johann Kastner. Microcrack characterization in loaded CFRP laminates using quantitative two- and three-dimensional X-ray dark- field imaging. *Composites Part A: Applied Science and Manufacturing*, 115:206–214, 2018. ISSN 1359-835X. doi: 10.1016/j.compositesa.2018.09.023.

[228] Sascha Senck, Michael Scheerer, Bernhard Plank, Christian Hannesschlaeger, and Johann Kastner. Characterization of fiber lay-up and defects in CFRP using Talbot-Lau grating interferometry. In *9th Conference on Industrial Computed Tomography*, Padova, Italia, 2019.

[229] N. Morimoto, K. Kimura, T. Shirai, T. Doki, S. Sano, A. Horiba, and K. Kitamura. Talbot-Lau interferometry-based X-ray imaging system with retractable and rotatable gratings for nondestructive testing. *Review of Scientific Instruments*, 91: 023706, 2020. ISSN 10897623. doi: 10.1063/1.5131306.

[230] Abhishek K. Pathak, Tomohiro Yokozeki, Masahiro Imada, and Kazuhiro Kido. In-situ observation of tensile failure mode in cross-ply CFRP laminates using Talbot-Lau interferometry. *Composite Structures*, 253:112758, 2020. ISSN 02638223. doi: 10.1016/j.compstruct.2020.112758.

[231] F. Yang, F. Prade, M. Griffa, I. Jerjen, C. Di Bella, J. Herzen, A. Sarapata, F. Pfeiffer, and P. Lura. Dark-field X-ray imaging of unsaturated water transport in porous materials. *Applied Physics Letters*, 105:154105, 10 2014. ISSN 00036951. doi: 10.1063/1.4898783.

[232] Friedrich Prade, Kai Fischer, Detlef Heinz, Pascal Meyer, Jürgen Mohr, and Franz Pfeiffer. Time resolved X-ray Dark-Field Tomography Revealing Water Transport in a Fresh Cement Sample. *Scientific Reports*, 6:29108, 2016. ISSN 20452322. doi: 10.1038/srep29108.

[233] Gerd Morren, Jun Gu, Hugo Sol, Bart Verleye, and Stepan Lomov. Stereolithography specimen to calibrate permeability measurements for RTM flow simulations. *Advanced Composites Letters*, 15(4):119–125, 2006. doi: 10.1177/096369350601500401.

[234] Gerd Morren, Massimo Bottiglieri, Sven Bossuyt, Hugo Sol, David Lecompte, Bart Verleye, and Stepan V Lomov. A reference specimen for permeability measurements of fibrous reinforcements for RTM. *Composites Part A: Applied Science and Manufacturing*, 40(3):244–250, 2009. ISSN 1359-835X. doi: 10.1016/j.compositesa.2008.11.011.

[235] F Sket, A Enfedaque, C Alton, C González, J M Molina-aldareguia, and J Llorca. Automatic quantification of matrix cracking and fiber rotation by X-ray computed tomography in shear-deformed carbon fiber-reinforced laminates. *Composites Science and Technology*, 90:129–138, 2014. ISSN 0266-3538. doi: 10.1016/j.compscitech.2013.10.022.

[236] B. J. Carroll. The accurate measurement of contact angle, phase contact areas, drop volume, and Laplace excess pressure in drop-on-fiber systems. *Journal of Colloid and Interface Science*, 57(3):488–495, 1976. doi: 10.1016/0021-9797(76)90227-7.

[237] Johannes Schindelin, Ignacio Arganda-Carreras, Erwin Frise, Verena Kaynig, Mark Longair, Tobias Pietzsch, Stephan Preibisch, Curtis Rueden, Stephan Saalfeld, Benjamin Schmid, Jean Yves Tinevez, Daniel James White, Volker Hartenstein, Kevin Eliceiri, Pavel Tomancak, and Albert Cardona. Fiji: An open-source platform for biological-image analysis. *Nature Methods*, 9(7):676–682, 7 2012. ISSN 15487091. doi: 10.1038/nmeth.2019.

[238] Stuart Berg, Dominik Kutra, Thorben Kroeger, Christoph N. Straehle, Bernhard X. Kausler, Carsten Haubold, Martin Schiegg, Janez Ales, Thorsten Beier, Markus Rudy, Kemal Eren, Jaime I. Cervantes, Buote Xu, Fynn Beuttenmueller, Adrian Wolny, Chong Zhang, Ullrich Koethe, Fred A. Hamprecht, and Anna Kreshuk. ilastik: interactive machine learning for (bio)image analysis. *Nature Methods*, 16:1226–1232, 2019. ISSN 15487105. doi: 10.1038/s41592-019-0582-9.

[239] Qingrong Xiong, Todor G. Baychev, and Andrey P. Jivkov. Review of pore network modelling of porous media: Experimental characterisations, network constructions and applications to reactive transport. *Journal of Contaminant Hydrology*, 192:101–117, 2016. ISSN 18736009. doi: 10.1016/j.jconhyd.2016.07.002.

[240] Yong Li, Yanmeng Chi, Chaojie Zhao, Yanan Miao, Shanling Han, and Long Chen. Modelling fluid flow in carbon fibre porous media based on X-ray microtomography and lattice Boltzmann method. *Composite Structures*, 300:116085, 2022. ISSN 02638223. doi: 10.1016/j.compstruct.2022.116085.

[241] Antonio Coppola. Unimodal and Bimodal Descriptions of Hydraulic Properties for Aggregated Soils. *Soil Science Society of America Journal*, 64(4):1252–1262, 2000. ISSN 03615995. doi: 10.2136/sssaj2000.6441252x.

[242] R. Allan Freeze. Three-dimensional, transient, saturated-unsaturated flow in a groundwater basin. *Water Resources Research*, 7(2):347–366, 1971. ISSN 19447973. doi: 10.1029/WR007i002p00347.

[243] Marcel G. Schaap and Feike J. Leij. Improved prediction of unsaturated hydraulic conductivity with the Mualem-van Genuchten model. *Soil Science Society of America Journal*, 64(3):843–851, 2000. doi: 10.2136/sssaj2000.643843x.

[244] Andre Peters, Wolfgang Durner, and Gerd Wessolek. Consistent parameter constraints for soil hydraulic functions. *Advances in Water Resources*, 34(10):1352–1365, 2011. ISSN 03091708. doi: 10.1016/j.advwatres.2011.07.006.

[245] John Hennig, Max Elfner, and Jacob Feder. MPh-py/MPh: MPh 1.1.1, 2021.

[246] Pauli Virtanen, Ralf Gommers, Travis E. Oliphant, Matt Haberland, Tyler Reddy, David Cournapeau, Evgeni Burovski, Pearu Peterson, Warren Weckesser, Jonathan Bright, Stéfan J. van der Walt, Matthew Brett, Joshua Wilson, K. Jarrod Millman, Nikolay Mayorov, Andrew RJ Nelson, Eric Jones, Robert Kern, Eric Larson, C. J. Carey, Ilhan Polat, Yu Feng, Eric W. Moore, Jake VanderPlas, Denis Laxalde, Josef Perktold, Robert Cimrman, Ian Henriksen, E. A. Quintero, Charles R. Harris, Anne M. Archibald, Antonio H. Ribeiro, Fabian Pedregosa, Paul van Mulbregt, and SciPy 1.0 Contributors. SciPy 1.0: fundamental algorithms for scientific computing in Python. *Nature Methods*, 17:261–272, 2020. doi: 10.1038/s41592-019-0686-2.

[247] Fuchang Gao and Lixing Han. Implementing the Nelder-Mead simplex algorithm with adaptive parameters. *Computational Optimization and Applications*, 51(1):259–277, 2012. ISSN 09266003. doi: 10.1007/s10589-010-9329-3.

[248] John A. Nelder and Roger Mead. A simplex method for function minimization. *The Computer Journal*, 7(4):308–313, 1965. doi: 10.1093/comjnl/7.4.308.

[249] O. Ippisch, H. Vogel, and P. Bastian. Validity limits for the van Genuchten – Mualem model and implications for parameter estimation and numerical simulation. *Advances in Water Resources*, 29:1780–1789, 2006. doi: 10.1016/j.advwatres.2005.12.011.

[250] Helena Teixidó, Baris Caglar, Vincent Revol, and Véronique Michaud. In-operando dynamic visualization of flow through porous preforms based on X-ray phase contrast imaging. *Composites Part A: Applied Science and Manufacturing*, 149:106560, 2021. ISSN 1359-835X. doi: 10.1016/j.compositesa.2021.106560.

[251] Sergey G. Abaimov, Oleg V. Lebedev, Viktor Grishaev, Bulat N. Gilmutdinov, and Iskander S. Akhatov. Edge flow profile under radial injection at constant pressure: Analytical predictions vs. experiment. *Composite Structures*, 242:112101, 2020. ISSN 02638223. doi: 10.1016/j.compstruct.2020.112101.

[252] Michael Chabior, Tilman Donath, Christian David, Manfred Schuster, Christian Schroer, and Franz Pfeiffer. Signal-to-noise ratio in x ray dark-field imaging using a grating interferometer. *Journal of Applied Physics*, 110:053105, 2011. ISSN 00218979. doi: 10.1063/1.3630051.

[253] W. Yashiro, Y. Terui, K. Kawabata, and A. Momose. On the origin of visibility contrast in x-ray Talbot interferometry. *Optics Express*, 18(16):16890–16901, 2010. doi: 10.1364/OE.18.016890.

[254] M. J. Berger, J. H. Hubbell, S. M. Seltzer, J. Chang, J. S. Coursey, R. Sukumar, D. S. Zucker, and K. Olsen. XCOM: Photon Cross Sections Database, 2010. URL `https://www.nist.gov/pml/xcom-photon-cross-sections-database`.

[255] Serguei Kuznetsov. X-ray Optics Calculator. URL `http://purple.ipmt-hpm.ac.ru/xcalc/xcalc_mysql/ref_index.php`.

[256] Helena Teixidó, Baris Caglar, and Véronique Michaud. Dual-scale visualization of resin flow for liquid composite molding processes. In *Composites Meet Sustainability – Proceedings of the 20th European Conference on Composite Materials*, pages 1007–1014, Lausanne, Switzerland, 2022. ISBN 978-2-9701614-0-0. doi: 10.5075/epfl-298799{_}978-2-9701614-0-0.

[257] Helena Teixidó, Guillaume Broggi, Baris Caglar, and Véronique Michaud. Measurement and modelling of dynamic fluid saturation in carbon reinforcements. *Composites Part A: Applied Science and Manufacturing*, 107520, 3 2023. ISSN 1359835X. doi: 10.1016/j.compositesa.2023.107520.

[258] A. Léger, J. M. Molina-Jordá, L. Weber, and A. Mortensen. Percolation and universal scaling in composite infiltration processing. *Materials Research Letters*, 3(1):7–15, 2014. ISSN 21663831. doi: 10.1080/21663831.2014.948692.

[259] Georgios Varnavides, Andreas Mortensen, and W. Craig Carter. Simulating infiltration as a sequence of pinning and depinning processes. *Acta Materialia*, 210, 2021. ISSN 13596454. doi: 10.1016/j.actamat.2021.116831.

[260] The Engineering TooBox. Surface Tension, 2005. URL `https://www.engineeringtoolbox.com/surface-tension-d_962.html`.

[261] G. Løvoll, M. Jankov, K. J. Måløy, R. Toussaint, J. Schmittbuhl, G. Schäfer, and Y. Méheust. Influence of viscous fingering on dynamic saturation-pressure curves in porous media. *Transport in Porous Media*, 86(1):305–324, 2011. ISSN 01693913. doi: 10.1007/s11242-010-9622-8.

[262] Bernd Schultze, Olaf Ippisch, Bernd Huwe, and Wolfgang Durner. Dynamic nonequilibrium during unsaturated water flow. In *International Workshop on Characterization and Measurement of the Hydraulic Properties of Unsaturated Porous Media*, Riverside, CA, 1999.

[263] S. Majid Hassanizadeh, Michael A. Celia, and Helge K. Dahle. Dynamic effect in the capillary pressure-saturation relationship and its impacts on unsaturated flow. *Vadose Zone Journal*, 1:38–57, 2002. doi: 10.2136/vzj2002.3800.

[264] Luwen Zhuang, C. J. Van Duijn, and S. Majid Hassanizadeh. The effect of dynamic capillarity in modeling saturation overshoot during infiltration. *Vadose Zone Journal*, 18:180133, 2019. doi: 10.2136/vzj2018.07.0133.

[265] S. Bottero, S. M. Hassanizadeh, P. J. Kleingeld, and T. J. Heimovaara. Nonequilibrium capillarity effects in two-phase flow through porous media at different scales. *Water Resources Research*, 47(10), 2011. ISSN 00431397. doi: 10.1029/2011WR010887.

[266] Sabine Manthey, S. Majid Hassanizadeh, and Rainer Helmig. Macro-scale dynamic effects in homogeneous and heterogeneous porous media. *Transport in Porous Media*, 58(1):121–145, 2005. ISSN 01693913. doi: 10.1007/s11242-004-5472-6.

[267] Yin Chen, Yadan Mao, Liu Yang, Wei Wei, Qingbang Meng, and Jianchao Cai. A comprehensive review of factors affecting dynamic capillary effect in two-phase flow. *Transport in Porous Media*, 144:33–54, 2022. ISSN 15731634. doi: 10.1007/s11242-021-01723-x.

[268] Ying Li, Chang Liu, Haitao Li, Shengnan Chen, Kuan Lu, Qihui Zhang, and Hongwen Luo. A review on measurement of the dynamic effect in capillary pressure. *Journal of Petroleum Science and Engineering*, 208:109672, 2022. ISSN 0920-4105. doi: 10.1016/j.petrol.2021.109672.

[269] Jian Chao Cai, Yin Chen, Jun Cheng Qiao, Liu Yang, Jian Hui Zeng, and Chen Hao Sun. Determination of dynamic capillary effect on two-phase flow in porous media: A perspective from various methods. *Petroleum Science*, 19(4):1641–1652, 2022. ISSN 19958226. doi: 10.1016/j.petsci.2022.01.017.

[270] Abay Molla Kassa, Sarah Eileen Gasda, Kundan Kumar, and Florin Adrian Radu. Impact of time-dependent wettability alteration on the dynamics of capillary pressure. *Advances in Water Resources*, 142:103631, 2020. ISSN 03091708. doi: 10.1016/j.advwatres.2020.103631.

[271] Shmulik P. Friedman. Dynamic contact angle explanation of flow rate-dependent saturation-pressure relationships during transient liquid flow in unsaturated porous media. *Journal of Adhesion Science and Technology*, 13(12):1495–1518, 1999. ISSN 01694243. doi: 10.1163/156856199X00613.

[272] C. D. Tsakiroglou, M. A. Theodoropoulou, and V. Karoutsos. Nonequilibrium capillary pressure and relative permeability curves of porous media. *AIChE Journal*, 49(10):2472–2486, 2003. doi: 10.1002/aic.690491004.

[273] C. D. Tsakiroglou, D. G. Avraam, and A. C. Payatakes. Transient and steady-state relative permeabilities from two-phase flow experiments in planar pore networks. *Advances in Water Resources*, 30:1981–1992, 2007. ISSN 0309-1708. doi: 10.1016/j.advwatres.2007.04.002.

[274] Viet Hoai Nguyen, Adrian P. Sheppard, Mark A. Knackstedt, and W. Val Pinczewski. The effect of displacement rate on imbibition relative permeability and residual saturation. *Journal of Petroleum Science and Engineering*, 52:54–70, 2006. ISSN 09204105. doi: 10.1016/j.petrol.2006.03.020.

[275] Abay Molla Kassa, Sarah E. Gasda, Kundan Kumar, and Florin A. Radu. Modeling of relative permeabilities including dynamic wettability transition zones. *Journal of Petroleum Science and Engineering*, 203:108556, 2021. ISSN 09204105. doi: 10.1016/j.petrol.2021.108556.

[276] D. E. Smiles, Georges Vachaud, and Michel Vauclin. A test of the uniqueness of the soil moisture characteristic during transient, nonhysteretic flow of water in a rigid soil. *Soil Science Society of Maeris Journal*, 35(4):534–539, 1971.

[277] Santosh Konangi, Nikhil K. Palakurthi, Nikolaos K. Karadimitriou, Ken Comer, and Urmila Ghia. Comparison of pore-scale capillary pressure to macroscale capillary pressure using direct numerical simulations of drainage under dynamic and quasi-static conditions. *Advances in Water Resources*, 147:103792, 2021. doi: 10.1016/j.advwatres.2020.103792.

[278] Xiaokang Guo, Runcong Liu, Jiang Wang, Sansan Shuai, Degan Xiong, Shuxin Bai, Nianmei Zhang, Xiufang Gong, and Xiaodong Wang. 3D actual microstructure-based modeling of non-isothermal infiltration behavior and void formation in liquid composite molding. *Applied Mathematical Modelling*, 94:388–402, 2021. ISSN 0307904X. doi: 10.1016/j.apm.2021.01.018.

[279] Sajjad Foroughi, Branko Bijeljic, and Martin J. Blunt. A closed-form equation for capillary pressure in porous media for all wettabilities. *Transport in Porous Media*, 145:683–696, 2022. ISSN 15731634. doi: 10.1007/s11242-022-01868-3.

[280] D. B. Das and S. M. Hasssanizadeh, editors. *Upscaling Multiphase Flow in Porous Media. From Pore to Core and Beyond*. Springer, Dordrecht, The Netherlands, 2005. ISBN 1-4020-3513-6. doi: 10.1007/1-4020-3604-3.

[281] Haiyong Zhang, Shunli He, Chunyan Jiao, Guohua Luan, Shaoyuan Mo, and Gang Lei. Investigation of dynamic effect of capillary pressure in ultra-low permeability sandstones. *Indian Geotechnical Journal*, 45(1):79–88, 2015. ISSN 22773347. doi: 10.1007/s40098-014-0109-3.

[282] Rumbidzai A. E. Nhunduru, Amir Jahanbakhsh, Omid Shahrokhi, Krystian L. Wlodarczyk, Susana Garcia, and M. Mercedes Maroto-Valer. The impact of wettability on dynamic fluid connectivity and flow transport kinetics in porous media. *Water Resources Research*, 58, 2022. doi: 10.1029/2021WR030729.

[283] Aubin Geoffre, Yanneck Wielhorski, Nicolas Moulin, Julien Bruchon, Sylvain Drapier, and Pierre Jacques Liotier. Influence of intra-yarn flows on whole 3D woven fabric numerical permeability: from Stokes to Stokes-Darcy simulations. *International Journal of Multiphase Flow*, 129:103349, 2020. ISSN 03019322. doi: 10.1016/j.ijmultiphaseflow.2020.103349.

[284] Aubin Geoffre, Maydine Ghestin, Nicolas Moulin, Julien Bruchon, and Sylvain Drapier. Bounding transverse permeability of fibrous media: a statistical study from random representative volume elements with consideration of fluid slip. *International Journal of Multiphase Flow*, 143:103751, 2021. ISSN 03019322. doi: 10.1016/j.ijmultiphaseflow.2021.103751.

[285] Aubin Geoffre, Nicolas Moulin, Julien Bruchon, and Sylvain Drapier. Reappraisal of Upscaling Descriptors for Transient Two-Phase Flows in Fibrous Media. *Transport in Porous Media*, 2023. ISSN 15731634. doi: 10.1007/s11242-023-01912-w.

[286] Luwen Zhuang, S. Majid Hassanizadeh, Chao Zhong Qin, and Arjen de Waal. Experimental investigation of hysteretic dynamic capillarity effect in unsaturated flow. *Water Resources Research*, 53:9078–9088, 2017. ISSN 19447973. doi: 10.1002/2017WR020895.

[287] Jassem Abbasi, Mojtaba Ghaedi, and Masoud Riazi. A multiscale study on the effects of dynamic capillary pressure in two-phase flow in porous media. *Korean Journal of Chemical Engineering*, 37(12):2124–2135, 2020. ISSN 19757220. doi: 10.1007/s11814-020-0645-8.

[288] Christopher Zahasky and Sally M. Benson. Spatial and temporal quantification of spontaneous imbibition. *Geophysical Research Letters*, 46(21):11972–11982, 2019. doi: 10.1029/2019GL084532.

[289] Behrouz Harimi, Mohsen Masihi, Abouzar Mirzaei-Paiaman, and Esmaeil Hamidpour. Experimental study of dynamic imbibition during water flooding of naturally fractured reservoirs. *Journal of Petroleum Science and Engineering*, 174:1–13, 2019. ISSN 09204105. doi: 10.1016/j.petrol.2018.11.008.

[290] Thomas Sweijen, Ehsan Nikooee, S. Majid Hassanizadeh, and Bruno Chareyre. The effects of swelling and porosity change on capillarity: DEM coupled with a pore-unit assembly method. *Transport in Porous Media*, 113:207–226, 2016. ISSN 15731634. doi: 10.1007/s11242-016-0689-8.

[291] Thomas Sweijen, S. Majid Hassanizadeh, and Bruno Chareyre. Unsaturated flow in a packing of swelling particles; a grain-scale model. *Advances in Water Resources*, 142, 2020. ISSN 03091708. doi: 10.1016/j.advwatres.2020.103642.

[292] Thomas Sweijen, S. Majid Hassanizadeh, Hamed Aslannejad, and Szymon Leszczynski. The effect of particle shape on porosity of swelling granular materials: Discrete element method and the multi-sphere approximation. *Powder Technology*, 360:1295–1304, 2020. ISSN 1873328X. doi: 10.1016/j.powtec.2019.09.036.

[293] Tian Chen, Mao Du, and Qiangling Yao. Evolution of hydraulic conductivity of unsaturated compacted Na-bentonite under confined condition—including the microstructure effects. *Materials*, 15:219, 2022. ISSN 19961944. doi: 10.3390/ma15010219.

[294] Zhi Wang, Jan Feyen, Donald R. Nielsen, and Martinus T. Van Genuchten. Two-phase flow infiltration equations accounting for air entrapment effects. *Water Resources Research*, 33(12):2759–2767, 1997. ISSN 00431397. doi: 10.1029/97WR01708.

[295] Zhi Wang, Jan Feyen, Martinus Th. Van Genuchten, and Donald R. Nielsen. Air entrapment effects on infiltration rate and flow instability. *Water Resources Research*, 34(2):213–222, 1998. ISSN 00431397. doi: 10.1029/97WR02804.

[296] Po Wei Huang, Bernd Flemisch, Chao Zhong Qin, Martin O. Saar, and Anozie Ebigbo. Relating Darcy-Scale Chemical Reaction Order to Pore-Scale Spatial Heterogeneity. *Transport in Porous Media*, 144(2):507–543, 2022. ISSN 15731634. doi: 10.1007/s11242-022-01817-0.

[297] M. Rücker, S. Berg, R. T. Armstrong, A. Georgiadis, H. Ott, A. Schwing, R. Neiteler, N. Brussee, A. Makurat, L. Leu, M. Wolf, F. Khan, F. Enzmann, and M. Kersten. From connected pathway flow to ganglion dynamics. *Geophysical Research Letters*, 42(10):3888–3894, 2015. ISSN 19448007. doi: 10.1002/2015GL064007.

[298] J. P. Stokes, D. A. Weitz, J. P. Goilub, A. Dougherty, M. O. Robbins, P. M. Chaikin, and H. M. Lindsay. Interfacial stability of immiscible displacement in a porous medium. *Physical review letters*, 57(14):1718–1721, 1986. doi: 10.1103/PhysRevLett.57.1718.

[299] Benzhong Zhao, Christopher W Macminn, and Ruben Juanes. Wettability control on multiphase flow in patterned microfluidics. 2016. doi: 10.1073/pnas.1603387113.

[300] Helmut Geistlinger, Iman Ataei-Dadavi, Sadjad Mohammadian, and Hans Jörg Vogel. The impact of pore structure and surface roughness on capillary trapping for 2-D and 3-D porous media: Comparison with percolation theory. *Water Resources Research*, 51(11):9094–9111, 2015. ISSN 19447973. doi: 10.1002/2015WR017852.

[301] Ran Holtzman and Enrico Segre. Wettability stabilizes fluid invasion into porous media via nonlocal, cooperative pore filling. *Physical Review Letters*, 115(16):164501, 2021. doi: 10.1103/PhysRevLett.115.164501.

[302] Mathias Trojer, Michael L Szulczewski, and Ruben Juanes. Stabilizing Fluid-Fluid Displacements in Porous Media Through Wettability Alteration. 054008:1–8, 2015. doi: 10.1103/PhysRevApplied.3.054008.

[303] Luman Zhang, Jian Wang, Carlos A. Fuentes, Dongxing Zhang, Aart Willem Van Vuure, Jin Won Seo, and David Seveno. Wettability of carbon nanotube fibers. *Carbon*, 122:128–140, 2017. ISSN 00086223. doi: 10.1016/j.carbon.2017.06.027.

[304] Si Qiu, Carlos A. Fuentes, Dongxing Zhang, Aart Willem Van Vuure, and David Seveno. Wettability of a single carbon fiber. *Langmuir*, 32(38):9697–9705, 9 2016. ISSN 15205827. doi: 10.1021/acs.langmuir.6b02072.

[305] Yi-ning Lee and Shu-min Chiao. Visualization of dynamic contact angles on cylinder and fiber. *Journal of Colloid and Interface Science*, 181(2):378–384, 1996. doi: 10.1006/jcis.1996.0394.

[306] Maria Jesus Vega, David Seveno, Ghislain Lemaur, Maria Helena Adão, and Joël De Coninck. Dynamics of the rise around a fiber: Experimental evidence of the existence of several time scales. *Langmuir*, 21:9584–9590, 10 2005. ISSN 07437463. doi: 10.1021/la051341z.

[307] J. S.U. Schell, M. Renggli, G. H. van Lenthe, R. Müller, and P. Ermanni. Micro-computed tomography determination of glass fibre reinforced polymer meso-structure. *Composites Science and Technology*, 66(13):2016–2022, 2006. ISSN 02663538. doi: 10.1016/j.compscitech.2006.01.003.

[308] M. A. Ali, R. Umer, K. A. Khan, and W. J. Cantwell. Application of X-ray computed tomography for the virtual permeability prediction of fiber reinforcements for liquid composite molding processes: A review. *Composites Science and Technology*, 184:107828, 2019. ISSN 02663538. doi: 10.1016/j.compscitech.2019.107828.

[309] I. Fatt. The network model of porous media. *AIME Petroleum Transactions*, 207:144–181, 1956. doi: 10.2118/574-G.

[310] J.-F Delerue, S. V. Lomov, R. S. Parnas, I. Verpoest, and M. Wevers. Pore network modeling of permeability for textile reinforcements. *Polymer Composites*, 24(3):344–357, 2003. doi: 10.1002/pc.10034.

[311] Yong Li, Yanmeng Chi, Shanling Han, Yanan Miao, and Long Chen. Investigation on CT characterization of pore structure in nylon-uncured rubber composite from a microscopic view. *Scientific Reports*, 11:15682, 2021. ISSN 20452322. doi: 10.1038/s41598-021-95178-1.

[312] Helena Teixidó and Véronique Michaud. Infiltration through fibrous carbon reinforcements, 2023.

[313] Frouke Hoogland, Peter Lehmann, Rajmund Mokso, and Dani Or. Drainage mechanisms in porous media: From piston-like invasion to formation of corner flow networks. *Water Resources Research*, 52(11):8413–8436, 2016. ISSN 19447973. doi: 10.1002/2016WR019299.

[314] Sahar Bakhshian, Harris Sajjad Rabbani, Seyyed Abolfazl Hosseini, and Nima Shokri. New Insights Into Complex Interactions Between Heterogeneity and Wettability Influencing Two-Phase Flow in Porous Media. *Geophysical Research Letters*, 47(14), 2020. ISSN 19448007. doi: 10.1029/2020GL088187.

[315] J. Bico and D. Quéré. Precursors of impregnation. *Europhysics Letters*, 61(3):348–353, 2003. ISSN 02955075. doi: 10.1209/epl/i2003-00196-9.

[316] Kamaljit Singh, Hannah Menke, Matthew Andrew, Qingyang Lin, Christoph Rau, Martin J. Blunt, and Branko Bijeljic. Dynamics of snap-off and pore-filling events during two-phase fluid flow in permeable media. *Scientific Reports*, 7:5192, 2017. ISSN 20452322. doi: 10.1038/s41598-017-05204-4.

[317] Kamaljit Singh, Michael Jung, Martin Brinkmann, and Ralf Seemann. Capillary-dominated fluid displacement in porous media. *Annual Reviews of Fluid Mechanics*, 51:429–449, 2019. doi: 10.1146/annurev-fluid-010518.

[318] Kamaljit Singh, Tom Bultreys, Ali Q. Raeini, Mosayeb Shams, and Martin J. Blunt. New type of pore-snap-off and displacement correlations in imbibition. *Journal of Colloid and Interface Science*, 609:384–392, 2022. ISSN 10957103. doi: 10.1016/j.jcis.2021.11.109.

[319] Helena Teixidó and Michaud. Véronique. 3D representation of meso-voids location and morphology within the fibrous pore space of three carbon fabrics, 2023.

[320] Martin J. Blunt, Branko Bijeljic, Hu Dong, Oussama Gharbi, Stefan Iglauer, Peyman Mostaghimi, Adriana Paluszny, and Christopher Pentland. Pore-scale imaging and modelling. *Advances in Water Resources*, 51:197–216, 2013. ISSN 03091708. doi: 10.1016/j.advwatres.2012.03.003.

[321] Paul Ross Thomson, Aizhan Aituar-Zhakupova, and Saswata Hier-Majumder. Image segmentation and analysis of pore network geometry in two natural sandstones. *Frontiers in Earth Science*, 6, 2018. ISSN 22966463. doi: 10.3389/feart.2018.00058.

[322] Y. Tanino and Martin J. Blunt. Capillary trapping in sandstones and carbonates: Dependence on pore structure. *Water Resources Research*, 48:08525, 2012. ISSN 00431397. doi: 10.1029/2011WR011712.

[323] Enno T. de Vries, Amir Raoof, and Martinus Th. van Genuchten. Multiscale modelling of dual-porosity porous media; a computational pore-scale study for flow and solute transport. *Advances in Water Resources*, 105:82–95, 2017. ISSN 03091708. doi: 10.1016/j.advwatres.2017.04.013.

[324] Mosayeb Shams, Kamaljit Singh, Branko Bijeljic, and Martin J. Blunt. Direct numerical simulation of pore-scale trapping events during capillary-dominated two-phase flow in porous media. *Transport in Porous Media*, 138(2):443–458, 2021. ISSN 15731634. doi: 10.1007/s11242-021-01619-w.

[325] Tarik Saif, Qingyang Lin, Ying Gao, Yousef Al-Khulaifi, Federica Marone, David Hollis, Martin J. Blunt, and Branko Bijeljic. 4D in situ synchrotron X-ray tomographic microscopy and laser-based heating study of oil shale pyrolysis. *Applied Energy*, 235:1468–1475, 2019. ISSN 03062619. doi: 10.1016/j.apenergy.2018.11.044.

[326] J. Dewanckele, M. A. Boone, F. Coppens, D. van Loo, and A. P. Merkle. Innovations in laboratory-based dynamic micro-CT to accelerate in situ research. *Journal of Microscopy*, 277(3):197–209, 2020. ISSN 13652818. doi: 10.1111/jmi.12879.

[327] Alberto Aliseda and Theodore J Heindel. X-Ray Flow visualization in multiphase flows. *Annual Review of Fluid Mechanics*, 53(1), 2020. doi: 10.1146/annurev-fluid-010719-060201.

[328] Katherine J. Dobson, Sophia B. Coban, Samuel A. McDonald, Joanna N. Walsh, Robert C. Atwood, and Philip J. Withers. 4-D imaging of sub-second dynamics in pore-scale processes using real-time synchrotron X-ray tomography. *Solid Earth*, 7 (4):1059–1073, 2016. ISSN 18699529. doi: 10.5194/se-7-1059-2016.

[329] M. Strobl, I. Manke, N. Kardjilov, A. Hilger, M. Dawson, and J. Banhart. Advances in neutron radiography and tomography. *Journal of Physics D: Applied Physics*, 42(24):243001, 2009. ISSN 00223727. doi: 10.1088/0022-3727/42/24/243001.

[330] Paul Scherrer Institute. Comparison to X-ray. URL `http://psi.ch/wU1Q`.

[331] Mohamad Yehya, Edward Andò, Frédéric Dufour, and Alessandro Tengattini. Fluid-flow measurements in low permeability media with high pressure gradients using neutron imaging: Application to concrete. *Nuclear Instruments and Methods in Physics Research, Section A: Accelerators, Spectrometers, Detectors and Associated Equipment*, 890:35–42, 2018. ISSN 01689002. doi: 10.1016/j.nima.2018.02.039.

[332] Mirhasan Hosseini, Muhammad Arif, Alireza Keshavarz, and Stefan Iglauer. Neutron scattering: A subsurface application review. *Earth-Science Reviews*, 221:103755, 2021. ISSN 00128252. doi: 10.1016/j.earscirev.2021.103755.

[333] Alessandro Tengattini, Nicolas Lenoir, Edward Andò, Benjamin Giroud, Duncan Atkins, Jerome Beaucour, and Gioacchino Viggiani. NeXT-Grenoble, the Neutron and X-ray tomograph in Grenoble. *Nuclear Instruments and Methods in Physics Research, Section A: Accelerators, Spectrometers, Detectors and Associated Equipment*, 968:163939, 2020. ISSN 01689002. doi: 10.1016/j.nima.2020.163939.

[334] Hani Cheikh Sleiman, Alessandro Tengattini, Matthieu Briffaut, Bruno Huet, and Stefano Dal Pont. Simultaneous x-ray and neutron 4D tomographic study of drying-driven hydro-mechanical behavior of cement-based materials at moderate temperatures. *Cement and Concrete Research*, 147:106503, 2021. ISSN 00088846. doi: 10.1016/j.cemconres.2021.106503.

[335] NMI3. Neutron imaging – past, present and future, 2012. URL `https://nmi3.eu/news-and-media/neutron-imaging-past-present-and-future.html`.

[336] Atma Sharma, Budhaditya Hazra, C. B. Gupt, Sreedeep Sekharan, and M. ASCE. Incorporating global distribution with site-specific data for probabilistic analysis of soil-water characteristic curve of bentonite. *Journal of Hazardous, Toxic, and Radioactive Waste*, 25(3):06021003, 2021. doi: 10.1061/(ASCE)HZ.2153-5515.0000624.

[337] Atma Prakash, Budhaditya Hazra, and Sreedeep S. Probabilistic analysis of soil-water characteristic curve using limited data. *Applied Mathematical Modelling*, 89:752–770, 2021. ISSN 0307904X. doi: 10.1016/j.apm.2020.08.023.

Helena Teixidó

Ph.D. student in Material Science

teixidohelena@gmail.com | +41 78 686 41 81 | St.Prex, Switzerland

Expertises

- Materials science
- Applied research
- Textiles
- Composite materials
- Flow through porous media
- X-ray imaging
- Image analysis
- Computational mechanics

Technical skills

Material Characterization

- Permeability measurement
- Mechanical testing
- Rheology
- Image analysis
- Microscopy

Software

- Matlab
- Image J
- Avizo
- Illustrator
- Microsoft Office
- LaTeX
- Solidworks
- Comsol

Languages

Catalan - mother tongue
Spanish - mother tongue
French - fluent
English - fluent

Activities

Work Experience

ÉCOLE POLYTECHNIQUE FÉDÉRALE DE LAUSANNE - EPFL, Switzerland

LABORATORY FOR PROCESSING OF ADVANCED COMPOSITES - LPAC

2018-2023 (4 years)

Ph. D. Assistant

Objective: Develop a visualization technique to in-situ track the infiltration of polymeric resins though fibrous preform to deeply probe the flow kinetics.

Main activities:

- Multidisciplinary research, project management, laborator work, data analysis, presentation of results and writing of scientific papers.
- Teaching assistant and supervision of students.

LABORATORY OF APPLIED MECHANICS AND RELIABILITY ANALYSIS - LMAF

2017-2018 (9 months)

Mechanical Engineer

Role: Development of a testing methodologoy to set the mechanical behaviour of composite windsurf masts by means of computational mechanics (FEM) and 3 point-bending flexural tests.

LABORATORY FOR PROCESSING OF ADVANCED COMPOSITES - LPAC

2017 (6 months)

Research Assistant

Role: Perform permeability experiments of textiles and characterization of physical properties of a TPU foam used in Red Cross prosthesis.

ADVANCED OXIDATION PROCESSES GROUP - GPAO

2016 (3 months)

Research Assistant

Role: Development of a glass fibre nonwoven coated with TiO_2 decorated with Cu for wastewater treatments.

Education

UNIVERSITAT POLITÈCNICA DE CATALUNYA - UPC, Spain

2014-2016

Master in Engineering of Fibrous Materials Technologies

Exchange program at Gent Univeriteit, Belgium

Master thesis: "TiO_2 functionalized nanofibrous membranes for water filtration".

Student intership: Perform corona and low-pressure plasma surface treatments on flax fiber with the aim of developping biogegradable composites.

2014-2016

Bachelor and Master in Mechanical Engineering (Materials speciality)

Exchange program at École de Technologie Supérieure (ETS), Canada

Publications

2023 — MEASUREMENT AND MODELLING OF DYNAMIC FLUID SATURATION IN CARBON REINFORCEMENTS
Composites Part A: Applied Science and Manufacturing
Helena Teixidó, Guillaume Broggi, Baris Caglar, Véronique Michaud

2022 — CAPILLARY EFFECTS IN FIBER REINFORCED POLYMER COMPOSITE PROCESSING: A REVIEW
Frontiers in Materials
Helena Teixidó*, Jeroen Staal*, Baris Caglar, Véronique Michaud
*same contribution

2021 — IN-OPERANDO DYNAMIC VISUALIZATION OF FLOW THROUGH POROUS PREFORMS BASED ON X-RAY PHASE CONTRAST IMAGING
Composites Part A: Applied Science and Manufacturing
Helena Teixidó, Baris Caglar, Vincent Revol, Véronique Michaud

2017 — PERMEABILITY AND CAPILLARY EFFECTS IN A CHANNEL-WISE NON-CRIMP FABRIC
Composites Part A: Applied Science and Manufacturing
Damiano Salvatori, Baris Caglar, Helena Teixidó, Véronique Michaud

2017 — TiO_2 FUNCTIONALIZED NANOFIBROUS MEMBRANES FOR REMOVAL ORGANIC (MICRO)POLLUTANTS FROM WATER
Separation and Purification Technology
Jozefien Geltmeyer, Helena Teixidó, Mieke Meire, Thibaut Van Acker, Koen Deventer, Frank Vanhaecke, Stijn Van Hulle, Klaartje De Buysser, Karen De Clerck

2017 — Cu-DECORATED RASCHIG-TiO_2 RINGS INDUCING MB REPETITIVE DISCOLORATION WITHOUT RELEASE OF Cu-IONS UNDER SOLAR LIGHT
ACS Applied Materials & Interfaces Journal
Laura Suárez, Zhang Wei, Helena Teixidó, Rosendo Sanjinés, Michaël Bensimon, César Pulgarín, John Kiwi

Conferences and Seminars

2022 — 20TH EUROPEAN CONFERENCE ON COMPOSITES MATERIALS - ECCM20
Lausanne, Switzerland. Oral Presentation

2022 — EDMX RESEARCH DAY
Lausanne, Switzerland. Oral Presentation

Personnal Information

Nationality	Spanish
Place of residence	Switzerland (B Permit)
Date of birth	09/08/1991
Driving licence	A1, B
Marital status	Single